Fatigue Crack Growth Behaviour of Cobalt-Based and Nickel-Based Superalloy Processed by Selective Laser Melting

Amir Anuar

A thesis submitted to Auckland University of Technology in fulfilment of the requirements for the degree of Doctor of Philosophy (PhD)

2021

School of Engineering, Computer and Mathematical Sciences

Abstract

The production of cobalt-based and nickel-based superalloys via Selective Laser Melting (SLM) has been successfully applied in low-mass production, particularly in producing components/equipment for the spacecraft and medical industries. SLM technique allows complex and customised parts to be produced rapidly, replacing the traditional process of investment casting and machining. The major concern in terms of trustworthiness and durability of SLM parts is its performance under fatigue loading (cyclic loading), which is the most common mode of mechanical failure in engineering structures. Although significant research has been conducted in optimising SLM process parameters, changes in building direction (BD) and laser power (P) can cause variation in microstructure which consequently affecting its mechanical properties. BD orientations of an SLM part significantly affect its columnar grain structure, while P settings influence the shape/size of its meltpool boundary.

Currently, there is a lack of research reported on the Fatigue Crack Growth Rate (FCGR) behaviour of SLM superalloys. FCGR studies provide a relationship between stress intensity factor (ΔK) and crack growth rate (da/dN), which can be used to predict the life of a structure that experiences cyclic loading. Most available literatures focus on discovering the differences between the FCGR parameters (FCGR threshold: ΔK_{th} and Paris constants: C and, m) for samples with different BD orientations, or between SLM build samples and traditionally build samples. Literature has not critically investigated the crack growth pathway in SLM's columnar grain structure, which influences the FCGR resistance, thus affecting the FCGR parameters. Since there is no FCGR experiment reported for SLM Co-Cr-Mo and Inconel 738 superalloys, these two materials will be used to fill the research gap. Therefore, by conducting FCGR experiment, which allows the monitoring of a controlled crack movement, the aim of this PhD research aims to investigate the effect of BD and P on the crack growth pathway of SLM superalloys.

The FCGR experiments in this study were conducted in accordance with ASTM E647 standard. FCGR graphs were generated by using standard Compact tension (CT) specimens, processed at selected BD orientations and P settings. In addition, interrupted FCGR tests were performed to produce microstructure samples with visible crack growth history. The mode of fracture and detail observations of the crack growth pathway was attained through SEM and EBSD analysis.

Based on the findings in this study, the effect of BD in relation to crack growth direction (C), either C⊥BD or C//BD on the FCGR parameter of SLM Co-Cr-Mo is contrary to the FCGR study that was reported in the literature for SLM Co-Cr-W. In this study, the FCGR threshold value (ΔK_{th}) is higher, and the values of C and m in Paris equation are slightly lower for C//BD samples

than the values for C⊥BD samples, respectively. Failure analysis has revealed that the effects of the commonly known defect, lack of fusion (LOF), on both ΔK_{th} and FCG rate are weak. It has been identified that crack has mainly propagated in a transgranular manner, consistent with the observation of the crack path being more tortuous, with a higher FCGR resistance determined in C//BD samples than in C⊥BD samples. This is due to the difference in the size of crack segment, which is BD- and thus grain length-dependent.

Fractographic analysis on SLM Inconel 738's samples revealed that majority of the cracks propagated transgranularly. Nevertheless, the minor occurrence of intergranular fracture (crack travelling through the grain boundaries) has deviated the crack pathway, especially for the C45BD sample. The occurrence of intergranular fracture is mainly dependent on the orientation of the grain boundary, i.e. crack does not propagate through a grain boundary that is perpendicular to the crack growth direction. The C45BD sample (crack growth direction 45° to BD) in SLM Inconel 738 have the highest threshold value and the roughest fractured surface compared to the C//BD and C⊥BD samples. The rough fractured surface in C45BD sample is caused by the continuous crack branching triggered by the constant encounter of the crack with grain boundaries that is orientated 45° to the crack growth direction. Consequently, a continuously high crack retardation effect is maintained throughout the threshold region which contributed to a higher FCGR resistance. On the other hand, because of the BD-dependent grain orientation, the cracks in the C//BD and C⊥BD have significantly lower chance of encountering a grain boundary that is orientated 45° to the crack growth direction, which resulted in a smooth surface fracture for both sample types. In addition, FCGR experiment of SLM Inconel 718 was also conducted in this thesis. Fractographic analysis revealed that the grain boundaries in SLM 718 are more brittle compared to the grain boundaries in SLM Inconel 738. Therefore, intergranular fracture is more dominant in SLM 718 compared to SLM 738 which resulted in a different crack growth pathway behaviour.

This thesis provides new understanding on the crack growth behaviour of SLM superalloy, highlighting the importance of the BD orientation in SLM superalloys and how it can influence the crack growth behaviour.

Acknowledgement

I would like to thank my supervisor, Prof. Zhan Chen for giving me the opportunity to join his research team and providing guidance throughout this research. Thank you for your advice and critical feedback, and for teaching me the methodology to present the research work as clearly as possible. Thank you for your support and encouragement. Thank you especially for reading my thesis even when you were on holiday. I would also like to thank my co-supervisor Dr. Maziar Ramezani, especially for your involvement in my PGR9 process and for checking up on my progress.

I would also like to express my gratitude to my parents. Your prayers and encouragement have kept me going in this challenging time. I am grateful for the time that you put aside to read and provide feedback on the drafts of my thesis. I am very thankful that both of you have nothing but love and support for me throughout my journey. I would not be where I am today if it wasn't for the both of you. To the rest of my family members, thank you for all your support, and for touching base every now and then making sure that I'm fine.

A special thanks of mine goes to my other half for her understanding and continuous support. Thank you for motivating me throughout my PhD, for keeping me companied during the long hours of writing including on weekends. Thank you for running and boxing with me, and for understanding when I was too busy writing and refused to run.

I would also like to extend my gratitude to Dr. Teresa Guraya. Thank you for the support that you have given me throughout my project, for printing the Inconel samples and the TEM analysis. Thank you for still checking up on me from time to time even after you left New Zealand to go back to Spain.

To Dr. Yuan Tao, thank you for your help with the SEM machine. I would also like to thank Mr. Mark Masterton and Mr. Jim Crossen for assisting me in the mechanical lab. To Mr. Ross Jamieson, thank you for wire-cutting my samples. Thank you to Ms. Louise Burnett for showing me and assisting me in the chemistry lab with the etching of my samples.

To my lab mates, I am grateful that each one of you made the time and effort to attend every meeting when I had to present my findings. The advice and feedback that came from all of you have not only improved my presentation skills, but also have given me an insight from a different point of view.

Table of Content

Contents

List of Figures

List of Tables

Nomenclature

ΔK	Stress intensity factor range
Θ	SLM laser spot size diameter
α	Normalised crack size
f	Frequency
µm	Micrometer
v	Displacement measurement between two points
a	Crack size
a_c	Critical crack size
AM	Additive manufacturing
ASTM	American Society for testing and materials
B	Thickness
BCT	Body centred tetragonal
BD	Build direction
BJ	Binder jetting
C	Paris constant
C//BD	Crack growth parallel to the SLM building direction
C⊥BD	Crack growth perpendicular to SLM building direction
C45BD	Crack growth direction 45º to BD
CAD/CAM	Computer-aided design / computer-aided manufacturing
CD	Coarse dendritic
Co-Cr-Mo	Cobalt chrome molybdenum
Co-Cr-Mo-Ni-Fe	Cobalt chrome molybdenum nickel iron
Co-Cr-W	Cobalt chromium tungsten
Co-Cr-W-Ni	Cobalt chromium tungsten nickel
COD	Crack opening displacement
CT	Compact tension
DLD	Direct laser deposition
E	Elastic modulus
EBM	Electron beam melting
EBSD	Electron backscatter diffraction
EDS	Energy dispersive x-ray spectroscopy
EDX	Energy dispersive x-ray

EPD	Electric potential difference
F	Force
f_{LOF}	Lack of fusion percentage
F_{ra}	Fractured surface roughness
FAA	Federation aviation administration
FCC	Face centred cubic
FCG	Fatigue crack growth
FCGR	Fatigue crack growth rate
FE	Fine equiaxed structure
FIB	Focused ion beam
h	Layer thickness in SLM
HCF	High cycle fatigue
HCP	Hexagonal close-packed crystal structures
HIP	Hot isostatic pressing
Hz	Hertz
In625	Inconel 625
In718	Inconel 718
In738	Inconel 738
K	Stress intensity factor
K_{1C}	Fracture toughness
K_c	Critical SIF value
LC	Low carbon
LCF	Low cycle fatigue
LEFM	Linear elastic fractured mechanics
LENS	Laser engineered net shaping
LOF	Lack of fusion
m	Paris constant
Mm	Millimetre
MPa	Megapascal
N	Number of cycles
NDE	Non-destructive evaluation
NDT	Non-destructive test
Ni	Nickel
P	Laser power
$P_{area\%}$	Area percentage of pores

$\mathbf{P_{max}}$	SLM machine maximum laser power
$\mathbf{P_{TK}}$	Meltpool penetration depth
Pb	Lead
PBF	Powder bed fusion
Q	Heat flux
R	Loading ratio
$\mathbf{R_a}$	Surface roughness
$\mathbf{r_p}$	Plastic zone length along the crack axis
Re	Rhenium
RICC	Roughness-induced crack closure
s	Hatching distance in SLM
$\mathbf{S_Y}$	Yield stress
$\mathbf{S_w}$	Working stress
SL	Sheet lamination
SEM	Scanning electron microscope
Si	Silicon
SIF	Stress intensity factor
SLM	Selective laser melting
SMIT	Strain-induced-martensite-transformation
SS	Scanning strategy
TEM	Transmission electron microscope
Ti	Titanium
UTS	Ultimate tensile strength
v	Laser speed
W	width
$\mathbf{W_{TK}}$	Meltpool width
Zr	Zirconium

Attestation of Authorship

I hereby declare that this submission is my own work and that, to the best of my knowledge and belief, it contains no material previously published or written by another person (except where explicitly defined in the acknowledgements), nor material which to a substantial extent has been submitted for the award of any other degree or diploma of a university or other institution of higher learning.

Auckland

Signature :

Name : ANUAR, AMIR

1 Introduction

1.1 Background on fatigue study for additively manufactured materials

1.1.1 An introduction to Additive Manufacturing (AM)

The American Society for Testing and Materials (ASTM) defined additive manufacturing (AM) as the "process of joining materials to make objects from three-dimension (3D) model data, usually layer upon layer, as opposed to subtractive manufacturing methodologies" [1]. The AM technique poses significant advantages over conventional manufacturing techniques, which includes highly versatile geometric capabilities and lower human interaction requirements [2]. In addition, the AM technique also offers a smaller operational footprint, lower material waste, and a direct translation from digital design data to the manufacturing process [3]. The assembly process during manufacturing could also be reduced as fewer number of parts are required, thus lowering the overall production cost [4-7].

Metallic AM technology can generally be classified into two main categories: 1) powder bed fusion (PBF), and 2) direct laser deposition (DLD). PBF uses a bed of metallic powder stock as the feeding system, such as the selective laser melting (SLM) printer and electron beam melting (EBM) printer. On the other hand, DLD uses a blown metal powder system as the feeding system, such as the laser engineered net shaping (LENS) [4]. Other AM systems such as binder jetting (BJ) and sheet lamination (SL) are less commonly used while liquid metal extrusion [8] and material jetting [9, 10] are still in the stage of development with no commercial availability. The near-future potential for these AM technologies is very promising, with plenty of research opportunity in material science, particularly in understanding the interrelations between its process parameters and the material's property. Table 1 below lists some of the commercial AM systems that are currently available, including their layer thickness range, source of laser power, and their respective manufactures.

Table 1 Example of commercially available metallic AM system [11]

Manufacturer	System	Process	Layer thickness, µm	Laser focus diameter, µm	Energy source
Concept laser	M1 cusing	PBF(SLM)	20-80	50	Fiber laser 200-400 W
Sisma	MYSINT300	PBF(SLM)	20-50	100-500	Fiber laser 500 W
SLM Solutions	SLM500	PBF(SLM)	20-74	80-115	Quad fiber lasers 4 × 700 W
Realizer	SLM300i	PBF(SLM)	20-100	N/A	Fiber laser 400-1000 W
Farsoon	FS271 M	PBF(SLS)	20-80	40-100	Yb-fiber laser, 200 W
EOS	M 400	PBF(DMLS)	N/A	90	Yb-fiber laser, 1000 W
Arcam AB	Arcam Q20plus	PBF(EBM)	140	…	Electron beam 3000 W
Optomec	LENS Print Engine	DED(LENS)	25	…	IPG fiber laser 1-2 kW
Sciaky	EBAM 300	DED (wire feed)	N/A	…	Electron beam
Trumpf	TruLaser Cell Series 7000	DED (powder feed)	N/A	…	CO2 laser (15,000 W) or YAG laser (6600 W)
ExOne	M print	BJ	150	…	…
Fabrisonic	SonicLayer 7200	SL(UAM)	150	…	20 kHz ultrasonic vibration sonotrode

SLM is one of the most commercially available metallic AM printers. SLM uses a high-power laser beam that passes through a system of lenses which is subsequently reflected by a scanner-mirror. The scanner-mirror controls the laser spot movement on the planar platform surface (in X and Y direction), melting the metal powder that spreads on top of it. After a layer of the metal powder has been selectively melted, the building platform moves downwards (in the Z direction) to allow a new layer of fresh powder to be spread on top of the building platform (above the previous layer). The laser scanning process repeats layer-by-layer until the whole structure is completed, turning metal powder into a meltpool that solidifies almost immediately. This layer-by-layer scanning process is illustrated in Figure 1, which highlights the unique structure of repeated "welded-like" metals.

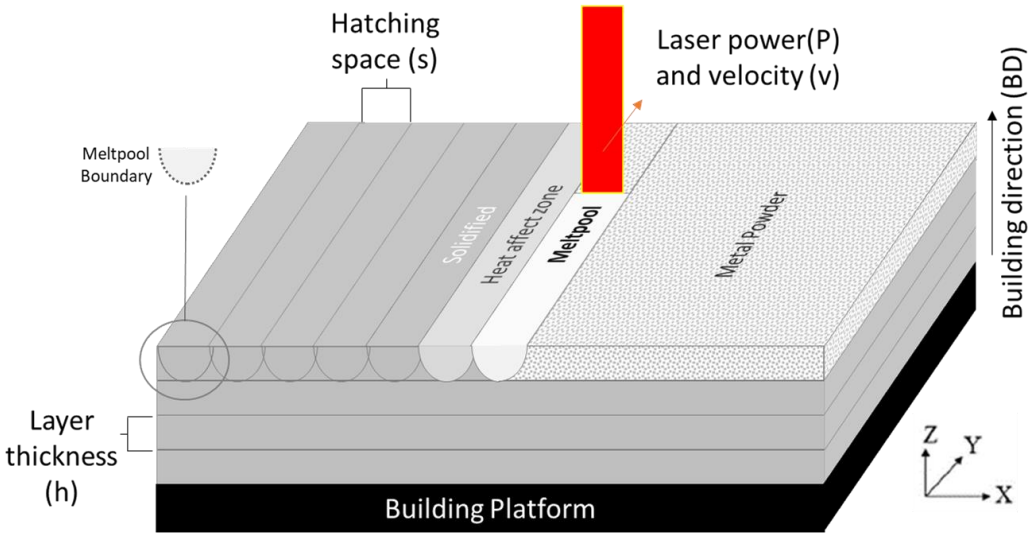

Figure 1 Schematic illustration of an SLM scanning process, highlighting its process parameters: P, v, s, h and BD.

Figure 1 identifies five major SLM process parameters namely: Laser power (P), scanning velocity (v), layer thickness (h), hatching space (s), and building direction (BD). These SLM parameters determine the amount of energy transferred by the laser beam, which affects the thermal history in the formation of the meltpool during the solidification process. The amount of energy can be described as the energy for a unit volume of material in a unit of time, $E = P / (v \times h \times s)$. Consequently, these parameters regulate the shape/size of the meltpool boundary, affecting grain size and number of defects presence in the material [12-14]. Another important SLM parameter is the building direction (BD) which refers to the direction of printing, as illustrated in Figure 1. Generally, the distribution and orientation of the grains are strongly influence by the BD.

SLM has penetrated industries that focus on low volume production of highly customised part such as the medical industries [11]. Customised medical implants/equipment can be produced rapidly at a reasonable price [15, 16], replacing the relatively slow traditional process of investment casting and machining. In addition, AM functional parts have also gained attention in low mass production industries, with applications in the production of complex aircraft engine components [17, 18], spacecraft components [19, 20], and automobile parts [21]. Examples of actual functioning parts produced by SLM are shown in Figure 2 below.

Figure 2 Example of functional additive manufacturing parts (a) Boeing's 777X aircraft fuel nozzle fabricated by General Electric (b) Cobalt-chrome tooth caps and crown produced by SLM Solution Group AG (c) Knee replacement implant produced by Arcam

While SLM manufacturing technique seem promising, its full potential, particularly with regard to its suitability for the production of load bearing parts (i.e. structural parts), has not be fully established to date [22]. The lack of research in the fatigue properties of SLM fabricated parts is currently one of the main challenges that prevent continuous adoption of SLM into industries [5, 7, 22]. Although significant research has been conducted in optimising the process parameters of SLM [4], any changes in building geometry and building direction will cause variation in microstructure and consequently affecting the mechanical properties of the part [23, 24]. Therefore, there are still significant gaps to be filled in establishing the relationship between process parameters, microstructure, and mechanical performance of SLM parts, particularly its fatigue behaviour [25].

1.1.2 Fatigue behaviours of SLM materials

In general, the mechanical properties of SLM parts under static loading, as assessed by the tensile test, hardness test, and compressive test are comparable to the conventionally (i.e. casting and forging) fabricated parts [26]. A major concern in terms of trustworthiness and durability of SLM parts is the performance under fatigue loading (cyclic forces), which is the most common mode of mechanical failure in engineering structures [22, 23, 27]. Contrary to mechanical failures that occur due to static loadings, fatigue failures are mostly a local phenomenon influenced by microstructure heterogeneity, impurities, and stress concentration. Therefore, it is very important to thoroughly understand the relationship between the fatigue damage mechanism and the microstructures of SLM materials in order to improve the durability and trustworthiness of SLM parts.

1.1.2.1 Fatigue endurance factor 1: Microstructural defects

The high cycle fatigue (HCF) test for 17-4 PH Stainless Steel reported by Yadollahi et al. [23] highlights one of the most critical fatigue endurance factors for SLM materials, namely microstructure defects such as voids and lack of fusion (LOF). The fractography of the specimen's fractured surface reported by Yadollahi et al. in Figure 3 shows the presence of

microstructure defects near the surface of the specimen, which accelerate the development of cracks at the initiation stage, thus reducing the fatigue life. It is widely known that the size, shape, and location of the defects play an important factor in SLM fatigue performance [23, 28]. The defects in SLM materials could take various shapes due to different reasons; for instance, it may be spherical-shaped due to air form the vapour bubbles during key-hole meltpool formation, be irregularly-shaped due to un-melted powder, or be slit/sharply shaped due to a lack of fusion (LOF). Furthermore, in terms of the defect's location, result of HCF test conducted by Leuders et al. [29] on SLM TiAl64 suggests that defects located far from the surface do not exceed the detrimental and dominating influence of a near-surface defects with regards to crack initiation.

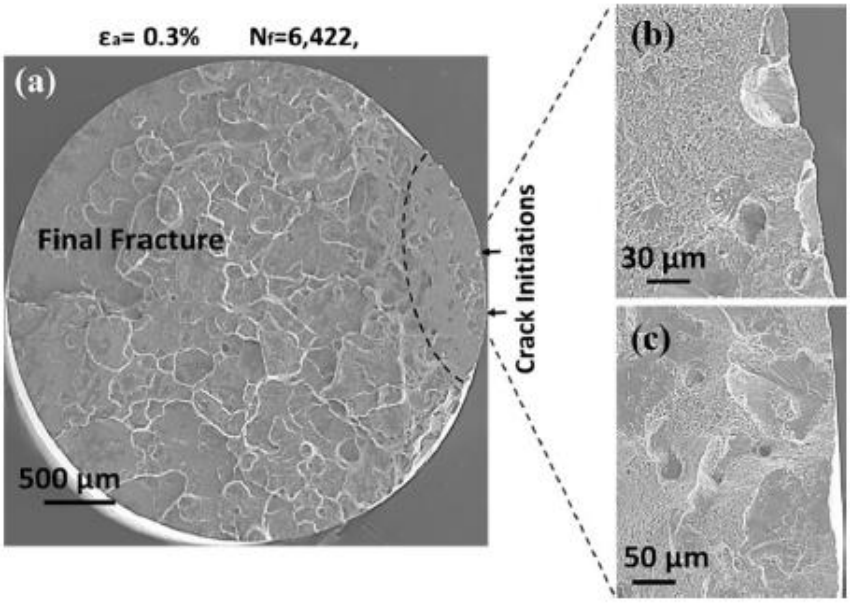

Figure 3 Facture surface of SLM stainless steel, highlighting the microstructure defects near the crack initiation site which resulted in a low fatigue life a) overall view b) high magnification image of pores c) high magnification image of LOF [23]

Post manufacturing heat treatment such as hot isostatic pressing (HIP) is often suggested for SLM parts in order to reduce the amount of microstructure defects, as well as to create a regular and uniform grain structure that can improves its fatigue performance [30-32]. HIP is a combined action of high temperature and pressure that can homogenise the microstructure of SLM parts, as well as densifying the material. Figure 4 shows a microscopy image of how the HIP process (1200ºC at 100MPa for 4 hours) on SLM Co-Cr-Mo alloy has completely changed the weld-like SLM structure and eliminate the presence of LOF. In addition, Kasperovich et al. [33] reported

a significant increase in fatigue life (of a HCF test) for SLM TiAl6V4 after HIP process (900ºC at 100MPa for 2 hours). Figure 5 shows evidence of a reduction in defects after the HIP process, with smoother and fewer crack initiation sites on its fractured surface compared to the sample without HIP process. Note that the HIP sample in Figure 5 is also machined to reduce its surface roughness, which has also contributed to the significant difference between the fatigue life of the as-build and the HIP conditions.

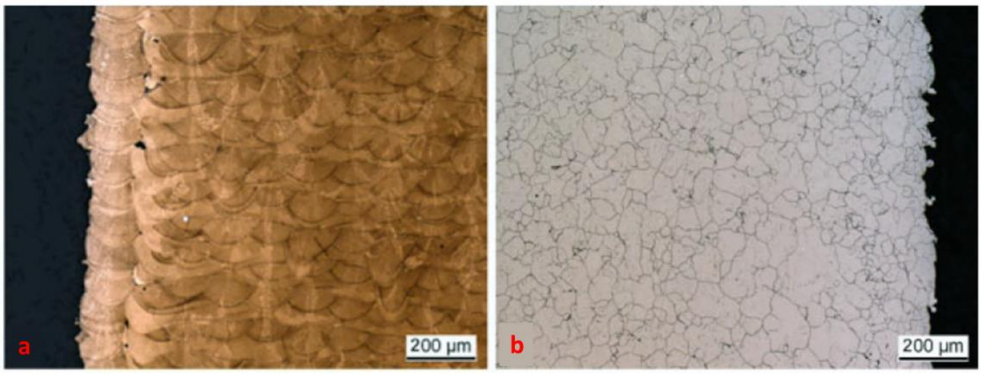

Figure 4 Optical microscope image of SLM Co-Cr-Mo alloy a) as-build condition b) after heat treatment (HIP) [32]

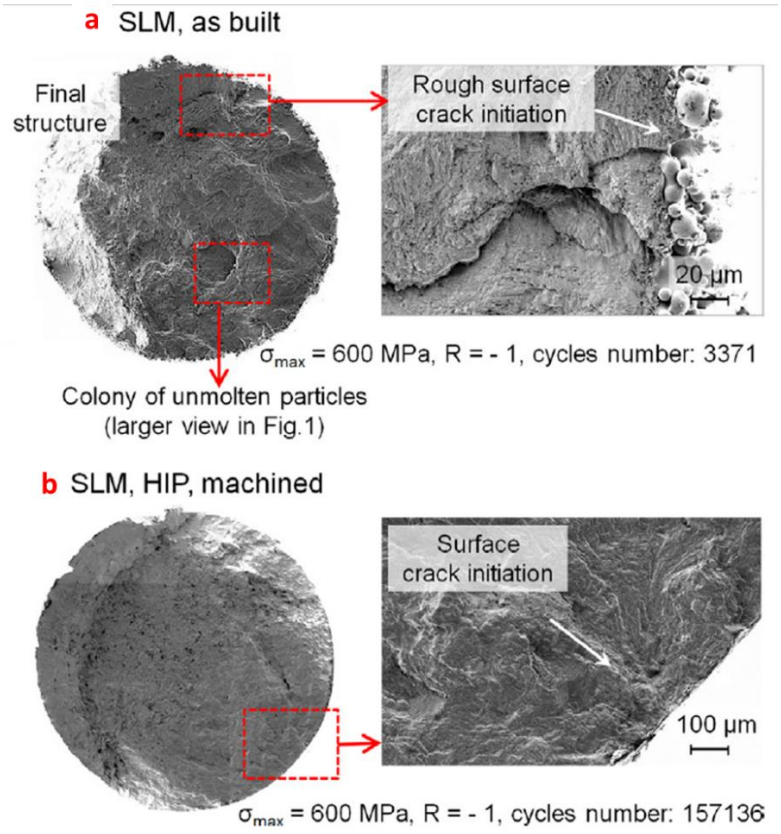

Figure 5 Fracture surface and fatigue life (noted as cycles number) of SLM TiAl6V4 a) as-build condition b) HIP and machined condition[33]

The amount of defects such as LOF in SLM materials is highly dependent on the ability of each neighbouring "weld" to be completely infused with each other, with sufficient overlap and no un-melted powder. Therefore, in order to achieve a highly dense (defined as when fraction of LOF, $f_{LOF} < 0.1\%$) SLM part, the size of the meltpool during the solidification process needs to have sufficient depth and width to fuse with the neighbouring solidified metal below and on the side of the meltpool. The geometrical features of the meltpool during solidification of SLM part is mainly influenced by the laser spot size and the four major SLM parameters: Laser power (P), scanning velocity (v), layer thickness (h), and hatching space (s). As shown in Figure 6, a geometrical study conducted on Co-Cr-Mo's "weld" tracks revealed that by increasing the laser power from 180 W to 240 W (thus increasing the size of the meltpool), f_{LOF} is reduced from 0.75% to less than 0.1%. Hence, in addition to HIP process, optimisation of SLM process parameters also plays a major role in reducing the amount of defects in SLM parts.

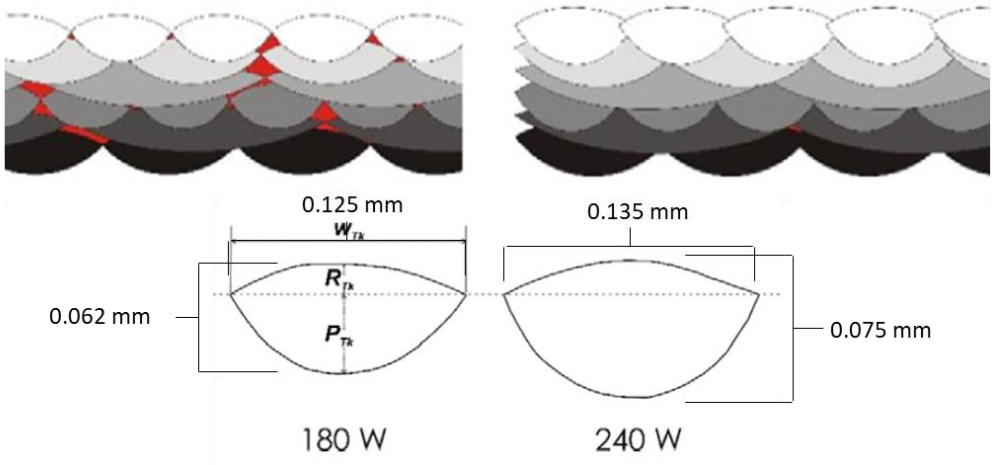

Figure 6 Schema of track arrangement layer-by-layer for 67⁰ scanning strategy. The red markings show the LOF suspected areas. P = 180 resulted in a smaller meltpool compared to P = 240 W. Other SLM parameters are: v = 700 mm/s, h = 0.03 mm, s = 0.125 mm amd laser spot size = 0.14 mm [13].

1.1.2.2 Fatigue endurance factor 2: Surface roughness

Another critical factor that affects the fatigue endurance for SLM materials is the surface roughness. It is well established that surface roughness is one of the most detrimental factors that can adversely affect the fatigue performance of a structural part [27, 34]. Even though SLM parts are expected or desired to be used in their as-built condition, especially for geometrically complex parts, surface finishing treatments are often recommended. It is not surprising that most

studies in the literature show that reducing surface roughness (R_a) by machining or polishing of SLM parts generally improve its fatigue resistance, especially for HCF test [31, 35-37]. The surface roughness (presented as R_a value) for as-build SLM parts varies between each reported study. Table 2 shows the differences of the surface finishes for as-build SLM parts, which are higher compared to machined surface finishes of $R_a \approx 1$ - 10 µm.

Table 2 Surface roughness of as-build SLM parts reported in the literature

Author	Material	As-build R_a (µm)
Spiering et al. [35]	316 Stainless Steel	50
Edwards et al. [31]	Ti6Al4V	39
Aboulkhair et al. [38]	AlSi10Mg	17
Stoffregen et al. [36]	17-4 PH Stainless Steel	14
Wycisk et al. [37]	Ti6Al4V	12
Kajima et al. [39]	Co-Cr-Mo	10

The surface roughness of as-build SLM parts can be affected by the size of metal powder used, the type of SLM machine, the SLM parameters (such as scanning velocity, v or hatching space, s), and the building direction [7]. Though the building direction for SLM is always upward, it poses small effect on the R_a values of different surface angle. Edwards et al. [31], for instance, reported that the surface roughness of SLM Ti-6Al-4V on an MTT 250 SLM machine ($P = P_{max}$ = 200 W, v = 200 mm/s, s = 0.180 mm and h = 0.050 mm), with grade 23 Ti powder have an R_a value of 39 µm and 30 µm for the surface parallel to build direction and perpendicular to the build direction, respectively. This is largely due to the stair-step-effect [40-42] which is the formation of "steps" on the surface due to the layer-by-layer manufacturing process. Figure 7 illustrates the stair-step-effect at two different surfaces, where the surface parallel to the build direction have a rougher surface, which consequently increase stress concentration and crack initiation development at its surface as compared to the surface perpendicular to the build direction that have a smoother surface finish.

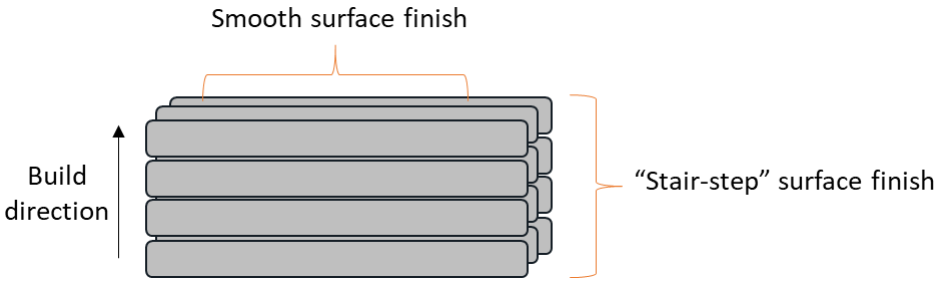

Figure 7 Schematic illustration of stair step effect on the surface of SLM parts

1.1.2.3 Motivation on Fatigue Crack Growth Rate (FCGR) studies for SLM materials

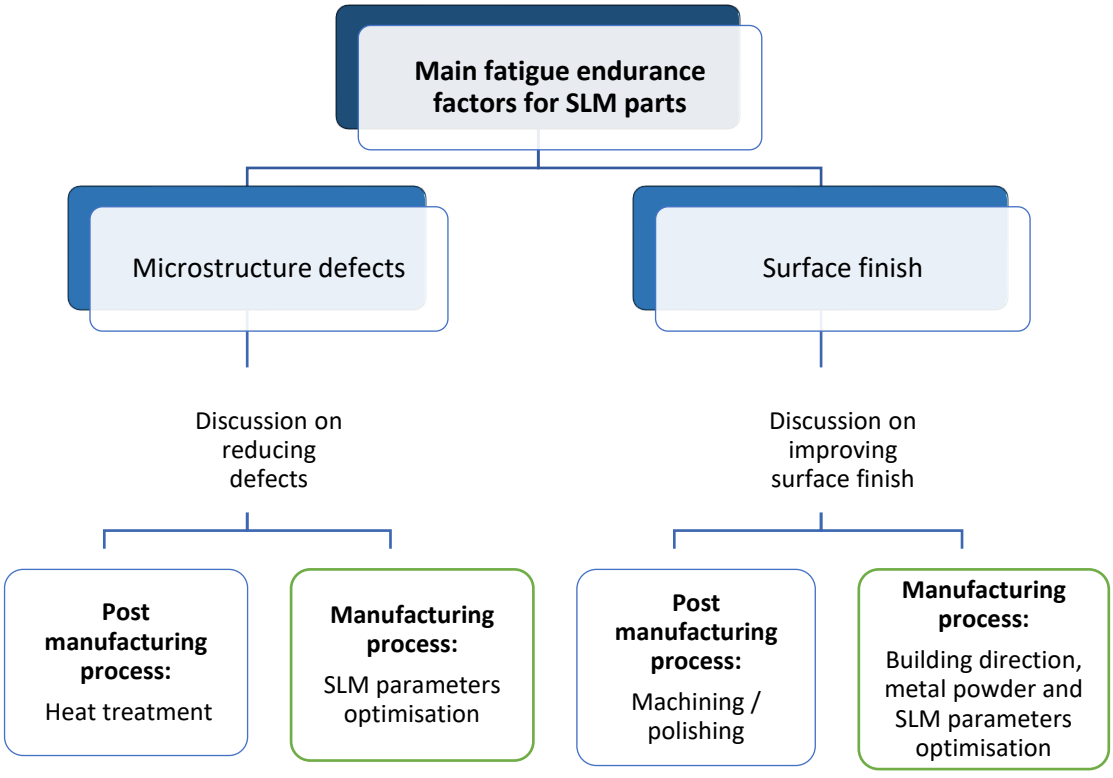

Figure 8 Main factors affecting fatigue endurance for SLM parts and ways of improvement

Based on the discussion in section 1.1.2.2, the two major fatigue endurance factors for SLM materials are 1) microstructure defects (such as LOF, pores, etc.) and 2) surface finish. This is expected as fatigue performance in general is known to be highly dependent on those two factors. Figure 8 above summarises the two main approaches (post and during manufacturing) for reducing LOF and improving surface finish. Since this study focuses solely on the behaviour of an as-build SLM part, post manufacturing treatment is not considered in this thesis.

In 2016, Kajima et al. [39] reported a fatigue strength study of SLM 63Co-29Cr-6Mo alloy, demonstrating that if an appropriate building direction is adopted (with SLM parameters optimisation), as-build SLM parts can surpass the fatigue endurance of a conventionally manufactured (investment casting) part. Although the SLM process parameters were not reported, it is assumed that the SLM parts used in the study consist of high density materials (low defects) as they have previously reported a study on SLM parameter optimisation of the same alloy [43]. In addition, the SEM images of the fractured surface presented in their study shows no evidence of defects. Figure 9 shows the results for their fatigue test, which displays a high degree of anisotropy; the FL90 specimen has a higher fatigue strength compared to the cast specimens (FCP and FCI), followed by the FL45 specimen and the FL0 specimen (Fatigue endurance in terms of cycle to failure: FL90 > FCI > FCP > FL45 > FL0). The FL90, FL45, and FL0 represent specimens where the loading direction is 90°, 45°, and 0° with respect to the the building direction, respectively.

Table 4 – Mean values (standard deviations) of fatigue test results. Values marked with identical letters showed no significant difference ($p > 0.01$). Permanent deformation was obtained from the values at the first cycle.

	Preset deflection (mm)	Material FL0	FL45	FL90	FCP	FCI
Cycle to failure	0.25	389,317[a] (82,864)	492,976[a] (149,534)	No failure	No failure	No failure
	0.5	28,484[a] (11,786)	43,465[a] (6,730)	205,418[b] (45,103)	112,770[c] (17,663)	125,300[c] (24,971)

Figure 9 Fatigue test on Co-Cr-Mo alloy, where "FL0", "FL45", "FL90" represent SLM Co-Cr-Mo with 0°, 45°, 90° loading direction, with respect to the build direction. FCP, FCI represent cast Co-Cr-Mo with powder and alloy ingot respectively [39].

The authors concluded in the paper that the dominant factor that affects the observed fatigue strength remains unknown and that further studies are required to explain its anistropicy behaviour. Gaps or important questions that merge from this study are: 1) Why does the FL90 specimen showed double fatigue strength as compared to the casting speciment (FCP and FCI), whereas the fatigue strength for the FL0 and FL45 specimens are significantly lower? Why does BD significantly affect the fatigue performance of SLM materials? 2) What are the mechanisms of crack growth during the fatigue life of SLM parts? How does a fatigue crack grow and propagate through the microstructure of SLM parts at different build directions?

An extensive study on monitoring the crack movement under cyclic loading is required to understand how the microstructure of SLM parts influence its fatigue behaviour. This can be achieved by conducting the Fatigue Crack Growth Rate (FCGR) experiment, which allows the observation of a single crack growth pathway. FCGR studies can provide insights into the nucleation and the growth of a crack throughout the unique microstructure of SLM materials. In addition, the fractured samples from FCGR experiments can also provide fractographical evidence of fracture features (i.e. intergranular or transgranular fracture) that help explain crack growth behaviour at different stress magnitude. Furthermore, an "interrupted" FCGR test (explained in Chapter 3.3.4) can also offer a clear image on the crack path, illustrating its preference pathways, thus explaining the relationship between the SLM microstructure characteristic and its FCGR behaviours. Therefore, the mechanisms of crack growth in SLM material at different build direction or different microstructure can be discovered.

In the next sub-chapther, Chapter 1.2, the fundamental concept of FCGR study will be presented. Then, Chapter 1.3 will discuss the influence of SLM parameters (i.e. build direction, BD and laser power, P) on the microstructure of SLM superalloys. Finally, all reported FCGR studies on SLM superalloy will be discussed in Chapter 2.0: Literature review.

1.2 An introduction to Fatigue Crack Growth Rate (FCGR) studies

The FCGR testing is originally designed to measure the rate of a crack that grows under specified fatigue loading conditions. This information is necessary for a variety of engineering purposes such as estimations of fatigue life based on critical crack size, calculations for damage tolerant designs, and determinations of inspection intervals for critical components [44]. This sub-chapter explains the parameters and concepts that are applied in FCGR studies, while details on the experimental procedure is included in Chapter 3.0.

1.2.1 Stress intensity factor (SIF)

The FCGR study is based on the theory of Linear Elastic Fractured Mechanics (LEFM) that was originally proposed by Griffith in 1921 [45] and was later further developed in its essential form by Irwin and Rice in 1968 [46, 47]. LEFM utilizes the concept of stress intensity factor (SIF), K, which can be determined by stress analysis [46], to quantify the force that is responsible in driving the growth of a crack tip. Since the dimension of a crack is usually small compared to the dimension of a component, a crack can be viewed as being contained within an infinite body. As illustrated in Figure 10, for a small crack that is contained in a large sheet of material, the SIF (also known as the K value) can be expressed as a function of global nominal stress and crack size. This relationship is captured in the following equation:

$$K = S\sqrt{\pi}\sqrt{a}\,\alpha \qquad (1)$$

Where:

S = Nominal stress, assuming the crack did not exist (MPa)

a = crack length, sometimes refer as crack size (m)

α = dimensionless geometry correction parameter

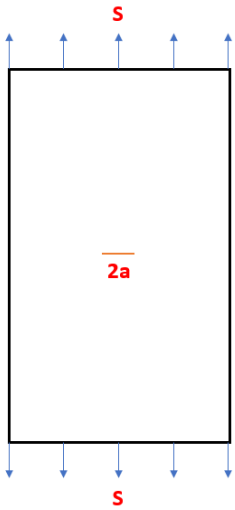

Figure 10 An illustration of an infinite 2D sheet with a centre crack of size 2a, subjected by a uniform tensile stress, S. For this particular crack and component configuration, α = 1.

For other crack and component configurations, the value of α (dimensionless geometry correction parameter) can be found in most mechanical engineering handbooks [44] as a function of crack size and width, *f(a/w)*. Moreover, the shape of a crack (i.e. elliptical shaped crack or circular shaped crack) also affects the relationship between SIF, the applied stress, and the crack size. The relationship of SIF for a unique configurations and loading can be calculated using finite element analysis (FEA) software or experimental methods i.e. photo-elasticity experiment. As for a particular cracking set-up such as the Compact Tension (CT) sample that was used throughout this study, the relationship between SIF and crack size (a) is described in Chapter 3.0, equation (6).

There are three modes in which a crack can be extended, as shown in Figure 11 below. Mode I is known as the crack opening mode, which refers to those cases where the surface of a crack moves opposite to each other. Mode I represents the most common type of crack mode in fatigue as cracks tend to grow on the plane of maximum tensile stress. This is reflected in the fatigue analysis literature, which has focused more extensively on Mode I compared to the other two types. Mode II is known as the sliding mode or in-plane shearing mode, and Mode III is known as the tearing mode that is typically loaded under torsion force. Combinations of these three Modes can also occur; for example, a crack on an inclined plane (relative to the loading direction) is extended by Mode I and Mode II. Most fatigue analysis only incorporate Mode I because 1) it

commonly occurs in real engineering application 2) Mode II and III in combination with Mode I will often be negligible, and 3) There are no FCGR experimental standards specifically design for Mode II or III.

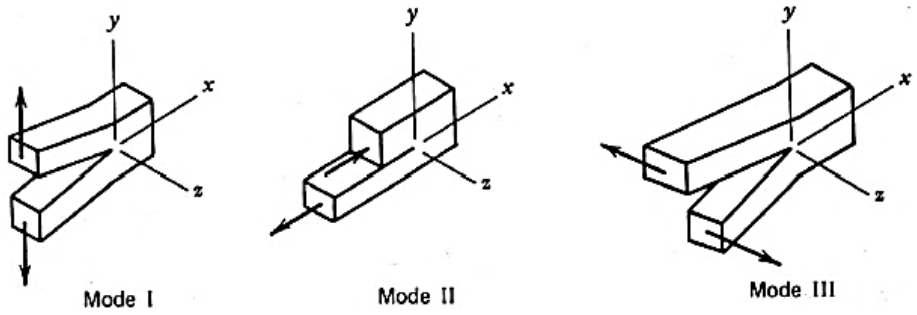

Figure 11 Three modes of fractures

Theoretically, for a crack to advance through a material, the local stress concentration in front of the crack-tip needs to be high enough until it reaches a critical SIF value, K_C. Subsequently, the high stress concentration in front of the crack-tip can causes a small area in front of the crack tip to plasticise. The plastic zone length along the crack axis, r_p was modelled by Irwin [48] based on the Tresca yield criterion and later was refined by Dugdale [49]. It is interesting to note that the lack of pictorial evidence by Dugdale in his original paper had caused a slow acceptance on his work, until Hand and Rosenfield [50] provided evidence in 1965. Table 3 below summarises the r_p model proposed by Irwin and Dugdale. It is important to note that the impact on SIF due to the effective crack length, a_{eff} is negligible since the applied stress, S (in the formula for K) is typically low compared to the yield stress, S_Y. This plastic zone size in front of the crack tip is important in this study as LEFM calculation was developed based on the assumption of a linear elastic material condition. Therefore, as parts of its limitation, the elastic assumptions are violated when 1) the loading stress magnitude is too high, resulted in significant plasticity in front of the crack tip or 2) the crack size is small in comparison to the plastic zone in front of the crack tip.

Table 3 Formula of plastic zone length in front of the crack tip and effective crack length proposed by Irwin [48] and Dugdale [49]

	Irwin's model		**Dugdale's model**	
Plastic zone length in front of crack tip, r_p	Plane stress	Plane strain	Plane stress	Plane strain
	$\frac{1}{\pi}\left(\frac{K}{S_Y}\right)^2$	$\frac{1}{3\pi}\left(\frac{K}{S_Y}\right)^2$	$\frac{1}{8\pi}\left(\frac{K}{S_Y}\right)^2$	-
Effective crack length, a_{eff}	$a_{eff} = a + r_p/2$		$a_{eff} = a + r_p$	

The global critical SIF value for Mode I, K_{1C}, also known as fracture toughness, is determined experimentally [51] under a certain set of conditions i.e. plane strain condition. However, it is equally applicable to other conditions and is considered as a true material property. K_{1C} refers to the condition when a crack grows rapidly (fracture or unstable crack growth), therefore it provides quantitative design parameters which involve the three critical fracture parameters: fracture toughness, K_{1C}, critical crack size, a_c, and working stress, S_w. These three parameters can be substituted into equation (1) and since K_{1C} and S_W are usually known, the critical crack size, a_c can be calculated. For components that are subjected to fatigue loading, fracture failure usually occurs in the final stage of its 'life', also known as crack growth in Stage 3.

1.2.3 Fatigue crack growth, da/dN

In the conventional S-N fatigue test, namely the high-cycle-fatigue (HCF) test and low-cycle-fatigue (LCF) test, multiple cracks/flaws grow inside the material until it reaches a critical level (fatigue strength) which then leads to fracture. S-N diagram that is produce by HCF or LCF tests does not provide insight into the crack growth behaviour as it was not designed to detect or monitor cracks. Therefore, in an attempt to monitor the crack growth behaviour, a-N curve is plotted using a standard specimen for fracture, for various specimens at different stress levels, as illustrated in Figure 12. The figure shows that crack growth is a function of 1) fatigue load and 2) crack length. To generate a general crack propagation law, Paris et al. [52, 53] combined the results from the a-N curves and plotted the crack growth rate, da/dN (the gradient on a-N curve)

vs SIF range, ΔK (as defined in equation (2)) into a single log-log graph known as the FCGR graph. It was a significant task that opens many research ideas/opportunities in understanding crack growth by fracture mechanics.

$$\begin{aligned} \Delta K &= K_{max} - K_{min} \\ &= S_{max}\sqrt{\pi a}\,\alpha - S_{min}\sqrt{\pi a}\,\alpha \\ &= (S_{max} - S_{min})\sqrt{\pi a}\,\alpha \\ &= \Delta S\sqrt{\pi a}\,\alpha \end{aligned} \qquad (2)$$

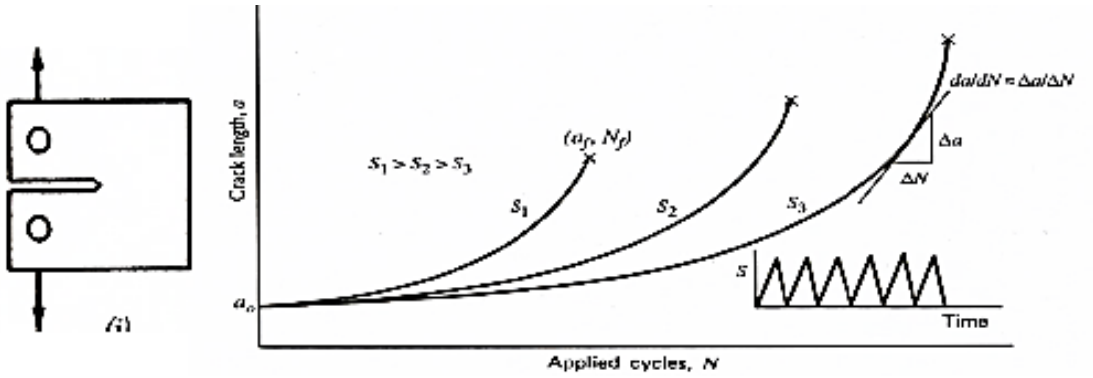

Figure 12 An example of an a-N curves with three fatigue tests at different stress levels.

A typical FCGR curve of da/dN vs ΔK is shown in Figure 13. It has a sigmoidal shape that can be divided into three regions. Region 1 represent a situation when a crack is growing at the initiation stage, Region 2 represent a situation when a crack is growing at a stable rate (also known as the Paris region/stage) and Region 3 represent a situation when a crack growing at an unstable rate (also known as fracture stage).

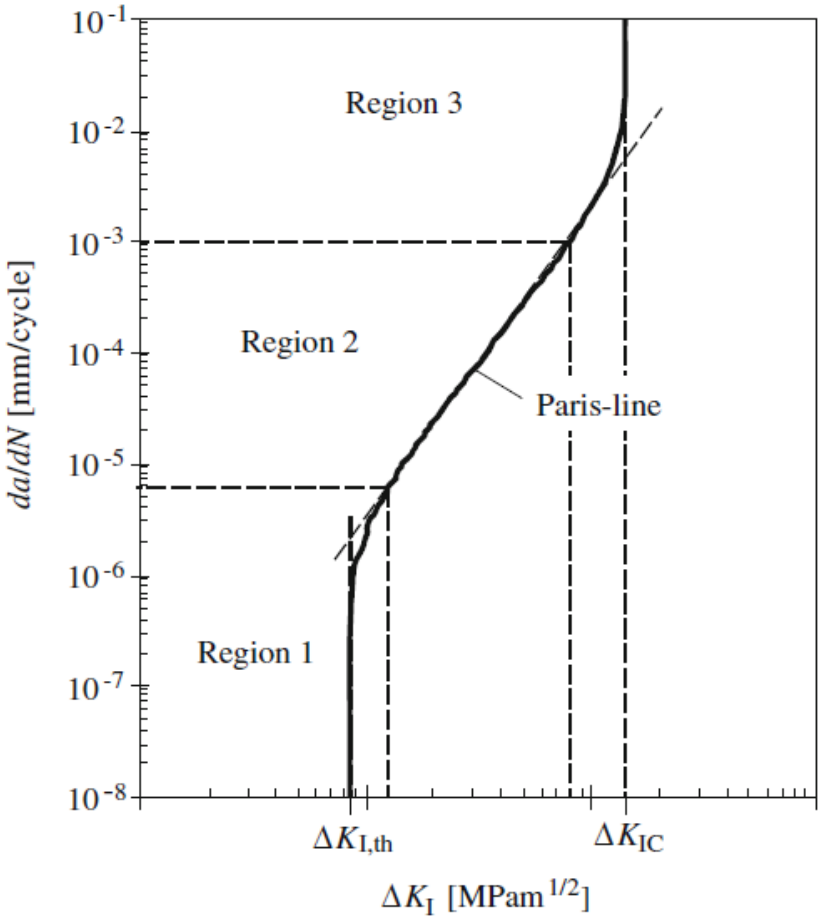

Figure 13 An example of a typical FCGR graph with an indication of "Paris line" in Region 2, ΔK_{th} in Region 1 and ΔK_{1C} in Region 3 [44]

1.2.3.1 Region 2: Paris Region

Generally, crack growth rate in the Paris region is in the order of 10^{-7} m/cycle to 10^{-5} m/cycle. In most materials, fatigue striations are formed at this stage [54], and it is the only region where crack growth can be monitored by a non-destructive test (NDT). Region 2 shows a linear relationship between log da/dN and log ΔK, as firstly suggested by Paris et al. Paris law states that the relationship between da/dN and ΔK in Region 2, is governed by equation (3). It is important to note that this simple empirical relation is achieved by assuming no environmental factors (such as high humidity or high temperature) are involved in the crack growth process.

$$\frac{da}{dN} = C\ (\Delta K)^m \qquad (3)$$

Where:

C = FCGR parameter, also known as Paris constant (Y-intercept of Paris-line)

m = FCGR parameter, also known as Paris constant (gradient of Paris-line)

It is also important to note that the relationship in equation (3) is purely empirical, that is based on the linear FCGR curve in Region 2. As mentioned earlier, identifying the Paris constants, C and m allows for the prediction of a component's fatigue-life based on the detection of flaws/cracks. The relationship between fatigue-life and crack size can be achieved by the integration of Paris law, as shown below:

By substituting equation (2) into equation (3):

$$\Delta K = \Delta S \sqrt{\pi a}\ \alpha \qquad \text{into} \qquad \frac{da}{dN} = C\ (\Delta K)^m$$

$$\frac{da}{dN} = C\ (\Delta S \sqrt{\pi a}\ \alpha)^m$$

$$\frac{da}{dN} = C\ (\Delta S)^m\ (\pi\ a)^{m/2}\ \alpha^m$$

$$N_f = \int_0^{N_f} dN$$

$$N_f = \int_{a_i}^{a_f} \frac{da}{C(\Delta S)^m\ (\pi\ a)^{m/2}\ \alpha^m}$$

$$N_f = \frac{1}{C(\Delta S)^m\ (\pi\ )^{m/2}} \int_{a_i}^{a_f} \frac{da}{(a)^{m/2}\ \alpha^m}$$

Now, assuming that α does not change significantly between the limit of a_i and a_f, i.e. when crack is very small compared to the geometry of the component:

$$N_f = \frac{1}{C(\Delta S)^m\ (\pi\ )^{m/2}\ \alpha^m} \int_{a_i}^{a_f} \frac{da}{(a)^{m/2}}$$

$$N_f = \frac{{a_f}^{\left(-\frac{m}{2}\right)+1} - {a_i}^{\left(-\frac{m}{2}\right)+1}}{\left(-\frac{m}{2}+1\right) C\ (\Delta S)^m\ (\pi)^{m/2}\ \alpha^m}$$

For fracture calculation, a_f can be calculated as follow:

a_f = critical crack length, $a_c = \frac{1}{\pi}\left(\frac{K_{1c}}{S_{max}}\right)^2$

1.2.3.2 Crack initiation stage (Region 1) and catastrophic failure (Region 3)

Generally, Region 1 occurs at an extremely small crack growth rate, in the order of nanometers ($< 10^{-9}$ m/cycle). Furthermore, the crack growth rate is non-uniform, even across a small distance along the crack front. As a result, clear fatigue striations cannot be found in this Region. The main factors that influence the crack growth behaviour in this region are 1) microstructure of the material, i.e grain distribution, 2) fatigue mean stress ratio, R, defined as S_{max}/S_{min} (as illustrated in Figure 14 below), and 3) crack closure effect, which will be discussed Chapter 1.2.5.

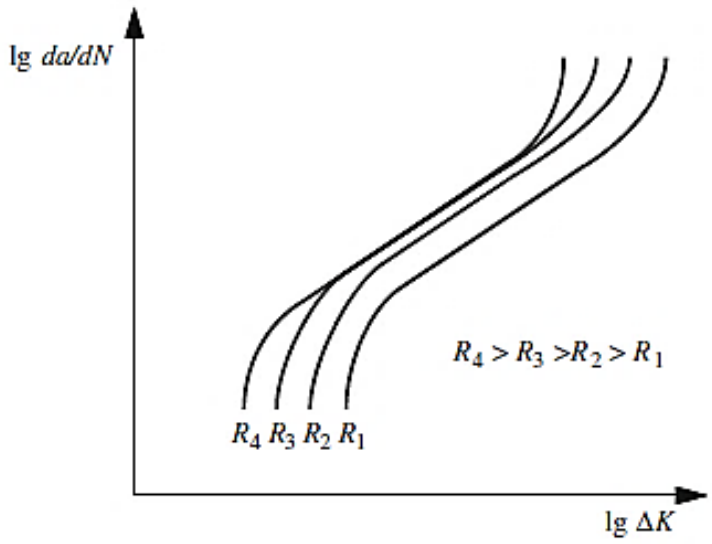

Figure 14 An illustration of the relationship between fatigue mean stress ratio R and FCGR curve [44]

Region 1 cracks are also commonly referred to the near threshold region where an extrapolation of the FCGR curve (as shown in Figure 13) can determined the FCGR threshold value (ΔK_{th}). ΔK_{th} is the lowest value of ΔK at which a crack propagation will occur. In other words, cracks will not grow if the applied ΔK is below the ΔK_{th} value. This concept is similar to the endurance-limit in the traditional HCF test, where it is well known that some ferrous materials exhibit "unlimited" fatigue life, if the applied stress is below its endurance limit. The effect of ΔK_{th} value

on the life of a component can be estimated by the integration of Donahue's law [55], which is a modification of the Paris law that account for the change of slope in Region 1.

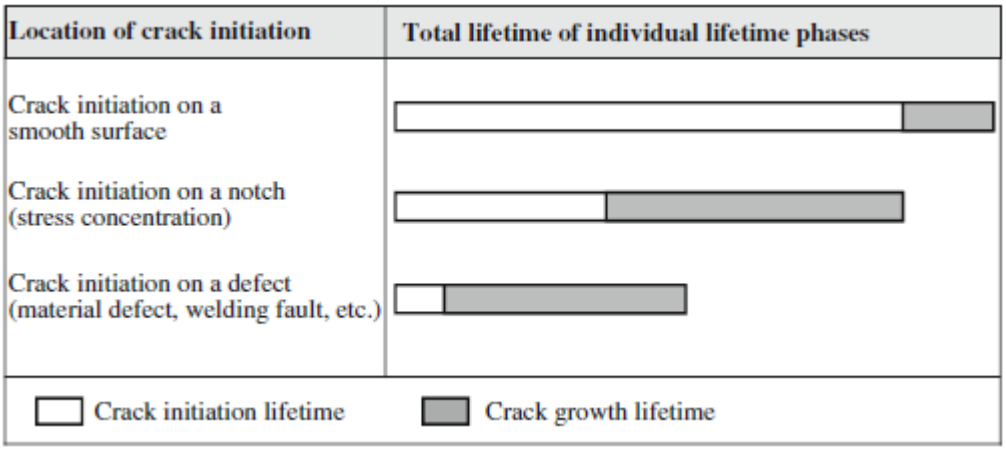

Figure 15 Prediction on the proportion of the fatigue-life between crack initiation lifetime (initiation stage, Region 1) and crack growth lifetime (Paris stage, Region 2), at different crack initiation position [44]

The crack initiation stage is often considered to be the most crucial FCGR stage, as it often comprises a large fraction of a component's fatigue-life [56]. However, it is also important to highlight that this statement is not always true as the fraction between Stage 1 and Stage 2 crack of a component's fatigue-life also depends on the location of the crack, as shown in Figure 15. In addition, the shape/sharpness/stress-concentration of the initial defect also plays an important role. For example, cracks will initiate significantly slower through a blunt defect/notch as compared to a sharp one. To illustrate this point further, equation (4) below demonstrates that for the same amount of applied stress, the K value for a circular defect/notch is 1.57 times smaller compared to a sharp notch [44]. The SIF equation for a sharp crack in a comparatively large body is $K = S\sqrt{\pi}\sqrt{a}$, as shown in equation (1), but for a circular defect:

$$K = S\sqrt{\pi}\sqrt{a}\left(\frac{2}{\pi}\right) \qquad (4)$$

Where:

a = radius of defect/crack

For Region 3, the crack growth rate is very high, in the order of 10^{-4} m/cycle to 10^{-3} m/cycle. The crack growth in this region is often described as unstable where the crack runs through the entire grain in just one cycle. Based on Figure 13, it can be seen that the K value in Region 3 approaches the material's fracture toughness, K_{1C}, of the material. In real-life engineering practices, components should be discarded before the crack enters this region to avoid catastrophic failure. It is also important to mention that crack growth behaviour in this region is highly influenced by the stress ratio (as shown in Figure 14) and the thickness of the component. In addition, crack in stage 3 can fracture at a higher K value in a plane stress condition (thin part) compared to a plane strain condition, which is due to the larger plastic zone in plane stress condition. This relationship is illustrated by Lai and Ferguson [57] in Figure 16, where they have shown the effect of specimen thickness on fracture toughness value.

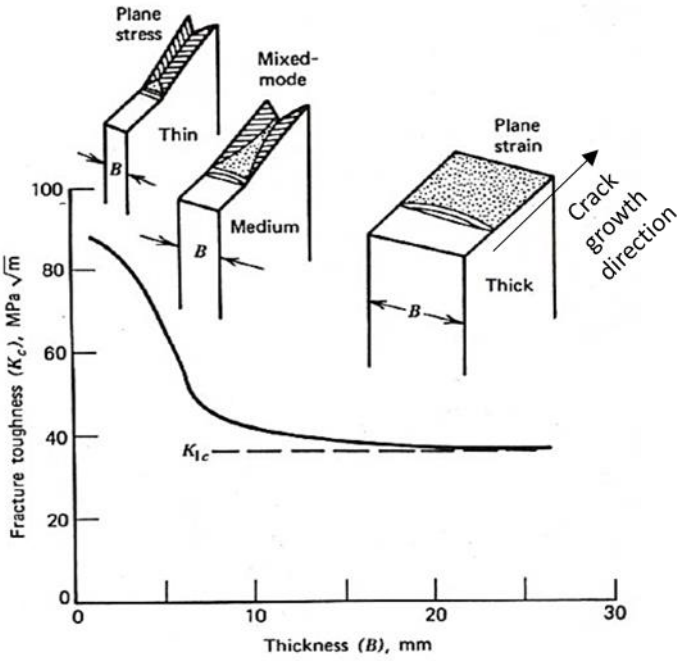

Figure 16 Relationship between thickness and K_C. As material's thickness increase, K_C approaches an asymptotic minimum value called the "plane strain fracture toughness" which is the true material property; fracture toughness, K_{1C}

1.2.4 Modification on Paris Law

As mentioned before, Paris Law only represents the linear region (Region 2) of the FCGR graph. Thereupon, many new laws are being proposed to incorporate other regions (Region 1 & 3) on the FCGR graph. Note that all the FCGR models mentioned below are based on a curve-fitting-

exercise (essentially based on Paris Law which is purely empirical). Therefore, these models may not be applied to all metallic materials that have different FCGR behaviours compared to the tested data set. For example, Donahue et al. [55] tested his model with 65 sets of data and listed only 30 materials in their report, including titanium, copper, and nickel alloys. Therefore, nickel alloys and other superalloys with similar FCGR behaviour can utilise this model. The list of FCGR laws is listed below:

1) Donahue Law [55] – to account the change of slope at Region 1

$$\frac{\mathrm{da}}{\mathrm{dN}} = \mathrm{C}\,(\Delta\mathrm{K} - \Delta K_{th})^{\mathrm{m}}$$

Where:

ΔK_{th} $= (1 - \mathrm{R})^{\gamma}\Delta K_{th(0)}$

$\Delta K_{th(0)}$ = the threshold value at R = 0

γ = material dependent constant, for material tested by Donahue et al. $\gamma = 2$

R = Stress ratio

2) Forman's Law [58] – to account for Region 3

$$\frac{\mathrm{da}}{\mathrm{dN}} = \frac{\mathrm{C}\,(\Delta\mathrm{K})^{\mathrm{m}}}{(1 - \mathrm{R})\,\Delta K_C - \Delta\mathrm{K}}$$

3) Erdogan and Ratwani Law [59] – complete sigmoidal curve (all 3 Regions)

$$\frac{\mathrm{da}}{\mathrm{dN}} = (\Delta\mathrm{K} - \Delta K_{th})^{\mathrm{m}} \cdot \mathrm{C}\,(1 + \beta)^{\mathrm{m}} \cdot \frac{1}{\mathrm{K}_C - (1 + \beta)\Delta\mathrm{K}}$$

Where:

$$\beta = \frac{K_{max} + K_{min}}{K_{max} - K_{min}}$$

$(\Delta\mathrm{K} - \Delta K_{th})^{\mathrm{m}}$ accounts for experimental data at low stress level

$\mathrm{K}_C - (1 + \beta)\Delta\mathrm{K}$ accounts for experimental data at high stress level

1.2.5 Crack closure

In 1971, Elber [60, 61] proved the significance of the crack closure phenomenon under cyclic tension loading. His finding was based on the observation of FCGR experiment where the load-deflection curve is bi-linear (the first linear line is due the effect of crack closure, which he proved by the striation pattern). Based on his finding, for the stress ratio of R = 0, the crack tip can be closed even under tension loading, making it ineffective in propagating the crack. As illustrated in Figure 17, crack closure implies that the ΔK is only effective (in propagating the crack) when the crack starts to open at which SIF is at the value of K_{op} (K opening).

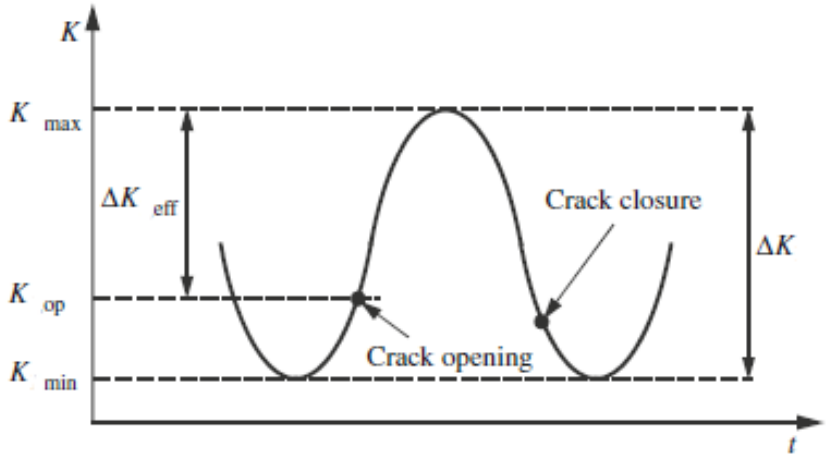

Figure 17 An example of ΔK vs t graph to illustrate "ΔK effective" and "ΔK opening" due to crack closure [44]

The effect of crack closure is reduced as the stress ratio is increased. According to Elber [60], for 2023-T3 Aluminium, the effect of crack closure can be detected up until a stress ratio of, R < 0.7. Moreover, Gray et al. [62] proposed that the crack closure effect can have an impact on the FCGR behaviour due to the roughness of the fractured surface. As shown in Figure 18, an increase in the fractured surface roughness would result in a higher ΔK_{th} value. This effect is more dominant when the R = 0.1 (higher crack closure effect), compare to when R = 0.7 (almost no crack closure effect). This graph indicates a possibility that the effect of crack closure is responsible for the increase in ΔK_{th} value. Figure 19 illustrates the mechanisms of crack growth resistance that causes the ΔK_{th} value to increase due to the roughness of the fractured surface as explained by Gray et al. An inclined crack (that causes the fractured surface to be rough due to the "zig-zag"

crack pathway) would experience a crack extension of Mode I and Mode II (mix-Mode). As mentioned previously, Mode II crack openings involve shearing/sliding, which cause friction resistance between the top and the bottom fracture surface during crack-closing, thus inducing the crack closure effect. This phenomenon is known as the roughness-induced crack closure (RICC). In addition, there are also other studies that are related to crack closure such as fluid-induced crack closure, plasticity-induced crack closure, and oxide-induced crack closure that need to be considered for FCGR under extreme conditions such as high humidity and temperature.

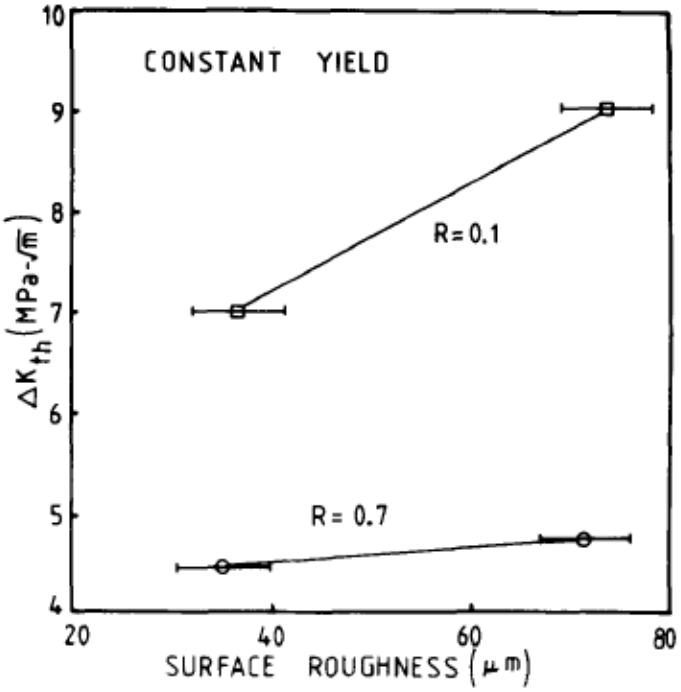

Figure 18 Relationship between surface roughness and ΔK_{th} for AISI 1080 steel at R= 0.1 and R = 0.7 [62]

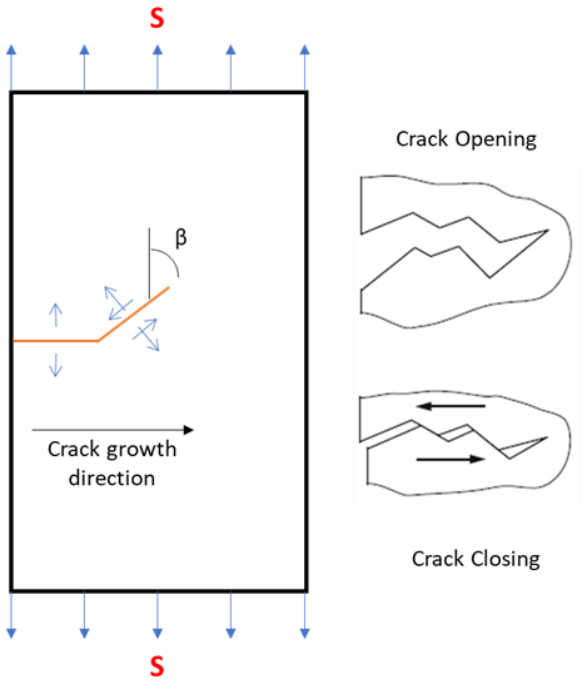

Figure 19 Mix-mode crack extension (Mode I and Mode II) when crack is in an inclined position relative to the loading direction, resulting in a shear stress during crack closing. If $\beta = 90$, pure Mode I.

1.3 SLM Introduction to SLM Cobalt Chrome and Inconel 738 Superalloys

Superalloys are generally used in high temperature applications (above 550 ºC) and because of their high strength and corrosion resistance, some superalloys have become a standard material for biomedical/dental application [63]. Superalloys can be divided into nickel-based and cobalt-based alloys. This study focuses on 1) SLM Co-29Cr-6Mo, a cobalt-based superalloy that has been successfully produced commercially, and 2) SLM Inconel 738, a nickle-based superalloy that is considered as a difficult-to-weld alloy and is known to have microstructure defects such as micro pores. This section aims to introduce these two SLM materials by looking into their microstructure characteristics such as grain distribution, microstructure defects, and meltpool shape.

1.3.1 Cobalt Chrome (Co-29Cr-6Mo)

Cobalt-chrome based alloys are one of the most common metals in orthopaedic and dental industries due to its high biocompatibility [64]. The Co-29Cr-6Mo alloy is one of the materials that has been commercially produced by using SLM process, replacing the traditional

subtractive manufacturing process. Some examples of its production parts are shown earlier in Figure 2. In 2015, the Federal Aviation Administration (FAA) had given the approval for the manufacturing of Co-29Cr-6Mo alloy via SLM for aerospace parts to be used in Boeing 777X aircraft [65]. The chemical composition and minimum mechanical strength requirements for cast Co-29Cr-6Mo alloys are shown in Figure 20 below, established by the ASTM F75 standard [66]. Despite its application often being subjected to constant fatigue stress, fatigue strength has not been included as a requirement in the ASTM F755 standard. This has led to several fatigue studies which involve HCF experiments to compare the fatigue strength between cast and SLM process [32, 39].

Element	Composition, % (Mass/Mass)	
	min	max
Chromium	27.00	30.00
Molybdenum	5.00	7.00
Nickel	...	0.50
Iron	...	0.75
Carbon	...	0.35
Silicon	...	1.00
Manganese	...	1.00
Tungsten	...	0.20
Phosphorous	...	0.020
Sulfur	...	0.010
Nitrogen	...	0.25
Aluminum	...	0.10
Titanium	...	0.10
Boron	...	0.010
Cobalt[A]	balance	balance

[A] Approximately equal to the difference of 100 % and the sum percentage of the other specified elements. The percentage of the cobalt difference is not required to be reported.

Property	
Ultimate tensile strength, min, MPa (psi)	655 (95 000)
Yield strength, (0.2 % offset), min, MPa (psi)	450 (65 000)
Elongation,[A] min, %	8
Reduction of area, min, %	8

[A] Elongation of material 0.063 in. (1.6 mm) or greater in diameter (D) or width (W) shall be measured using a gauge length of 2 in. or 4D or 4W. The gauge length must be reported with the test results. The method for determining elongation of material under 0.063 in. (1.6 mm) in diameter or thickness may be negotiated. Alternately, a gauge length corresponding to ISO 6892 may be used when agreed upon between supplier and purchaser. (5.65 times the square root of S_o, where S_o is the original cross-sectional area.)

Figure 20 Chemical composition and minimum mechanical strength requirement for Co-29Cr-6Mo alloy based on ASTM F75 standard [66]

1.3.1.1 Mechanical Properties

A review paper on the static strength of SLM Co-Cr-Mo was previously reported by Koutsoukis et al. [67] to evaluate its mechanical properties and compare it to those produced by conventional casting method. The mechanical test results were collected from four different SLM Co-Cr-Mo manufacturers (EOS, Germany; Dentaurum, Germany; Sint-Tech, France; and Bigo Medical, Germany) and from a paper reported by Castillo-Oyague et. al [68]. All the mechanical test results presented by Koutsoukis et al. are compiled in Table 4, which concluded that the SLM manufacturing technique is capable of producing Co-Cr-Mo alloys with higher static strength compared to casting and CAM. Table 4 also includes mechanical test results reported by Takaichi et al. [43] and Kajima et al. [39], who came to the same conclusion as Koutsoukis et al. and subsequently highlighted the need of fatigue behaviour studies for this material.

Table 4 Static strength of SLM Co-29Cr-6M. The range of values is subjected to different build directions. Green and red indicate that the value is respectively higher or lower compared to ASTM 75 requirements.

Source	Yield strength 0.2% (MPa)	Tensile strength (MPa)	Elongation %
EOS [67] - 2015	880 - 960	1150 - 1300	N/A
Compare to F75 req.	213%	198%	-
Dentaurum [67]	653	1030	N/A
Compare to F75 req.	145%	157%	-
Sint-Tech [67]	815	N/A	N/A
Compare to F75 req.	181%	-	-
Bego Medical [67]	470	650	N/A
Compare to F75 req.	104%	99%	-
Castillo [68] - 2012	516 - 562	889 - 912	4.5 – 10.7
Compare to F75 req.	125%	139%	134%
Takaichi [43] - 2014	516	918	12.2
Compare to F75 req.	115%	140%	153%
Kajima [39] - 2016	837 - 896	1170 - 1274	9.1 - 12.7
Compare to F75 req.	199%	195%	158%

There are only two HCF tests reported for SLM Co-Cr-Mo alloy. In 2015, Haan et al. [32] reported the S-N curves for Co-Cr-Mo alloy that were processed by the three following methods: 1) as-cast, 2) as-SLM, and 3) SLM + HIP. The HCF results showed the hierarchy of

fatigue strength as: SLM + HIP > as-cast > as-SLM, which led to the conclusion that the HIP process is necessary for SLM Co-Cr-Mo alloy to eliminate microstructure defects (that cause low fatigue strength). Though, the as-SLM's microstructure photographs reported by Haan et al. clearly show high number of LOF, which suggests that the SLM parameters were not optimised. However, there was no SLM parameters reported by the author to confirm this claim.

It was later proven by Kajima et al. [39] that the fatigue strength for an as-SLM specimen could significantly surpass the fatigue strength of an as-cast specimen even without the HIP process (but with SLM parameter optimasation), provided that the right building direction (BD) is applied. The HCF test results were discussed and presented earlier in section 1.1.2.3, Figure 9. As mentioned previously, the authors concluded that the dominant factor that causes anisotropic fatigue strength between the different BD specimens remained unknown. They have suggested that grain orientation, surface roughness, residual stress, and meltpool boundaries as the main suspects. In order to investigate this, literature review on how SLM parameters (Laser power and BD) would affect the SLM Co-Cr-Mo microstructure is firstly presented in the next section.

1.3.1.2 Microstructure

The grain (a group of cells growing in the same orientation) distribution for SLM Co-Cr-Mo metals are highly distinctive when compared to cast Co-Cr-Mo. SLM Co-Cr-Mo alloys contain columnar gain structures that grow cellularly, without forming a planar zone first during its solidification process [14]. In contrast, cast Co-Cr-Mo alloys contain equiaxed grain structures or dendritic and equiaxed grain structures, depending on the colling rate during the solidification process [69]. Generally, majority of the columnar grain growth directions in SLM metals is upwards direction (same direction as BD) [31, 32, 39, 43], opposite to the heat flux (Q) direction. Chen et al. [70] explained that the shape of the meltpool boundary would influence the Q direction, and ultimately, the columnar grains growth direction will follow the

same orientation of the previous layered grain (epitaxial growth). The growth direction can either follow the same direction or change direction by 90°, depending on the orientation of grain in the previous layer and the angle of Q. Therefore, as shown in Figure 21 the columnar grains in SLM Co-Cr-Mo could vary in shape, size, and orientation depending on the meltpool size (which can be influenced by the laser power).

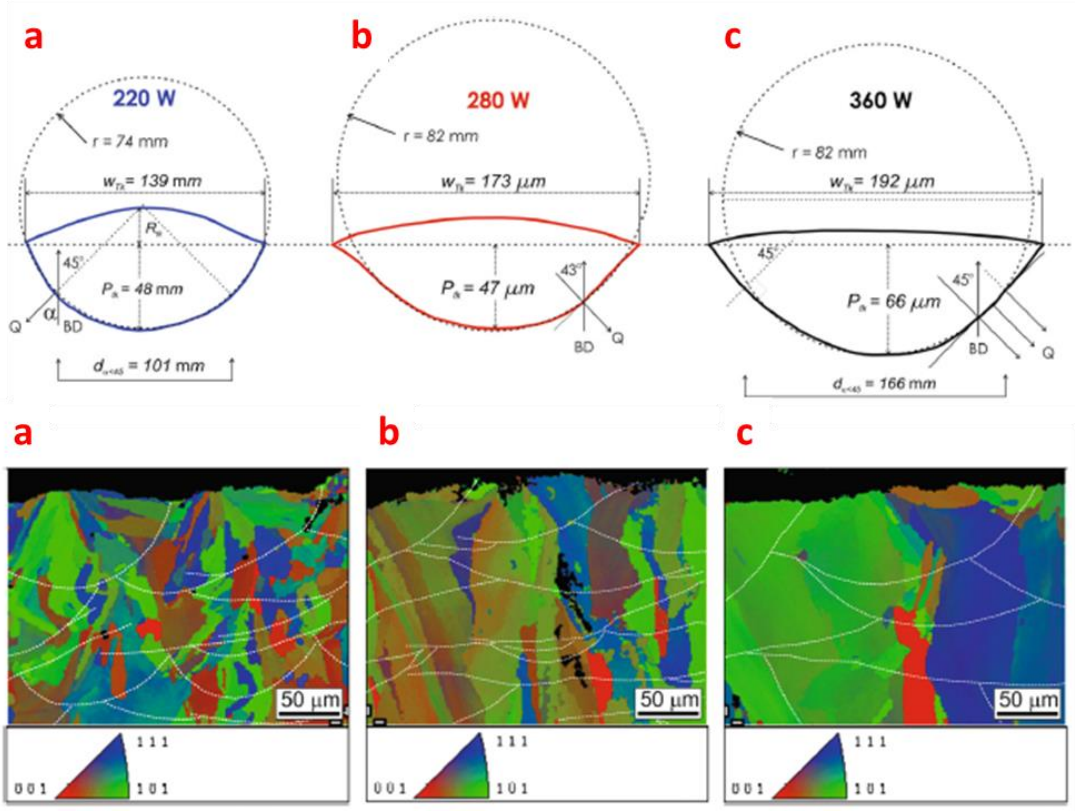

Figure 21 The shape of meltpool boundary and grain distribution maps for SLM Co-Cr-Mo alloys. (a) samples made with P = 220 W, (b) P = 280 W and (c) P = 360 W [70].

Based on Figure 21, it can be seen that as the laser power (P) is increased (with other recommended SLM parameters kept constant), the shape of the meltpool boundaries becomes bigger and flatter (i.e. higher circular arc radii). A meltpool boundary with bigger arc radii provides a more favourable condition for the grains to grow dominantly along the BD direction, as well as generating larger grain size. On the other hand, if the laser power (P) is decreased, the meltpool boundaries become smaller (i.e. smaller circular arc radii), which result in smaller columnar grains as it has less dominancy to grow in the direction along the BD direction.

An investigation of the relationship between the geometrical features of meltpool boundaries and the density of lack of fusion (LOF) for Co-Cr-Mo alloy has been conducted by Darvish et al. [13]. Their samples were firstly printed based on the SLM parameters recommended by the printer manufacturer, Renishaw (P = 180 W, v = 700 mm/s, s = 0.125 mm, h = 0.03 mm, and scanning strategy, SS = 67º). As shown in Figure 22, P was increased by 20 W for other tested samples until it reached 360 W, while other recommended SLM parameters were kept constant. Since the laser power parameter influences the average size/shape of the meltpool boundaries, the recommended SLM parameter (P = 180 W) has resulted to generate a meltpool boundary size that was not sufficient to completely overlap its neighbouring track. Thus, resulting in a high number of LOF, i.e. area fraction of LOF, f_{LOF} = 0.75%. However, at P = 320 W, the size of the meltpool boundary increased (significantly in terms P_{TK}) and the fraction of LOF is significantly reduced to f_{LOF} << 0.1%.

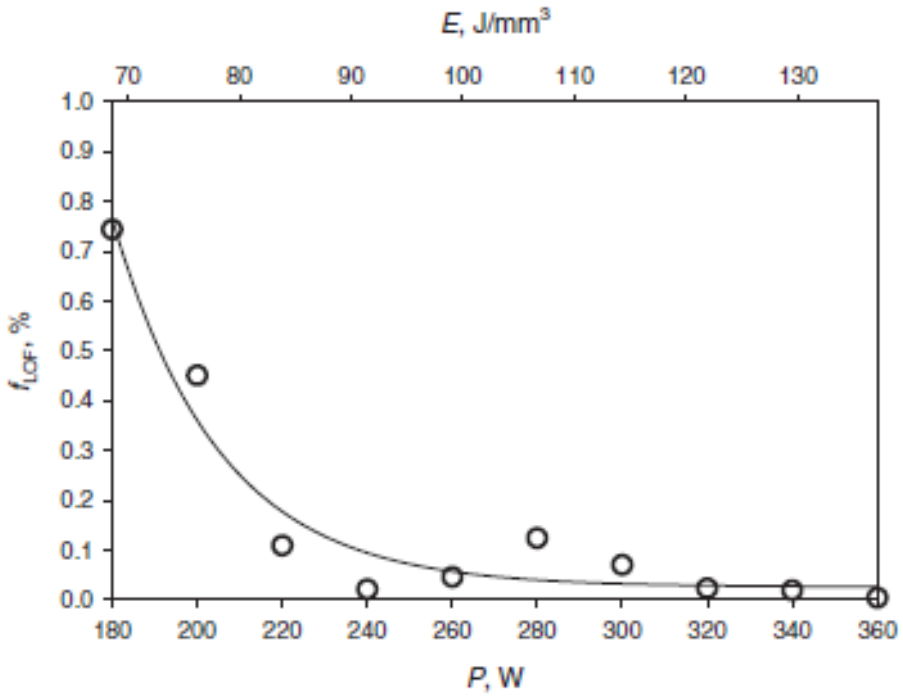

Figure 22 Relationship between the area fraction of LOF, f_{LOF} vs laser power, P, for SLM Co-Cr-Mo alloy [13].

The studies reported by Darvish et al. and Chen et al. above are important references for this thesis in terms of the selection of SLM parameters in order to manipulate the microstructure of SLM Co-Cr-Mo. Based on these studies, the expected microstructure feature of SLM Co-Cr-

Mo when printed at low power, P = 180 W (recommended by manufacturer) and at high power, P = 320 W (after optimisation) could be summarised as follows:

1) P = 180 W samples have significantly more LOF compared to P = 320 W samples.
2) Both P = 180 W and P = 320 W samples consist of only columnar grains, with cellular cells growing epitaxially (i.e. no equiaxed grains and planar growth).
3) P = 180 W samples have a smaller meltpool boundary size compared to P = 320 W samples
4) P = 180 W samples have a smaller columnar grain size compared to P = 320 W samples
5) Both P = 180 W and P = 320 W samples have majority of its columnar grain orientated parallel to BD, but columnar grains in P = 180 W samples are less dominantly oriented in the BD direction.

Darvish et al. [13] also reported that SLM Co-Cr-Mo samples are vulnerable to an occasionally extra-large LOF that is believed to be caused by spatters during laser scanning. One of these infrequent LOFs was found to be at a size of 5000 μm^2 in the P = 340 W sample. An example of the large LOF for the P = 240 W sample is shown in Figure 23. The presence of large LOF in this material emphasises the importance of fatigue studies, specifically FCGR studies, as these kind of defects (large size with sharp geometry shown in Figure 23) could very easily act as an initiation crack growth area due to its high stress intensity factor, K during loading.

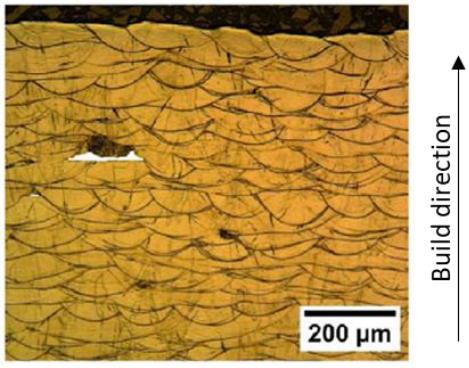

Figure 23 Micrograph of SLM Co-Cr-Mo alloy at P = 280 W, showing occasionally extra-large LOF [13]

As-cast Co-Cr-Mo alloys consist of the α-Co (F.C.C) primary phase and a very small amount of the ε-Co (H.C.P) phase that formed by martensitic transformation from α-Co to ε-Co during cooling [71]. This is consistent with the as-built SLM Co-Cr-Mo alloy reported by Takaichi et. al [43]. The property of this alloy is reported to depend on the ratio of these phases; elongation of the Co-Cr-Mo alloy increases with the increase of the α-Co (F.C.C) phase fraction [72-74] and wear resistance increases with the increase of the ε-Co phase fraction for the metal-on-metal condition [75]. This is expected as the F.C.C structure would display more ductility (deform longer under load before it plasticises) as it has 12 slip systems (three {111} family of planes and four <110> direction) compared to H.C.P that is more brittle with only 3 slip systems (one plane and three directions). Therefore, the presence of a H.C.P structure is also expected to influence the crack growth behaviour due to its brittleness.

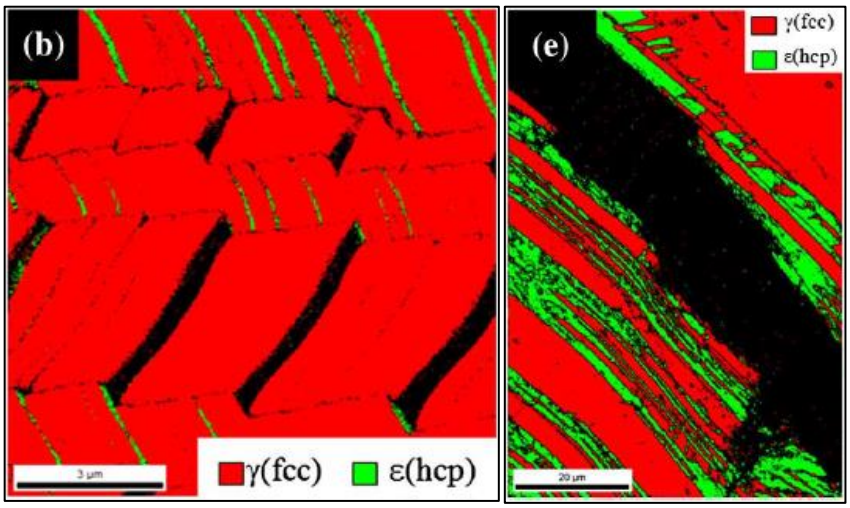

Figure 24 EBSD phase map for Co-Cr alloy under strained (b) 20% and (e) 24.2%. α-Co (F.C.C) phase, marked as red are shown to transform into ε-Co (H.C.P) phase, marked as green under tensile deformation [76]

Under static loading (tensile deformation), Lee et al. [76] claims that there could be a strain-induced-martensite-transformation (SMIT) phenomenon that transforms α-Co (F.C.C) into ε-Co (H.C.P) as shown in Figure 24 above. This event might cause the plastic zone area in front of a crack tip (as illustrated in Figure 25) to be more brittle as the ε-Co (H.C.P) phase fraction increases. In addition, the plastic zone length in front of the crack tip will also increase as the SIF value increases (according to the formula in Table 3). This might also factor into the crack growth behaviour of the alloy since crack growth is a local fracture phenomenon where a material locally

experiences K > K_C. However, Ueki et al. [77] show that the α-Co (F.C.C) does not transform into ε-Co (H.C.P). Therefore, it is important to confirm whether the SMIT transformation occurs or not under the cyclic loading in this study.

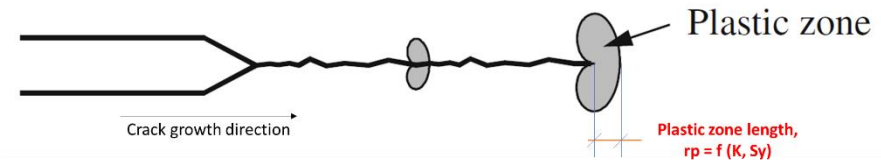

Figure 25 An illustration of a plastic zone in front of a crack tip during fatigue crack growth due to high stress concentration

1.3.2 Inconel 738

The Inconel 738 alloy was designed to provide the gas turbine industry with a material that possesses a high creep and fatigue strength combined with high hot corrosion resistance. According to the International Nickel Company (INCO)'s specs sheets [78], its manufacturing process requires vacuum melted and vacuum investment casting. Figure 26 shows an example of a cast Inconel 738 turbine wheel part used in a turbo supercharger system, where the turbine is driven by hot exhaust gasses that can reach up to 1000 ºC. The chemical composition and its recommended range of Inconel 738 based on INCO's specification is shown in Figure 27.

Figure 26 Turbine wheel for a turbo supercharger parts manufactured by Yili Power Technology Co. Ltd.

Although it was initially designed for casting, many studies have explored its 3D printability using SLM and LDM [12, 79-81]. Similar to most nickel-based superalloys, Inconel 738 is considered as a difficult to weld metal. This has constrained its 3D printability, especially in terms of its high susceptibility to micro defects that were caused during the solidification process. There have been reports on the optimisation of its SLM parameters [79, 80] where the SLM Inconel 738 had surpassed cast and INCO's tensile strength requirements of S_y = 896 MPa, S_T = 1034 MPa, and ε = 7%. Nevertheless, there are still evident of porosity and micro-cracks presence in its microstructure. The unique microstructure of the as-built SLM Inconel 738 will be discussed in the next section, and the behaviour of crack growth passing through its microstructure will be a focus of the FCGR study in this thesis.

Composition of Alloy IN-738

	Composition, weight percent			
	High Carbon IN–738C		Low Carbon, Low Zirconium IN–738LC	
Element	Range	Nominal	Range	Nominal
Carbon	0.15-0.20	0.17	0.09-0.13	0.11
Cobalt	8.00-9.00	8.50	3.00-9.00	8.50
Chromium	15.70-16.30	16.00	15.70-16.30	16.00
Molybdenum	1.50-2.00	1.75	1.50-2.00	1.75
Tungsten	2.40-2.80	2.60	2.40-2.80	2.60
Tantalum	1.50-2.00	1.75	1.50-2.00	1.75
Columbium (Niobium)	0.60-1.10	0.90	0.60-1.10	0.90
Aluminum	3.20-3.70	3.40	3.20-3.70	3.40
Titanium	3.20-3.70	3.40	3.20-3.70	3.40
Aluminum + Titanium	6.50-7.20	6.80	6.50-7.20	6.80
Boron	0.005-0.015	0.010	0.007-0.012	0.010
Zirconium	0.05-0.15	0.10	0.03-0.08	0.05
Iron	0.05 max	LAP†	0.05 max	LAP†
Manganese	0.02 max	LAP	0.02 max	LAP
Silicon	0.30 max	LAP	0.30 max	LAP
Sulfur	0.015 max	LAP	0.015 max	LAP
Nickel	Balance	Balance (61)	Balance	Balance (61)

Figure 27 Chemical composition for Inconel 738 based on INCO's spec sheet [78]. Note that this study uses In-738 LC (low carbon) powder.

1.3.2.1 Microstructure

Unlike some printable nickel-based superalloys such as Inconel 718, 600 or 625, where process parameters could successfully prevent the formation of micro defects [82-84], Inconel 738 consists high volume fraction of the γ'- (Ni_3(Al, Ti)) intermetallic strengthening phase in its F.C.C matrix, γ. The micro defects problem has not been effectively eliminated yet for Inconel alloys with a total Ti + Al content over 6 wt% [81, 85], such as Inconel 738. One way of reducing micro crack defects is by having a key-hole meltpool shape (by manipulating the SLM parameters), yet, key-hole meltpool shape could cause micro pores defects (also known as key-hole pores) [12, 79]. Conclusions on the effects of minor elements on the micro cracks for additively manufactured Inconel 738 vary. For example, Engeli et al. [86] claimed that Si and Pb have a detrimental effect on micro cracks density, while Cloots et al. [87] evaluated the segregation of minor elements near grain boundaries and suggested that B and Zr enhance the formation of micro cracks. Figure 28 shows an example of a micro crack and a micro pore that were found on an SLM Inconel 738.

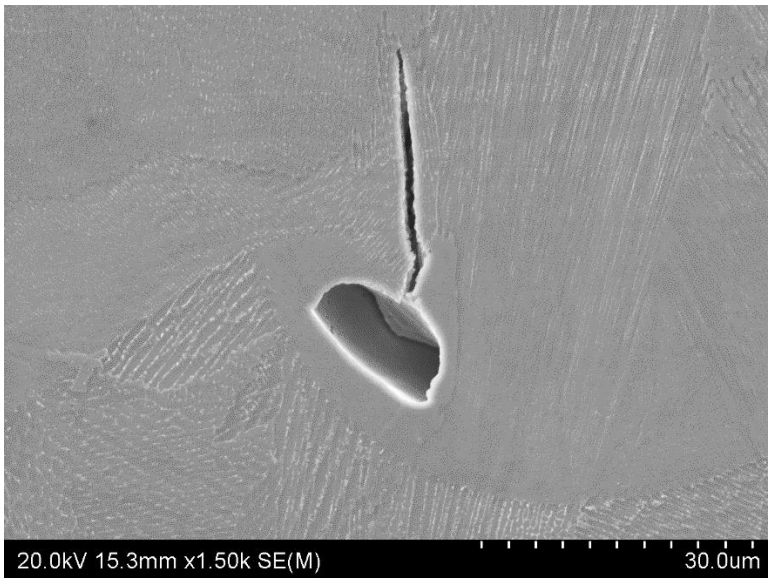

Figure 28 SEM image of a typical microstructure defects in Inconel 738; micro pore and micro crack.

Chen et al. [12] suggested that a 67º scanning strategy, SS (laser scanning direction to be rotated 67º after each layer) during SLM printing process can benefit in disrupting the uniformity of grain growth direction, thus reducing the length of long columnar grains. As a result, the length

of micro-cracks found along the grain boundaries can be reduced. They also measured the density and length of the micro-cracks based on a 16.5 mm^2 cross-section micrograph. Figure 29 shows their measurements of micro-cracks found in SLM Inconel 738 samples, printed with laser power 270 W and 320 W. The 320 W sample has slightly fewer cracks compared to the 270 W sample and the size of these micro-cracks are mostly below 40 µm in length with few long ones reaching up to 120 µm. On the other hand, the 320 W sample produced a higher number of micro-pores as compared to the 270 W sample due to its deeper meltpool penetration depth (illustrated in Figure 30).

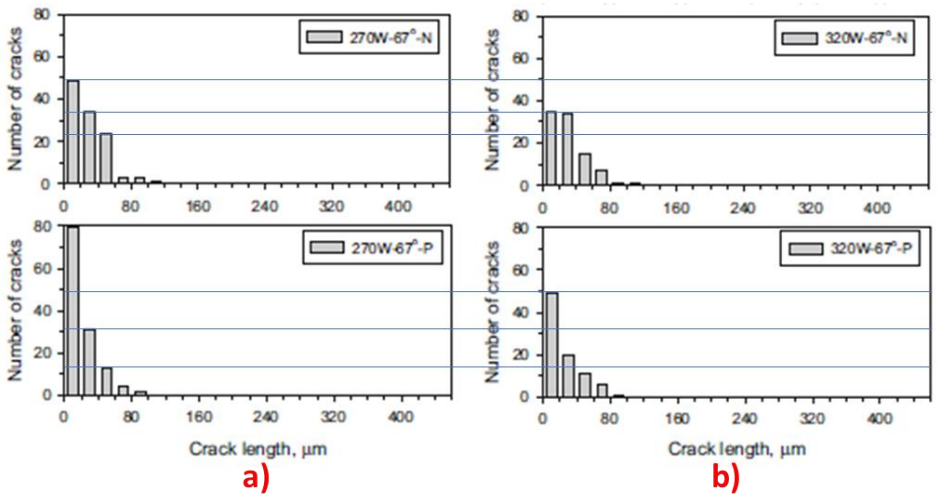

Figure 29 Amount and length of micro cracks in SLM Inconel 738 for a) P = 270 W and b) P = 320 W. The "67°" in the label refers to its SS, and "P" or "N" refer to the view angle at which the data was collected [12].

The meltpool shape for SLM Inconel 738 (keyhole meltpool mode) is different compared to the previously discussed SLM Co-Cr-Mo (conduction meltpool mode). As shown in Figure 30, the meltpool's penetration depth, P_{TK} for SLM Inconel 738 is deeper in relation to its width, W_{TK}, which resulted in a steeper meltpool boundary. The distinctions between conduction mode and keyhole mode meltpool can be defined through the ratio between W_{TK} and P_{TK}; it is suggested that the keyhole mode is dominant when $W_{TK}/P_{TK} \leq 2$ [88, 89]. Qi et al. have reported that the keyhole meltpool mode would not only result in fine, irregular grain distribution, but also reduce the density of micro cracks as compared to the conduction meltpool mode [90].

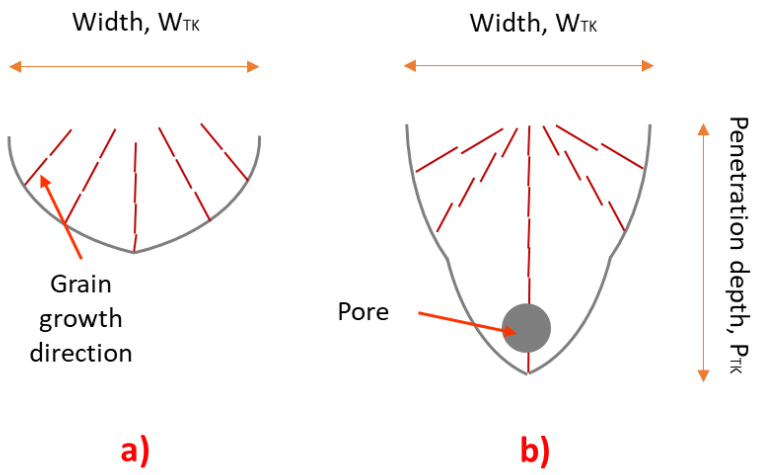

Figure 30 An illustration of a) conduction meltpool (SLM Co-Cr-Mo) and b) keyhole meltpool.(Inconel 738)

It is also important to mention that having higher laser power, P (while all other SLM parameters were kept constant) will increase the depth, P_{TK} of the keyhole meltpool. This will result in a slightly more irregular grains (more grains might grow askew away from the BD) due to the steep meltpool boundary, forcing the grains to grow horizontally. In addition, higher laser power can also increase the density of the keyhole pores defect that was shown in Figure 30. It should be noted that this defect is not the same as the lack of fusion (LOF) defect mentioned in the SLM Co-Cr-Mo alloy. As mentioned earlier in Chapter 1, section 1.1.2.1, keyhole pores defect are spherical in shape, caused by the entrapped air in the powder, forming vapour bubbles that periodically collapse during the keyhole meltpool formation, while LOF defects are irregular in shape with slit/sharp ends. In addition, Inconel 738 is composed of carbide phases that might affect the fatigue behaviour. Carbides are carbon in the amounts of 0.02 to 0.2 wt.%, which combine with reactive elements to form brittle metal carbides. These brittle carbide phases usually form near the grain boundary and can appear in different shapes, depending on the type of carbide, such as MC, $M_{23}C_6$, M_6C and M_7C_3 [63]. Based on these studies, the expected microstructure feature of SLM Inconel 738, having them printed at low power, P = 270 W and at high power, P = 320 W, can be summarised as follows:

1) P = 320 W samples have significantly more micro-pores compared to P = 270 W samples.

2) Both P = 320 W and P = 270 W samples have columnar grains, with growth direction parallel to BD, but the columnar grains in P = 320 W samples are slightly irregular (less dominantly parallel to BD).
3) Both P = 320 W samples and P = 270 W samples have a keyhole shaped meltpool. P = 320 W samples have a deeper penetration depth and steeper meltpool boundary compared to P = 270 W samples
4) P = 320 W samples have slightly fewer micro cracks compared to P = 270 W samples.
5) Most of the micro cracks and carbides will be located at the grain boundaries, with an average size of 40 μm, up to 120 μm.

To conclude, Chapter 1.3 discusses the effect of SLM parameters on the microstructure of Co-Cr-Mo and Inconel 738 alloys. Changing laser power (P) will affect the meltpool size, while changing build direction (BD) will significantly change the grain orientations. By using alloy powders of these two materials, Renishaw AM 250 SLM machine is set to produce standard FCGR specimens (CT specimen, discussed in Chapter 3.0) at different P and BD to create samples with different microstructure conditions. The objective of this study is to address the gap in the understanding of the parameters-microstructure-fatigue relationship by performing FCGR experiment [91]. Figure 31 [22] schematically presents a broad view of the interrelationships between the process parameters and the mechanical/fatigue behaviour of SLM parts where the fatigue behaviour of an SLM part is dictated by the service load and microstructural features of the material.

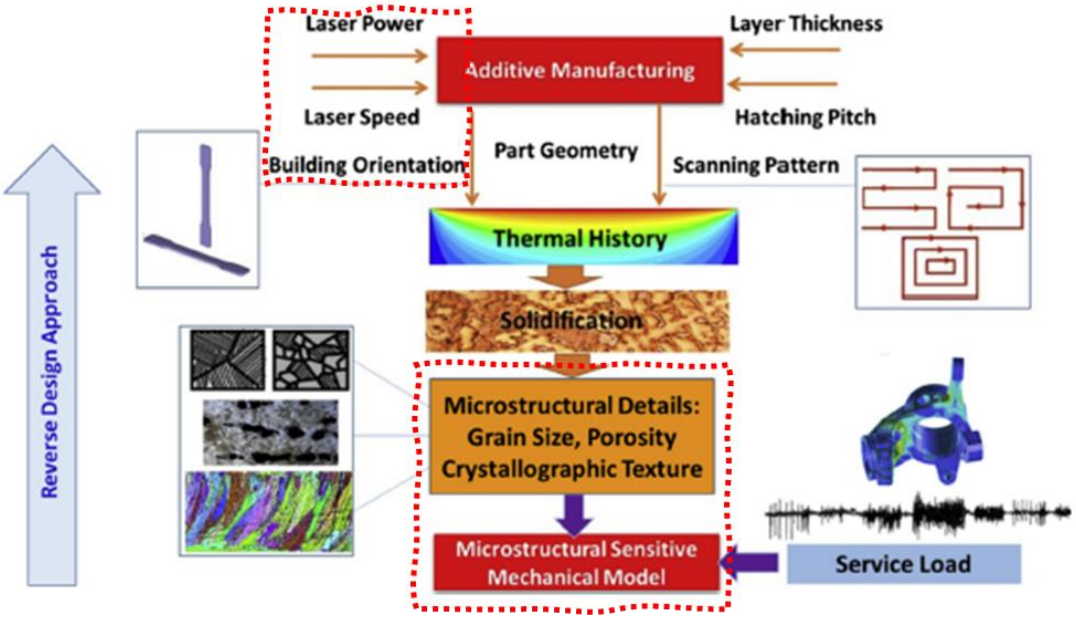

Figure 31 Interrelationships between mechanical behaviour and process parameters for additive manufactured parts [22]

The FCGR parameters and the mechanism of crack growth pathway in each microstructure condition will be discussed in Chapter 4.0 and 5.0 for Co-Cr-Mo and Inconel 738 alloys, respectively. The literature review in Chapter 2.0 presents and discusses reported FCGR studies on SLM Cobalt-based and Nickel-based superalloys to identify and clarify the literature gap in this study.

2 Literature review

The FCGR experiment allows the monitoring of a controlled crack movement, which can provide insight into how cracks behave under a specific microstructure condition. The examination of a crack movement in terms growth rate and pathway would further contribute to our understanding of the parameters-microstructure-fatigue relationship. It is also important to note that a specific material system responds uniquely to different combinations of SLM process parameters. Different materials undergo different thermal history and solidification process during SLM, which then leads to unique microstructural features (as discussed in Chapter 1.3). As there is a lack of research being reported on the FCGR behaviour of SLM materials, especially for superalloys, this Chapter will delve into reported FCGR study for Cobalt-based and Nickel-based superalloys to identify further research opportunities that would contribute to the understanding of fatigue crack growth behaviour in SLM superalloys.

2.1 Fatigue crack growth (FCG) studies of Co-based superalloys

Despite the need in understanding the effects of SLM microstructure on the crack growth behaviour for SLM Co-Cr-Mo superalloy (ASTM F75) as highlighted by Kajima et al. [39], there has been no reported FCGR experiment for this particular material. Recently, Lee et al. [92] published a paper on the microstructure and mechanical anisotropy of another SLM Cobalt-based alloy: Co-Cr-W. In their study, they have included a FCGR experiment for two different BD samples, following the ASTM E647 standard. Thus, the current research offers the only available FCGR study available SLM Co-based superalloys. Co-Cr-W has similar biomedical applications as Co-Cr-Mo, and according to Lu et al. [93] SLM Co-Cr-W printed using the line and island scanning strategy also comply with the ISO standard for medical implants.

It is also useful to have an insight into the FCGR behaviour of traditionally manufactured Co-Cr alloys to compare and investigate the preferred crack path or resistance in its microstructure. Okazaki [94] conducted a FCGR experiment on a wrought Co-Cr-Mo-Ni-Fe alloy (ASTM F90) to ultimately compare the FCG behaviour of various implantable metals, while Ritchie and

Lubock [95] conducted a FCGR experiment on a Co-Cr-W-Ni alloy (Haynes 25) to determine the acceptable flaws size on a non-destructive evaluation (NDE) test for a cardiac valve prosthesis. The last FCGR experiment reported for a Co-Cr-Mo alloy was in 1989 by Zhuang and Langer [69]. The authors investigated how cracks would propagate in two different grain sizes, namely: fine and coarse grains size, for a cast Co-Cr-Mo alloy (F75). Table 5 below summarises all the FCGR result parameters for Co-based superalloys; only one of them was manufactured via SLM.

Table 5 Summary of FCGR parameters on Co-based superalloys from the literature

Sources and material	Process condition	Region I	Region II		Region III
		ΔK_{th} (MPa$\sqrt{m}$)	C	m	ΔK_C (MPa$\sqrt{m}$)
Lee et al., 2019 [92] Co-Cr-W	SLM C⊥BD	4.8	2.6×10^{-12}	4.3	13
	SLM C//BD	3.6	3.6×10^{-12}	4.6	12
Okazaki, 2012 [94] Co-Cr-Mo-Ni-Fe	Vacuum-induction melting cast + annealed	5.0	1.5×10^{-12}	3.2	53
Ritchie and Lubock, 1986 [95] Co-Cr-W-Ni	N/A	10.5	1.0×10^{-13}	3.7	N/A
Zhuang and Langer, 1989 [69] Co-Cr-Mo	Cast + air cooling (coarse grains)	10.5	4.0×10^{-20}	8.7	55
	Cast + water cooling (fine grains)	14.0	7.3×10^{-18}	6.7	N/A

2.1.1 Critical review on the FCGR studies of SLM Co-Cr-W superalloy

Lee et al.'s research [92] is the only reported FCGR study for SLM Co-based superalloys. Firstly, to avoid any confusions on the abbreviations of the Compact Tension (CT) sample's name used in Lee et al.'s work and this report, Figure 32 shows the two build directions of Lee et al.'s CT samples. The figure was taken directly from Lee et al.'s report and the labels for their CT specimens differ from the ones employed in this study. Thus, to ease discussion 1) the CT-V (TD//BD) sample will be referred as C⊥BD and 2) the CT-H (TD⊥BD) sample will be referred as C//BD. C⊥BD is when the crack growth direction is perpendicular to BD, while C//BD is when crack growth direction is parallel to BD. Figure 32 also shows the characteristic size of the CT samples used, which is W = 50.8 mm (W is the maximum crack length for a CT sample, W = 63.5mm/1.25 = 50.8 mm). The loading ratio and frequency of the fatigue loading are similar to the one used in this study which is R = 0.1 and f = 10 Hz, respectively.

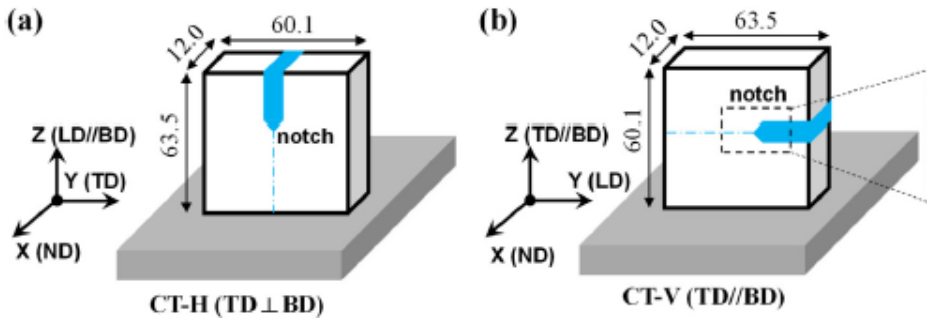

Figure 32 CT sample's dimensions and orientation used in Lee et al.'s FCGR experiment. a) C//BD and b) C⊥BD [92]

As shown in Figure 33, the FCGR curve reported by Lee et al. is typical for metallic materials, except in Region 3 where the result suggest that both CT specimens start to fracture at an extremely low ΔK value. The crack growth in the C⊥BD specimen reaches a rate of 10^{-4} m/cycle and continues to rise vertically at only 13 MPa$\sqrt{m}$, while the C//BD specimen starts to enter Region 3 at around 12 MPa$\sqrt{m}$. This is unusual because Co-Cr-based alloys have a fracture toughness value of $K_{1C} \approx 60$ MPa$\sqrt{m}$ [96], therefore the magnitude of ΔK values at a catastrophic crack growth rate is expected to be around 60 MPa$\sqrt{m}$. Based on their report, there is no clear indication as to why their CT samples appeared to fracture at very low ΔK values. This could

possibly be due to several factors. One of the factors could be that, since the electric potential difference (EPD) drop technique was used, crack size measurements were not valid/accurate when the crack size (a) reached the value of a/W ≥ 0.7 [97], while the fractured CT samples (shown in Figure 36) appears to suggest that the crack growth fractured well beyond the a/W ≤ 0.7 limit. Alternatively, it may be due to the loosening of the wires placed at high ΔK amplitude (if the wires were not welded properly to the CT samples) since EPD technique requires wires to be fixed at the mouth opening of the CT sample. Therefore, due to this issue, only Region 1 and 2 will be discussed in this report. It is also important to note that based on the micrograph presented, the unusual curve in Region 3 is unlikely due to the integrity of the printed material.

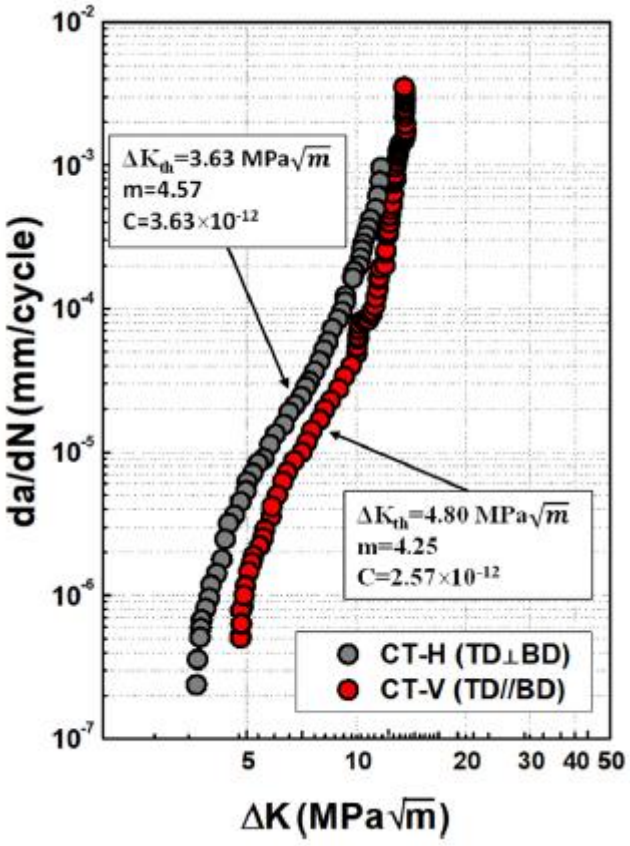

Figure 33 FCGR graph for SLM Co-Cr-W for two different build directions; crack growth perpendicular to build direction, C⊥BD (marked as red) and crack growth parallel to build direction, C//BD (marked as grey) [92]

Prior to discussing the relationship between fatigue behaviour and its microstructure, it is also useful to look at the SLM parameters used in this experiment. The SLM machine used in Lee et al.'s experiment was Concept Laser M2, made in Germany. The energy, E (E = P / (v × h × s))

transferred by the laser beam is unknown since the hatching space (s) value was not reported. Other SLM parameters were provided as follows: laser power, P = 200 W, laser velocity, v = 800 mm/s, and layer thickness, h = 0.03 mm. There was no discussion on the selection or optimisation for the SLM parameters, but the tensile test showed excellent results that were similar to Kajima et al.'s findings[39]. Based on the optical microscope images shown in Figure 34, there were few instances of lack of fusions (LOF) present in between the track boundaries, but the effect of those micro-defects on the FCGR behaviour were not discussed.

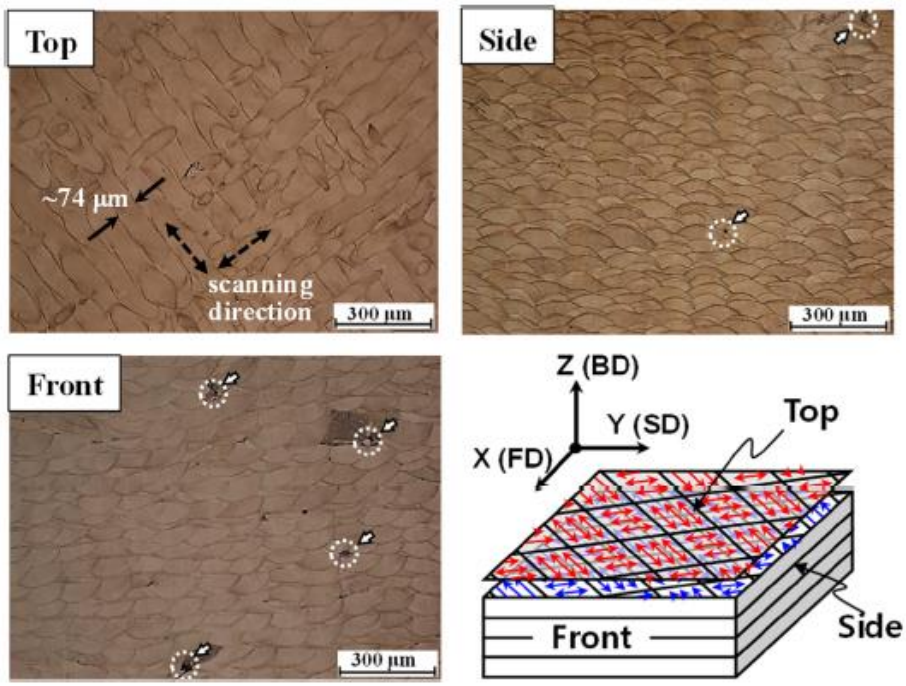

Figure 34 Optical microscope images of SLM Co-Cr-W, revealing LOF and meltpool boundaries [92]

The FCGR graph in Figure 33 suggested an anisotropic FCGR behaviour for the SLM Co-Cr-W alloy. In Region 2, the C//BD sample displays a slightly higher gradient (which is represented by the Paris constant, *m*) and higher Paris constant, C, as compared to the C⊥BD sample. As for Region 1, the threshold value for the C//BD sample (ΔK_{th} = 3.6 MPa$\sqrt{m}$) is lower compared to the C⊥BD sample (ΔK_{th} = 4.2 MPa$\sqrt{m}$). This suggests that it is easier for a crack to initiate and propagate inside the C//BD microstructure. In other words, the C⊥BD samples are shown to be tougher, or having higher FCG resistance. While no in-depth analysis on the relationship between the microstructure and the crack growth pathway was presented, the authors suggested that it is generally easier (and therefore faster) for a crack to grow in the direction parallel to BD compared

to perpendicular to BD because of the orientation of the columnar grains. For the C⊥BD sample, the long columnar grains (shown in Figure 35), which are oriented parallel to the BD, build-up many vertical grain boundaries that act as a resistance against the crack growth (as crack grows horizontally).

Figure 35 Columnar grain orientation of SLM Co-Cr-W alloy. Majority of the grain boundaries are orientated upwards. Build direction (BD) is upwards [92]

The image of the fractured CT samples (shown in Figure 36 below) shows that the C⊥BD CT sample has a jagged crack profile and a rougher fractured surface, while the C//BD CT sample has a straight crack profile with a smooth crack surface. This image was used to support their claims that the grain boundary is responsible for interrupting the crack path, which has resulted in a tortuous crack path for C⊥BD sample. Apart from this, there was no further analysis conducted on the fractured samples. Nevertheless, a fatigue study on 316L stainless steel [98] was cited by Lee et al. to describe how cracks pass through the grain boundary (illustrated in

Figure 37). The explanation on the crack growth pathway however remains a hypothesis [98] and further verification is needed to verify how crack propagate in C⊥BD and C//BD samples. Observations on the crack pathway can be made by conducting an "interrupted FCGR test" which is explained in Chapter 3.0.

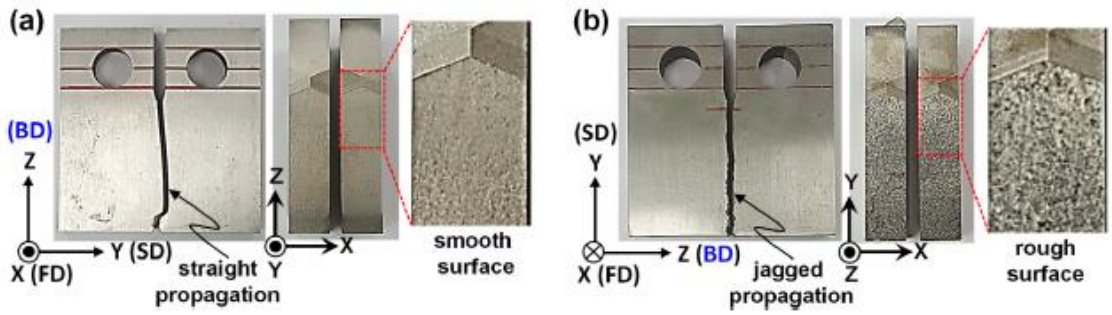

Figure 36 Fractured CT samples for Co-Cr-W alloy a) C//BD and b) C⊥BD. C//BD sample has a smooth fractured surface and straight crack growth direction while C⊥BD sample has a rough fractured surface and a jagged crack growth direction [92]

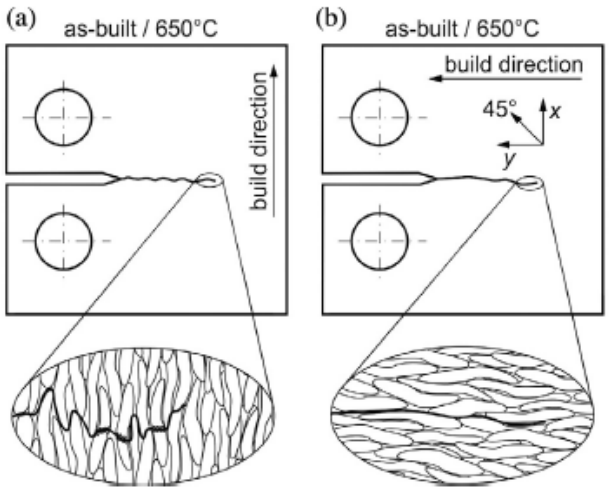

Figure 37 Schematic illustration on crack passing through columnar grains at two different BD orientation for SLM stainless steel [98]

Moreover, it is also important to comment on the statement made by Lee et al. regarding the fatigue life of an SLM material. The authors claimed that for a HCF test, the fatigue life is shorter if the crack growth direction is parallel (perpendicular in terms the of loading axis) to the BD, which they attributed it to the FCGR resistance of the grains boundary, thus justifying their result. This assumption was inconsistence with Kajima et al.'s finding [39], who have conducted a HCF test with the crack growth direction in a vertical direction (instead of the typical HCF test with vertical loading axis). The result shows that the FL90 samples (crack growth direction

perpendicular to BD, C⊥BD) had a shorter fatigue life compared to FL0 (crack growth direction parallel to BD, "C//BD"). In fact, with reference to Figure 9, the fatigue life for the FL0 is substantially higher compared to the FL90 samples (205,418 cycles compared to 28,484 cycles). Even though this is not an indication that crack growth is slower when it is moving parallel to the build direction (contradicting the explanation given by Lee et. al), such conclusion cannot be made since the nature of fatigue-life tests are different compared to FCGR testing. Based on in this literature review, the following direction for research can be identified:

- Investigate the effect of the grain boundary on the FCGR of SLM Co-Cr alloys by examining the crack growth pathway in the C⊥BD and C//BD samples, with fractographic evidence.
- Clarify whether the C//BD or C⊥BD would demonstrate a better toughness in terms of FCGR since HCF result suggested otherwise.
- Discuss how other SLM microstructure features (such as the meltpool boundary, cell boundary or LOF) affect the crack growth pathway and the mechanisms that causes FCGR resistance.
- Conduct a complete FCGR test, with a more reliable Region 3 result.

2.1.2 FCG studies of cast Co-Cr-Mo alloy

To date, the only FCGR graph for Co-Cr-Mo (F75) alloy was provided by Zhuang and Langer [69]. A three-point bending specimen based on ASTM E399 [51] (standard test method to determine fracture toughness) was used to conduct the FCGR experiment. Multiple modifications on the ASTM E399 standard were implemented to measure the crack growth rate[99-101] with an optical camera to track the crack length. The FCGR graph reported, as shown in Figure 38, indicated a possibility that the results in Region 2 were inaccurate because the Paris constants, *C,* and *m values* ($C = 4.0\times10^{-20}$ and $m = 8.7$) were too far off from the typical metallic range. However, the results in Region 1 and 3 were in range of a typical metallic material. Typically, "C" and "m" value is in the range of $10^{-10} – 10^{-13}$ m/cycle and 2 – 4, respectively [44]. This study,

along with previously published studies [102, 103] by the same authors focused on the microstructure and fracture for Cast Co-Cr-Mo, therefore, the relationship between microstructure and the crack growth behaviour have been well discussed.

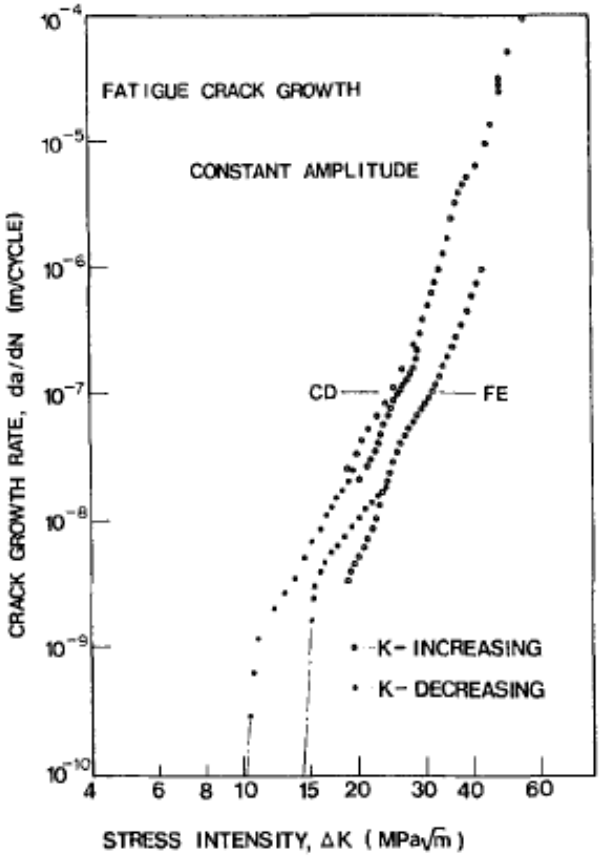

Figure 38 FCGR result for a cast Co-Cr-Mo alloy with reference to two types of microstructure, namely: fine equiaxed structure (FE) and coarse dendritic grain structure (CD) [69]

The two different types of microstructures (FE and CD) used in this experiment are schematically presented in Figure 39. Both were prepared through an investment casting process but with different cooling rates, resulting in different grain distribution and size. The FE sample has an average grain size of 60 µm with a yield strength of S_y = 578 MPa, and tensile strength of S_T = 954 MPa, while the CD sample has the corresponding values of 400 µm, S_y = 523 MPa, and S_T = 739 MPa. The threshold value for the FE and CD samples are ΔK_{th} = 14.0 MPa$\sqrt{m}$, and ΔK_{th} = 10.5 MPa$\sqrt{m}$ respectively, indicating that FE samples are tougher and better in resisting crack growth. Note that the accuracy of the threshold value is uncertain since the Y-intercept and the

gradient (the Paris constant C and m value) in Region 2 curve (connected to the curve in Region 1) is too far off from a typical FCGR graph.

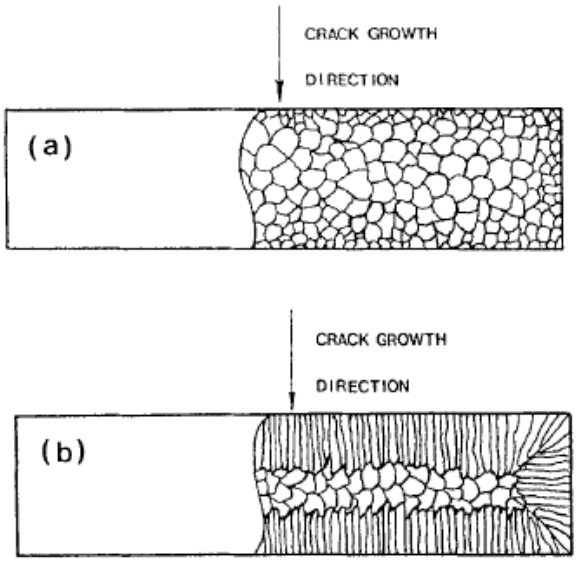

Figure 39 Schematic representation of cast Co-Cr-Mo grain distribution for a) Fine equiaxed structure, FE and b) Coarse dendritic structure, CD [69]

There is no universal relationship between grain size and fatigue threshold (ΔK_{th}); some studies report an increase in the FCGR threshold with an increase in grain size [104-106], fitting the equation of $\Delta K_{th} = A + B\sqrt{d}$, where d is the grain size, while Higo et al. [107] suggested an inverse relationship with an alternative equation of $\Delta K_{th} = A + B/\sqrt{d}$. Zhuang and Langer [69] appeared to agree that gain size is not the determinant factor on the ΔK_{th} parameters. In the discussion, the author did not reference the difference in grain size between the two materials (FE and CD) to be a factor for the different FCGR parameters, instead, they identified and suggested the following microstructure features to be the main influence 1) Grain shape (equiaxed or dendritic structure), 2) the distribution of precipitate, and 3) Crystal growth orientation.

Based on Figure 39, Zhuang and Langer [69] suggested that cracks could grow easier in the CD samples because it is moving in the direction parallel to the directional growth of the dendritic structures (along the grain boundary), while there is no dendritic structure that might favour crack propagation in the FE samples. The authors suggested that it is easier for cracks to pass through

grain boundaries because most carbide phases precipitated near the grain boundary, making this region more brittle. This theory is discussed in more detail in their previous paper [103]. Thus, because of the precipitation of Carbide, the grain boundary can be an influential factor on the crack growth pathway. Nonetheless, the fractured surface of the two samples shown in Figure 40 reveals that the fracture mode is dominantly transgranular (crack propagating inside the grain).

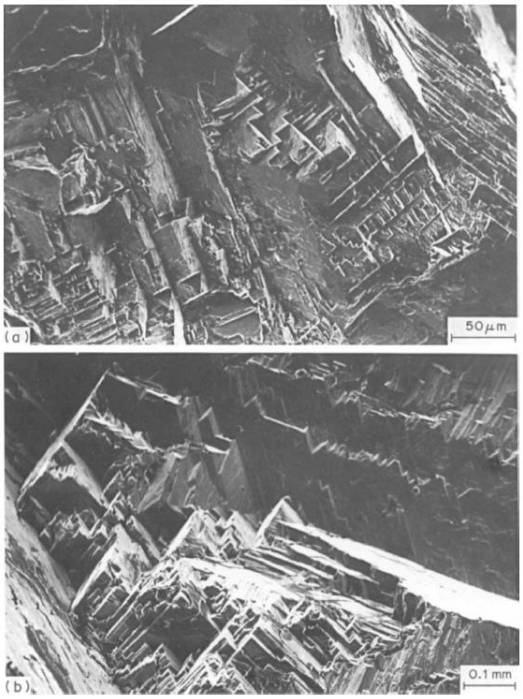

Figure 40 Fracture surface near Region 1 of cast Co-Cr-Mo alloy a) FE sample and b) CD sample [69]

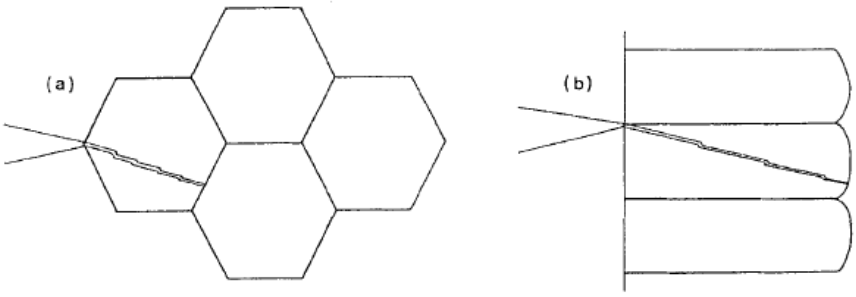

Figure 41 Schematic illustration of crack propagation in cast Co-Cr-Mo alloy a) FE sample and b) CD sample [69]

It was reported in Zhuang and Langer previous study [102, 103] that the $\{111\}_{\text{f.c.c.}}$ planes family dominates the fatigue fracture surface features for cast Co-Cr-Mo alloy. Based on the fracture surface of the samples, a well-developed faceted fatigue fracture can be observed, which is being

attributed to the low stacking fault of the alloy leading to a brittle fracture along the $\{111\}_{f.c.c.}$ planes. The fractured surface for both samples are shown in Figure 40. The authors claimed that the facets fracture size is bigger for CD sample compared to FE sample because there are much longer "free paths" of for cracks to propagate in the CD samples compared to FE samples. This is illustrated in Figure 41. While the authors do not clearly describe the term "free path", it can be assumed that it means that cracks can travel in a longer segment in the CD sample (compared to the FE sample) before it changes direction as it reaches the next grain (with different crystal orientation, thus different orientation on the $\{111\}_{f.c.c.}$ planes).

2.1.3 FCGR studies on the application of Co-based alloys

Okazaki [94] conducted multiple FCGR experiments to compare the FCGR parameters between various implantable metal which included titanium alloys, stainless steel, and Co-based alloys. The testing methods and procedures are in accordance with ASTM E647. Although the microstructure and the crack growth pathway are not discussed in his study, all the FCGR graphs produced, including the FCGR graph for Co-Cr-Mo-Ni-Fe alloy (ISO 5832) (shown in Figure 42 below) lie within the typical rage of a metallic material. Therefore, the FCGR parameters reported by Okazaki (as stated in Table 5) will be used in the current research to compare the expected life between SLM and the traditional manufactured (cast) Co-based alloy.

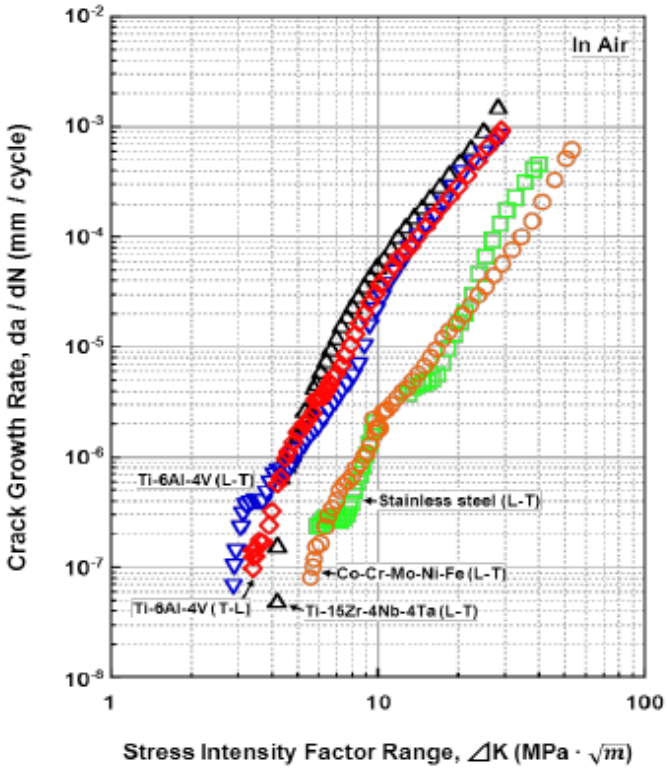

Figure 42 FCGR graph of implantable metals produce by casting [94]

In 1986, Ritchie and Lublock [95] conducted a FCGR experiment on Heynes® 25 alloy (Co-Cr-W-Ni) to estimate the fatigue endurance of a cardiac valve prostheses by using linear elastic fracture mechanics (LEFM) analysis. By considering the pulsatile physiological loading of 76 MPa at the inlet strut and 34 MPa at the outlet strut, it was concluded that NDE should reject components containing flaws larger than 500 µm. Since then, biomedical technology has progressed substantially and now the implantation of endo- and cardiovascular stents in vain arteries is a considered a preferred alternative. An illustration on how the stent sits inside the artery is shown in Figure 43 below. In 2006, in the conjunction with the collaboration between the international company Johnson & Johnson company and Marrey et al. [96], a fracture mechanics analysis was conducted to determine the acceptable size of pre-existing flaws in stents that were processed by casting + laser cutting + electropolished surface finish. Based on LEFM analysis with the assumption of 40 million loading cycles per year (heart rate of 1.2 Hz) and a design life of 10 years (4 x 10^8 cycles), the recommended allowable pre-existing crack size proposed by Marrey et al. [96] is 90 µm.

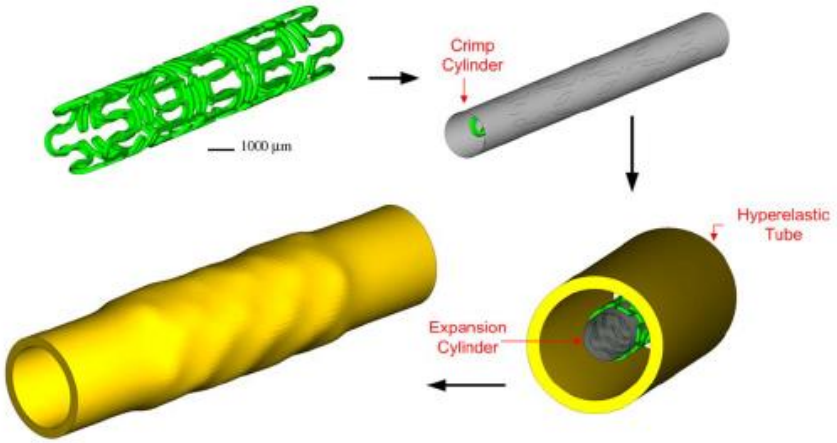

Figure 43 An illustration on the sequence of how the "balloon expendable Co-Cr stent" is being transferred into an artery [96]

Up to this date, there has been no LEFM analysis on SLM Co-based superalloys. Although there has been two HCF test reported [32, 39], an assessment only on the basis of survival (i.e. maximum fatigue strength at 10^6 or 10^6 cycles) does not offer the additional information obtainable by fracture mechanics analysis, such as (i) a basis of quality control for the product, (ii) a quantitative evaluation on the damage or defects in the material (iii) a more invariably conservative analysis. Therefore, it is important to investigate how SLM Co-Cr parts would compare to the traditionally manufactured Co-Cr parts in terms of fracture mechanic calculations. Since Co-Cr-Mo alloy is being used in this study, it is appropriate to perform LEFM calculation based on the case study reported by Bonnheim et al. [108], where a 55- years old patient with a cast Co-Cr-Mo stem-hip-implant experiences immature fracture after 24 years of in vivo. The fractured hip stem is shown in Figure 44.

Figure 44 Photograph of immature fracture failure of cast Co-Cr-Mo hip implant [108]

Despite the rapid improvements in stem design [109], femoral stem implant fractures remain a serious complication for hip arthroplasty [110-112]. Therefore, it is important to investigate whether SLM process can help improve the fatigue performance of femoral stem implant. Based on the optical images provided by Bonnheim et al. [108] (Figure 45 below), there is a significant difference in the grain size/shape between cast and SLM Co-Cr-Mo alloy. According to Bonnheim et al. the average grain size of cast Co-Cr-Mo alloy is 1.3 ± 0.6 mm, while SLM has a columnar grains structure with average width of 0.025 mm. The LEFM calculation between SLM Co-Cr-Mo stem implant (with different BD orientation) and cast Co-Cr-Mo stem implant will be included in Chapter 4.5. In addition, the LEFM analysis in Chapter 4.5 would also suggest the allowable size of micro-defects in the Co-Cr-Mo hip-stem-implant.

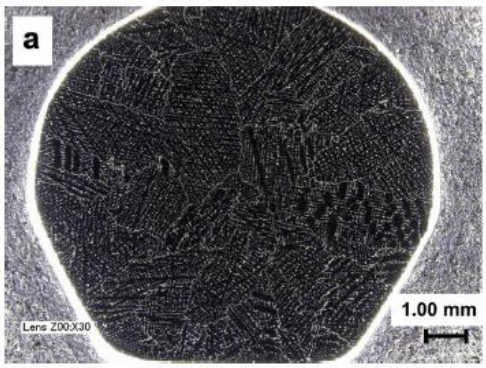

Figure 45 Optical microscope image of surface cross section of cast Co-Cr stem near the fractured area a) grain distribution [108]

2.2 Fatigue crack growth (FCG) studies of SLM Inconel superalloys

Similar to SLM Cobalt-based alloys, the literature on the crack growth behaviour for SLM nickel-based alloys is also limited despite various engineering components of Inconel alloys being subjected to continuous cyclic loading. Available reports on FCGR studies for SLM Inconel alloys have focused more on discovering the difference in FCGR parameters (ΔK_{th} and Paris constant, C and m) with the traditionally manufactured Inconel alloys (cast or wrought) or between different BD samples. Currently, the FCGR of Inconel 738 has not been study yet, and there are only two FCGR reports on SLM Inconel 625 and SLM Inconel 718.

Recently, Hu et al. [113] and Poulin et al. [114] showed that the ΔK_{th} value for SLM Inconel 625 alloy is highly influenced by the building direction (BD) orientation. While contribution on the effect of stress ratio and post-processing heat treatment are included in their reports, neither study examined the crack growth pathway. Brynk et al. [115] conducted a study on the short-crack (physically small crack, explained in Chapter 2.2.2) behaviour of SLM Inconel 718 for three BD orientations (C⊥BD, C//BD and C45BD), which suggested that the ΔK_{th} value reported by Konecna et al. [116] on Inconel 718 was extremely low. The only FCGR graph available for Inconel 738 (cast) was provided by Scarlin [117], who conducted the FCGR test under room temperature, at 750 ºC and at 850 ºC. This section presents a detail literature review on the aforementioned FCGR tests for SLM Inconel alloys. The summaries for their FCGR parameters are compiled in Table 6.

Table 6 Summary of FCGR results on Inconel superalloys from the literature

Sources and material	Process condition	Region I	Region II		Region III
		ΔK_{th} (MPa$\sqrt{m}$)	C	m	ΔK (MPa$\sqrt{m}$)
Hu et al., 2019 [113] Inconel 625	SLM C⊥BD + Annealed (1 hr, 1100 ºC)	9.1	9.1×10^{-13}	4.2	65
	SLM C//BD + Annealed (1 hr, 1100 ºC)	8.1	8.2×10^{-13}	4.4	55
Poulin et al., 2018 [114] Inconel 625	SLM C⊥BD + Ann. (1 hr, 870 ºC)	7.5	4.7×10^{-12}	3.0	N/A
	SLM C//BD + Ann. (1 hr, 870 ºC)	7.1	3.0×10^{-12}	3.2	N/A
	SLM C"45"BD + Ann. (1 hr, 870 ºC)	8.8	2.0×10^{-12}	3.3	N/A
	SLM C"FLAT"BD + Ann. (1 hr, 870 ºC)	10.6	2.4×10^{-12}	3.2	N/A
Brynk et al., 2017 [115] Inconel 718	SLM C⊥BD	"Short cracks" behaviour: Between 8 to 90 MPa$\sqrt{m}$, da/dN are constant at $2\text{x}10^{-8}$ m/cycle for C⊥BD & C//BD and increase from $4\text{x}10^{-9}$ to $2\text{x}10^{-8}$ m/cycle for C45BD. The threshold value is $K_{th} \approx 10$ MPa$\sqrt{m}$ (slightly higher for C45BD compared to C⊥BD & C//BD.			
	SLM C//BD				
	SLM C45BD				
Konecna et al., 2016 [116] Inconel 718	SLM C//BD	3.0	4.5×10^{-11}	2.3	N/A
Scarlin, 1975 [117] Inconel 738	Cast	11.0	1.0×10^{-18}	6.8	70

2.2.1 Review on FCGR studies of SLM Inconel 625

In 2019, Hu et al. [113] conducted an FCGR study for SLM Inconel 625 CT samples, manufactured with the Bright Laser Technologies BLT-S300 printer, China. The laser power used was P = 1000 W and the layer thickness was h = 0.04 mm, but the scanning velocity, v and hatching space, h was not reported. The printed material went through solution annealing heat treatment at 1100 ºC for 1 hour as recommended by the manufacturer. The dimension and building orientation for the CT samples is shown in Figure 46. To assist with the discussion in this thesis, the samples labelled ZX-ver and YZ-par in Figure 46 are being referred to as C⊥BD and C//BD respectively. The FCGR compliance method based on the ASTM E647 standard was used to conduct the FCGR experiment.

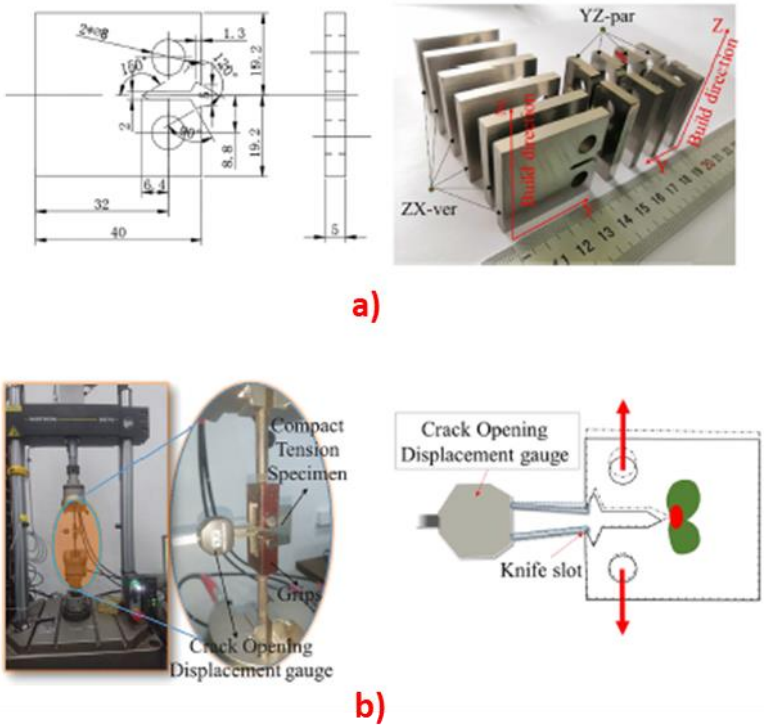

Figure 46 a) SLM Inconel 625 CT samples geometry and build direction and b) FCGR experimental setup [113]

The FCGR graph presented by the authors is shown in Figure 47. Note that the FCGR graph produced by Poulin et al. [114] was also included in their graph for comparison purposes. Since all FCGR lines appeared to merge at the Paris region (here defined as when the ΔK value is between 20 MPa$\sqrt{m}$ - 40 MPa$\sqrt{m}$), Hu et al. [113] concluded that the FCGR in the Paris region

for SLM Inconel 625 is independent of the building direction. However, at the near threshold region where the crack growth rate, da/dN, is low (da/dN ≈ 1 x 10^{-9} - 1 x 10^{-10} m/cycle), the effect of different BD orientations start to become more prominent. The authors concluded that the higher ΔK_{th} value recorded for the C⊥BD sample (ΔK_{th} = 9.1 MPa$\sqrt{m}$) as compared to the C//BD sample (ΔK_{th} = 8.1 MPa$\sqrt{m}$) implies that crack growing perpendicular to the build direction would have encountered higher FCGR resistance as compared to growing parallel to the build direction.

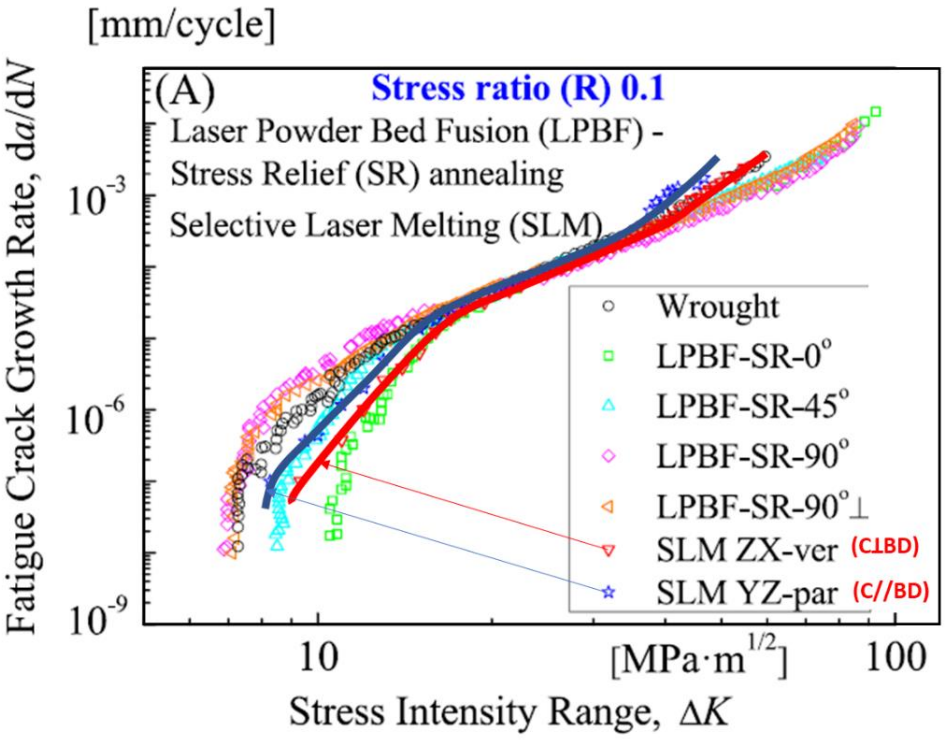

Figure 47 FCGR graph on SLM Inconel 625, blue and red lines (C⊥BD and C//BD) are the results produced by Hu et al. [113] while the rest of the graph are results produced by Poulin et al.[114]

Hu et al. [113] included SEM images of the fractured samples near the threshold and the Paris region in their study to examine the fractographic differences. Figure 48 below shows the SEM images of the fractured surface for both samples (C⊥BD and C//BD) in the threshold region. Based on the fractographical featured marked in Figure 48, the authors claimed that the "micro-voids" did not play a significant role in FCGR behaviour due to the high stress concentration at the crack tip. Hu et al. [113] also claimed that the continuous vertical lines in Figure 48b represent a fatigue striations pattern, which is very unlikely as striation pattern is only visible when crack

growth reaches da/dN = $1x10^{-7}$ mm/cycle (in the Paris region) [109]. Figure 48b also highlights a fractographical featured labelled as Ridges, which was not analysed by the authors.

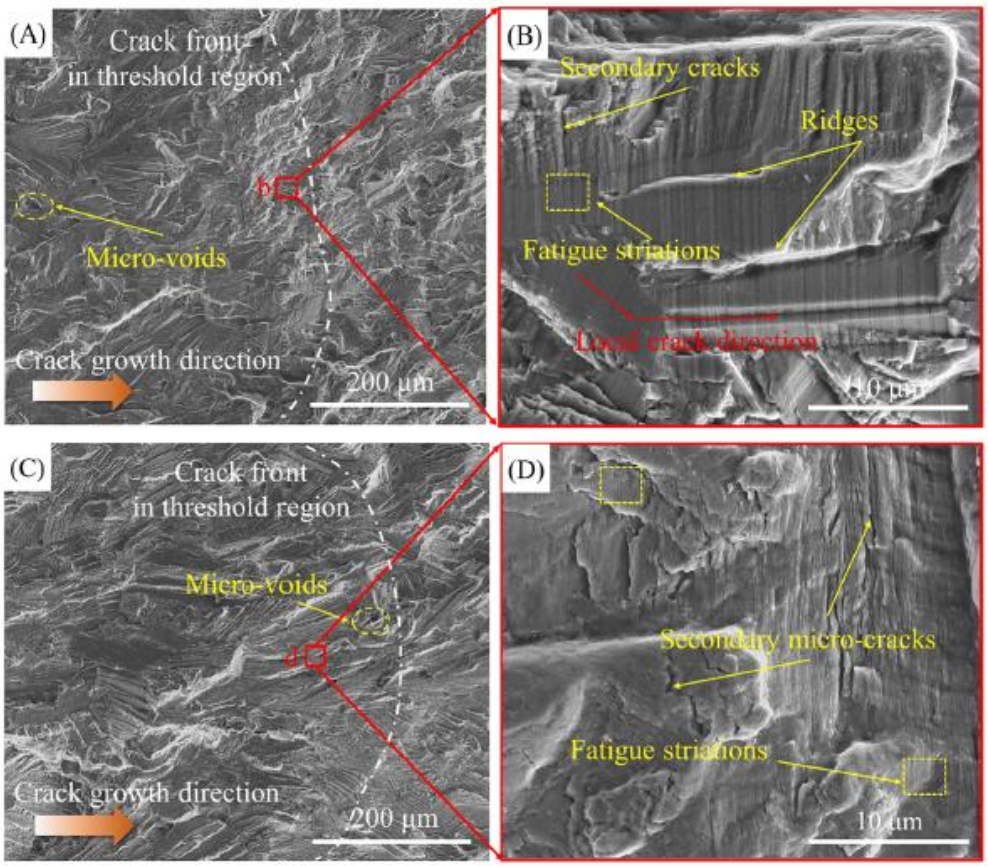

Figure 48 SEM images of fractured surface of SLM Inconel 625 alloys in the threshold region A) and B) represent the C⊥BD samples in low and high magnification respectively, while C) and D) represent the C//BD samples in low and high magnification respectively. [113]

The term "secondary crack" has been generalised to represent cracks that grow into the fractured surface (as illustrated in Figure 49 below). The cause of these secondary cracks ware argued to be generated by 1) progression of fatigue striation, 2) slip lines caused by shear stress [118], 3) pre-existing micro cracks [119] or 4) intergranular crack branching [120]. Figure 48b and Figure 48d show the examples of secondary cracks that were found in Hu et al.'s [113] samples. Based on observation, the authors mentioned that the C//BD samples contained more secondary cracks than the C⊥BD samples, indicating that there is higher intragranular cracking in the local region for the C//BD samples compared to the C⊥BD samples. The local intragranular cracking can deviate the global crack growth direction, causing crack branching that subsequently resulted in higher FCGR resistance.

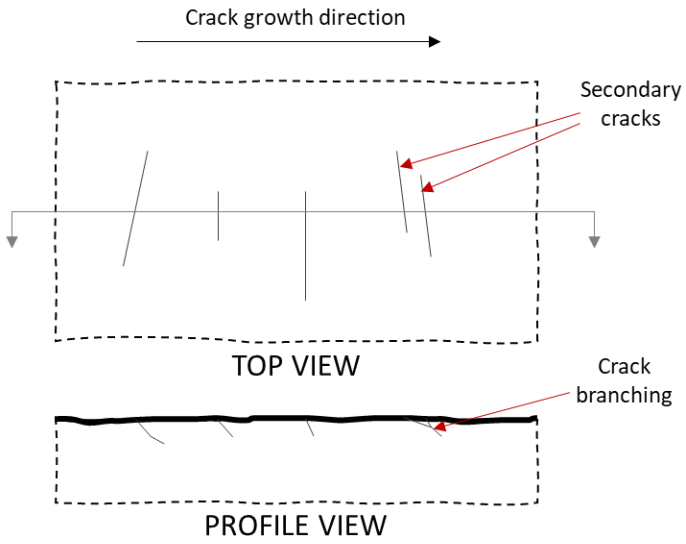

Figure 49 Illustration on the connection between secondary crack and crack branching. Top view represents the fractured surface, while profile view represents the fracture profile

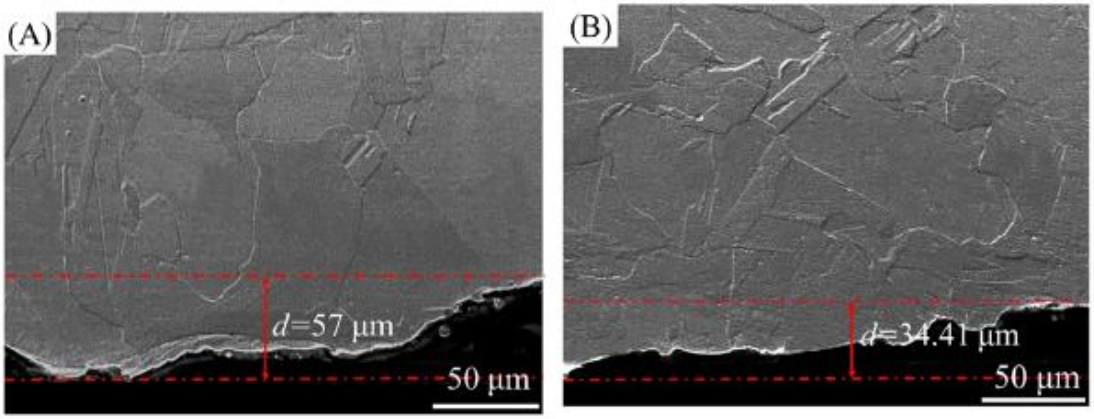

Figure 50 Crack profile of SLM Inconel 625 in the threshold region for A) C⊥BD and B) C//BD [113]

The asperities of the crack profile which represent the fractured surface roughness of was measured by the "d" value shown in Figure 50. The measured distance between peak and valley on the crack profile indicates the magnitude of surface roughness. Based on Figure 50, The C⊥BD sample has a higher "d" value (d = 57 µm) compared to the C//BD sample (d = 34.41 µm). However, the "d" value was only measured based on one micrograph (crack length of ≈ 250 µm) which might not represent the whole threshold region. A more global crack profiles at lower magnifications were not provided by the authors.

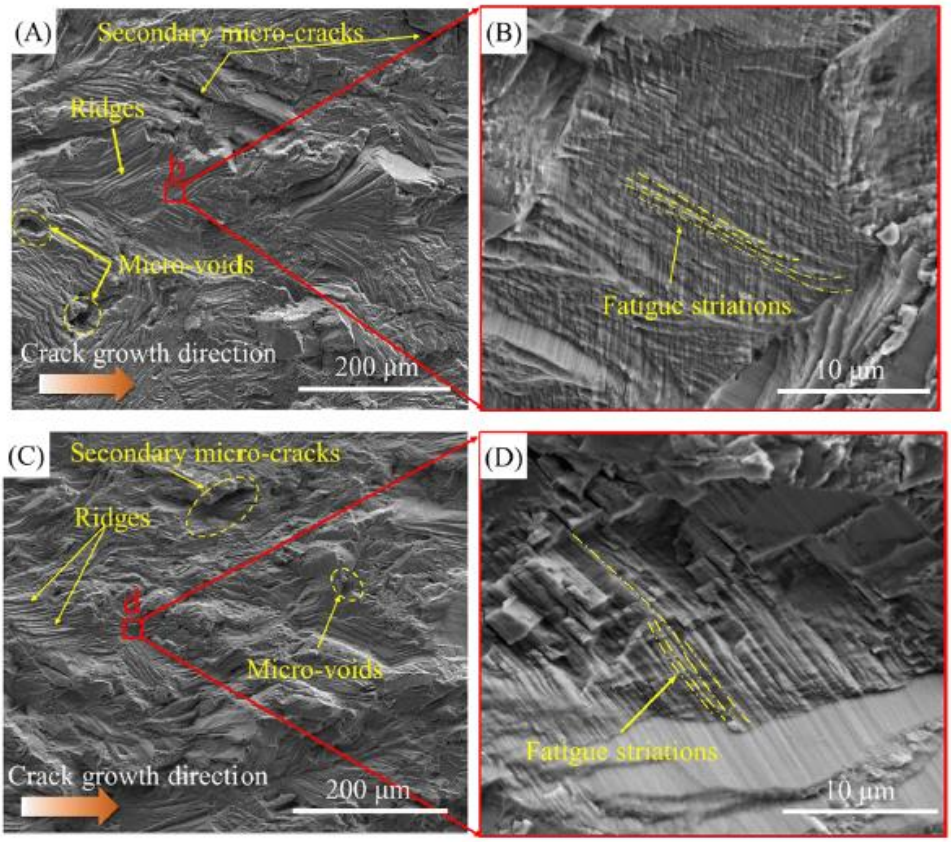

Figure 51 SEM images of fractured surface of SLM Inconel 625 alloys in the Paris region A) and B) represent the C⊥BD samples in low and high magnification respectively, while C) and D) represent the C//BD samples in low and high magnification respectively. [113]

Figure 51 shows an image of the fractured surface in the Paris region where a fully developed striation pattern of 0.5 µm spacing can be seen. The spacing value translates to $\approx 5 \times 10^{-7}$ m/cycle, which confirms that it represents the fatigue striation pattern, unlike the parallel lines that was pointed in the threshold region in Figure 48b and Figure 48d. The main fractographical feature that was discussed for the Paris region is the fractured surface roughness. Hu et al.'s [113] demonstrated that the fracture surface for the Paris region is smoother compared to the threshold region, which is very uncommon since in all other FCGR studies, the crack surface gets rougher as the ΔK magnitude is increased. The authors claimed that, because of the reduction in surface roughness at the Paris region, compared to the threshold region (reduction in "d" value from 57 µm to 46 µm for the C⊥BD sample and from 34 µm to 32 µm for the C//BD sample as shown in Figure 50 and Figure 52) the effect of BD orientation on the crack growth at the Paris region is low. As a result, both samples have similar Paris constants "C" and "m".

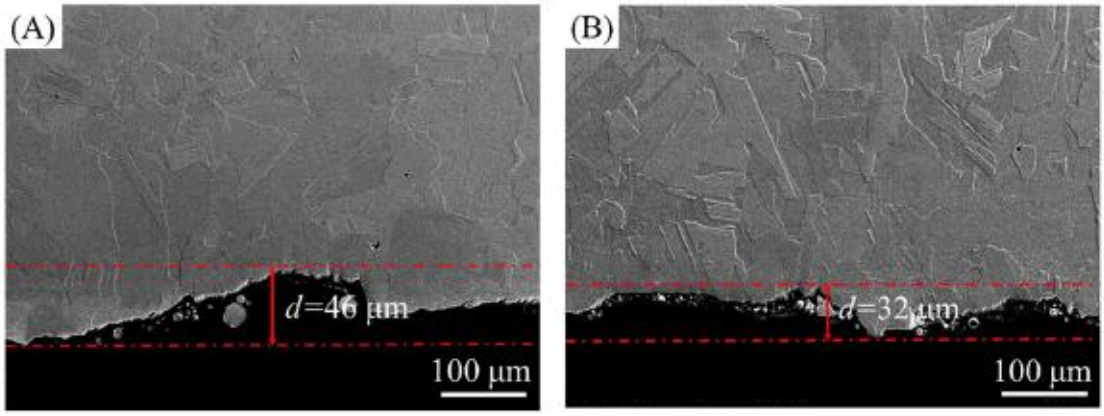

Figure 52 Crack profile of SLM Inconel 625 in the Paris region for A) C⊥BD and B) C//BD [113]

To summarise, Hu et al. concluded that BD only significantly affects the FCGR at the threshold region. Based on their microstructure analysis, the effect of micro-pores on the FCGR behaviour was not discussed. In addition, the fractographic features labelled as striation on the fractured surface near the threshold region might not have been interpreted accurately. Furthermore, the fractured surface roughness was evaluated based on only one measurement, and the overall crack profile at low magnification was not provided. Since the paper focuses more on the effect of loading ratio (R) on FCGR behaviour, the crack growth pathway through the microstructure of SLM Inconel alloys with different BD orientation were not discussed.

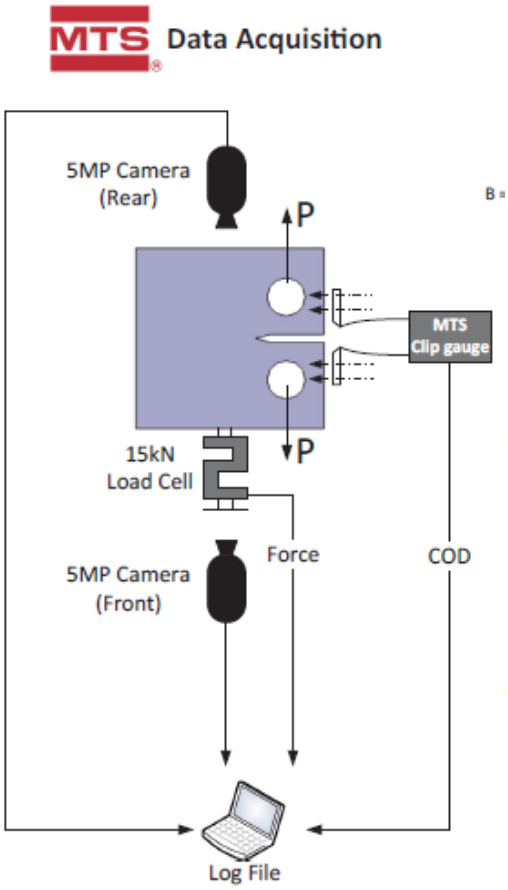

Figure 53 FCGR experimental set-up for SLM Inconel 625 CT samples, conducted by Poulin et al. [114]

The second FCGR studies on SLM Inconel 625 was conducted in 2018 by Poulin et al. [114]. Four CT samples were manufactured at different building directions using EOSINT M280 SLM printer, Germany. The SLM parameters used to print the CT samples are; laser power, P = 300 W, laser velocity, v = 1000 mm/s, hatching space, s = 100 µm, and layer height, h = 40 µm. All samples went through annealing heat treatment of 870 ºC for 1 hour. The experiment was conducted in accordance with the FCGR–compliance method outlined in ASTM E647. The experimental set-up is shown in Figure 53, where two 5MP DIC cameras were used to validate the crack size. The width and thickness of the CT sample are W = 38 mm and B = 9.5 mm, and the loading ratio and loading frequency are R = 0.1 and f = 20 Hz.

The four building directions of the CT samples are illustrated in Figure 54, where the label “90º” represents the C⊥BD sample, “90º ⊥” represents the C//BD sample, “45º” represents the C”45”BD sample, and “0º” represents the C”FLAT”BD sample as noted in Table 6.

Microstructure analysis reveals that these specimens have microstructure defects of pores up to 50 µm in diameter with a 0.05% area fraction, and most of these pores segregated near the surface of the printed material. All of the specimens went through an annealing heat treatment process for 1 hour at 870 ºC under argon atmosphere as recommended by the manufacturer.

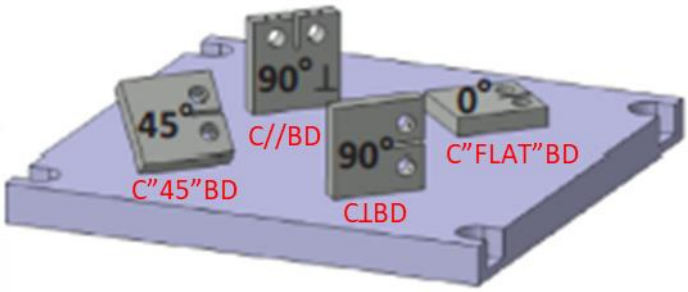

Figure 54 An illustration of BD orientation for the SLM Inconel 625 CT samples that were used by Poulin et al. for FCGR experiment [114]

The FCGR graphs presented in this report establish the same result as the previously discussed paper (Hu et al.'s [113]) where the FCGR behaviour in the threshold region is highly affected by the building direction. The FCGR graph in Figure 55 shows the result for sample C⊥BD, C"45"BD, and C"FLAT"BD. The C⊥BD sample has the lowest threshold value of ΔKth = 7.5 MPa$\sqrt{m}$, followed by the C"45"BD sample with a threshold value of ΔKth = 8.8 MPa$\sqrt{m}$, and the C"FLAT"BD sample with the highest threshold value of ΔKth = 10.6 MPa$\sqrt{m}$. The author claims that the reason for the differences in the threshold value is due to the different amount of grain boundaries encountered by the main crack. Based on an EBSD map shown in Figure 56, the authors explained that the main crack in C"FLAT"BD sample encountered fewest grain boundaries, and the C⊥BD sample encountered the most grain boundaries, while C"45"BD sample was in between.

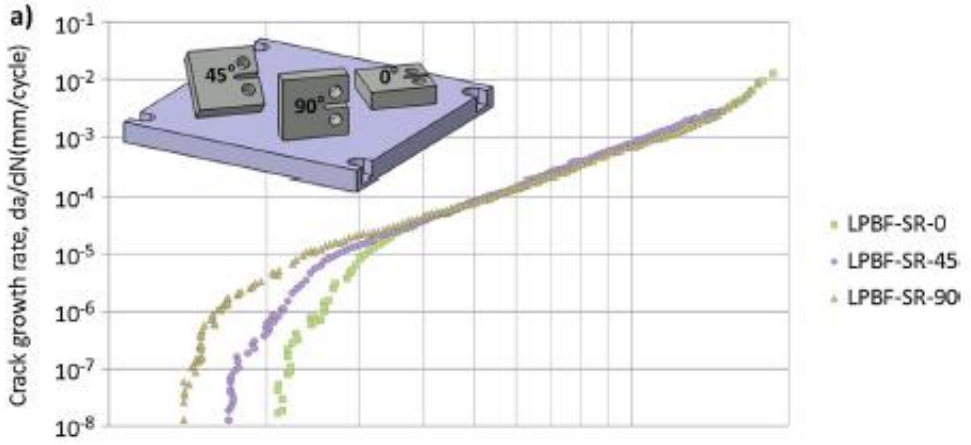

Figure 55 FCGR graph of SLM Inconel 625 at three different build direction. The green line represents sample C"FLAT"BD, the purple line represents sample C"45"BD and the brown line represents sample C⊥BD [114]

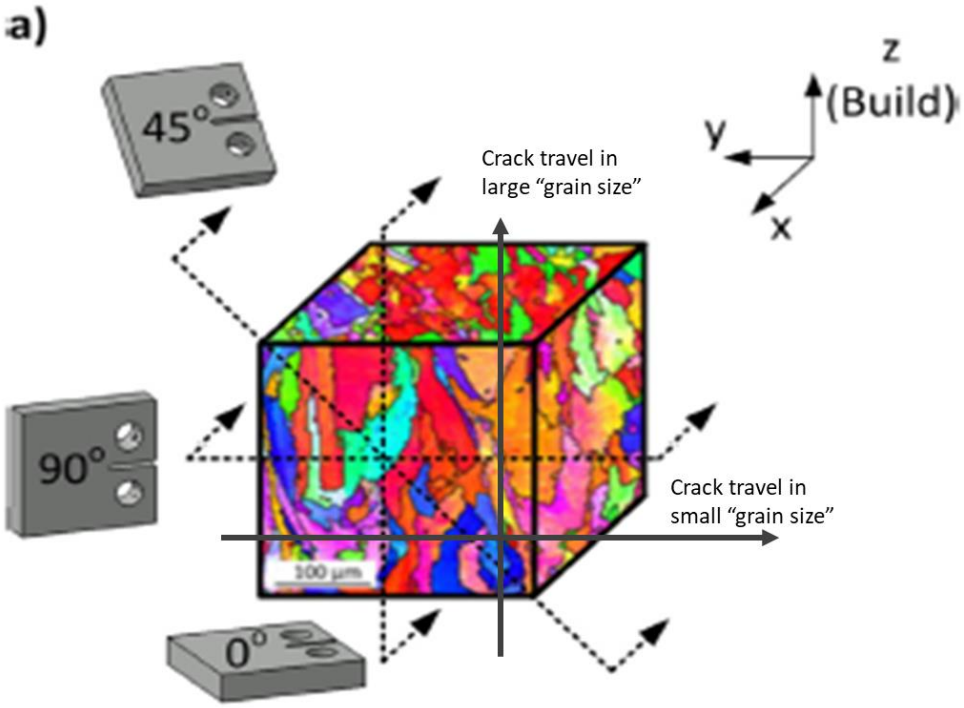

Figure 56 Grain map of SLM Inconel 625 alloy in the x,y and z plane, BD is upwards [114]

The authors suggested that having a crack that encountered fewer grain boundaries is similar to having a crack that is propagating in a bigger grain size, while having a crack that encountered a high number of grain boundaries is similar to having a crack that is propagating in a smaller grain size. This is illustrated in Figure 56, assuming that the main crack is travelling in a straight line. It appears that the authors suggested that a bigger grain size results in a rougher fracture surface, which then results in a greater crack closure effect (according to RICC), thus causing it to have higher threshold value. However, this theory does not agree with the FCGR result between the

C⊥BD sample and the C//BD sample, shown in Figure 57 below. Both samples had similar threshold value of despite having different "grain size".

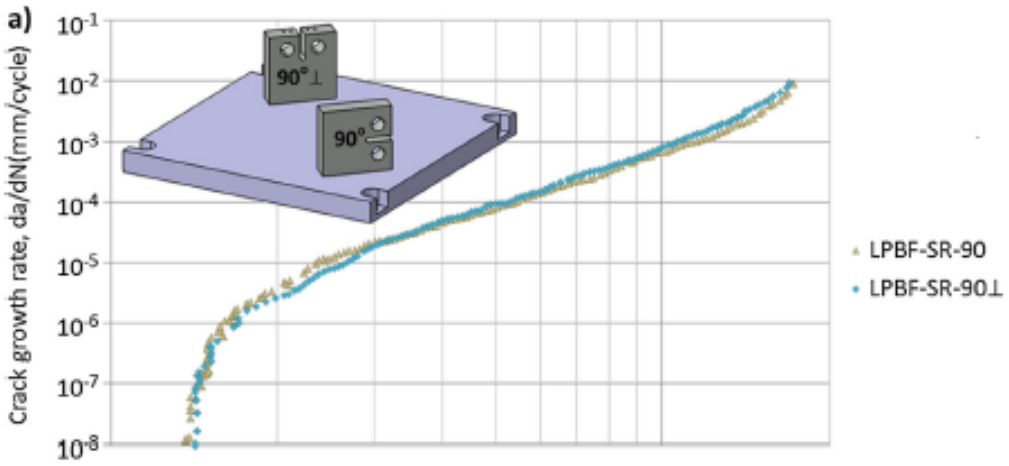

Figure 57 FCGR graph of SLM Inconel 625 at two different build direction. The green line represents sample C//BD and the brown line represents sample C⊥BD [114]

The FCGR result in Figure 57 was unexpected as the authors anticipated that the C//BD sample to have a higher threshold value, similar to the C"FLAT"BD sample with ΔK_{th} = 10.6 MPa$\sqrt{m}$. They expected this is because the number of grain boundaries encountered by the main crack in C//BD sample was expected to be much less (i.e. bigger "grain size") compared to the C⊥BD sample. The authors did not offer a clear explanation on the results, while they mentioned that both C//BD and C⊥BD have smooth fracture surfaces, and thus low ΔK_{th} values. Therefore, clear evidence is still needed to determine whether the number of grain boundaries encountered by the main crack is a determining factor for FCGR resistance. The current thesis aims to clearly examine the crack growth pathway in C⊥BD and C//BD samples, and to provide an explanation for the observed threshold values.

2.2.2 Review on FCGR studies of SLM Inconel 718

The latest FCGR study reported for SLM Inconel 718 was conducted by Brynk et al. [115], who they studied the short crack behaviour by using non-standard "FCG mini-samples" as shown in Figure 58. The samples were printed via MCP Realizer II – SLM 250 AM printer, Germany. The SLM parameters used in this study are as follows: laser power setting of P = 400 W, laser velocity

of v = 500 mm/s, layer thickness of h = 50 um, and a hatching space of s = 160 um. The "FCG mini-samples" were subjected to fatigue loading ratio of R = 0.1, and the crack size measurement was taken by using a digital image correlation (DIC) camera.

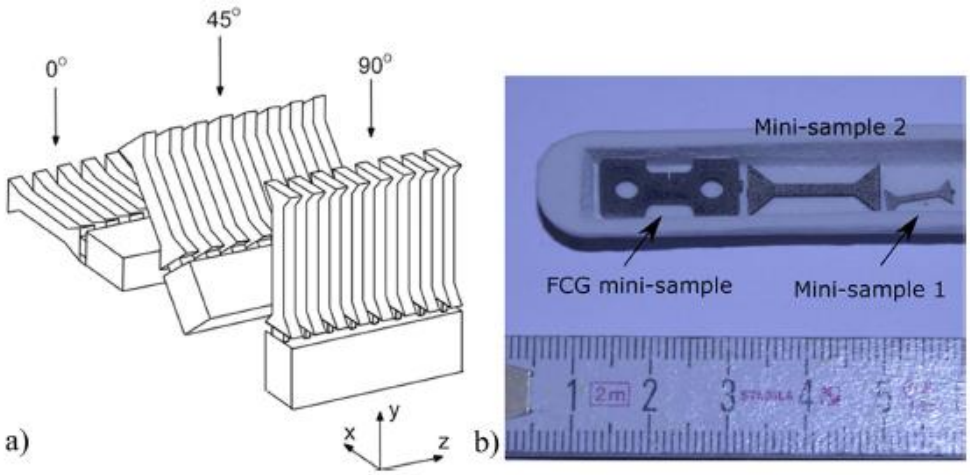

Figure 58 Illustration of the non-standard samples of SLM Inconel 718 a) building direction orientation where 0º represents C//BD, 45º represents C45BD and 90º represents C⊥BD. b) "FCG mini-sample" used for FCGR experiment while "Mini sample 1 and 2" were used for tensile testing [115].

It has been reported that when a crack is physically small, the crack shows a lower threshold value compared to a long crack [121-123]. Physically small crack is also referred as "short cracks", a term used by researchers in Europe to denote a meaning that the length of the crack is small in comparison to the plastic zone in front of the crack tip. Typically, short cracks have a length of, a = 0.1 – 2.0 mm, while a long crack is defined as cracks with a size of more than 2 mm in length. A comparison of the FCGR curves between long cracks, short cracks and microstructurally small cracks (defined as cracks with a length comparable to the grain size) is shown in shown in Figure 59.

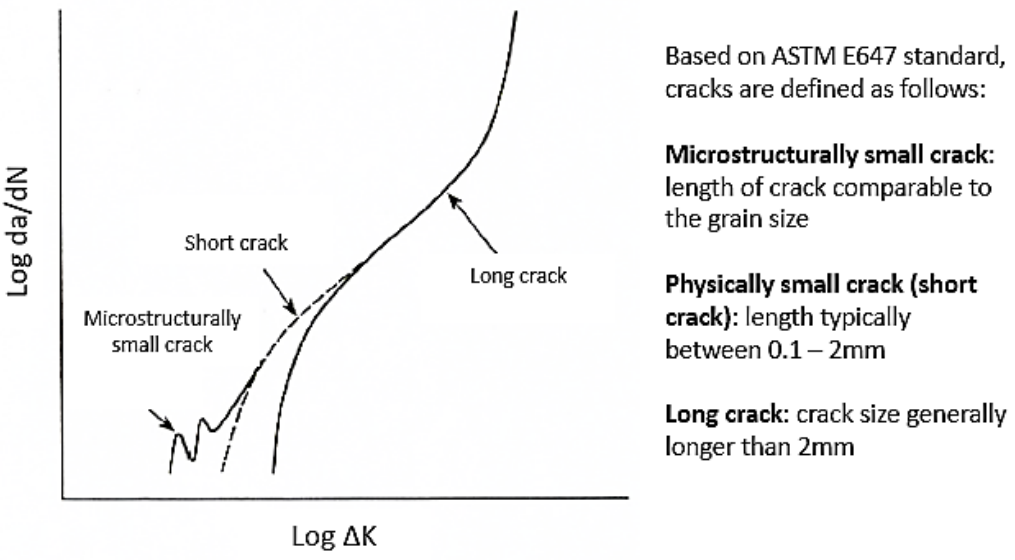

Figure 59 An illustration of the FCGR behaviour between a microstructurally small crack, a physically small crack (short crack) and a long crack.

In terms of the microstructure assessment for their samples, a small number of micro-cracks and pore defects were detected in the sample. In addition, TEM analysis reveals that brittle hcp-Laves phases and carbides were segregated near the grain boundary, as shown in Figure 60 below. In terms of the tensile test, the C45BD samples show slightly higher yield strength and tensile strength compared to the C⊥BD and C//BD samples, while the C⊥BD sample shows the highest elongation, followed by the C45BD and C//BD samples.

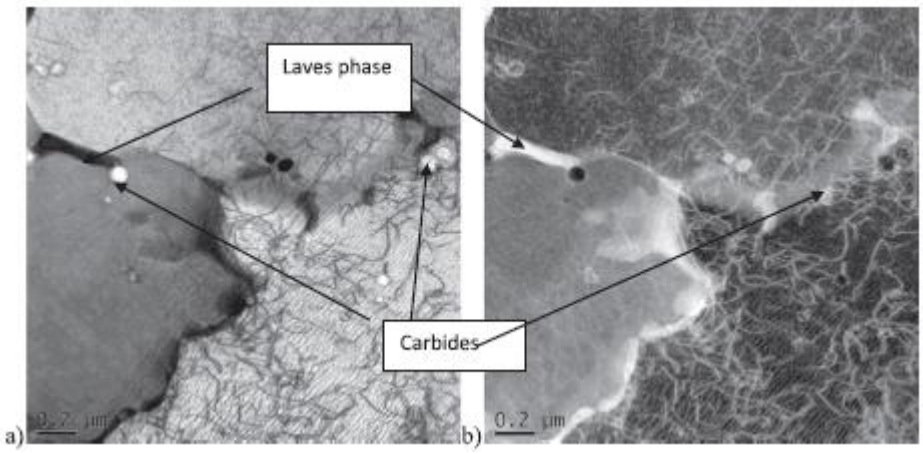

Figure 60 TEM images of SLM Inconel 718 showing hcp-Laves phase and carbides near grain boundary [115]

As shown in Figure 61, the FCGR results were conducted at a starting SIF value of K ≈ 100 MPa$\sqrt{m}$, and reduced to a value at which da/dN = 10^{-9} – 10^{-10} m/cycle. The K decreasing method was used to obtain the graph, and the fatigue loading was stopped before the crack size reached

a = 1.5 mm. Similar to the tensile test result, the C45BD sample shows a better FCGR performance compared to the C⊥BD and C//BD samples, regardless of the Re percentage added (for the purpose of this literature review, only pure Inconel 718 is discussed, i.e. 0% Re, marked by the red box in Figure 61). Since the FCGR graph provided is highly scattered (due to the nature of short cracks), the threshold value can only be estimated to be around $\Delta K_{th} \approx 8 - 10$ MPa$\sqrt{m}$, and the C45BD sample shows a slightly higher threshold value compared to the C⊥BD and C//BD samples. Note that the objective of this paper is to study the effect of Re modified SLM Inconel 718, therefore, a non-standard FCGR test is justified.

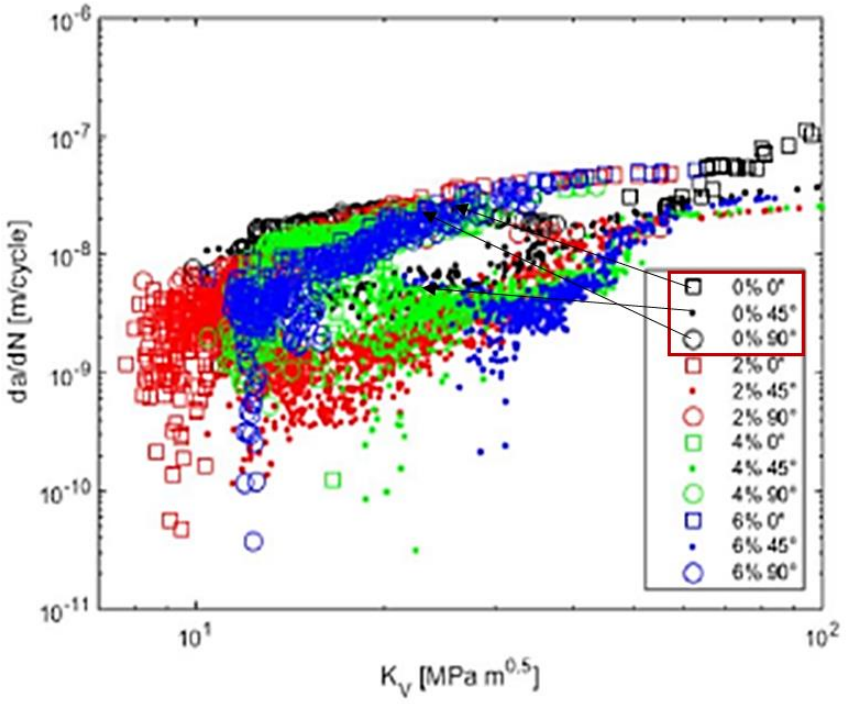

Figure 61 FCGR for the SLM Inconel 718 "FCG mini-samples". Legend shows the percentage of Re composition added into the Inconel 718 alloy [115]

No microstructure analysis related to the 0% Re FCGR behaviour was provided in the report, as the study focused on comparing the mechanical testing results between different percentages of Re added into SLM Inconel 718. Thus, the question on how cracks propagate inside the microstructure of the C45BD sample, that resulted in a higher threshold value is not discussed in this paper.

Another FCGR experiment on SLM Inconel 718 was conducted in 2016 by Konecna et al. [116]. Only one building direction was considered in the FCGR test, which is C//BD. A CT sample was printed using a Renishaw AM250 SLM printer with a laser velocity of v = 200 mm/s, hatching space of s = 180 µm, layer height of h = 50 µm and the laser power was not reported. However, the authors mentioned that the maximum laser power setting for the SLM machine was 200 W. The width and thickness of the CT sample were W = 30 mm and B = 6 mm respectively. The fatigue loading ratio was R = 0.1 and the crack measurement was taken optically using a CCD camera (a digital camera).

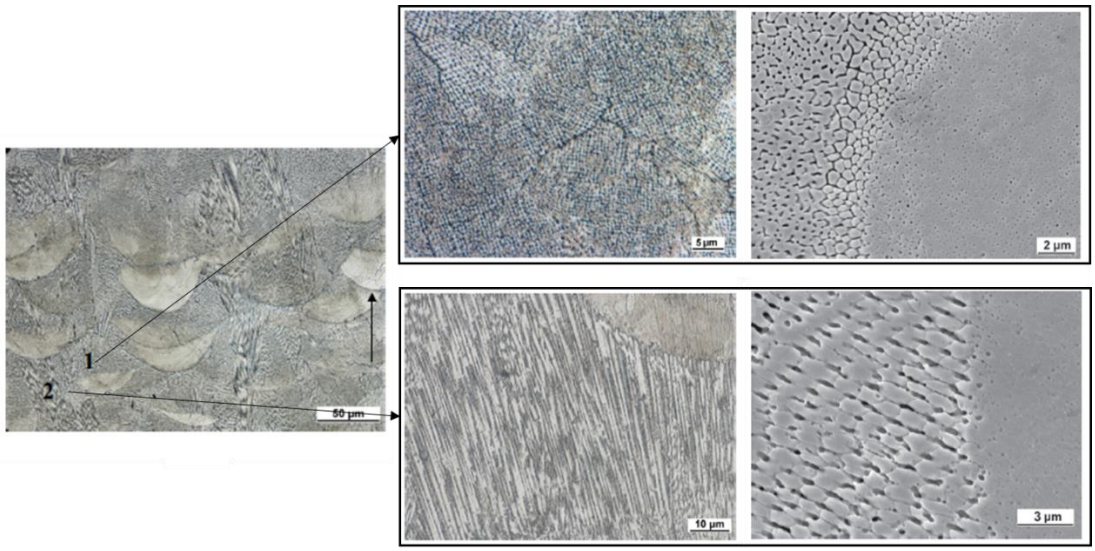

Figure 62 SEM image of SLM Inconel 718. Low magnification image on the left side, and high magnification images at Region 1 and Region 2 on the right side. Region 1 was characterised as bct - γ'' phase while region 2 was characterised as fcc - γ' phase [116]

The microstructure features as presented and described by the authors is presented in Figure 62. The low magnification image suggests that it has a key-hole meltpool with deep penetration. Region 1 is characterised as the bct - γ'' phase, which is a principal strengthening phase in Inconel 718, while region 2 shows the fcc - γ' phase with columnar grains, changing in size as it passes through the meltpool boundary. The authors also mentioned that micro-cracks and pores were identified, but rarely.

The fractographical analysis was discussed by presenting two SEM images at the threshold and Paris region as shown in Figure 63. In Figure 63T(a) and Figure 63P(a) secondary cracks appear to be larger and more opened in the Paris region. The reason for the secondary cracks were not discussed, but they look similar to the ones shown by Hu et. el.s' in Figure 48 which may have been caused by local intergranular cracking due to the presence of brittle secondary phases in the material. With regard to Figure 63T(b), the authors identified the linear marks pointed by the yellow as slip lines, which differs from Hu et al.'s identification in their micrograph, who labelled them as striation patterns. This fractographic feature at the threshold region will be investigated in this thesis.

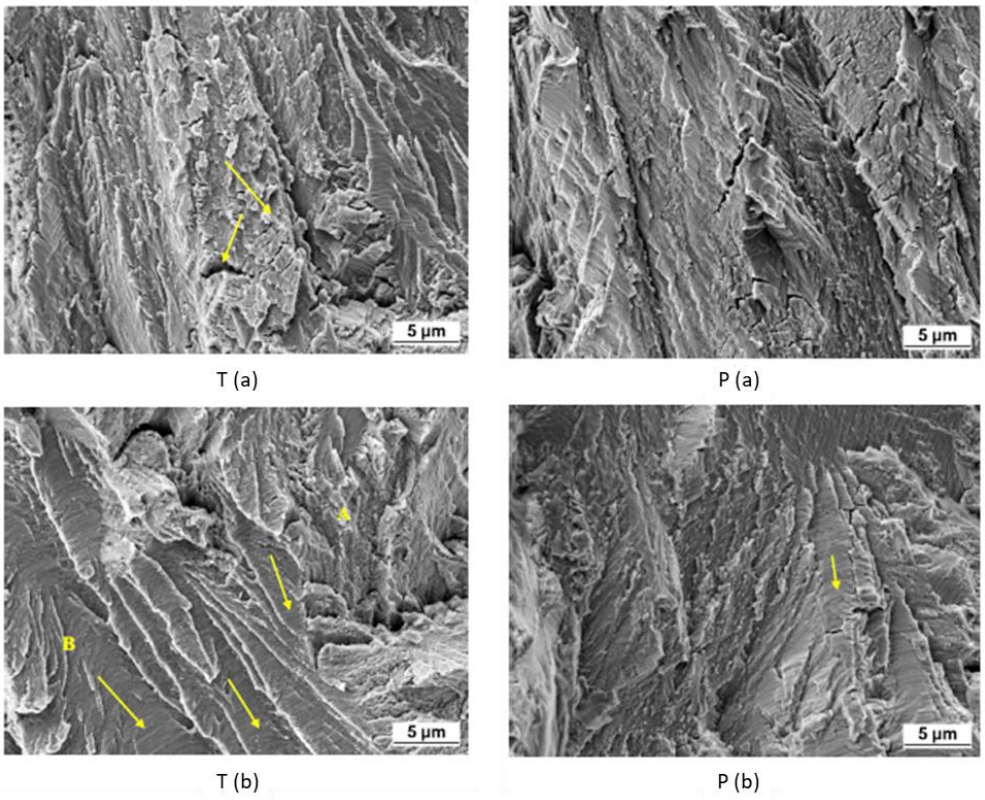

Figure 63 SEM image of fractured surface of SLM Inconel 718 alloy. "T (a) and (b)" were fractured surface located at the threshold region, while "P (a) and (b)" were located at Paris region [116].

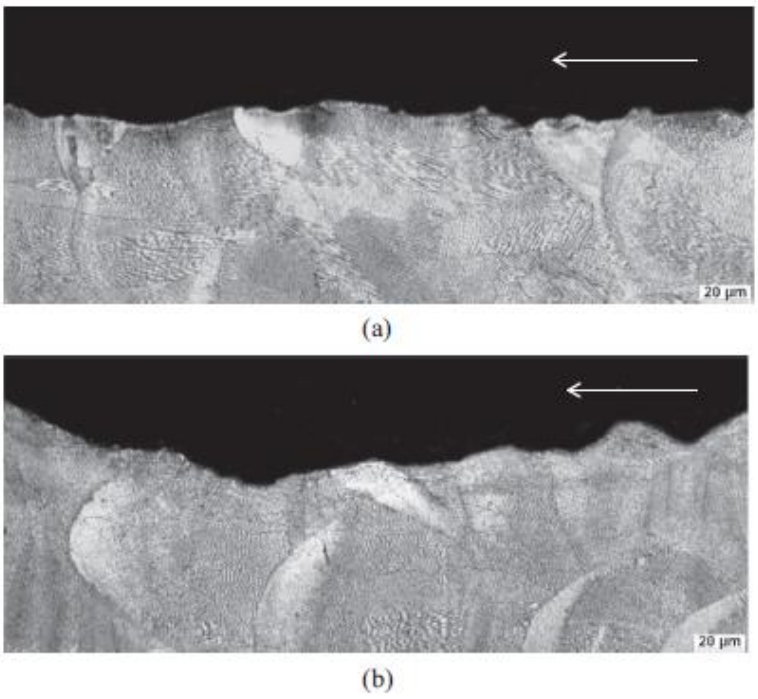

Figure 64 Fractured profile of SLM Inconel 718. (a) at the threshold region and (b) at the Paris region. The white arrows indicate the crack growth direction [116]

The fractured profiles shown in Figure 64 indicate that the crack surface is rougher in the Paris region compared to the threshold region. This is a common observation for a FCGR experiment since the material is subjected to higher stress/strain in the Paris region. The authors claimed that based on their analysis, the crack in the threshold region propagates without any influence of the specific SLM microstructure. However, proof of evidence was not provided. An EBSD analysis and high magnification images of the crack path were also not presented. In addition, the FCGR graph shown in Figure 65 below indicates that the SLM Inconel 718 alloys have a very low threshold value of ΔK_{th} = 3.0 MPa$\sqrt{m}$ compared to other conventionally manufactured Inconel 718 alloys, which is between $\Delta K_{th} \approx 8.0 – 10.5$ MPa$\sqrt{m}$. The reported ΔK_{th} value by Konecna et al. [116] is too small compared to a typical ΔK_{th} value of superalloys. To demonstrate this, the finding reported by Hu et al. and Poulin et al. [113, 114] on SLM Inconel 625 have a ΔK_{th} value of between ≈ 7.1 – 10.6 MPa$\sqrt{m}$ (depending on the BD), while the conventionally manufactured Inconel 625 alloys is around $\Delta K_{th} \approx 7.2$.

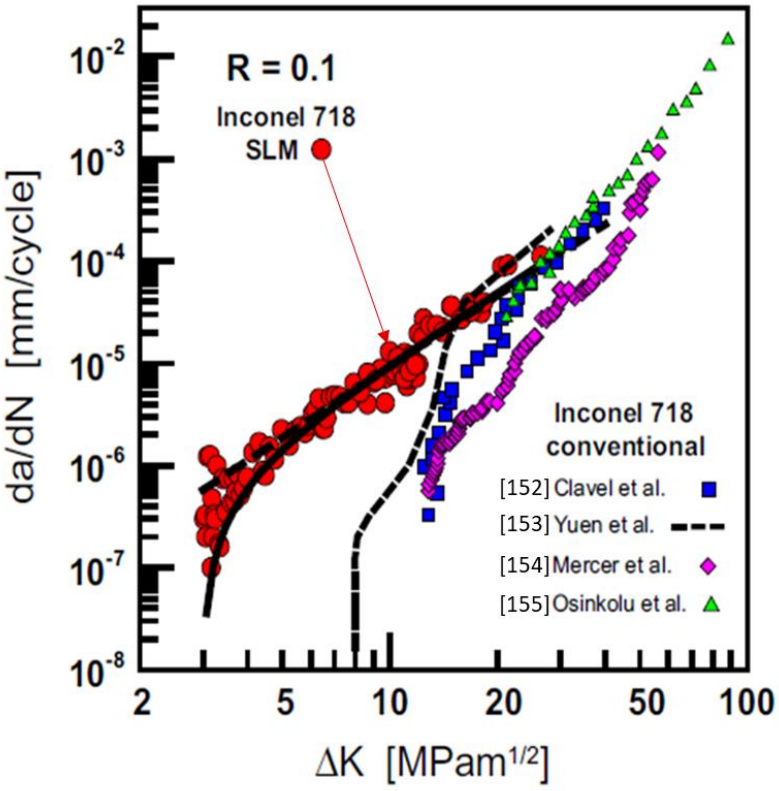

Figure 65 FCGR graph of SLM Inconel 718 (red) compared with conventionally manufactured Inconel 718 [116]

The authors offered three suggestions to explain the low threshold value of the SLM Inconel 718 alloy. Firstly, the authors claimed that the Boron content in their material was too low (0.003 wt%) compared to a standard Inconel 718 (≤ 0.006 wt%), which affect its FCGR behaviour by decreasing the threshold value of the material [124]. However, based on a study on the effect of Boron on FCGR behaviour of Inconel 718 alloy [124] as cited by the authors, the threshold value of low Boron content for Inconel 718 does not go lower that ΔK_{th} = 7.0 MPa$\sqrt{m}$. The second explanation offered by the authors was to link the low threshold value to the smaller "grain size" of SLM material, compared to the other conventionally produced alloys. This suggestion is not consistent with an earlier statement made by the authors, claiming that the specific microstructure does not have any influence on the FCGR behaviour. As discussed in chapter 2.1.2, research has established that there is no general relationship between grain size and threshold value. Thirdly, the authors suggested that the low threshold value is due to the presence of residual stress inside the material.

Another reason for low threshold value could also be a measurement error due to the equipment used for the crack size measurement. The measurement of the crack size/length was taken optically using a digital camera. However, the thickness of a crack near the threshold region, especially at the crack tip, is usually very small (smaller than 5 μm), which could lead to an underestimation of the crack length. The authors also did not use a data acquisition system during the FCGR experiment to sync the measurement of the crack length and the loading cycle accurately, which may have led to inaccuracies in the data recorded. Furthermore, the short crack behaviour reported by Brynk et al. does not support the possibility of a very low threshold value for Inconel 718. Based on the arguments above, it is unlikely that an SLM Inconel 718 has a naturally low threshold value.

Finally, Konecna et al.'s [116] study also did not sufficiently address the question of how cracks propagate through the microstructure of SLM Inconel 718 microstructure. Even though the authors claimed that there was no microstructure influence on the crack growth pathway near the threshold region, no proof of this claim was presented.

2.2.3 Review on FCGR of Inconel 738

There are no data from an FCGR experiment involving SLM Inconel 738 alloy available in the literature. The latest FCGR experiment data available for Inconel 738 alloy (cast) was reported by Scarlin [117], where the experiment was conducted at three different temperatures (room temperature, 750 ºC, and 850 ºC). However, the experiment was not conducted according to ASTM testing standard. The crack length was determined based on a potential different drop measurement, and its relationship was determined from the slop of a voltage vs crack length graph, which is -90 µV/mm. The specimen used appeared to be a modified version of the single-edge-crack-tension-specimen [97], with an additional groove in the middle of the sample to keep the crack growth straight. Figure 66 shows the experimental set-up and specimen size used in this experiment.

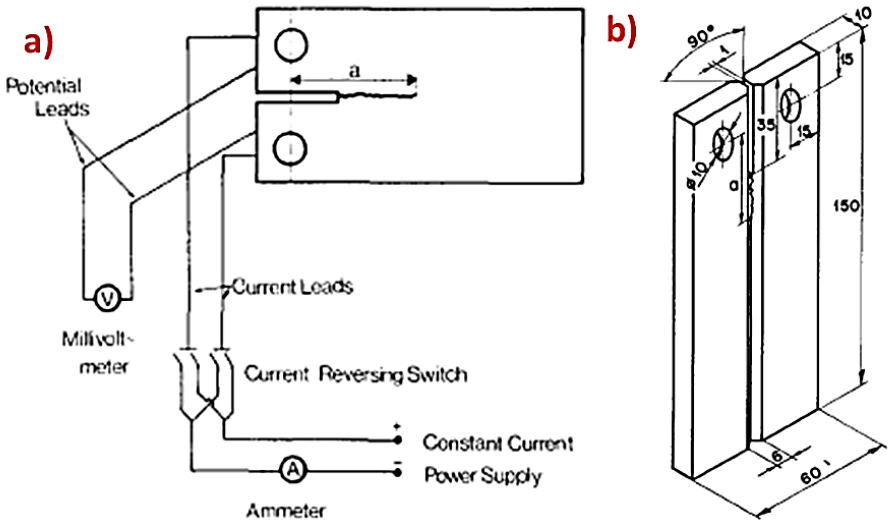

Figure 66 a) FCGR experimental set up for cast Inconel 738 alloy b) FCGR specimen, all dimensions in mm [117]

The FCGR graph in Figure 67 shows that cracks are growing at a higher rate (subjected to the same stress) for high ambient temperatures compared to room temperature. The fatigue threshold value for specimens in room temperature is ΔK_{th} = 12 MPa$\sqrt{m}$ compared to ΔK_{th} = 10 MPa$\sqrt{m}$ for 750 ºC and 850 ºC. The specimen started to fracture at a ΔK value that is also higher for room temperature, namely $\Delta K \approx$ 70 MPa$\sqrt{m}$ compared to 30 – 40 MPa$\sqrt{m}$ for the high temperature. Due to the lack of log-scale graphs provided by the author, Figure 67 provides a re-plotted graph in log-log scale to determine the value of Paris constant, "C" and "m". The value of "C" and "m"

for the room temperature specimen is 1.0×10^{-18} and 6.8, while for both 750 ºC and 850 ºC specimens the values are 1.0×10^{-16} and 6.7 (similar for both specimens). The Paris constant values were not in the typical range of a metal, suggesting the possibility of inaccuracies in the results. Typically, "m" and "C" values are in the range of 2 – 4 and 10^{-10} to 10^{-13} m/cycle, respectively [44].

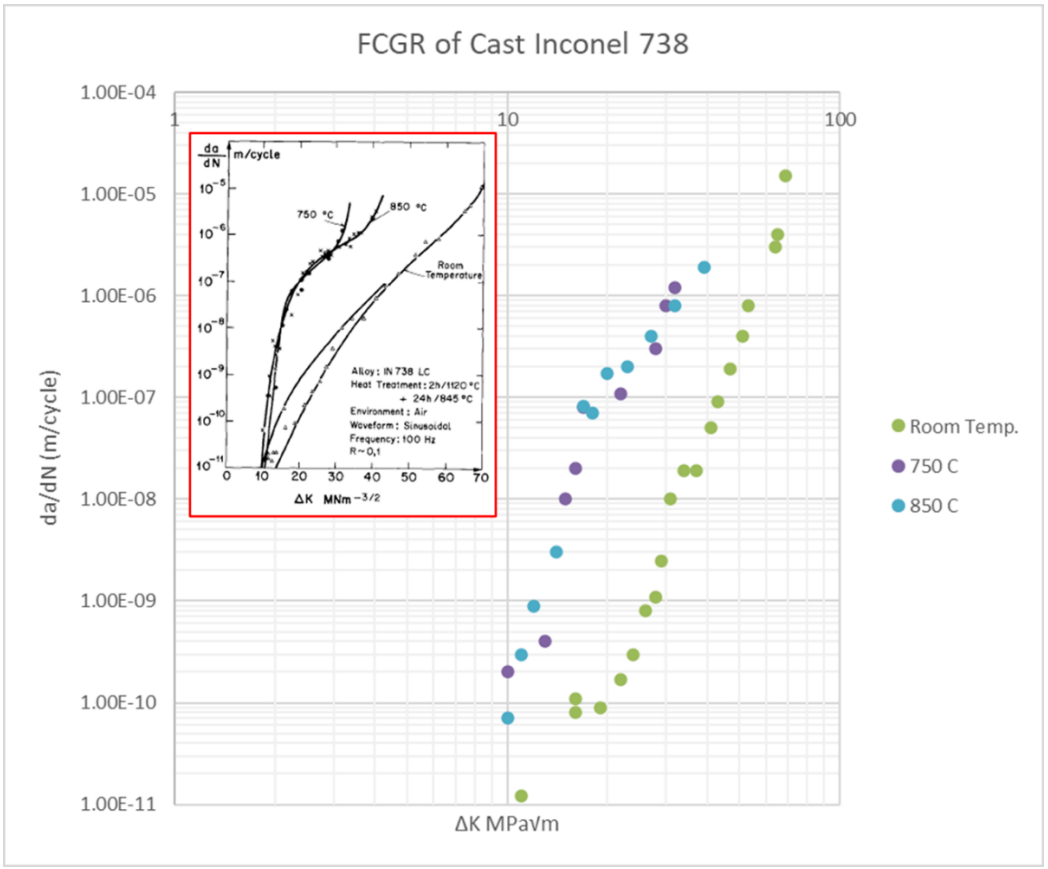

Figure 67 FCGR graph for cast Inconel 738. Original data as per graph inside the red box, while the big graph was replotted on a log-log scale [117]

Fractographical analysis reveals that the room temperature specimen had a more tortuous fractured surface compared to the high temperature specimens. Figure 68 shows that the crack profile at room temperature was deviated or branched more, i.e. was not as straight as the ones at high temperature. The author suggested that the crack branching at room temperature causes the crack to grow at a slower rate. Mazur et al. [125] suggested that fatigue fractures of Inconel 738 alloy at high temperature occurs due to a mix mechanism between FCGR and creep. They claimed that the brittleness of the material increases at high temperatures due to the

transformation of carbides (from MC type carbides to $M_{23}C_6$ type), creating a network of carbide at the grain boundary, which reduces the material toughness by 30%.

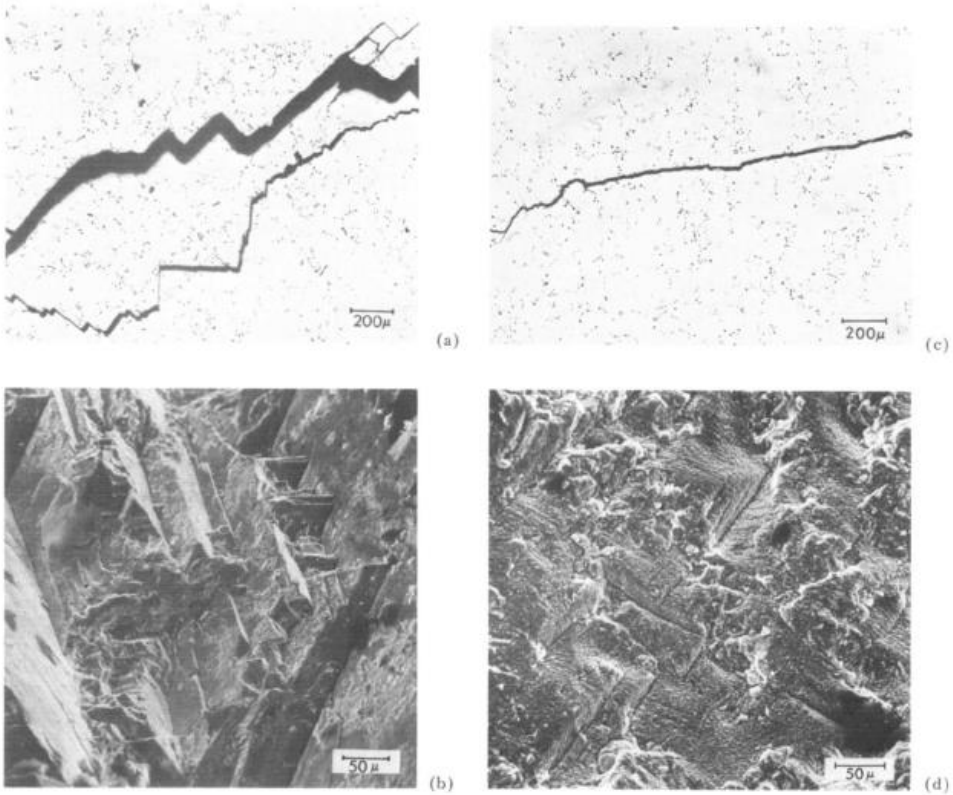

Figure 68 Optical image of fracture profile of cast Inconel 738 a) at room temperature b) at high temperature. c) and d) are SEM image of fracture surface at room temperature and high temperature respectively [117].

TEM analysis on an Inconel 738 alloy conducted by Mazur et al. revealed that most of the carbides segregated near the grain boundary. As shown in Figure 69, at low temperature, carbides reside randomly near the grain boundary, and as the ambient temperature increases (900 – 1000 ºC operating temperature), the carbide forms a continuous network along the grain boundary. The presence of these brittle carbides near the grain boundary could cause the grain boundary to be a preferred crack pathway. Ultimately, the preferred crack pathway for SLM Inconel 738 alloy remains unknown, and the FCGR behaviour of SLM Inconel 738 has also never been recorded.

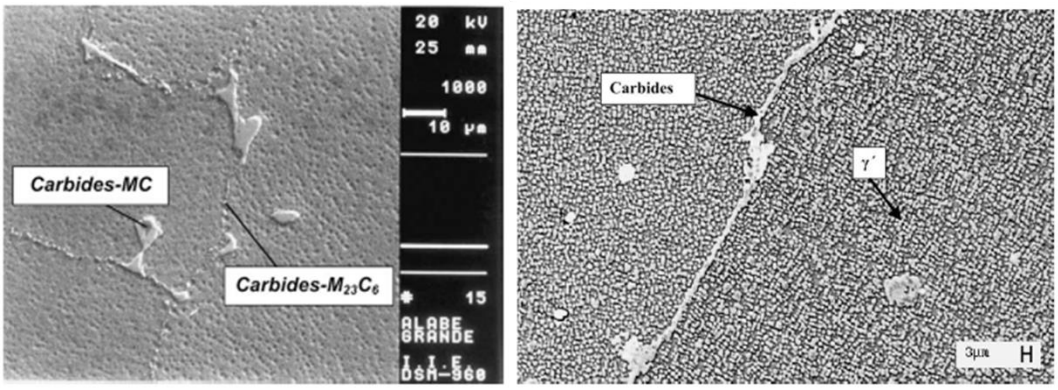

Figure 69 TEM image of an Inconel 738 alloy showing carbide a) exposed to low temperature (≈room temperature) b) exposed to high temperature (≈900 – 1000 ºC) [125]

2.3 Scope of Research

Based on the literature review presented, it is clear that there is a lack of research on the FCGR behaviour of SLM superalloys. Since the build direction (BD) orientation has been shown to highly influence the fatigue strength of an SLM material, most available literature focuses on discovering the differences between the FCGR parameters (ΔK_{th} and Paris constant, C and m) for samples with different BDs, or between SLM build samples and traditionally build samples (wrought or cast manufacturing process). One consistent point based on the studies reviewed in this thesis is that the crack growth rate is lower for samples with a rougher fractured surface or a more tortuous crack growth. However, the literature has not investigated the crack growth pathway behaviour in different BDs or identify the main microstructure features (i.e. shape/orientation of meltpool boundary or grain boundary) that influence the local crack growth direction in SLM superalloy materials. A greater understanding of the factors influencing the crack pathway in SLM superalloy is important as it directly contributes to the differences in the crack tortuosity, which subsequently affect the FCGR resistance.

As build SLM materials comprise of long columnar grains that generally orientated parallel to BD, Therefore, by assuming that the main crack moves in a straight line, graphically it would pass through fewer grain boundaries in a C//BD sample compared to a C⊥BD sample. The speculative relationship between the number of grain boundaries encountered by a crack with the ΔK_{th} value suggested by some of the researchers were inconsistent with some of the results

reported. Thus, the FCGR resistance mechanism between SLM superalloys with different BD is still unclear. In addition, there is a lack of discussion on the effect of LOFs and keyhole pores on the FCGR behaviour of SLM superalloys, despite many reports claiming that SLM materials are susceptible to these microstructure defects. Furthermore, there is a lack of study on how SLM parts would compare to traditionally manufactured parts in terms of linear elastic fracture mechanic (LEFM) calculations. Therefore, based on an arbitrary usage, the minimum defect size allowed, or the best BD orientation had never been investigated.

As identified in the literature review, no FCGR experiment reports on SLM Co-Cr-Mo and Inconel 738 superalloys are available. By utilising these two materials, this Ph.D. study intends to answer the following questions:

1. How does the main crack propagate through the SLM microstructure of Co-Cr-Mo alloy in C//BD and C⊥BD sample? How does the grain distribution in the C//BD and C⊥BD sample affect the FCGR parameters? Does LOF at the amount of less than 1% significantly influence the FCGR behaviour?

2. Based on the FCGR graph of SLM CoCrMo alloy generated in this study, we aim to identify the ideal BD orientation for an SLM Co-Cr-Mo hip-stem-implant by utilising the LEFM concept. In terms of FCGR performance, how does the SLM Co-Cr-Mo hip-stem-implant compares to a conventionally manufactured hip-stem-implants. In addition, what is the minimum defect size allowed in SLM and conventionally manufactured hip stem implants?

3. How does the main crack propagate through the SLM microstructure of Inconel 738 for C//BD, C⊥BD and C45BD sample? How does the grain distribution in the C//BD, C⊥BD, and C45BD sample influence the crack growth pathway? How would key-hole pores influence its FCGR behaviour?

4. What is the main microstructure feature that influence the crack growth pathway in SLM Inconel 718? This question arises because there is only one literature that reported the threshold value of that material, and it was very low (ΔK_{th} = 3.0 MPa$\sqrt{m}$).

The next chapter will explain the experimental procedure and analytical facilities used in this study. Question 1 and 2 will be answered in Chapter 4.0 (FCGR study on Co-based alloys), while question 3 and 4 will be answered in Chapter 5.0 (FCGR study on Ni-based alloys).

3 Experimental Design and Procedures

3.1 Introduction

This chapter describes the methodology used in this study. Details on sample preparation, experimental procedures, microstructure measurements and analytical technique are outlined in the following order: Firstly, the preparation process of SLM compact tension (CT) specimens are presented, followed by details on the fatigue crack growth rate experiment technique and procedure. Then, the procedure for fractured specimens sampling for metallography analysis is described followed by crack surface analysis using SEM. Finally, the parameters and method for EBSD and TEM analysis used in this study are presented. The overall research process of this study is illustrated by the flowchart in Figure 70 below.

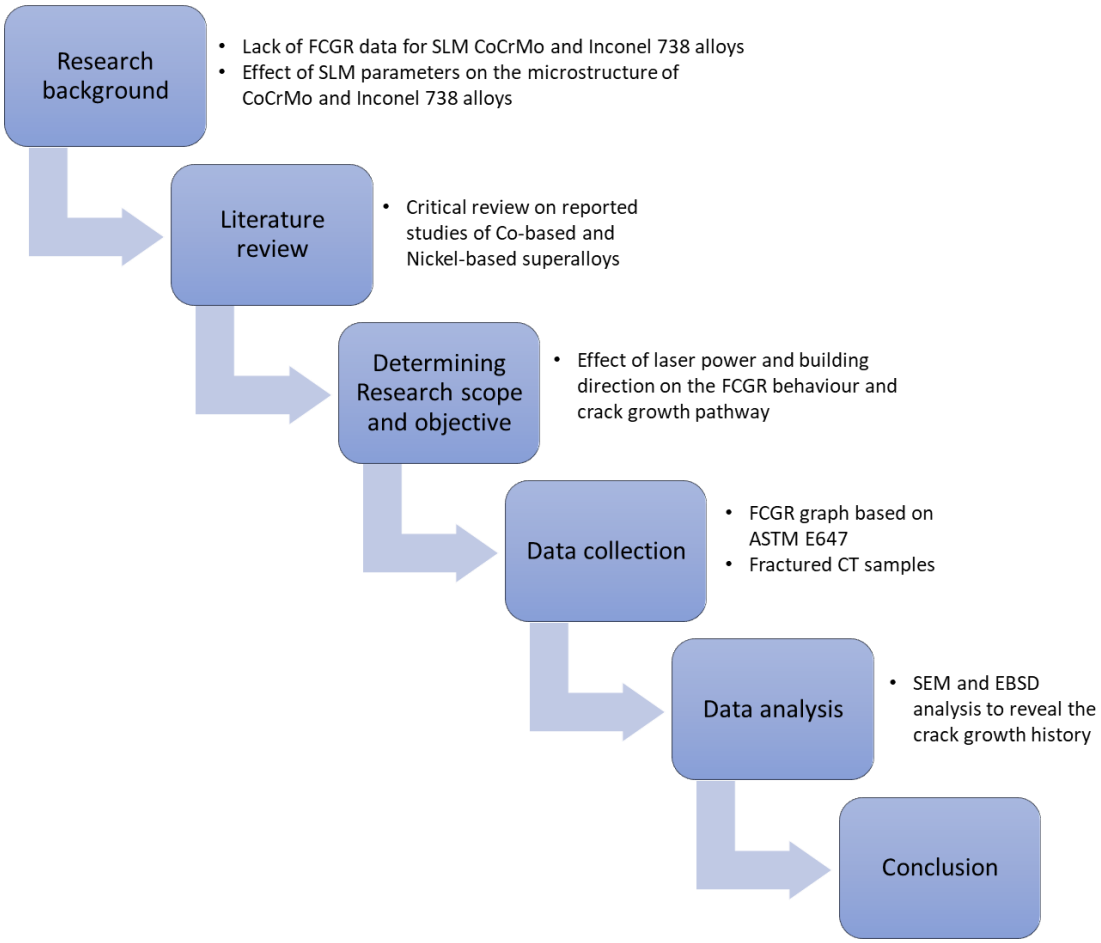

Figure 70 Overall research flowchart

3.2 Compact tension sample preparation

3.2.1 SLM Machine

All specimens were produced by an industrial 3D printer made by Renishaw plc. (England, UK). The model of the printer is Ren AM 250 SLM (Figure 71) with an upgraded laser system, which enables it to deliver a maximum laser power of P_{max} = 400 W. The build volume of the SLM machine is 250 mm x 250 mm x 300 mm (Z-axis) and the default laser spot size diameter is Θ = 140 µm. During printing, the oxygen concentration inside the building chamber was kept below 50 ppm. According to the manufacturer, the optimum powder should be in spherical shape with particle size in the range of 15 µm to 45 µm. The recommended range of metal powder that can be used by this printer includes aluminium alloy (AlSi10Mg), cobalt chromium alloy, maraging steel, nickel alloys (INCONEL ®), stainless steel (316L) and titanium alloy (Ti6Al4V) [126].

Figure 71 Renishaw AM250 SLM machine [126]

3.2.2 Material and SLM parameters

Co-Cr-Mo specimens were printed using a metal powder that was provided by Renishaw, which compliant to the Co-Cr-Mo ASTM F75 standard [66]. The specification of the powder particle size is in the range of 15 µm to 45 µm with a nominal composition in wt% of 27–30 Cr, 5–7 Mo,

0.5 Ni, 0.75 Fe, 0.35 C, 1.00 Si, 1.00 Mg, 0.20 W, 0.02 P, 0.10 S, 0.25 Ni, 0.10 Al, 0.10 Ti, 0.01 B, and Co (balance). The main SLM parameters used to produce the samples are listed in Table 7, similar to the printing specification reported by Darvish et al. [13]. The Co-Cr-Mo specimens were printed with a dimension of 60 mm x 62.5 mm x 6.25 mm as shown in Figure 72. These specimens are capable to produce four CT specimen with width, W = 25 mm. All CT specimens were wire-cut into the dimension shown in Figure 72, in accordance with the ASTM E647 standard [97].

Inconel 738 specimens were printed using Pearl® Micro Ni 738 alloy powder, which was provided by Aubert et Duval, Spain. According to the powder specification from the supplier, the spherical particle of the powder size is in the range of 10 µm to 53 µm, and the nominal composition in wt% is 16.1 Cr, 8.0 Co, 1.9 Mo, 2.7 W, 1.9 Ta, 0.9 Nb, 3.6 Al, 3.4 Ti, 0.033 Zr, 0.094 C, 0.013 B, and Ni (balance). The main SLM parameters are listed in Table 7, similar to the SLM printing specification reported by Chen et al. [12]. The Inconel 738 specimens were printed with a dimension of 32 mm x 32 mm x 6.25 mm, and subsequently cut into CT specimens using wire-cut technique to obtain a width of W = 25 mm, as shown in Figure 72. Similarly, the SLM parameters and dimensions for the Inconel 718 specimens are shown in Table 7 and Figure 72, respectively.

Table 7 SLM parameter for compact tension (CT) specimens of SLM Co-Cr-Mo, Inconel 738 and, Inconel 718 alloys.

Material	Co-Cr-Mo	In738	In718
Laser power, P (W)	180 & 320	270 & 320	275
Build direction (deg)	0 & 90	0, 45 & 90	45
Laser speed, v (mm/s)	700	1050	1000
Hatching distance, s (mm)	0.09	0.125	0.09

Layer thickness, h (mm)	0.04	0.03	0.06
Scanning strategy, SS	67º	67º	67º

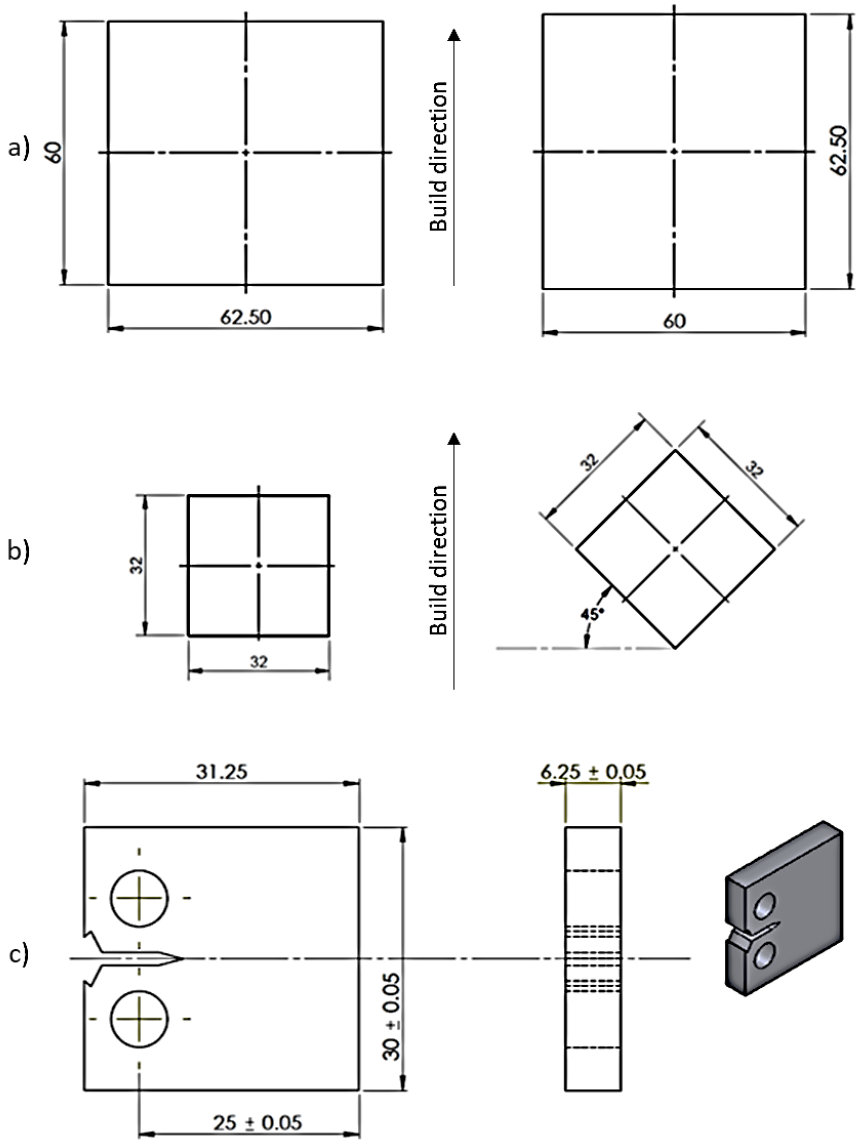

Figure 72 a) Co-Cr-Mo SLM specimens b) In738 and In718 SLM specimens c) Dimension of CT specimens (all dimension in mm and not to scale)

As shown in Table 7, Co-Cr-Mo specimens were printed at two different laser power; P = 180 W and P = 320 W. These two different laser power settings produce samples with different lack of fusion percentage, f_{LOF}, where 180 W samples will have f_{LOF} = 0.75% and 320 W samples will have f_{LOF} = 0.2% [13]. The wire-cut process for the CT specimens was chosen in a specific orientation so that both 180 W and 320 W specimen have crack growing perpendicular to the

build direction, C⊥BD and crack growing parallel to the build direction, C//BD. Therefore, there are four different conditions for Co-Cr-Mo CT specimens which are listed below:

i. 180 W with crack growth direction perpendicular to the build direction, **180 C⊥BD**
ii. 180 W with crack growth direction parallel to the build direction, **180 C//BD**
iii. 320 W with crack growth direction perpendicular to the build direction, **320 C⊥BD**
iv. 320 W with crack growth direction parallel to the build direction, **320 C//BD**

The Inconel 738 specimens were printed at two different laser power; P = 270 W and P = 320 W. These two different laser power settings produce samples with different amount *of hot cracks* (shrinkage cracks that were formed during the solidification process) where the 270 W samples have slightly more short cracks present as compared to the 320 W samples [12]. In addition, the 320 W samples are expected to have significantly more keyhole pores as compared to the 270 W samples. The wire-cut process for the CT specimens was chosen in a specific orientation so that both 270 W and 320 W specimens have crack growing perpendicular to the build direction, C⊥BD, crack growing parallel to the build direction, C//BD and crack growing 45º to the build direction, C45BD. Therefore, there are six different conditions for Inconel 738 CT specimens which are listed below:

i. 270 W with crack growth direction perpendicular to the build direction, **270 C⊥BD**
ii. 270 W with crack growth direction parallel to the build direction, **270 C//BD**
iii. 270 W with crack growth direction 45º to the build direction, **270 C45BD**
iv. 320 W with crack growth direction perpendicular to the build direction, **320 C⊥BD**
v. 320 W with crack growth direction parallel to the build direction, **320 C//BD**
vi. 320 W with crack growth direction 45º to the build direction, **320 C45BD**

The Inconel 718 specimens was produced by Dr. Teresa Guraya via Ren AM 500 SLM printer at the University of the Basque Country, Bilbao, Spain. The SLM parameter listed in Table 7 was

chosen after several combinations were tested, in effort to build a fully dense material. The SLM parameters optimisation process focuses on reducing the percentage of microstructure defects. The specimens were wire-cut into CT specimens at a specific orientation so that the main crack grows 45º to the build direction. Since this study does not intend to investigate the effect of laser power and build direction for SLM Inconel 718, there is only one condition for Inconel 738 CT specimens, which is C45BD.

3.3 Fatigue crack growth (FCG) experiment

3.3.1 Experimental set-up

The fatigue crack growth rate experiment was conducted in accordance with ASTM E647; "*Standard Test Method for Measurement of Fatigue Crack Growth Rates"*, following the guidelines in Annex A5: For the use of compliance to determine to crack size and Annex A1: The compact specimen [97]. The experimental result (FCGR graph) is expressed as a function of crack-tip stress intensity factor range, ΔK versus crack growth rate, da/dN. The stress intensity factor range value, ΔK is calculated based on the linear elastic fracture mechanics (LEFM) stress analysis concept explained in Chapter 1 [127, 128].

MTS Landmark Servohydraulic system was used to provide fatigue loading during FCGR experiments while an ASTM E647 standard-compliance template provided by MTS Multipurpose Elite software was used for crack size monitoring and recording purposes. The experimental setup mainly involves a fatigue loading machine, a CT specimen, an FCG grip, a clip-on gage and the MTS Multipurpose Elite software as shown in Figure 73.

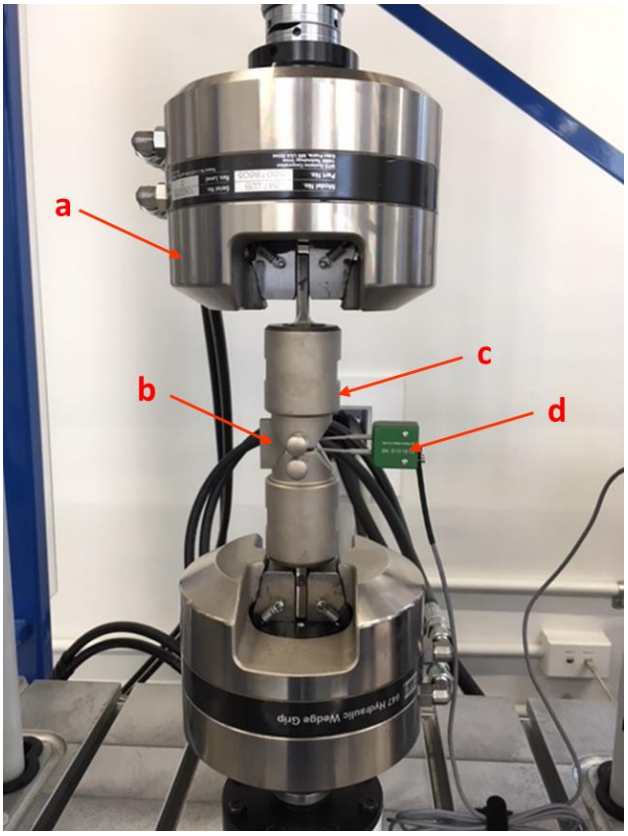

Figure 73 FCGR experimental setup comprising a) Loading machine b) CT specimen c) FCG grip d) Clip-on gage and FCG software for crack monitoring and recording (not in the picture)

The dimension and preparation of the CT specimens is shown in *section 3.2: Compact tension sample preparation.* CT specimen is a single edge-notched specimen which could only be loaded in tension loading condition. This specimen requires the least amount of material to evaluate crack growth behaviour as compared to other FCG test specimen, namely: Middle-tension specimen and Eccentrically-loaded-single-edge-crack-tension specimen. The specific dimension of the CT specimens used in this study follow the ASTM E647 standard, which is shown in Figure 75, applying the suggested minimum dimension of width, W = 25 mm.

A clevis and pin assembly were used to hold the CT specimen onto the FCG grip. The dimension proportion and critical tolerances of the grip is shown in Figure 75; in terms of CT specimen width, W and CT specimen thickness, B. The grip used in this study was manufactured by Grip Engineering (Nuremberg, Germany), custom made for CT specimen with width, w = 25 mm and thickness, B = 6.25 mm. The material used for the clevis pin and grip is steel hardened with

nickel coating. All ASTM E647 specifications are met and the detailed drawing for the grip is shown in Figure 74 as provided by the manufacturer.

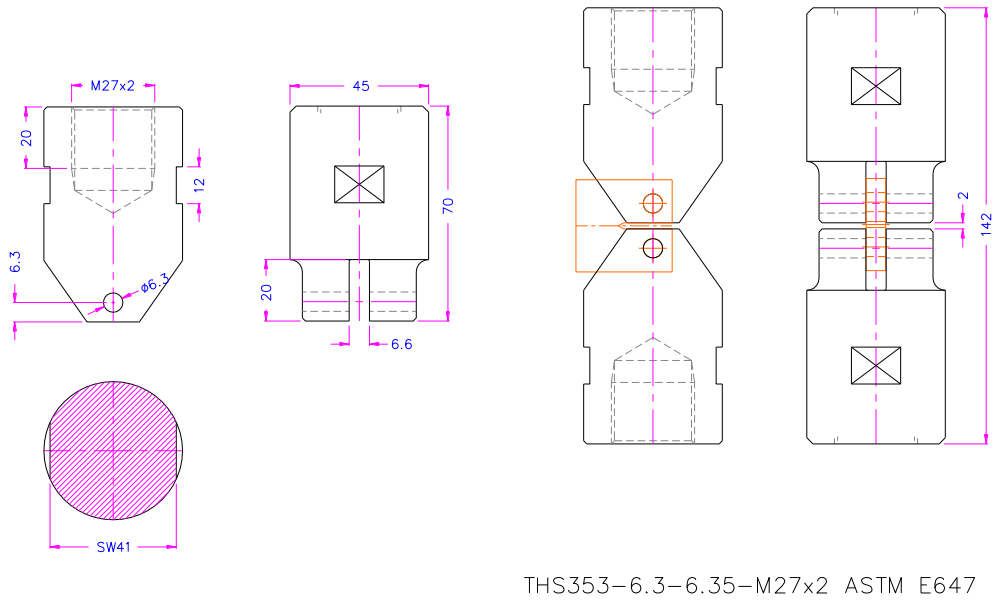

Figure 74 FCGR grip dimension

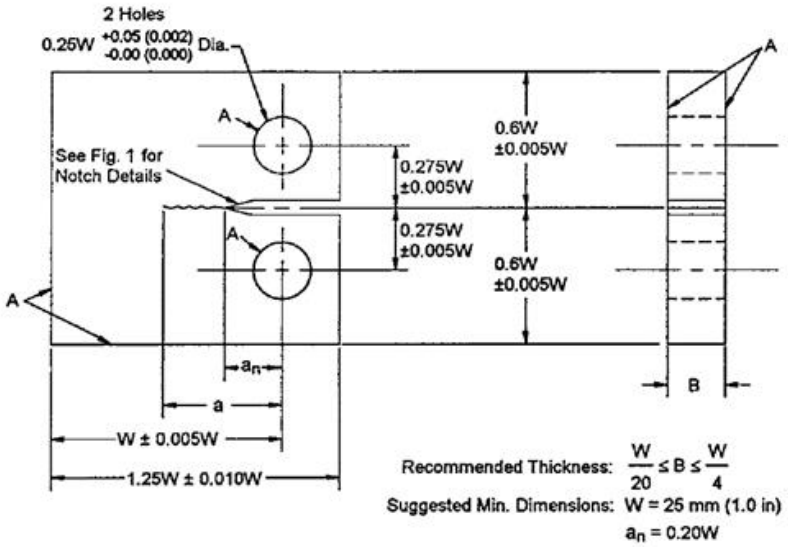

NOTE 1—Dimensions are in millimetres (inches).

NOTE 2—*A*-surfaces shall be perpendicular and parallel as applicable to within ±0.002 *W*, TIR.

NOTE 3—The intersection of the tips of the machined notch (a_n) with the specimen faces shall be equally distant from the top and bottom edges of the specimen to within 0.005 *W*.

NOTE 4—Surface finish, including holes, shall be 1.6 µm (63 µin.) or better. A surface finish of 0.8 µm (32 µin.) or better on the specimen faces may provide a better surface for making optical measurements of the crack.

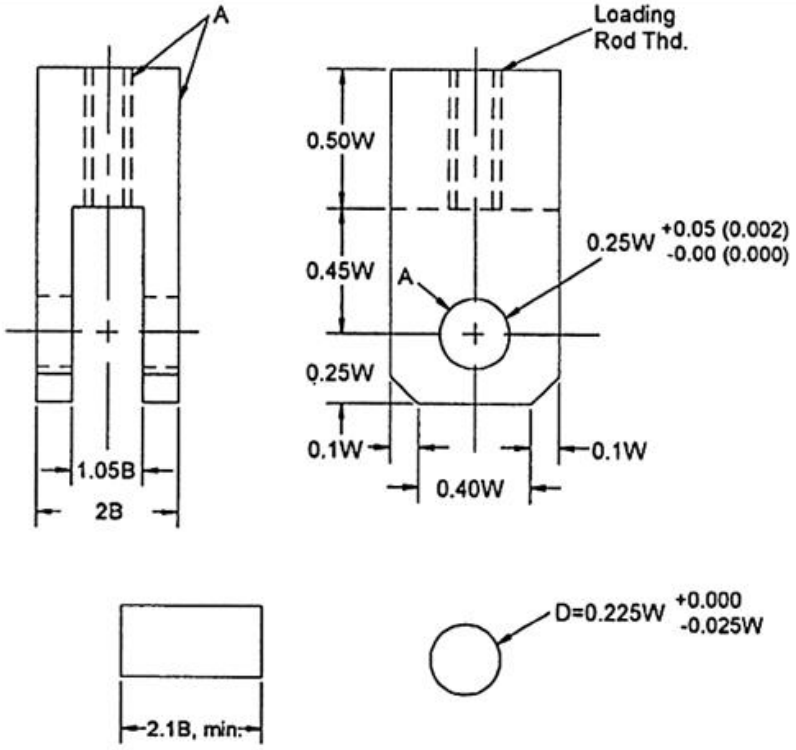

NOTE 1—Dimensions are in millimeters (inches).

A-surfaces shall be perpendicular and parallel as applicable to within ± 0.05 mm (0.002 in.) TIR.

Surface finish of holes and loading pins shall be 0.8 (32) or better.

Figure 75 Top: Standard CT specimen for FCGR testing. Bottom: Clevis and pin assembly for gripping CT specimen [97]

A clip-on gage was attached onto the mouth-end of the CT sample (location V_0) shown in Figure 77. It was used to measure the vertical mouth opening displacement (*v)* of the CT sample. The clip gage used in this study was custom made by Epsilon Tech. Corp. (Wyoming, USA), specifically to meet all the requirements in ASTM E647 standard. It is important that the gage remains linear over the range of displacement measured and having sufficient resolution and frequency response. The specific drawing of the clip gage used in this study is shown in Figure 76 with a gage length of 5 mm and measuring range of +4 mm / -1 mm.

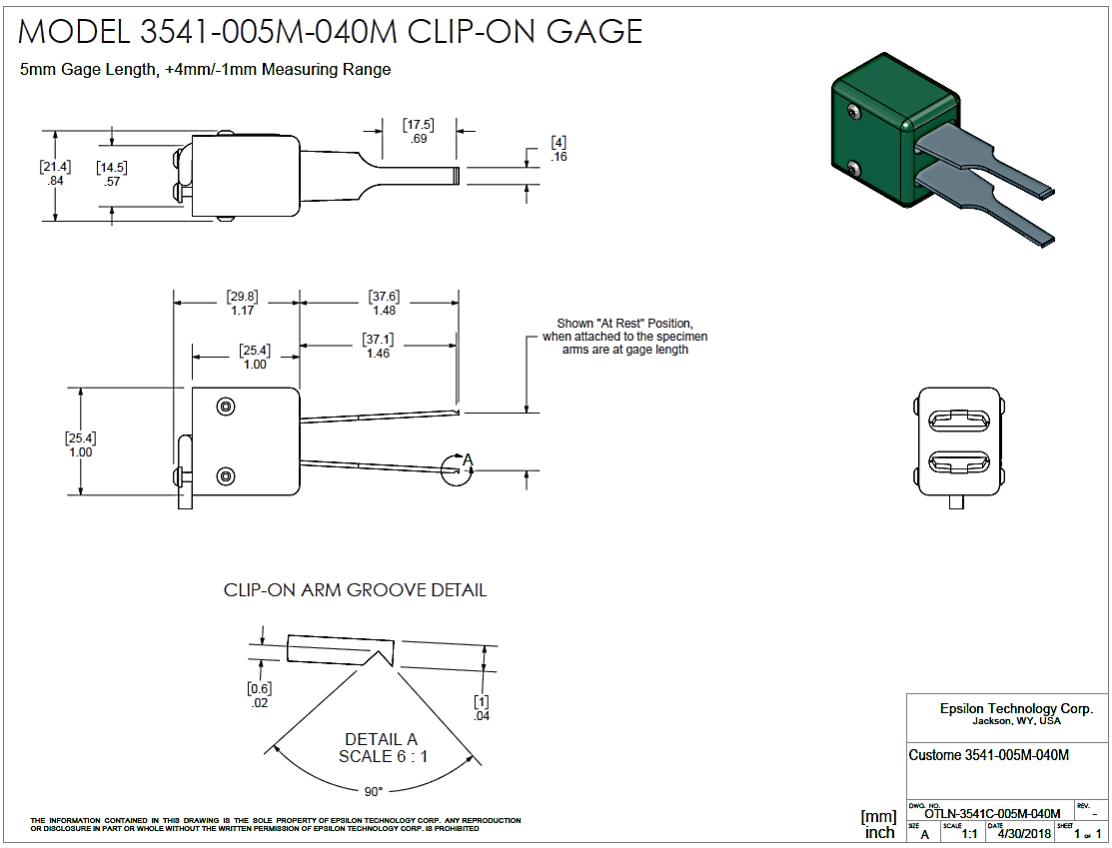

Figure 76 Clip-on gage drawing and specifications

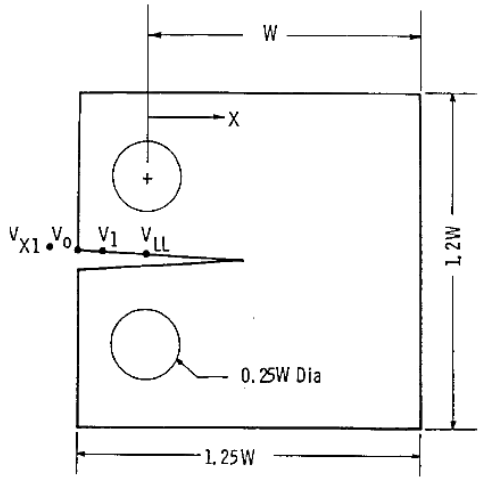

Meas. Location	X/W	C_0	C_1	C_2	C_3	C_4	C_5
			C(T) Specimen				
V_{X1}	–0.345	1.0012	–4.9165	23.057	–323.91	1798.3	–3513.2
V_0	–0.250	1.0010	–4.6695	18.460	–236.82	1214.9	–2143.6
V_1	–0.1576	1.0008	–4.4473	15.400	–180.55	870.92	–1411.3
V_{LL}	0	1.0002	–4.0632	11.242	–106.04	464.33	–650.68

Figure 77 Quintic function constant for CT specimen, based on COD measuring location [129, 130]

3.3.2 FCG compliance calculation

The FCG software used in this study is MTS TestSuite™ [131], provided by MTS Systems Corporation, a global supplier of engineering test system from Minnesota, USA. The software provides two versions of FCG templates which comply with ASTM E647: 1) FCG Compliance and 2) FCG DC Potential Drop. The main difference between the two templates is on the method of crack size measurement. The FCG DC Potential Drop template uses electrical leads that carry voltage through the CT specimen, and the change in voltage during crack growth is measured to determine the crack size. This study utilizes the FCG Compliance template which uses a clip gage to measure the Crack Opening Displacement (COD). Loading frequency and COD signals were recorded by the FCG software to measure the crack growth rate, da/dN and stress intensity factor range, ΔK in real-time. The relationship between FCG software and other apparatus is illustrated in Figure 78.

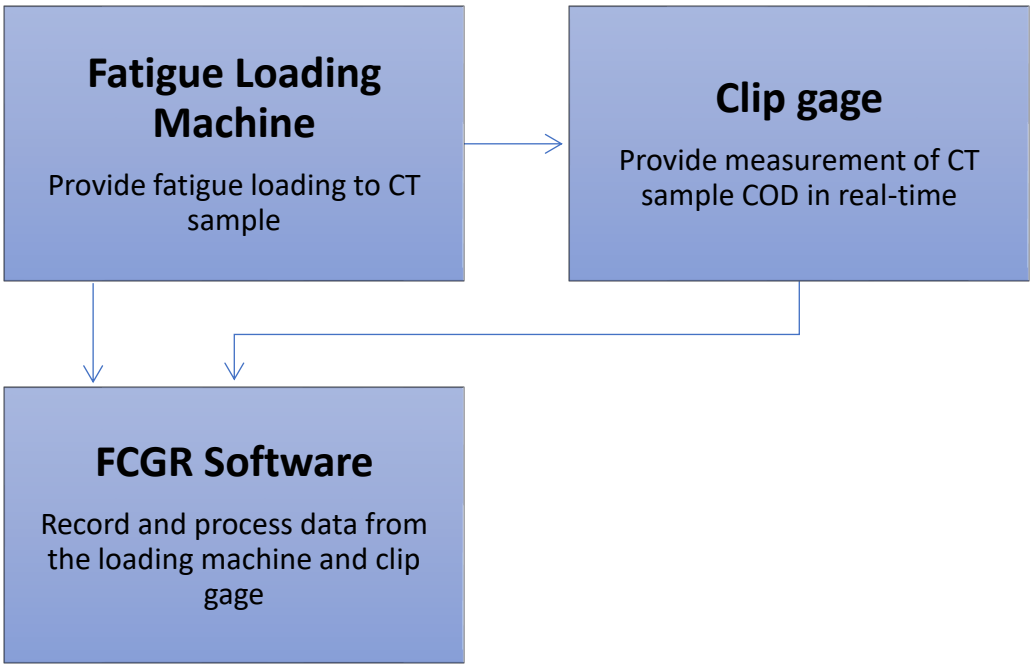

Figure 78 FCGR data collection process by the FCGR Software. Data input source: loading machine and clip gage.

Compliance is the inverse of the force-displacement slope, normalised for elastic modulus (also known as Young's modulus), E and specimen thickness (B). The relationship between compliance and crack size has been derived for most standard specimens including CT specimen[101, 130, 132]. Such relationships are usually expressed in terms of a dimensionless quantities of compliance, $\frac{EvB}{F}$ (or sometimes ECB where C = $\frac{v}{F}$) and the normalised crack size (α) where α = (a / W). Where:

E	Elastic modulus
v	Displacement between measurement points (COD)
B	Specimen thickness
F	Force
a	Crack size or crack length
W	Width of specimen

The relationship between $\frac{EvB}{F}$ and α for CT specimen is represented by a quintic function (polynomial of degree five). It is also depending on the location of where COD is measured. As

mentioned before, the clip-on gage was attached to the end mouth of the CT sample (location V_0) shown in Figure 77. By referring to Figure 77, the location V_0 will give a specific value on the five constants of the quintic function for the relationship between $\frac{EvB}{F}$ and α, where:

C_0 = 1.001

C_1 = -4.6695

C_2 = 18.460

C_3 = -236.82

C_4 = 1214.9

C_5 = -2143.6

These C_x constant values vary depending on the location of where COD is being measured, and only four different locations are recommended in E647 standard as shown in Figure 77. The quintic function that represents the relationship between compliance and crack size (specific for the conditions that were mentioned above) is as follows:

$$\alpha = a/W = C_0 + C_1 U_x + C_2 (U_x)^2 + C_3 (U_x)^3 + C_4 (U_x)^4 + C_5 (U_x)^5 \quad (5)$$

where:

$$U_X = \left\{\left[\frac{EvB}{F}\right]^{\frac{1}{2}} + 1\right\}^{-1}$$

equation (5) remains valid for:

$0.2 \leq \alpha \leq 0.975$

Therefore, for this study, where the width of the CT specimen is W = 25mm, the measurement of crack size using the compliance method is only valid when crack size is in the range of 5mm $\leq a \leq$ 24.3 mm. This range is well beyond the region of interest throughout this study because the initial crack size for the CT sample is a_0 = 5 mm and the FCGR measurement only starts after 1 mm of *pre-crack* at crack size a = 6 mm, also, the CT specimen fractured when crack size reaches a ≈ 20 mm.

By utilising the crack size value obtained from the compliance method mentioned above, the FCGR software will then be able to calculate the stress intensity factor range, ΔK for CT specimen by the following equation:

$$\Delta K = \frac{\Delta F}{B\sqrt{W}} \frac{(2+a)}{(1-a)^{3/2}} (0.886 + 4.64a - 13.32a^2 + 14.72a^3 - 5.6a^4) \quad (6)$$

where:

α = a/W

equation (2) remains valid for:

0.2 ≤ α [133, 134]

FCG software takes signal input from the fatigue loading machine and clip gage, and subsequently applying equation (5) and (6) to record the change of crack size and ΔK, in real-time. The computed ΔK value does not include potential effects or influences of residual stress [135, 136] that can affect the FCG rate measurement. The precision of da/dN and ΔK value is a function of inherent material variability, as well as errors in measurements. Providentially, loading precision is not a major concern due to the modern electrohydraulic test equipment used. In addition, the computerised FCGR software calculation by compliance method also greatly improve the precision of the FCGR result, in contrast to manual crack growth observation where crack growth rate greater than 10^{-8} m/cycles can have error of about a factor of two [137], and rates below 10^{-8} m/cycles can have error of about a factor of five [138]. Based on the compliance calculation, the FCG software will only store data when the crack size (a) is increased by 20 μm or every 20, 000 cycles.

3.3.3 Experimental procedure

As mentioned previously, the FCGR measurement only starts after the 1 mm of pre-crack had grown. The importance of pre-cracking is to provide a sharp crack tip of adequate size (more than 0.1B or 1 mm, whichever is greater), which remove the effect of blunt machined starter

notch on crack growth rate data. Pre-cracking is also important to establish a straight pathway for the crack to continue growing. The rate at which pre-crack is conducted was controlled to ensure $da/dN \leq 10^{-8}$ m/cycle, as suggested by ASTM E647 standard. It can also be used to validate the crack size measurement between compliance method and visual crack size reading. Therefore, each CT specimen will undergo a pre-crack stage, followed by the sequence of procedure shown in Figure 79.

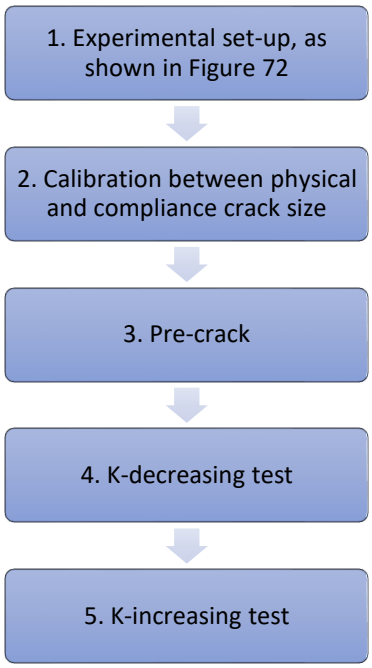

Figure 79 FCGR procedure flow chart

The calibration between physical and compliance crack size is conducted by performing a "Crack size check" action, which is a feature that is included in the FCGR software. The feature applies a small load onto the CT specimen and verifies the calculated crack size, 'a' and the elastic modulus, E. The calculated crack size should coincide with the initial crack length, a_0 which can be measured using a calliper before setting up the experiment. The difference between the physical and compliance (calculated) crack size must be used to adjust all compliance crack sizes. This is accomplished by adjusting the elastic modulus, E, and incorporate it into the compliance equation to adjust all crack size calculations. According to ASTM E647 standard, if the elastic modulus (E) differs from the typical elastic modulus by more than 10 %, then the test data generated are to be considered invalid by this method.

There are two fatigue loading *control modes* (“Delta K” and “Constant Load”) used in this study to obtain the complete FCGR graph, which includes all three stages of crack growth: Stage 1, Stage 2 and Stage 3. These two fatigue loading *control modes* are provided by the FCGR software, defined as follows:

- “Delta K”
    - The test cycles between the minimum and maximum loads that correspond to the desired stress intensities factor (K)
    - Usually used for FCGR measurement in Stage 1
- “Constant Load”
    - The test cycles between a specified minimum and maximum load.
    - Usually used for FCGR measurement in Stage 2 and 3.

The *K-decreasing test* uses the “Delta K” control modes where stress intensity can be controlled to decrease or increase as crack size increases. This test is recommended for da/dN < 10^{-8} m/cycles, where crack growth rate at Stage 1 (also known as crack initiation stage) data is recorded. This procedure starts by applying cyclic force at ΔK equal or greater than the final pre-crack values, and subsequently, as crack size increases, the cyclic force is decreased (shredded) until the low crack growth rate of interest is achieved. The force shedding process is conducted in a continuous manner by an automated program setting provided by the FCGR software. It is controlled by a normalised K-gradient constant, C, illustrated in Figure 80, where:

$$C = \left(\frac{1}{K}\right)\left(\frac{dK}{da}\right) \qquad (7)$$

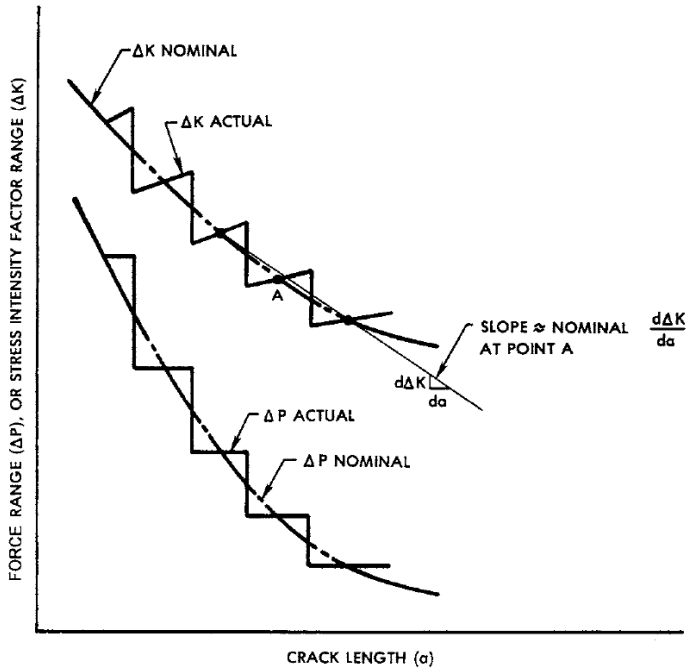

Figure 80 Graph of normalised K gradient, C (force shedding control) for K-decreasing test [97]

The *K-increasing* test uses the "Constant Load" control mode where magnitude of the cyclic force is maintained throughout the FCGR experiment, usually until the CT specimen fracture. This test is recommended for da/dN > 10^{-8} m/cycles, where crack growth rates at Stage 2 and Stage 3 data are recorded. The magnitude of fatigue load (F) was determined by using a "Calculator" function that is provided by the FCGR software, where the load is calculated by inputting the crack size (a) value and the desired starting stress intensity value (K). The "Calculator" function can also determine the stress intensity value (K) by inputting the crack size value (a) and loading value (F). This is achieved by simply substituting the K, 'a' and F values in equation (6), knowing that the width of CT specimen remains constant, W = 25mm. The fatigue loading frequency, *f* and loading ratio, R remains constant throughout the whole experiment (including Pre-crack, K-decreasing, K-increasing and FCGR "interrupted" test) where *f* = 10 Hz and R = 0.1 respectively.

3.3.4 FCGR interrupted test

FCGR interrupted tests were conducted by using the *K-increasing* test technique with the *Constant Load* fatigue loading control mode. Following the pre-crack process (step no. 3 in Figure 79), crack growth is started at a specific ΔK value and then stopped, also at a specific ΔK

value (before reaching its fracture toughness, K_c value), ensuring that the CT specimen does not fractured. An example of a CT specimen that had been through a FCGR interrupted test is shown in Figure 81, where the crack growth section was wire-cut to be mounted and prepare for metallography sample. The length of the crack before the FCGR test was stopped is around a = 8 to 9 mm.

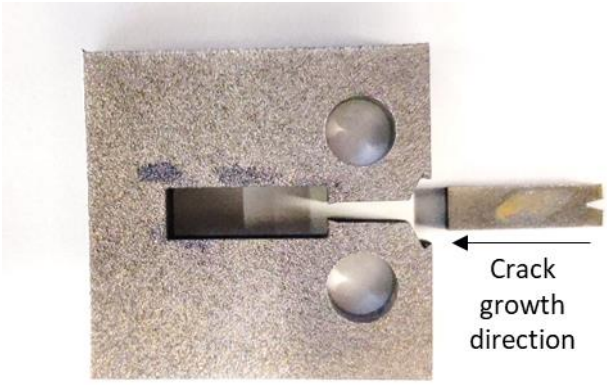

Figure 81 An image of an FCGR interrupted test specimen, with the crack growth section wire-cut for sample preparation

The FCGR interrupted test was conducted for all of the SLM parameter conditions listed in Section Material and SLM parameters, twice for each Co-Cr-Mo SLM condition and once for each Inconel 738 and Inconel 718 SLM conditions. The starting and stopping ΔK values for the FCGR "interrupted" test are as follows:

- For Co-Cr-Mo (180 C⊥BD, 180 C//BD, 320 C⊥BD and 320 C//BD)
    - Set 1: ΔK starts at 10.0 MPa.m$^{-0.5}$ and ends at 12.0 MPa.m$^{-0.5}$
    - Set 2: ΔK starts at 12.0 MPa.m$^{-0.5}$ and ends at 17.0 MPa.m$^{-0.5}$

- For Inconel 738 (270 C⊥BD, 270 C//BD, 270 C45BD, 320 C⊥BD, 320 C//BD and 320 C45BD)
    - Set 1: ΔK starts at 12.0 MPa.m$^{-0.5}$ and ends at 17.0 MPa.m$^{-0.5}$

- For Inconel 718 (C45BD)

- Set 1: ΔK starts at 9.0 MPa.m$^{-0.5}$ and ends at 13.0 MPa.m$^{-0.5}$

The purpose for this interrupted test was to verify the FCGR results produced by each of the CT samples by comparing the da/dN vs ΔK graph between the actual FCGR experiment and the FCGR "interrupted" test experiment. In addition, the fractured FCGR "interrupted" test specimen will be used to analyse the crack growth pathway. Detail observation of crack propagation through the microstructure (grains, meltpool boundaries and cells) of an SLM material at different ΔK values can be achieved by SEM and EBSD analysis,

3.4 Fractured sample for metallography analysis

3.4.1 Fractured Samples

Following FCGR experiment and FCGR "interrupted" test, three types of fractured samples were accumulated from the fractured/cracked CT specimens, namely 1) fracture surface sample 2) carack profile sample and 3) interrupted test sample . By referring to Figure 82, sample 'B' and 'C' were obtained by cutting (wire-cut) the FCGR test sample and the "intrrupted" test sample. These two samples (B and C) were later manually ground for at least 2 mm from the surface of the CT sample to attain a more representative crack pattern located in the middle of the samples, removing the possible effect of plane stress at the surface of the sample.

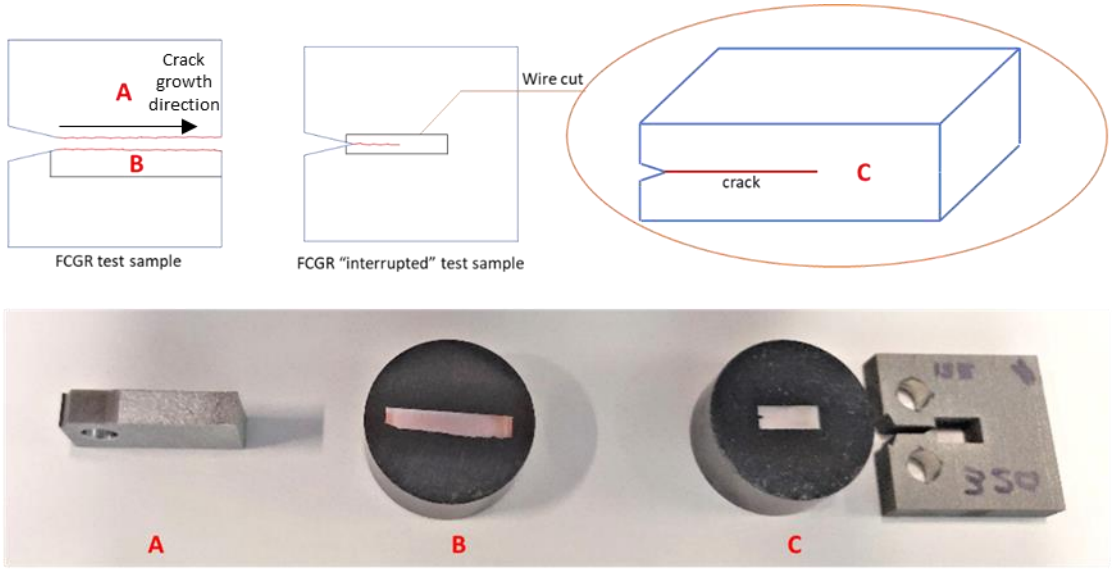

Figure 82 A) Fracture surface sample after FCGR test B) Crack profile sample after FCGR test C) Interrupted test sample after FCGR interrupted test

Both crack profile samples and interrupted test samples (marked as 'B' and 'C' in Figure 82) were mounted into resin powder using a heated mounting press machine made by Struers (Denmark). Two different resin powders provided by the supplier were used depending on the material of the sample to accommodate the difference in polishing/etching process for Co-Cr-Mo and Inconel 738/718.

3.4.2 Mounting resin

As shown in Figure 83, the mounting powder for Co-Cr-Mo samples consisted of two different resin layers; 1) Polyfast – an SEM resin made from Bakelite material, with carbon filler to secure the conductivity, necessary for SEM, and 2) CouduFast – a conductive powder made from Acryl material, with iron filler to ensure electrical conductivity, required for electronic polishing. On the other hand, Inconel 738/718 samples only use Polyfast resin because electronic polishing was not required as they were manually etched.

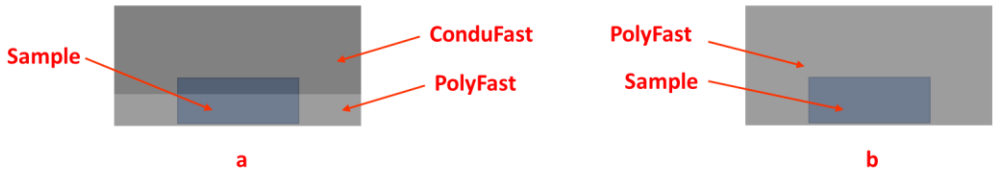

Figure 83 Sample resin used for a) Co-Cr-Mo and b) Inconel 738/718 samples

3.4.3 Polishing and etching

Following the mounting process for both crack profile samples and FCGR "interrupted" test samples, all samples were subsequently polished using a manual rotary disk grinding-polishing machine, wet coarse at four fining stages, following the order of 180, 500, 1200 and 2400 grit silicon carbide papers. Afterwards, all samples went through a finer polishing process using Struers TegraPol-25 automatic polishing machine, equipped with TegraForce-5 that holds and rotates the samples, and TegraDoser-5 that squirts polishing liquid. Cloths of 3 µm grit with "DiaPro" – a water-based diamond polishing liquid and cloth of 1 µm grit with "OP-S

Suspension" – a colloidal silica polishing liquid (both provided by Struers) were used successively to produce a mirror-like finish.

The final step for the samples' preparation was conducted differently for Co-Cr-Mo and Inconel 738/718. This step is important to reveal the microstructure features of the samples surface and for electron backscatter diffraction (EBSD) analysis. Detection of the diffracted electrons by the EBSD camera originated only from the top 50 – 100 nm of the sample, therefore, it is crucial to have a metal surface without oxide, distortion or any type of reaction products that might appear from the aforementioned polishing process. These samples were exposed faced down onto a specific etching solution:

- Co-Cr-Mo
    - Electrolic treatment using LectroPol-5 automatic polisher machine by Struers, in a solution of 10% H_2SO_4 and CH_3OH at 6 V for 25 seconds at room temperature [13].
- Inconel 738 and Inconel 718
    - Manually etched by immersing the samples into a solution containing 10 mL HNO_3, 15 mL HCl and 10 mL CH_3COOH for 13 seconds at room temperature [12].

3.5 SEM, EBSD, and TEM analysis

This study uses Hitachi SU-70 field emission SEM, equipped with Energy-Dispersive X-ray (EDX) and Electron Backscatter Diffraction (EBSD) detectors from Thermo Scientific™. Scanning electron microscope (SEM) is an electron microscope that produces a high magnification image of a sample in a vacuum condition by scanning the surface of the sample with a focused electrons beam. A 15-kV accelerated voltage setting is used to observe the microstructural detail and capture image of the fractured FCGR samples. An example of an SEM image taken using this machine is shown in Figure 84.

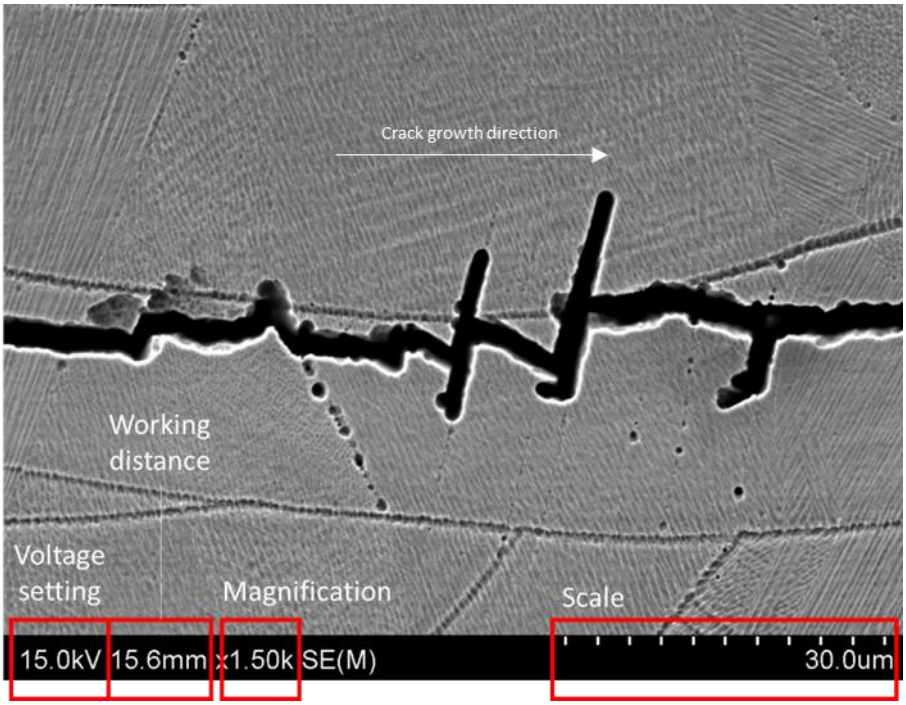

Figure 84 Example of an SEM image

EBSD technique is used to obtain crystallographic information from the samples inside the SEM machine. An EBSD detector contains phosphor screen to capture a pattern produced by incident electrons from the electron-beam that collide and backscatter elastically from atomic planes of a crystal grain that satisfy Bragg's law [139]. This pattern (also known as the EBSD pattern) contains Kikuchi bands [140], which allows the identification of crystal orientation. Identification of the crystal orientation information is processed and collected automatically by using Thermo Scientific's NSS Spectral Imaging Software.

The crystal orientation can be represented by Euler angles, which characterize the orientation of a 3D object by three angles, φ1, ϕ, φ2. Suppose that a 3D object having a standard global x, y and z axes, the change in orientation of the object can be describe by the three Euler angles: φ1 is the angle of rotation around the z axis, followed by ϕ, the angle of rotation around the x' axis and finally followed by φ2, the angle of rotation around the z'' axis. Therefore, by using Euler angle, the crystal orientation can be replicated and generated in a 3D drawing software. An example of an EBSD crystal orientation map provided by the EBSD system is shown in Figure 85.

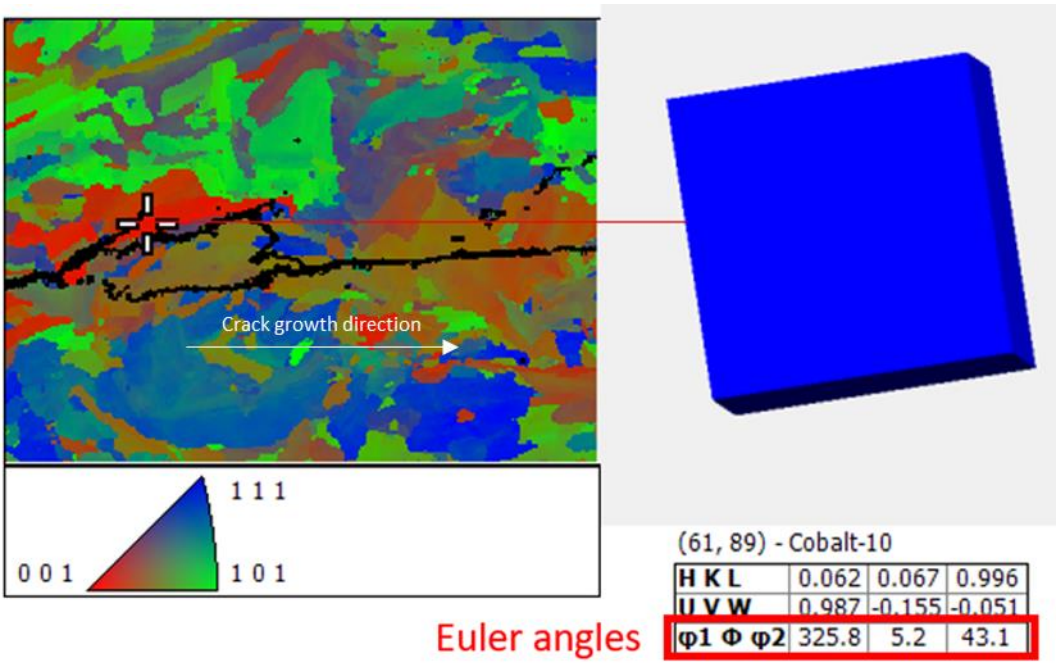

Figure 85 EBSD crystal orientation map (left) and crystal orientation represented by Euler angle (right)

While SEM detects electrons that were reflected near the surface region of a sample to generate its image, transmission electron microscope (TEM) detects electrons that pass through an ultrathin specimen usually below 100 nm in thickness, called lamella. This technique is a powerful tool in material science and one of its important features is to allow electron diffraction pattern to be obtained. The electron diffraction pattern is used in this study to determine the specimen's atomic arrangement, whether there is any evidence of hexagonal phase crystal structure.

TEM analysis was conducted by the courtesy of Dr. Teresa Guraya from the Department of Mining and Metallurgical Engineering and Material Science in the University of the Basque Country, Bilbao, Spain. The lamella was prepared by a combined focused ion beam and electron microscope (FIB-SEM) system. Simultaneous use of FIB cutting and SEM imaging allow high precision controls for cutting complex samples at nanometer resolution. The location of the lamella was taken precisely in front of the crack tip (within 5 μm radius) from an interrupted test sample, as shown in Figure 86.

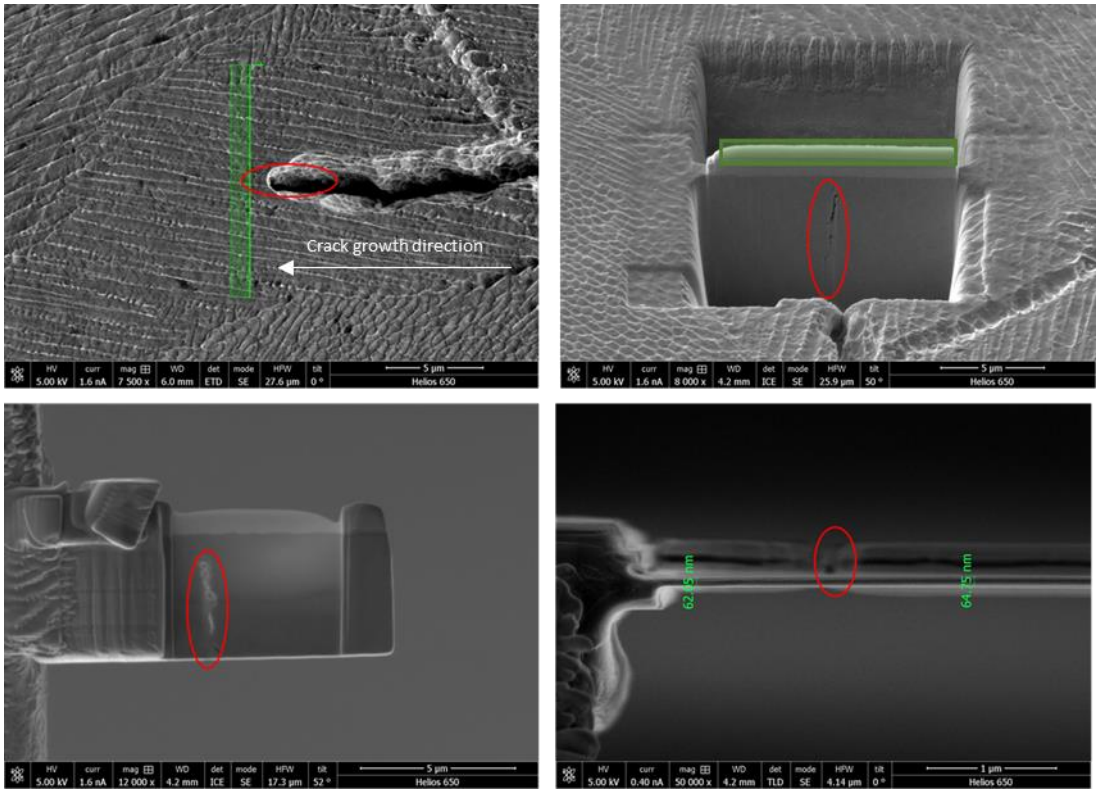

Figure 86 Preparation of lamella by FIB-SEM, evidence of crack tip is circled in red.

The electron diffraction pattern was obtained at more than 40 different locations. As shown in Figure 87, the selected locations were either inside the "rhomboids" regions or on top of the "white bands". The "white bands" was suspected to have a hcp crystal structure since cracks appear to navigate through the bands in a brittle manner.

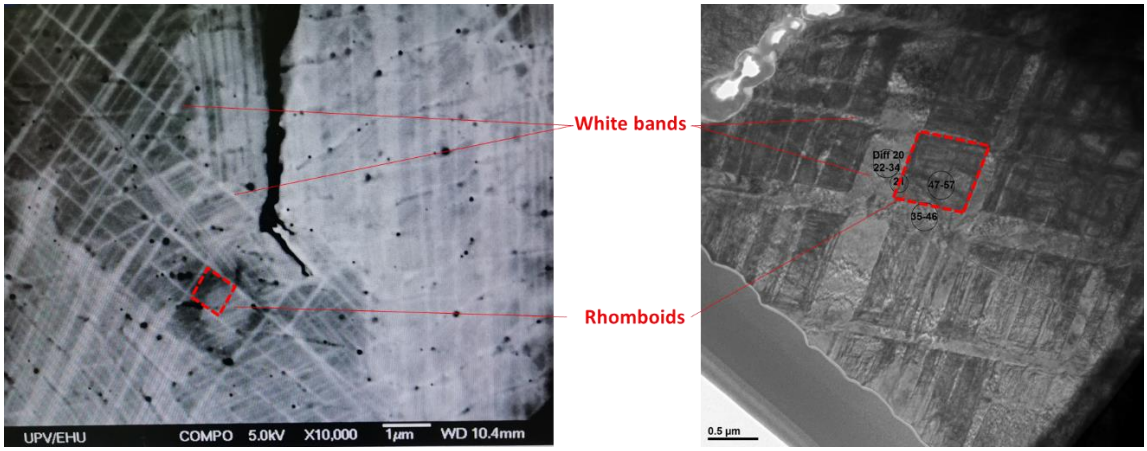

Figure 87 TEM locations, with examples of the "white bands" region and "rhomboids" region.

3.6 Software for 3D drawing and microstructure measurement

SolidWorks software was used to model CT specimens and other experimental equipment required to conduct the FCG experiment. Whilst SolidWorks is highly intuitive for designing process of an engineering part, AutoCAD software is used to generate 3D crystal structure to replicate the orientation of a crystal cube. This is because AutoCAD gives a more classic *pen-on-canvas* interface, where multiple unit cells with different orientation can be drawn easily on a single "3D sheet", while SolidWorks focuses more on engineering designing process, where a single part is drawn on a "3D drawing interface".

A representation of a 3D unit cell was drawn into the AutoCAD's 3D sheet by using the Euler angle information provided by the NSS Spectral Imaging Software following the EBSD analysis. Firstly, a cube is drawn with crystal direction [100] aligned with X-axis, [010] direction aligned with Y-axis and [001] direction aligned with Z-axis. Then, a built-in function in AutoCAD called *Rotate3D* is used to rotate the cube according to the Euler angles described earlier in this section. The rotation of the cube was done by specifying the magnitude of the angle and the start and end point of the axis at which the cube is to be rotated.

Finally, microstructure measurement such as average distance between grain boundaries and LOF area percentage value are conducted using ImageJ software. This software allows user to digitally measure the area or distance of a micrograph, based on the scale bar provided on the SEM and EBSD images.

4 Fatigue Crack Growth of SLM Co-29Cr-6Mo alloy

In this chapter, the measurement of FCGR for an SLM Co-Cr-Mo alloy based on two different build directions (BD) and two selected laser power (180 W and 320 W) is presented and compared with the result of SLM Co-Cr-W, which is the only published study on FCGR of SLM Cobalt-based superalloy. The fractured surface of the CT samples is firstly examined to determine the effect of lack of fusion (LOF) on the FCG behaviour. Afterwards, the mode of fracture is determine based on SEM and EBSD analysis. In addition, TEM analysis was conducted to identify a possible fcc→hcp phase transformation in front of the crack tip area. Then, based on the fractographic evidence, the preferred crack pathway is suggested, and the influence of SLM microstructure on the mechanisms of crack growth is addressed. Finally, based on the findings above, the best BD for an SLM hip-stem-implant is suggested and compared with cast Co-Cr-Mo alloy by using linear elastic fracture mechanic (LEFM) calculation.

4.1 The effect of build direction (BD) and laser power (P) on the FCGR graph

The FCGR graph of SLM Co-Cr-Mo alloy for all four conditions are presented in Figure 88. The C⊥BD samples have higher crack growth rates compared to the C//BD samples in the near threshold region (Region 1: da/dN < 1 x 10^{-9} m/cycle). This translates into a higher FCGR's threshold value for the C//BD samples ($\Delta K_{th} \approx 6.6$ MPa$\sqrt{m}$) as compared to the C⊥BD samples ($\Delta K_{th} \approx 5.2$ MPa$\sqrt{m}$), meaning that a lower stress intensity factor (SIF) value is needed for a crack to initiate in the C⊥BD samples. Moreover, C⊥BD samples also maintain a higher crack growth rate in the Paris region ($\Delta K = 20 – 40$ MPa$\sqrt{m}$), which can be expressed in terms of Paris constant, 'C' and 'm' as defined in Chapter 1, equation (3). All four graphs possess similar gradients within the Paris region, with an 'm' value of ≈ 2.7, while the 'C' values are higher for the C⊥BD samples. At the end of the Paris region, both graphs in Figure 88 gradually merge together in Region 3 (da/dN > 1 x 10^{-5} m/cycle), where the CT samples fractured at $\Delta K \approx 55$ MPa$\sqrt{m}$. The laser power setting of either 180 W or 320 W has no significant impact on the

FCGR behaviour, since similar graph trend can be observed for both samples as shown in Figure 88.

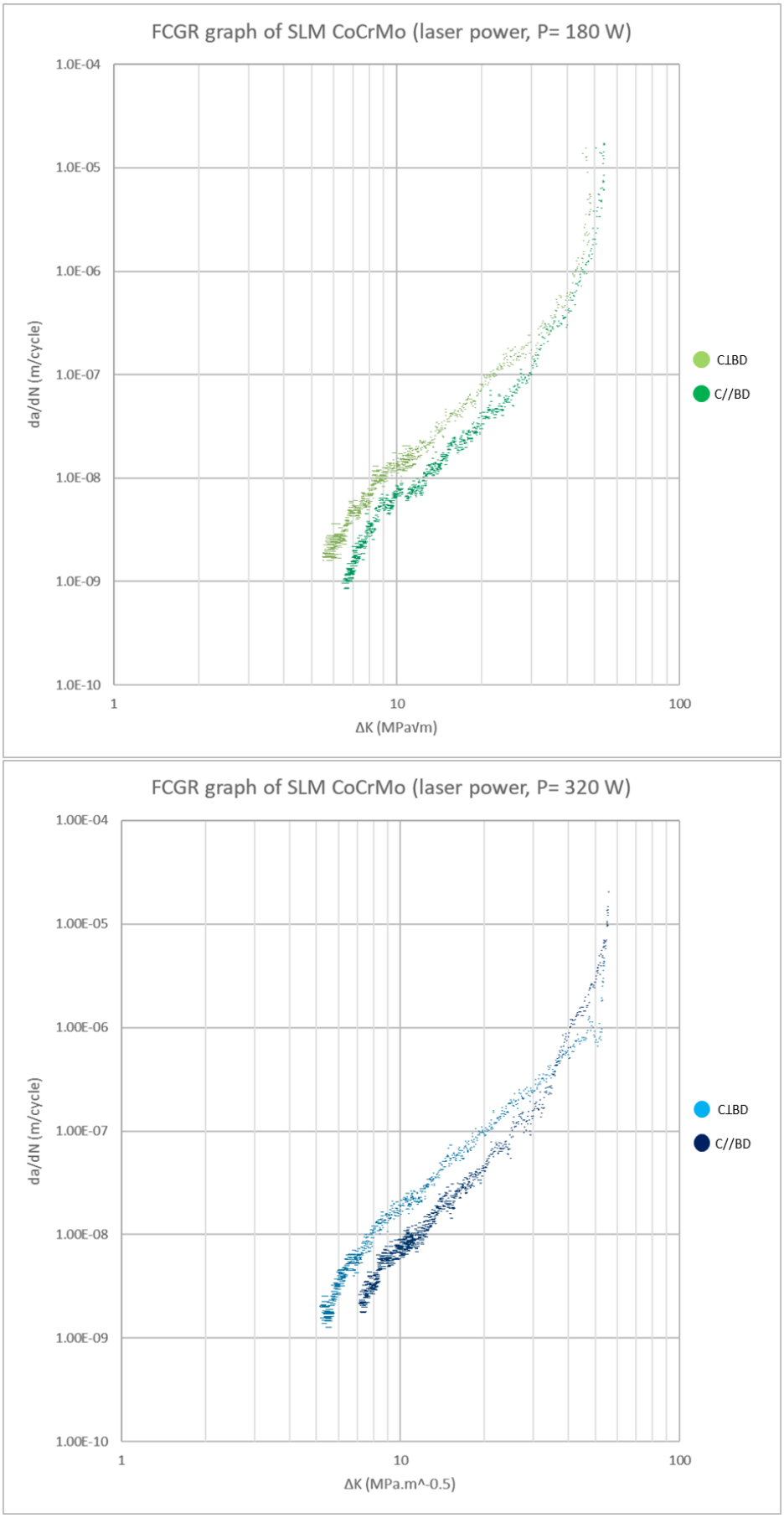

Figure 88 FCGR graph of SLM Co-29Cr-6Mo alloy. Top: SLM laser power setting of P= 180W. Bottom: SLM laser power setting for P = 320 W. The "Top" and "Bottom" graphs contain two FCGR curves of different build directions, showing that the C⊥BD samples have a higher crack growth rates compared to the C//BD samples.

The trends of data near the threshold region suggest that the ΔK_{th} has almost been reached at da/dN = 1 x 10^{-9} m/cycle. Therefore, the threshold values (ΔK_{th}) are determined by the extrapolation of a best-fit line across the growth rates of 10^{-9} and 10^{-10} m/cycle, as suggested by ASTM E647 standard [97]. Since the scattered data of the FCGR graphs in Figure 88 are minor, all data points collected by the FCGR software (data were stored each time the crack size (a) is increased by 20 μm or after every 20, 000 cycles) are included without any curve fit to reflect the original crack growth rate across all ΔK values. Table 8 below summarise the FCGR parameters (threshold value and Paris constant) for all four SLM Co-Cr-Mo samples. For comparison purpose, the only FCGR study available on SLM Cobalt-based superalloy reported by Lee et al. [92] is also included in Table 8.

Table 8 A list of FCGR parameters (threshold value, ΔK_{th} and Paris constants, "C" and "m") for SLM Cobalt-based superalloys. Data for the Co-29Cr-6Mo alloy is determined in this study, while data for Co-Cr-W alloy is from the literature

Sources and material	Crack growth direction in relation to BD		Region I	Region II	
			ΔK_{th} (MPa$\sqrt{m}$)	C	m
This work					
Co-29Cr-6Mo	P = 180 W	C⊥BD	5.1	3.0×10^{-11}	2.7
		C//BD	6.4	1.3×10^{-11}	2.7
	P = 320 W	C⊥BD	5.2	4.2×10^{-11}	2.8
		C//BD	6.7	1.5×10^{-11}	2.7
From literature					
Lee et al., 2019 [92] Co-Cr-W	C⊥BD		4.8	2.6×10^{-12}	4.3
	C//BD		3.6	3.6×10^{-12}	4.6

Based on Table 8, the FCGR parameters for both materials (determined in this study and from Lee et al. [92] are shown to be highly affected by the crack growth direction in relation to BD. The FCGR graph of SLM Co-Cr-W reported by Lee et al. is superimposed onto the FCGR graph of Co-Cr-Mo in Figure 89 to have a better illustration on the differences in the FCGR behaviour

between the two materials. The FCGR graphs between the two materials (Co-Cr-W and Co-Cr-Mo) in Figure 89 appear highly distinct at the high growth rate region (da/dN > 10^{-7} m/cycle), but gradually start to become more similar at the lower growth rate area (da/dN < 10^{-9} m/cycle). As mentioned in Chapter 2, the author did not provide any explanation as to why the SLM Co-Cr-W CT samples start to fracture at an extremely low SIF values of ΔK = 12 – 13 MPa$\sqrt{m}$. This is unusual because Co-Cr-based alloys have a fracture toughness of K_{1C} ≈ 60 MPa$\sqrt{m}$ [96]. Because of the low ΔK value in Region 3, the FCGR curves for the SLM Co-Cr-W alloy at the Paris region are very steep, and therefore the Paris constants presented are likely to be less accurate. Nevertheless, the crack growth rate in the Paris region for both materials are shown to be affected by the BD.

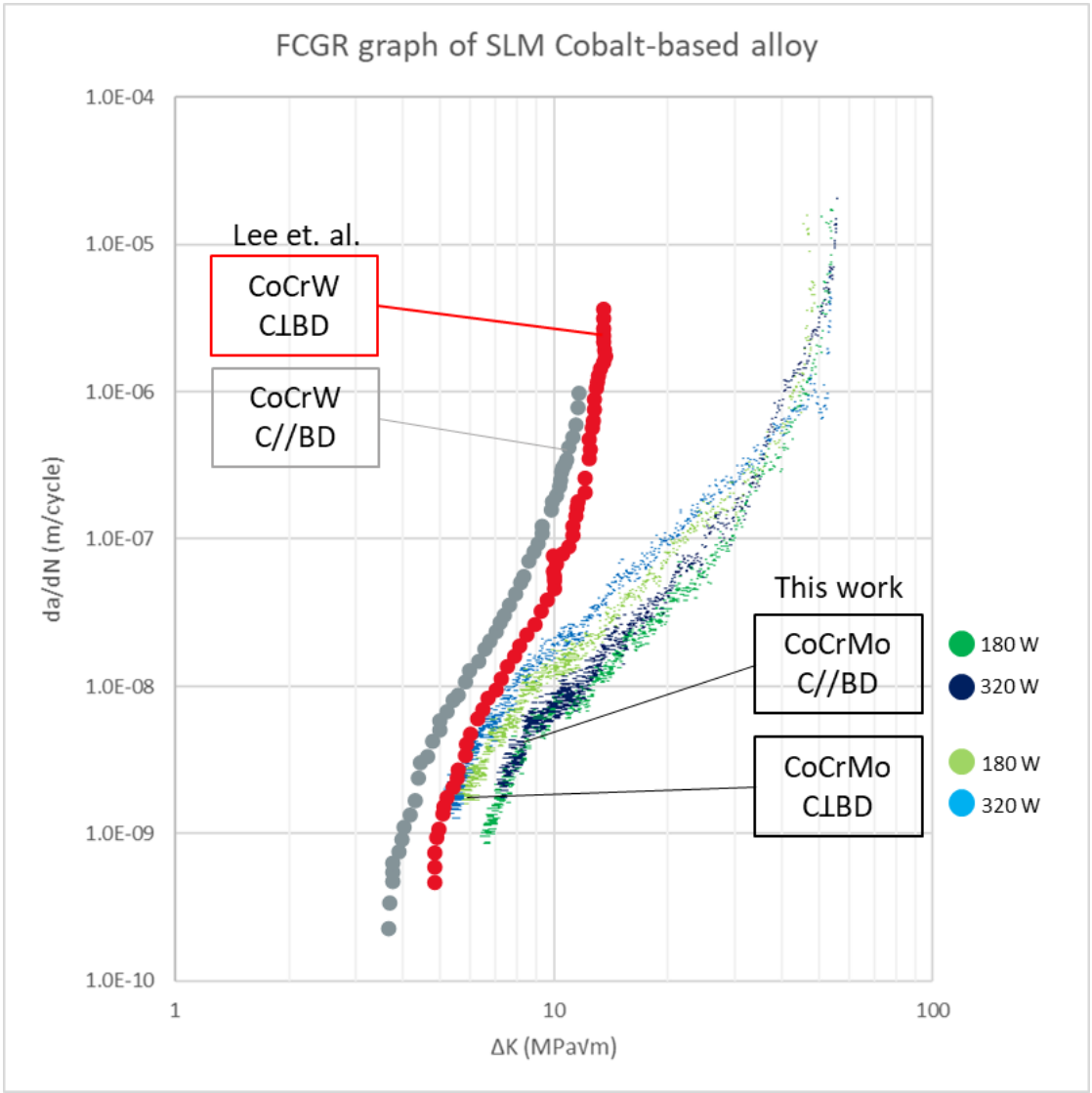

Figure 89 FCGR graph of SLM cobalt-based superalloys. The data for the SLM Co-Cr-Mo alloy were obtained in this study while the data for the SLM Co-Cr-W alloy were taken from Lee at. el. [92]

Although the difference in ΔK_{th} values between C⊥BD and C//BD samples is about 1.2 – 1.5 MPa$\sqrt{m}$ for both SLM Co-Cr-Mo and Co-Cr-W, the C//BD samples for SLM Co-Cr-Mo have higher threshold values compared to the C⊥BD samples, while an opposite relationship has been reported for SLM Co-Cr-W alloy. The contrasting ΔK_{th} results between the C⊥BD and C//BD samples for the two materials are noteworthy because the toughness of a material is generally based on the ΔK_{th} value. Moreover, the literature on the FCGR behaviour of SLM Co-Cr-W [92] did not provide any evidence on its suggestion that "*the crack growth resistance is expected to be higher provided that the crack growth is perpendicular to the elongated direction of the grain morphology because the grain boundaries act as barriers against crack growth*", justifying their result that the C⊥BD sample have a higher ΔK_{th} value compared to the C//BD sample. To verify the reported results, detailed fractographic analysis wss conducted later in this Chapter to analyse the crack growth pathway across the SLM microstructure.

Two characteristics of the SLM microstructure that could possibly affect the FCGR behaviour are 1) micro defects and 2) grain/cell structure (size, shape, and orientation). The major micro defects that could form during SLM process is lack of fusion (LOF), usually located between the meltpool boundary, giving it sharp edges [13]. The feature of the grain/cell structure is characterised by its growth direction during the solidification process as described by Chen et al. [14]. Since SLM is an upwards directional additive manufacturing process, the subsequent microstructure feature that could possibly influence the FCGR behaviour could also be directional. Therefore, the influence of LOF and the grain growth direction on the FCGR behaviour of the tested SLM Co-Cr-Mo samples are also discussed in this study.

4.2 Lack of fusion (LOF) on fractured surface

This section discusses the main feature that can be readily observed on the fracture surface of the CT samples, which is the presence of LOF. Due to the different amount of LOF reported on the 180 W and 320 W samples [13], the effect of LOF on the FCGR behaviour of the tested samples is determined by analysing their fracture surfaces. In addition, this section also intends to

investigate whether the presence of LOF is a source of different FCGR behaviour between the C⊥BD samples and the C//BD samples. Figure 90 shows the typical fracture surface of the 180 W samples, with a clear observation of LOF defects in various sizes up to > 100 µm distributed on the fracture surface. As shown in Figure 90a, planar LOF voids are exposed on the fracture surface of the C⊥BD sample. The higher magnification image shown on the right side of the figure indicates a tear drop appearance of a typical non-melted surface. This demonstrates that the formation of the LOF is due to the inability of the subsequent layer to fully melt the local surface of the previous track. For the C//BD sample, as shown in Figure 90b, LOF can also be readily identified. The high magnification micrograph on the right side of Figure 90b also indicates an insufficient laser scan overlapping, as explained in detailed by Darvish et al. [13].

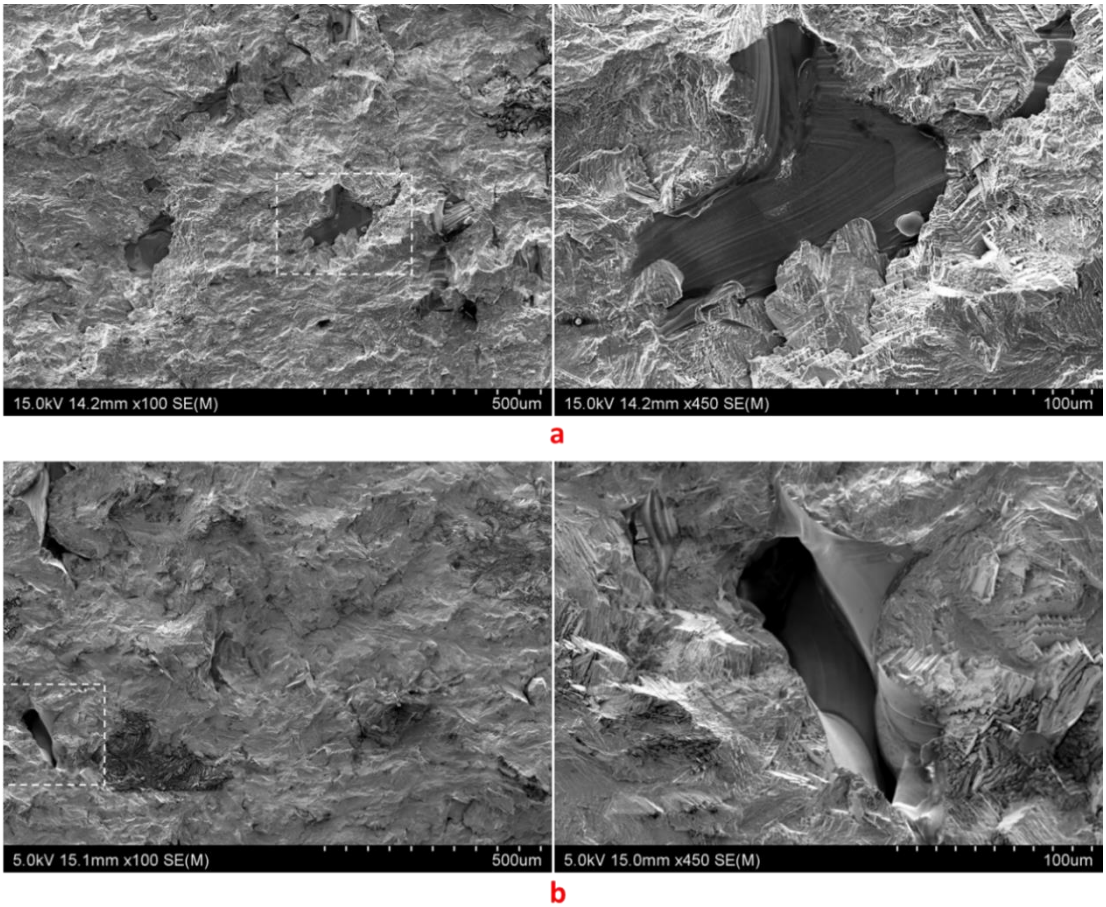

Figure 90 Micrographs on the left side show a typical fracture surface of the 180 W CT samples a) C⊥BD and b) C//BD. Micrographs on the right are higher magnification images, focusing on the LOF.

The area percentage of LOF, f_{LOF} on the fracture surface for both, C⊥BD and C//BD samples was estimated specifically for the 180 W samples. This was firstly done by identifying all LOF voids in an area of 880 µm x 600 µm on the fracture surface, and then by colouring these LOF voids as illustrated in Figure 91. By using ImageJ software, the accumulative area of LOF is determined by applying a proper threshold setting. Of the 180 W tested samples, C⊥BD sample has a LOF area percentage of $f_{LOF} \approx 1.0$ % and the C//BD sample had a LOF area percentage of $f_{LOF} \approx 0.7$ %. The latter agrees well with the f_{LOF} value of 0.73% that was measured in a cross-section parallel to BD on a sample made with the same SLM parameters, and the same alloy powder by Darvish et al. [13]. If the slightly higher amount of LOF on the C⊥BD sample is a source of the lower ΔK_{th} value for the C⊥BD sample as compared to the C//BD sample, it should also apply to the 320 W samples as their FCGR graphs (shown in Figure 88) have similar trends to the 180 W samples.

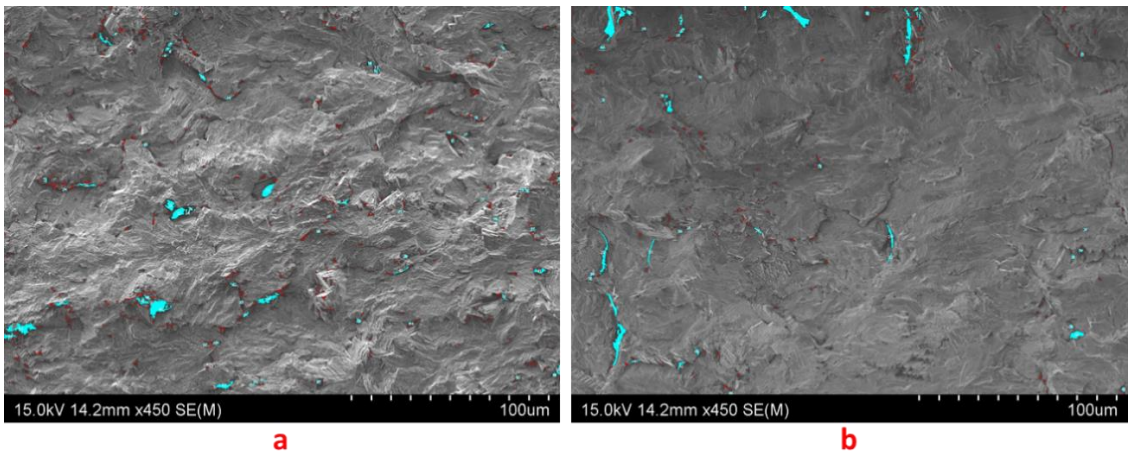

Figure 91 LOF highlighted (light blue) on the fracture surface of 180 W samples taken at the near threshold region ($da/dN = 3 \times 10^{-8}$) a) C⊥BD samples and b) C//BD samples

The selected fracture surfaces of the 320 W samples are shown in Figure 92 below. In contrast to the fracture surface of the 180 W samples shown in Figure 91, the presence of small LOF pores can hardly be detected, although large LOF appears occasionally. This is also consistent with the finding reported by Darvish et al. [13], where increasing the laser power from P = 180 W to 320 W for SLM Co-Cr-Mo, would reduce the f_{LOF} value from 0.73%, to less than 0.1%, but not to zero. The reason for the non-zero LOF had been explained by Darvish et al. as the effect of occasional large spatters that formed during the laser melting process, which subsequently

resulted in a large LOF. Therefore, the occasionally large LOFs observed in the present sample are likely caused by the spatter phenomenon, but in total, the average f_{LOF} for the 320 W sample is still less than 0.1 %.

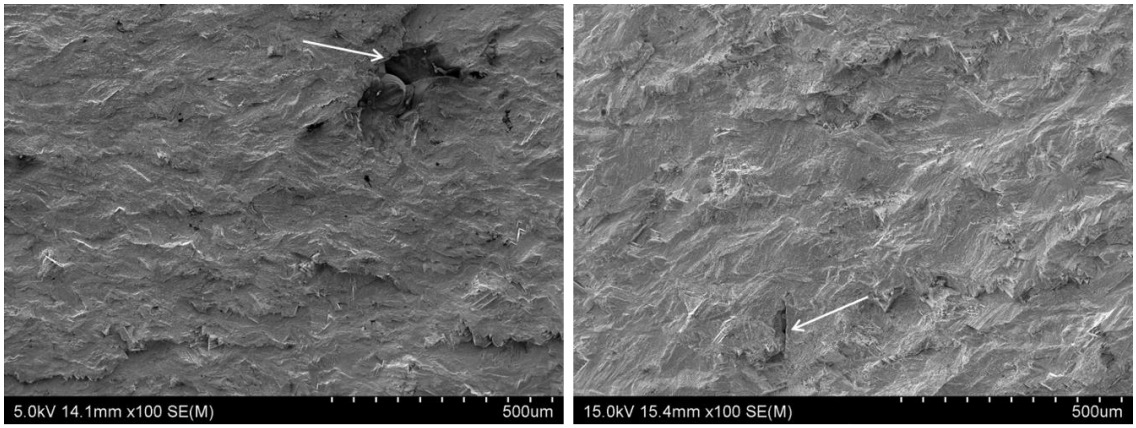

Figure 92 SEM image of the fracture surface for the 320 W samples taken at the near threshold region (da/dN = 3x 10^{-8}) a) C⊥BD sample and b) C//BD sample, displaying the occasionally large LOF, indicated by the arrows.

Two observations can be summarised from the above. Firstly, f_{LOF} (320 W) << f_{LOF} (180 W), as qualitatively observed on the fracture surfaces in the present work, similar to the qualitative measurement on a cross-section of an as build Co-Cr-Mo alloy conducted by Darvish et. al [13]. This indicates that the crack growth pathway is not significantly deviated by the presence of LOF. Secondly, the FCGR curves for the C⊥BD samples, nor the C//BD samples, are not significantly affected by the different laser power setting of 180 W and 320 W. Figure 93 grouped the four FCGR graphs according to its BD to illustrate the similar trends between the 180 W and 320 W samples. These two observations essentially suggested that the presence of LOFs in the tested samples have not significantly affected the FCGR parameters (ΔK_{th} and the Paris constants, C and m). Therefore, the difference in FCGR curves between the C⊥BD samples and the C//BD samples, meaning the significant difference in their FCGR parameters, must then be the effect of BD related microstructure. The discussion in following section of this Chapter attempts to interrogate the effect of the BD related microstructure on the crack growth behaviour of this alloy.

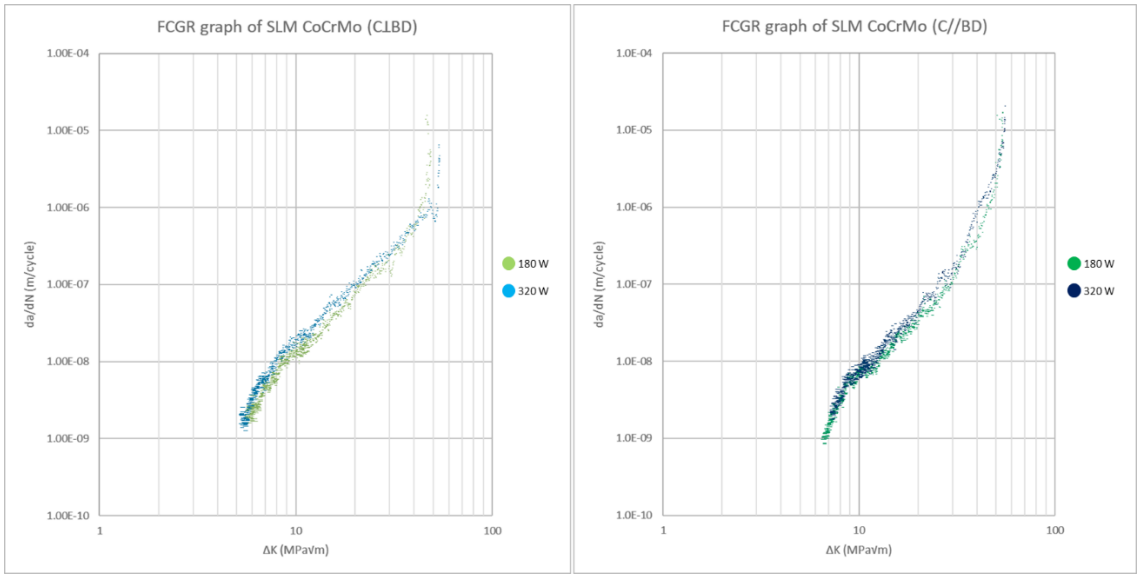

Figure 93 FCGR graph of SLM Co-29Cr-6Mo alloy. Left: C⊥BD samples. Right: C//BD samples. The "Left" and "Right" graphs contain two FCGR curves of different laser power setting, P = 180 W and P = 320 W, showing that the 180 W and 320 W samples have similar FCGR behaviour.

4.3 Transgranular/transcellular fracture dominant

The observation reported by Lee et al. [92] where a fractured sample with rougher fracture profile leads to a higher ΔK_{th} value (slower crack growth rate), also applies to this study. However, the BD effect on the roughness of the fracture profile is opposite to the result in this study. Figure 94 shows one half of the fractured CT samples, showing that the C⊥BD samples in this study have a straighter fractured surface compared to the C//BD samples. This observation is opposite to the fractured CT samples images provided by Lee et al. in Chapter 1, Figure 36. They suggestively link the columnar grain growth in BD direction to the anisotropic FCGR behaviour, claiming that the grain boundary acts as a barrier against the crack growth path. However, microstructure analysis was not conducted in their report to justify the claims. An attempt is thus made in this work to explain how crack path may relate to the SLM microstructure features in the two sample orientations (C⊥BD and C//BD), and thus to the effect of BD on the FCGR parameters. For this purpose, only 320 W samples were used, where the $f_{LOF} < 0.1$ %.

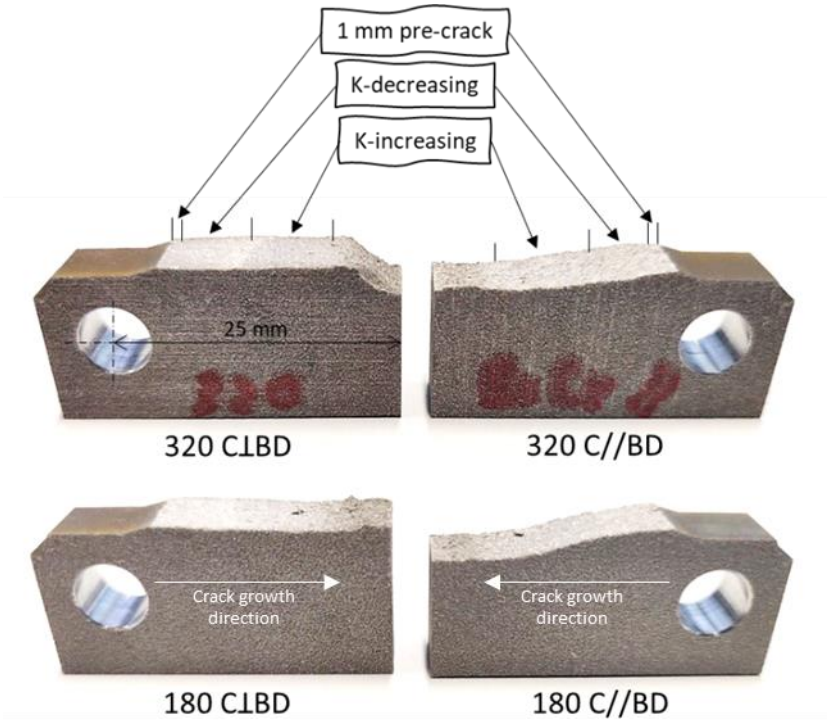

Figure 94 One half of each fractured CT samples tested for SLM Co-Cr-Mo alloy. Top: SLM laser power setting P = 320 W. Bottom: SLM laser power setting P = 180 W. The length for K-decreasing and K-increasing FCGR test is labelled on the two 320 W samples.

Figure 95 shows the cross-sectional micrographs of the crack path for the 320 W "interrupted FCGR test" samples, which is described in Chapter 3, section 3.3.4. The meltpool boundaries are clearly visible in these two micrographs, indicating that the BD is pointing upwards for the C⊥BD sample, and pointing to the right for the C//BD sample. Similar to the visual observation inFigure 94 One half of each fractured CT samples tested for SLM Co-Cr-Mo alloy. Top: SLM laser power setting P = 320 W. Bottom: SLM laser power setting P = 180 W.Figure 94, the micrographs below revealed that the crack path for C⊥BD sample is straighter and smoother compared to the C//BD sample. Clearly, based on the micrograph of C//BD sample, the main crack branches occasionally in an angle more than a few degrees to the BD. This subsequently creates a rougher fractured surface for the C//BD sample compared to the C⊥BD sample, which again contradicts the visual observation of Lee et al. [92]. Therefore, the conclusion that "*the crack growth resistance is expected to be higher provided that the crack growth is perpendicular to the elongated direction of the grain morphology because the grain boundaries act as barriers against crack growth*" proposed by Lee et al. is also not supported in this study since the crack growth path does not replicate the schematic illustration cited by the author, shown in Chapter 2,

Figure 37. To illustrate and understand further, EBSD analysis is conducted onto the "interrupted FCGR test" samples to reveal the grain maps across the crack growth path.

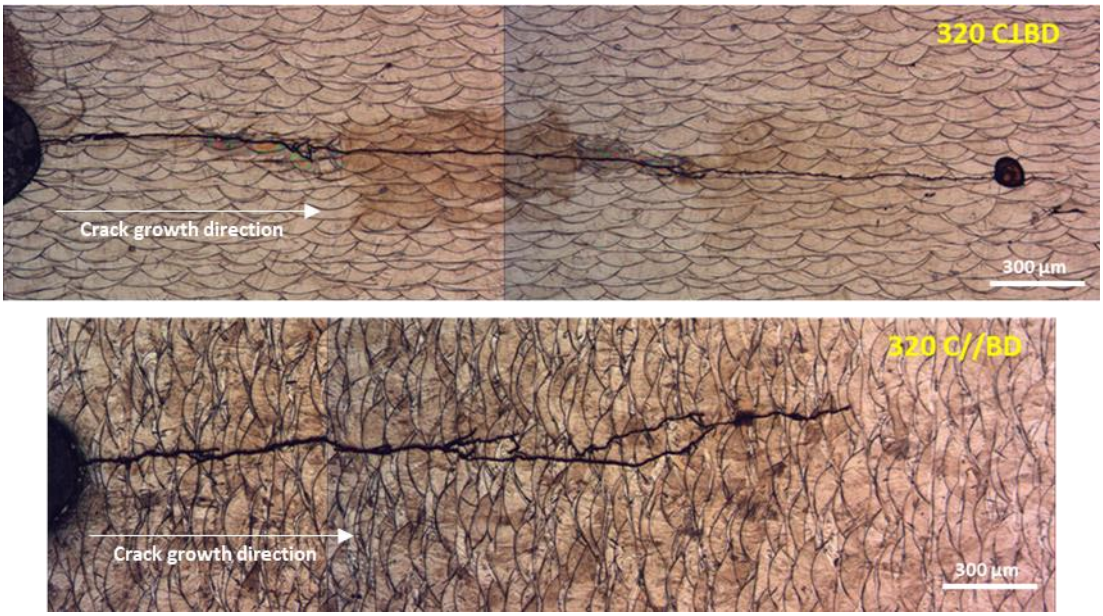

Figure 95 Optical micrograph of the "interrupted FCGR test" for the 320 W samples. Top: C⊥BD. Bottom: C//BD

Figure 96 below shows the EBSD maps and their corresponding SEM images of the tested C⊥BD interrupted FCGR test sample. Figure 96a is taken at the crack tip area where the crack growth rate is da/dN ≈ 5 x 10^{-8}, while Figure 96b is taken from a location of the crack nearer to the threshold region where the crack growth rate is da/dN ≈ 5 x 10^{-9}. Based on all four images in Figure 96, two important crack features can be identified. Firstly, the two SEM images indicate that the crack growth path does not preferably propagates along the meltpool boundaries. This can be clearly observed at the crack tip location in Figure 96a, where the SEM image shows that the crack path was not influenced by the meltpool boundaries and propagates mainly inside the meltpool shape. Secondly, both EBSD images suggest that the cracks are propagating in a transgranular manner, which means that the cracks do not propagate along the grain boundaries in the C⊥BD samples. Because of the transgranular fracture feature, the surface fracture becomes relatively smooth as the crack pass through the columnar grain boundaries that are oriented dominantly in the direction of BD. On the other hand, an intergranular fracture behaviour would have resulted in a severely tortuous/zigzagged crack path.

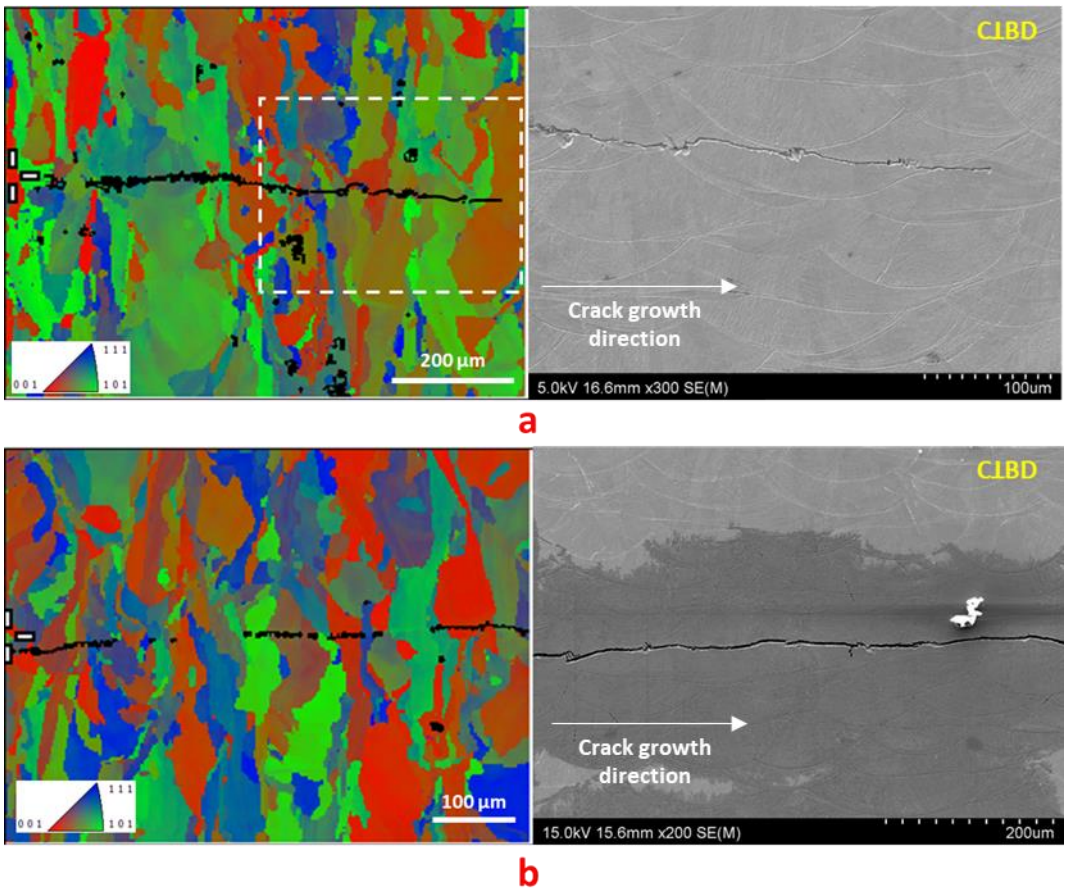

Figure 96 EBSD map and SEM micrograph for the interrupted FCG test of C⊥BD samples, a) taken at the crack tip area, b) middle of the crack where da/dN = 5 x 10^{-9} (near threshold region)

The EBSD maps and their corresponding SEM images for interrupted FCGR test of the C//BD sample are shown in Figure 97. Similar to the C⊥BD sample, there is no evidence of meltpool boundaries influencing the crack growth path, especially that the meltpool boundaries are now largely in high angles to BD. In addition, the two EBSD maps show that the cracks are mainly propagated transgranularly. While Figure 97a may have indicated that the main crack is preferably deflect towards region with smaller grain size as it was growing at a high angle (≈30°) to BD, the crack pathway is still predominantly inside the grain.

Crack branching are clearly visible in this sample as can be seen in Figure 97b. The two branched cracks (marked as C1 and C2) have grown at an angle, until they reached a certain length before they stopped. The branched crack C1 was growing in a high angle (≈50°) to BD (also relative to the maximum tensile plane), thus stopped, giving way to other branch(es) of the crack to grow instead. A similar observation is recorded with the branched crack C2, but it may not be for the

reason of the high growing angle as it was significantly less steep compared to C1. It appears that, as indicated in the EBSD map, the crack stopped without propagating to the next grain on its path. All these features suggest that the crack in the C//BD sample branches more easily compared to the C⊥BD sample, yet both are still predominantly growing in a transgranular manner.

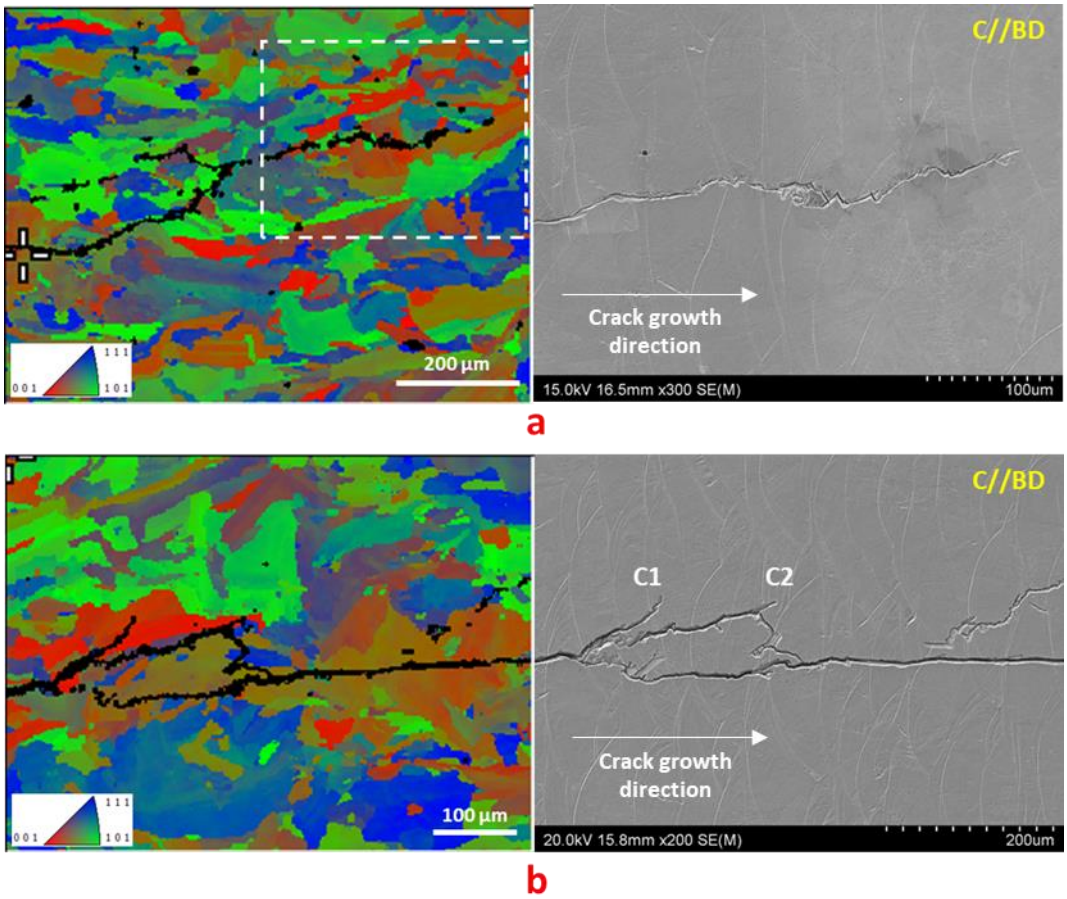

Figure 97 EBSD map and SEM micrograph for the interrupted FCGR test of C//BD samples, a) taken at the crack tip area, b) middle of the crack where da/dN = 5 x 10^{-9} (near threshold region)

Selected fractographic images of the fractured surface in a relatively high magnification of the 320 W samples are shown in Figure 98, showing dominant faceted (transgranular) fracture. These images represent the whole fracture surface within the area of Region 1 (near threshold region) and Region 2 (Paris region), including the fracture surfaces of the 180 W samples. The mode of transgranular fracture observed in Figure 98 is in agreement with the EBSD maps in Figure 96 for C⊥BD and Figure 97 for C//BD, revealing that cracks predominantly propagate through grains. The yellow lines in Figure 98a and Figure 98b are marked to indicate a change in the faceted fracture pattern that are likely to be the grain boundary.

Zhuang and Langer [102, 103] have analysed the fatigue fractured samples of cast Co-Cr-Mo alloy and show that the fracture is dominantly faceted fracture for fine grain (average grain size of 60 µm) and coarse grain (average grain size of 400 µm) samples as indicated in Chapter 2, Figure 40. They commented that the faceted fracture is the result of a low stacking fault of the alloy which then leads to a brittle fracture along the $\{111\}_{fcc}$ family of planes. The angle of the romboid shape from the faceted fracture is also consistent with the angle between the $\{111\}_{fcc}$ planes family which is 71º/109º. In addition, the faceted fatigue fracture of Co-Cr-Mo alloy was also extensively shown by Kannan [141] for as-cast and solution treated Co-Cr-Mo specimens.

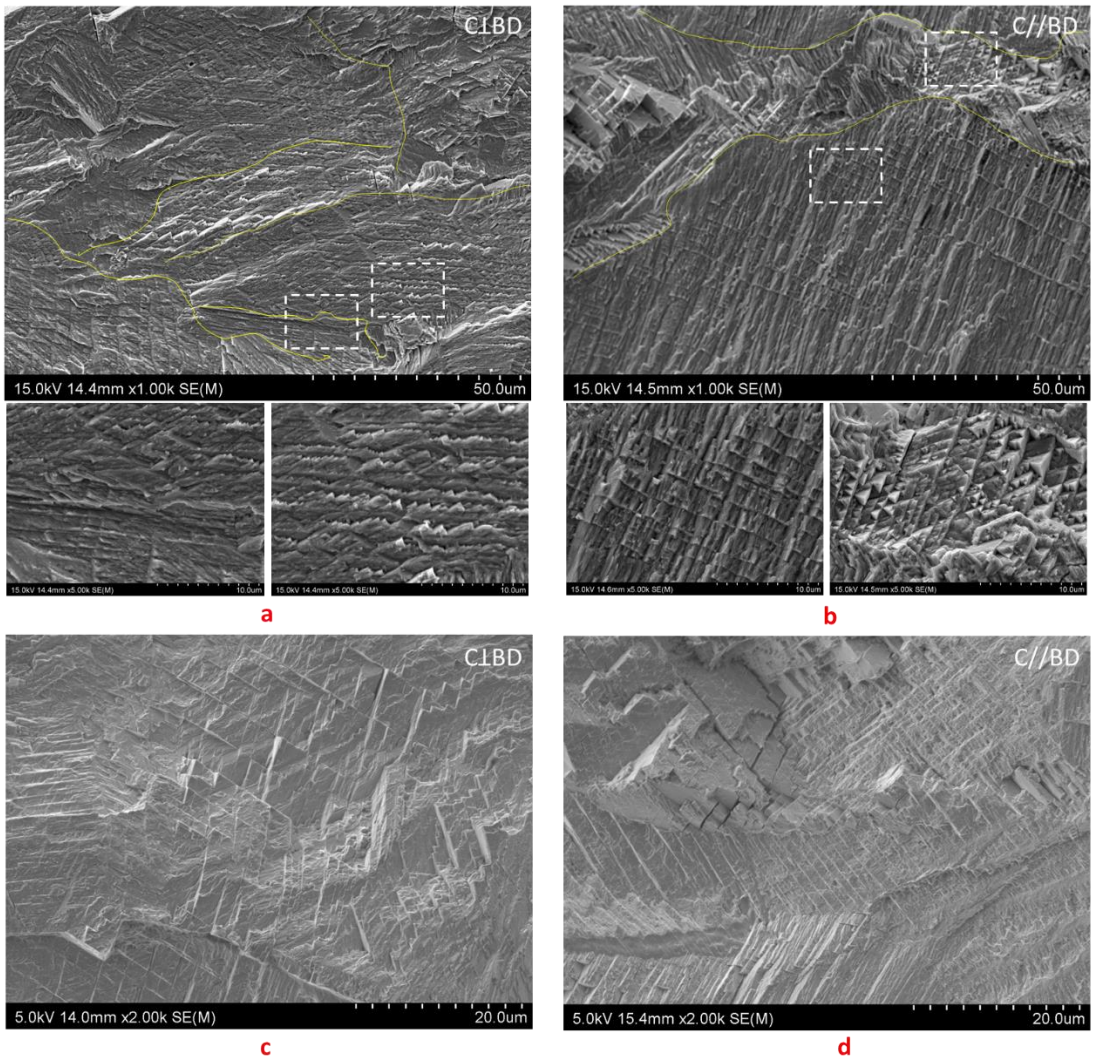

Figure 98 SEM images of the fractured surface for the 320 W CT samples, a) near threshold region for C⊥BD sample, b) near threshold region for C//BD sample, c) Paris region for C⊥BD sample, and d) Paris region for C//BD sample. The yellow line in (a) and (b) indicate a change in the faceted structure.

Another important factor that may affect the crack growth path is the so-called "strain-induced-martensite-transformation" (SMIT) phenomenon that transform the fcc α-Co phase into a more

brittle hcp ε-Co phase under high strain magnitude. As mentioned in Chapter 1, under high stress/strain condition (tensile deformation), Lee et al. [76] shows that SMIT may happened but Ueki et al. shows that the α-Co phase did not transformed into ε-Co phase. To ascertain whether the transformation may have taken place in this study, TEM diffraction analysis has been conducted in the material within 5 μm radius from the crack tip (well within the plastic region), as has been described in the experimental design and procedure, Chapter 2, section 2.5. The TEM bright-field image in Figure 99 shows a banded structure that could be associated to a dual fcc-hcp phase structure as suggested by Murr [142]. Numerous locations have been analysed on the selected area and the electron diffraction patterns show a [001] surface orientation at the three locations in the TEM image. There is no evidence of hcp phase presence near the plastic region, suggesting that there has not been a deformation assisted by the fcc→hcp transformation.

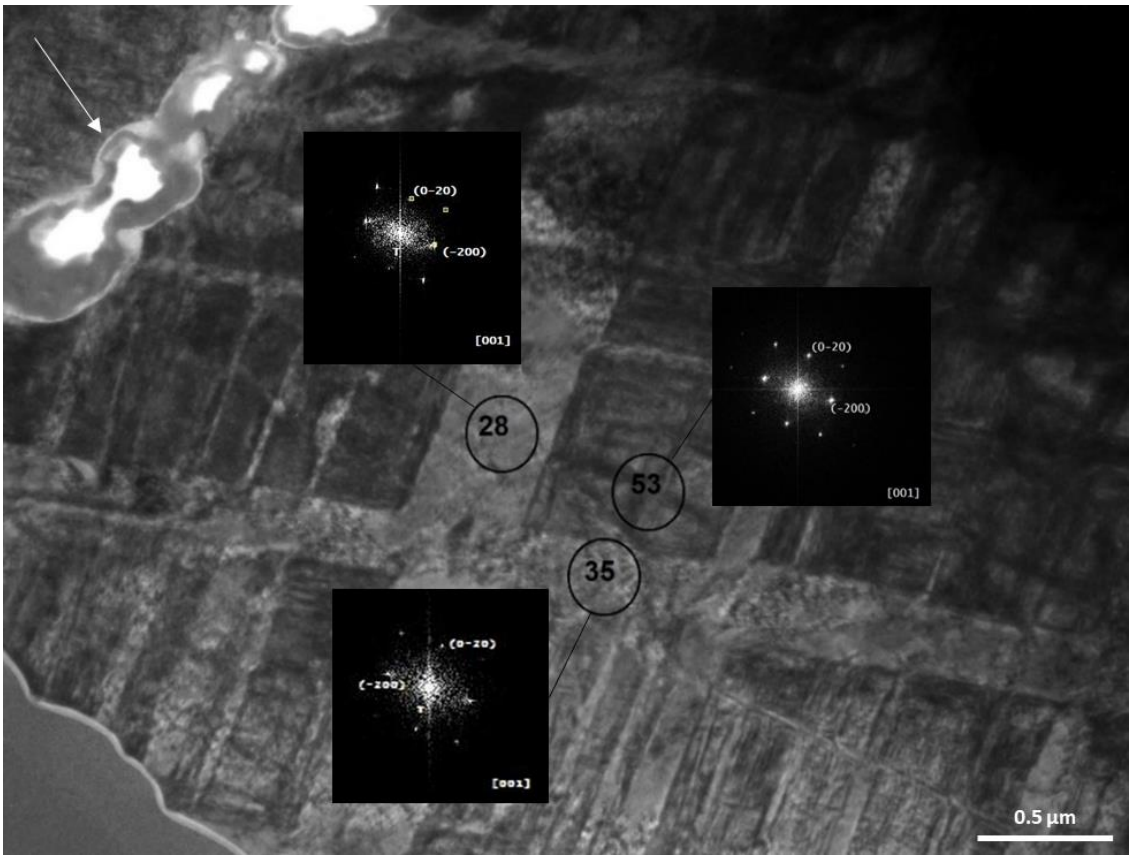

Figure 99 TEM bright-field image near the crack tip of an interrupted FCGR test sample. Elected area diffraction patterns corresponding to the spots are marked as point 28, 53 and 35, indicating FCC crystal structure. The crack is growing in a direction normal to viewing plane and the arrow at the top left corner of the image indicates a scratched surface at which the crack propagation is interrupted (crack tip).

4.4 The crack growth mechanism

The SEM micrographs in Figure 100 are shown to provide a clearer observation on how the crack has propagated through the grains of the cellular structure of the material. Both images were taken at high magnifications than those in Figure 96 and Figure 97, representing the C⊥BD and C//BD samples, respectively. As has been characterised in detail by Chen et al. [14] and Darvish et al. [143], the grain growth during SLM process is in cellular mode, with each grain (that consists many cells) grow epitaxially from the meltpool boundary to either the surface, or to where the grain is outgrown by another grain. In addition, a grain (that consist of many cells) could grow epitaxially in either the same direction or with a change of 90° across meltpool boundary, depending on the direction of temperature gradient.

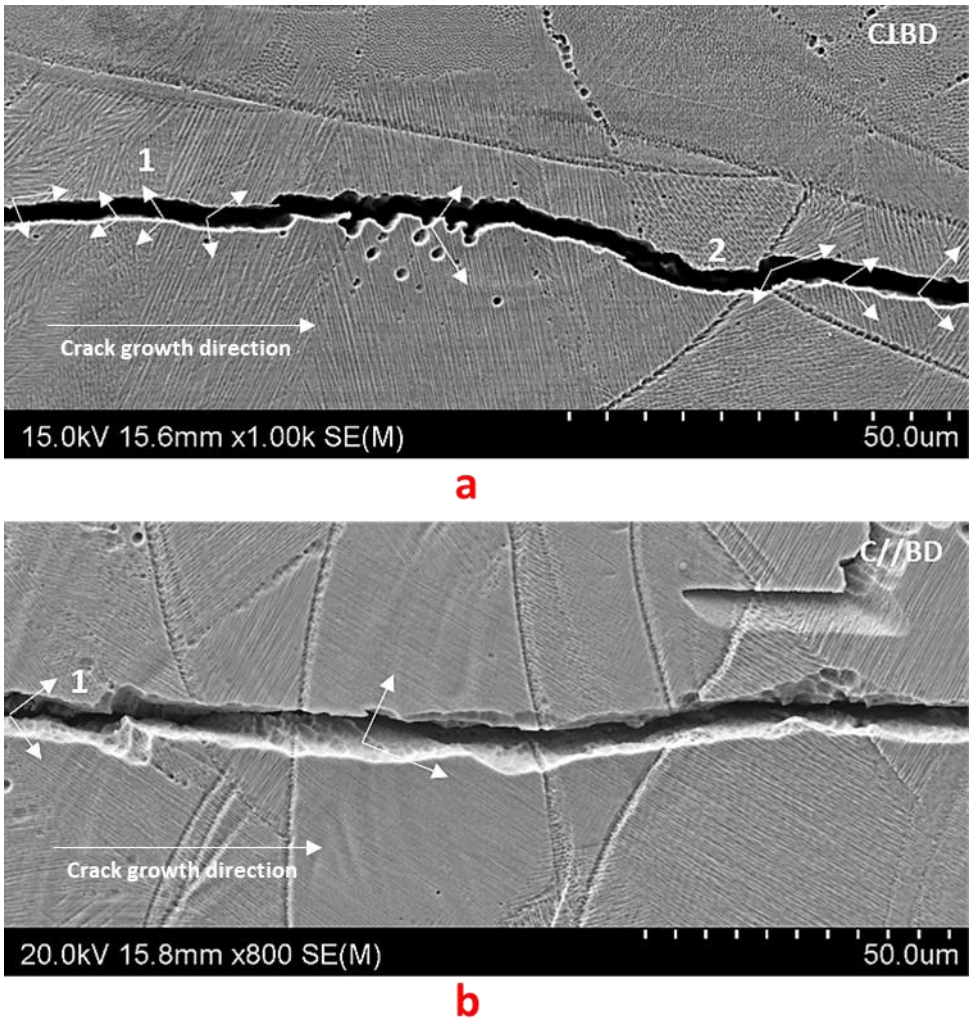

Figure 100 SEM micrograph taken along the crack path of the 320 W sample a) C⊥BD and b) C//BD. Each pairs of arrows point onto the same grain after fracture. "1" denotes an area where the cells growth direction is normal (into or protruding out) to the viewing plane, while "2" denotes an intergranular fracture behaviour.

Figure 100a represents the C⊥BD sample, where the crack propagates through many (9) grains of different sizes (as appeared in the image plane and EBSD analysis) within the span of the SEM micrograph, which is ≈ 120 µm. The grain marked as "1" is a situation where that the cells have grown with a growth direction close to the direction normal to the image plane (into or protruding out of the page). Thus, whether the crack has propagated through the cells (transcellular) or between the cells (intercellular) cannot be made certain. For the location marked as "2", the crack appears to briefly deviate along the grain boundary (intergranularly). For the rest of the grains (7), and thus most grains, the crack has propagated across the grains/cells (transgranularly and trancellularly).

Figure 100b represents the micrograph of the crack in the C//BD sample where the crack is quite straight and almost normal to the loading direction. Similar to the C⊥BD sample, the crack in C//BD sample has almost entirely propagated in a transgranular manner. Although a crack in a C//BD sample has a higher chance of encountering a low angle boundary that may cause intergranular cracking, majority of the crack growth are still transgranular. In this micrograph, the crack has fully propagated transgranularly and transcellularly, except for the observation uncertainty in the small section marked as "1", where the cells have grown close to the direction normal to the image plane.

One clear distinctive attribute between the crack growth path in C⊥BD sample and the C//BD sample is the number of grains per unit crack length. Figure 100b shows that the crack in C//BD samples has propagated through only one single grain from where it is marked "1", to beyond the right edge of the micrograph. This means that the crack has propagated through at least 100 µm in the same grain. In contrast, Figure 100a shows that the crack in C⊥BD sample has propagated through only 15 µm (in average) of the same grain (120 µm / 8 grains = 15 µm/grain).

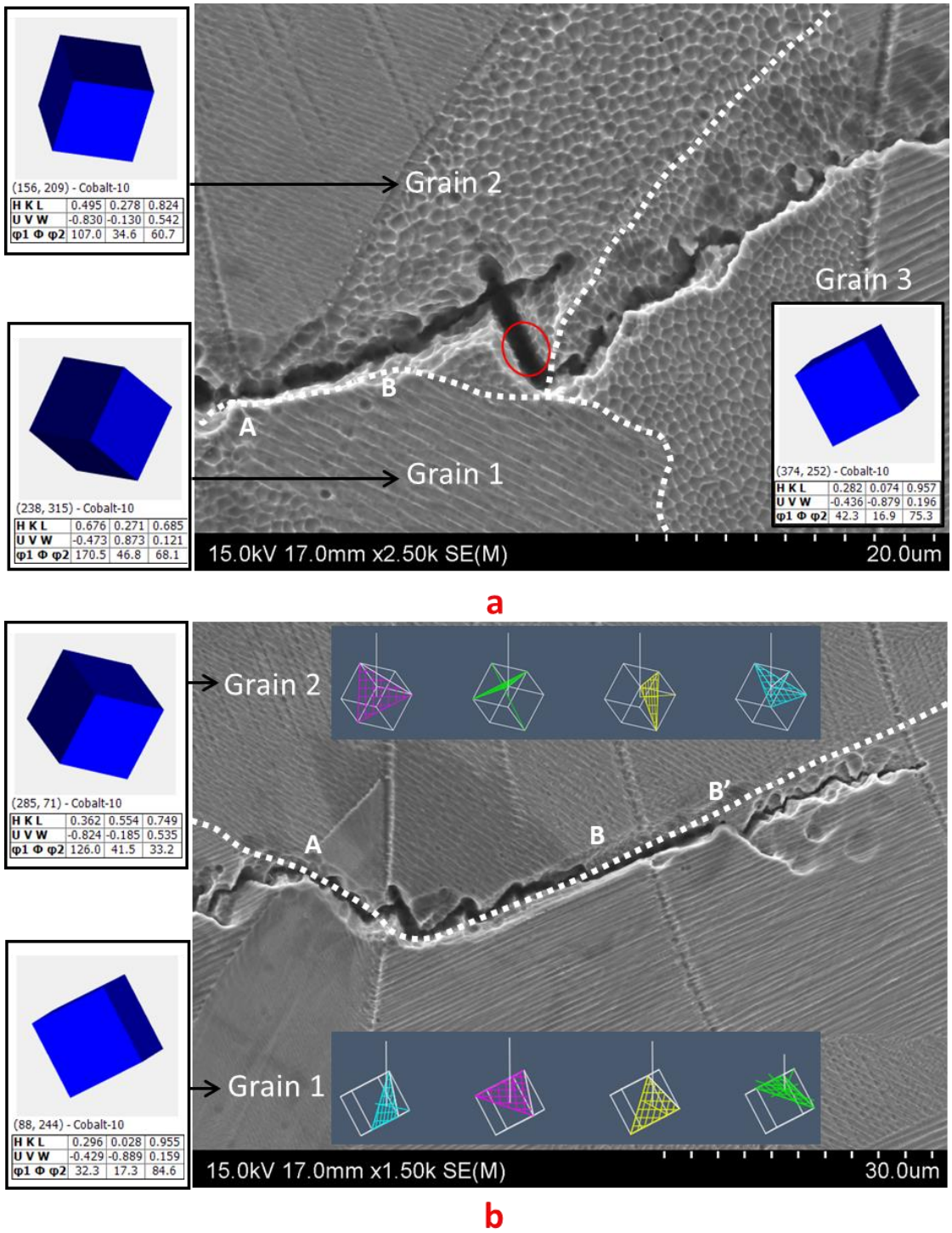

Figure 101 SEM micrograph of crack path in 320W C//BD sample. Dotted line indicates the grain boundary. The crystal orientation for each grain and four of the non-parallel (111) planes in (b) are illustrated by the "3D" cubes. Each grains are marked to ease the discussion.

As has been shown previously, the crack growth path in the C//BD sample is quite irregular as compared to the C⊥BD sample. Figure 101a shows an example of a crack path for the C//BD sample in a relatively high magnification. Only small portion of the crack between point "A" and "B" appears to be intergranular, where it briefly travel through the grain boundaries, while the rest is transgranular. The red circle highlights an area where the cells appear to have cracked

open and separated into two halves, again confirming the transcellular fracture. Furthermore, the crack path seems to avoid propagating into Grain 1, and as it enters into Grain 3 the angle (into the page) of the crack appears different compared to when it was in Grain 2.

Another example of irregular crack path in the C//BD sample is shown in Figure 101b, where a section of the crack, including the crack tip can be observed. While the crack path from "A" to "B" appears to travel along the grain boundary, a close observation shows that the crack is actually travelling inside Grain 2. Therefore, the zigzag pathway between "A" and "B" is likely to be influenced by the $\{111\}_{fcc}$ planes in Grain 2. The section between "B" to " B' " clearly indicate that the crack follows the grain boundary, but after point " B' ", the crack path has departed the grain boundary and propagated inside Grain 1. As the grain boundary is in an angle (27º) to the BD (in this particular local area of the C//BD sample) the crack enters into Grain 1 after point "B'" to follow the maximum tensile plane. Again, the zigzag pattern and angle (into the page) of the crack appears different as it enters into Grain 1 (from Grain 2) due to the different $\{111\}_{fcc}$ planes orientation.

The evidence presented above on the crack growth relation to BD, grains and cell orientations can be further discussed with the aid of a schematic illustration in Figure 102. The illustration of meltpool boundaries, cells and grains has been based on the characterisation of cell/grain growth for the same alloy by Chen et. al [14] and Darvish et. al [143], as well as other alloys that was well studied by Pham et al. [144]. Two main growth features have been identified in these studies and are illustrated in Figure 102. First, an individual grain (that contains many cells) can often grow across several layers with the growth direction in a low-mid angle to BD. Second, cell growth direction can continue or change direction by 90º as it crosses the meltpool boundary. The most important factor that affects the crack pathway is the difference in number of grains that a crack needs to pass through, here referred as the "grain size". As illustrated in Figure 102, because of the BD dependent columnar grain orientation, the number of grains per unit length in the direction normal to BD is significantly higher than parallel to BD. In other word, the C⊥BD have smaller "grain size" compared to C//BD. Measurement of the average "grain size",

calculated by counting the number of grain boundary encountered by a straight line across the 320C⊥BD and 320C//BD samples is 24.0 μm and 45.9 μm respectively.

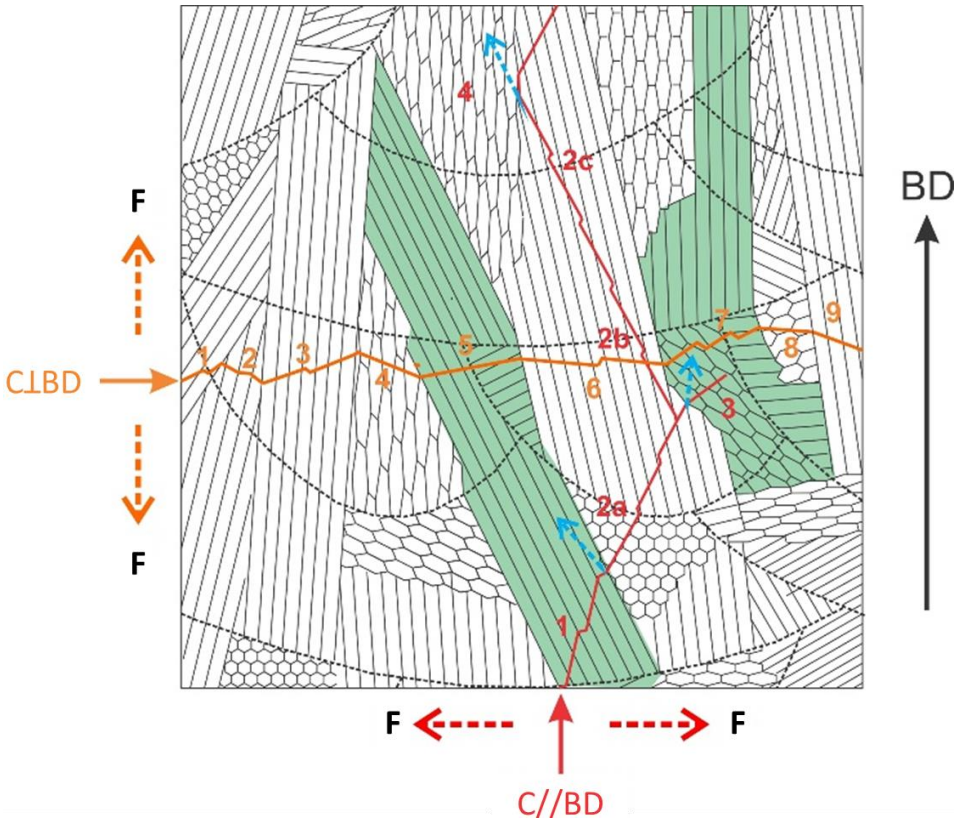

Figure 102 Illustration of C⊥BD and C//BD cracking pathway through grains with multiple cells formed during SLM process. The two green grains (grain 1 and 3) are coloured to aid the discussion.

An example of a C⊥BD crack and a C//BD crack are also drawn in Figure 102 to aid the discussion. As has been clearly shown earlier, both C⊥BD and C//BD cracks are predominantly transgranular, with the possibility of propagating along the grain boundaries, although rare. The transgranular fracture is also consistent with the faceted fracture surfaces shown in Figure 98. This feature is also represented in the two cracks drawn in Figure 102. The C⊥BD crack has propagated transgranularly across 9 grains in the presented width of the area. When a crack has propagated through a grain and reaches the grain boundary, the crack plane changes orientation so that it can maintain to propagate in a $(111)_{fcc}$ plane that is most favourable for crack propagation. As schematically illustrated in Figure 102, the crack plane has changed its orientation 9 times for the C⊥BD crack. Geometrically, the propagation of a C⊥BD crack can be viewed as a “short distance” crack, propagating across the width (shorter axis) of the columnar

grain and then change its propagation direction as it enters the next grain. A short distance or a short crack segment may be viewed as 10 – 30 μm, as indicative in Figure 100a.

A C//BD crack differs to a C⊥BD crack significantly in crack propagation length within a grain. The C//BD crack drawn in Figure 102 schematically represents a crack having propagated within a grain for a "long distance" and having branched occasionally as shown in Figure 97. Since columnar grains can grow through several layers in an angle to BD, a crack can also propagate within a grain across several layers. As illustrated in Figure 102, the C//BD crack has propagated into the area starting in Grain 1. When the crack reaches the Grain 1/2 boundary (the boundary between Grain A and Grain B is termed Grain A/B boundary from here on), the crack can propagate in two possible ways. The first possibility (possibility 1) is the change of the crack plane to another $\{111\}_{fcc}$ plane within Grain 1, as indicated by the blue arrow, and the second being propagating into Grain 2. For a C⊥BD crack as illustrated in Figure 102, there should be no condition for a crack to propagate into another orientation in the same grain to continue the propagation as it reaches the grain boundary.

Returning to the C//BD crack reaching the Grain 1/2 boundary, possibility 1 would mean changing propagation direction into Grain 1 and continue a long crack growth in Grain 1. If it is assumed that propagating into Grain 2 is more favourable, then the crack will continue to propagate to the Grain 2/3 boundary. The crack that grew into Grain 3 has been assumed to be having a large angle to BD and thus the continuation of crack propagation in Grain 3 is increasingly difficult and will stop. This represents the branched crack marked as C1 in Figure 97b. Note that it is also possible for the grain boundary to initiate crack branching if it is orientated at a low angle in reference to the BD, as shown in the branched crack marked as C2 in Figure 97b.

If the crack propagates in a small angle to BD into Grain 3, as pointed by the blue arrow, the crack in Grain 3 will propagate a long distance upward within that grain. Now, assuming that the

crack is more favourable to propagate by changing the direction and to continue in Grain 2, the crack will propagate along the grain and across two meltpool boundaries to reach Grain 2/4 boundary. Then, the crack will again have two possible ways to continue propagating, as previously explained, eventually resulting in a reasonably "long distance" crack within a grain. Therefore, as consistent with observation, the C//BD crack is highly probable to propagate at a "long distance" within a grain across several meltpool layers. A "long distance" crack or a long crack segment may well be over 3 – 4 layers and thus over 100μm.

The discussion above, which was based on the fractographic observations, has aimed to clarify the geometrical features of the cracks within the grain distribution of the C⊥BD and C//BD samples. On average, a transgranular C⊥BD crack travels "short distance" (10 – 30μm) before finding another favourable orientation of crack plane in the next grain. In contrast, a C//BD crack can propagate in a relatively "long distance" (>100μm) within a columnar grain and the crack can branch more easily. The higher chance of crack branching in the C//BD sample compared to the C⊥BD sample causes higher crack retardation effect and thus reduces the crack growth rate at low stress intensity factor (SIF), therefore increasing its ΔK_{th} value. Also, because the C⊥BD crack appears smoother while the C//BD crack has higher zigzagging amplitude, the roughness induced crack closure (RICC) can be a factor in increasing the ΔK_{th} value of the C//BD sample due to its higher fractured surface roughness, as proposed by Lee et al. [92].

4.5 Suggestion on BD for an SLM hip-stem-implant

This section aims to study the effect of BD-dependent FCGR parameters on an arbitrary biomedical prothesis implant (SLM Co-Cr-Mo hip-stem-implant) based on linear elastic fracture mechanics (LEFM) calculation. In addition, to compare the FCGR performance between SLM and cast hip-stem-implant, LEFM calculation for cast Co-Cr-Mo hip-stem-implant based on the FCGR parameters reported by Okazaki [94] is also included. This analysis will utilise the FCGR parameters measured in this study and a case study on a premature fractured hip-stem-implant reported by Bonnheim et al. [108] shown in Figure 44, Chapter 2.

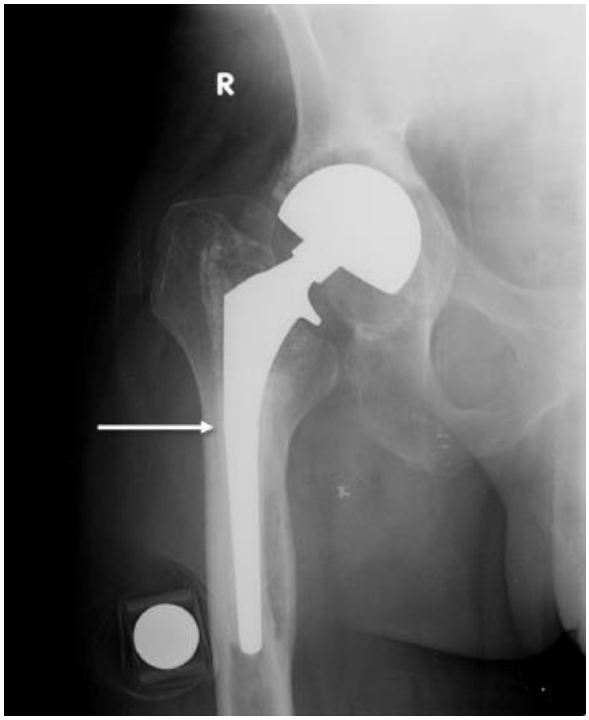

Figure 103 Radiograph of the cast Co-Cr-Mo hip-stem-implant. White arrow points to the location of fracture [108].

The hip-stem-implant in discussion is a cast Co-Cr-Mo Omnifit® Plus stem size #6, coupled with a skirted formal head and a UHR Universal Head. The implant failure is reported to be caused by fatigue fracture at approximately mid-section of the stem as shown in Figure 103. The ultimate tensile strength (UTS) of a femur bone is reported to be S_T = 135 -150 MPa [145], depending on gender, weight, age, and height. Therefore, for the purpose of this analysis, the nominal fatigue tensile stress is assumed to be constant at 33% of the S_T, which is 0 – 50 MPa.

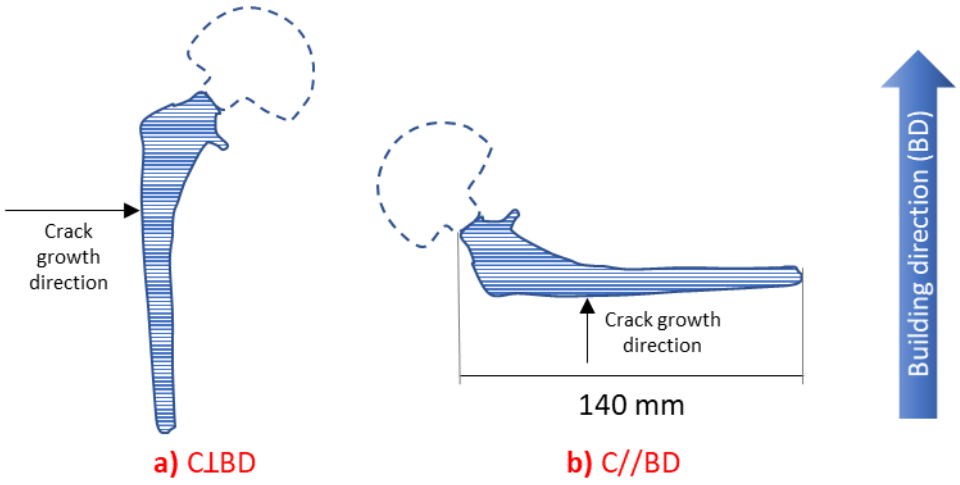

Figure 104 Illustration of SLM Co-Cr-Mo hip-stem-implant a) crack growth perpendicular to BD, C⊥BD, b) crack growth parallel to BD, C//BD.

The SLM building conditions of the two C⊥BD and C//BD CT samples discussed previously in this Chapter can be represented by the two building orientations of SLM ship-stem-implant shown in Figure 104. The threshold value of the 320C⊥BD and 320C//BD samples (5.2 MPa$\sqrt{m}$ and 6.7 MPa$\sqrt{m}$, respectively) theoretically establish the minimum SIF value at which there is no crack growth. The FCGR graph produced by Okazaki [94] on Cast Co-Cr-Mo-Ni-Fe (ΔK_{th} = 5.0 MPa$\sqrt{m}$) will be used to compare the differences between SLM and cast Co-Cr-Mo hip-stem-implant.

To determine the minimum size of defect (crack size) allowed for zero crack growth, the role of "short cracks" (also known as small cracks) need to be considered. Small size cracks (relative to the local plasticity in front of the crack tip) can still propagate at a rate of da/dN ≈ 10^{-9} – 10^{-10} mm/cycle, even though the SIF magnitude is below the threshold value. The most popular FCGR model that describes the "short cracks" behaviour is the crack size constant, a_0, introduced by Kitagawa-Takashi diagram [146]. The a_0 value is defined by the ratio of threshold value to fatigue endurance limit, at which Radaj [147] proposed as a fictitious intrinsic crack length that is incapable of further growth. The equation of a_0 can be written as follows:

$$a_0 = \frac{1}{\pi}\left(\frac{\Delta K_{th}}{\sigma_{ED}}\right)^2 \quad (8)$$

Where, σ_{ED} represent the fatigue endurance limit.

As shown in equation (8), the a_0 value can only be determined if the fatigue endurance limit is known (not fatigue strength, which is normally defined as the stress value at 1 – 10M cycles on a S-N curve for HCF test [148, 149]). The only available fatigue endurance limit for SLM Co-Cr-Mo was reported by Hann et al. [32] which is σ_{ED} ≈ 35 MPa. The reported fatigue endurance value is extremely low due the high amount of LOF as they did not optimise the SLM parameters (laser power used was less than 200 W). As shown earlier in Figure 9, the non-standard HCF test conducted by Kajima et al. [39] shows that SLM Co-Cr can have a higher fatigue life compared to cast CoCr. Therefore, the σ_{ED} value for as-cast Co-Cr (300 MPa as reported by Hann et al.

[32]) has become the basis of a conservative estimate for SLM Co-Cr alloy. Based on the assumption that the endurance limit for an optimised SLM CoCr is 300 MPa, the a_0 value for C⊥BD, C//BD and Cast are 95 µm, 158 µm and 88 µm, respectively. These values are useful to set the benchmark for maximum allowable defect size (crack size), in the case where zero crack growth is required.

Since the purpose of damage-tolerant life prediction calculation of hip-stem-implant in this study is to compare between C⊥BD, C//BD and Cast, the analysis will only be based on the LEFM calculation of a long crack behaviour. It is also important to note that LEFM was originally developed for elastic condition, and therefore, as parts of its limitation, the elastic assumptions are violated when 1) the operating stress magnitude is high, resulted in significant plasticity or 2) the crack size is small in comparison to the plastic zone in front of the crack tip. Based on Irwin's model shown in Table 3 (Chapter 1), Figure 105 below shows the size of the plastic zone in front of the crack tip across a range of ΔK. The size of the plastic zone at low ΔK values is well below the a_0 values, suggesting that LEFM calculation are valid across Region 1, as long as the crack size/flaw size is not small (or smaller) compared to the corresponding plastic zone length in Figure 105.

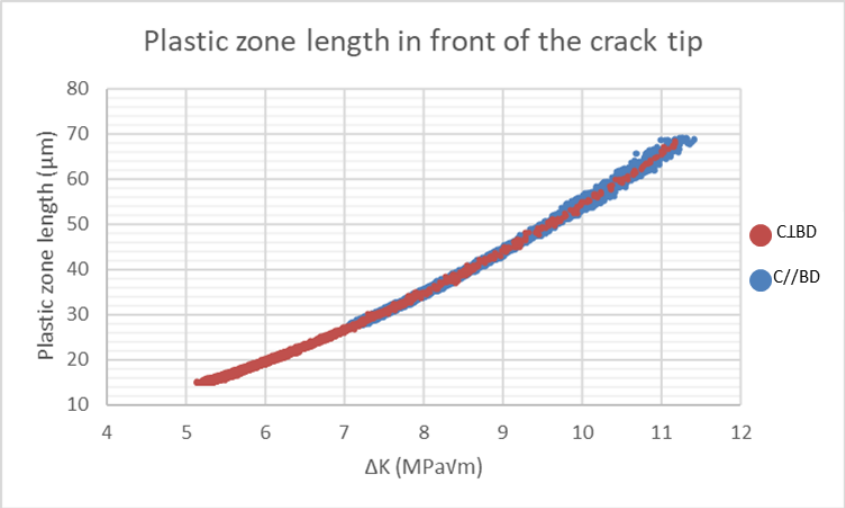

Figure 105 Graph of plastic zone length in front of the crack tip vs ΔK. The plastic zone length was calculated based on the data collected from the FCGR K-decreasing test for 320C⊥BD and 320C//BD samples.

Based on the FCGR parameters and the Donahue Law described in section 1.1.3.3, Chapter 1, the equation to model the behaviour of crack growth for the three manufacturing conditions (C⊥BD, C//BD and Cast) can be represented as follows:

C⊥BD : $da/dN = 4.2 \times 10^{-11} (\Delta K - 5.2)^{2.8}$

C//BD : $da/dN = 1.5 \times 10^{-11} (\Delta K - 6.7)^{2.7}$

Cast : $da/dN = 1.5 \times 10^{-12} (\Delta K - 5.0)^{3.2}$

Donahue Law is being used in this analysis to account for the different threshold value for each of the manufacturing conditions. The integration of the above equation is complex since the curvature of the FCGR graph in Region 1 is included, unlike the integration of a straight line for Paris Law which neglect the effect of ΔK_{th}. To illustrate the difference between Paris law and Donahue law, Figure 106 shows the representation of FCGR curve for both of the equations.

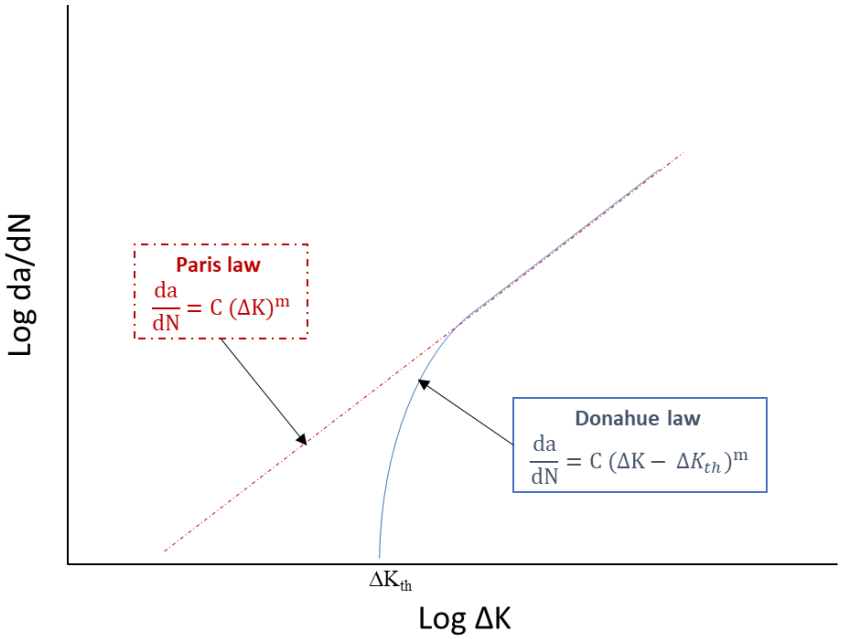

Figure 106 An illustration on the representation of FCGR curve for Donahue law and Paris law. Paris law assumed that crack growth (in log) is linear across all ΔK values (in log), while Donahue law acknowledge the curvature in Region 1 due to the ΔK_{th} effect, emulating a natural logarithm (ln) graph.

The initial flaw size, a_i is chosen to be 0.5 mm, and the final crack size is taken as the diameter of the hip-stem-implant, which is 12 mm. This because at S = 50 MPa and K_{1C} = 60 MPa, the

critical crack size is far greater than the diameter of the implant at the fractured area, which is a_c = 353 mm (as calculated based on the equation in section 1.1.3.2.1). Due to the complexity of the mathematical integration for Donahue's Law, Matlab software is used to compute the cycle life of each samples. As shown in Figure 107, the number of cycle calculated based on the equation above is 4.2 x 10^4, 6.4 x 10^5 and 7.1 x 10^4 for C⊥BD, C//BD and Cast, respectively. Interestingly, the result is similar to the non-standard HCF test (cycle to failure of dental clasps) reported by Kajima et al. [39], shown in Figure 9, Chapter 1. The fatigue life based on LEFM calculation is in the order of C//BD >> Cast > C⊥BD. This further support the importance of BD parameters in SLM production. C//BD shows better FCGR resistance and better fatigue life compared to C⊥BD and cast CoCr alloy. Therefore, the SLM building parameters for C//BD is recommended for SLM CoCr hip-stem-implant.

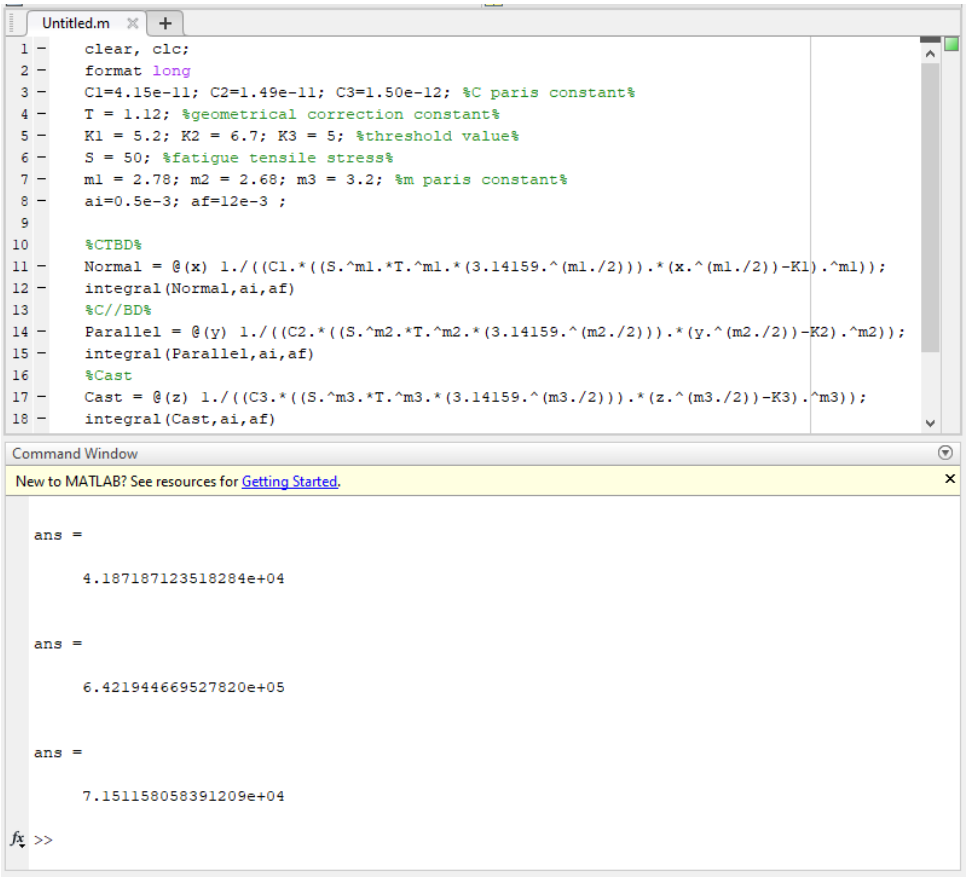

Figure 107 Matlab editor codes used to calculate definite integral of Donahue's law based on the FCGR parameters for three manufacturing conditions. The "Normal", "Parallel" and "Cast" functions represent the C⊥BD, C//BD and as Cast FCGR Donahue law equations.

4.6 Summary

Fatigue crack growth rate (FCGR) resistance of Co-Cr-Mo alloy processed by selective laser melting (SLM) is known to be dependent on the crack growth direction in relation to the build direction (BD). This study highlights, the threshold stress intensity factor, ΔK_{th} is higher for C//BD sample compared to C⊥BD sample, while the Paris "C" and "m" constants are slightly higher for C⊥BD compared to C//BD. The effects of the lack of fusion (LOF) at the amount of less than 1% area fraction on the FCGR parameters (ΔK_{th} and the Paris constants "C" and "m") have been found to be insignificant.

Based on the two sample orientations tested (C⊥BD and C//BD), it has been identified that cracks have not preferentially propagate along the grain and cell boundaries, i.e. it have dominantly propagated in a transgranular and transcellular manner. Consistent with the BD dependent columnar grains orientation in SLM materials, and the dominant transgranular fracture during FCG, a segment of a C//BD crack is generally longer as compared to the C⊥BD crack. Because of this the zigzagged crack path in C//BD has higher amplitude and wider distance, thus creating a more rougher fracture surface.

In addition, crack branching is more prevalent to occur in C//BD sample as compared to C⊥BD sample. Crack branching in C//BD sample mainly occurs due to 1) the orientation of $\{111\}_{fcc}$ planes that sometimes force the main crack to branch in an unfavourable direction, 2) the encountering of crack with low angle grain boundary, since crack sometimes propagate intergranularly. The higher chance of crack branching in the C//BD sample causes higher crack retardation effect and thus reducing the crack growth rate. The roughness induced crack closure (RICC) can also be a factor in increasing the ΔK_{th} value for the C//BD sample due to its higher fractured surface roughness.

Based on Kitagawa-Takashi diagram, the a_0 (maximum allowable LOF/flaw size, at which crack will not propagate) is estimated to be 95 µm, 158 µm and 88 µm, for C⊥BD, C//BD and Cast,

respectively. This gives an indication that the as-SLM material has a higher tolerant to micro defects compared to cast. Based on the LEFM calculation using Donahue's Law, the fatigue life of a hip-stem-implant is in the order of C//BD >> Cast > C⊥BD, highlighting the importance of BD parameters in SLM production. The selection of BD could either make as-SLM material tougher or weaker compared to cast. Since C//BD has the highest life expectancy, it is recommended that the BD for SLM CoCr hip-stem-implant is parallel to the crack growth direction (or perpendicular to the loading direction).

For future work, different BD angles in relation to the crack path direction should be tested to further investigate the relationship between BD and FCGR parameters of SLM alloys. For a start, the next Chapter that study the FCGR behaviour of SLM Inconel alloys will include CT sample of C45BD (crack growth direction 45º to BD).

5 Fatigue Crack Growth of SLM Inconel 738 and Inconel 718

In this chapter, the measurement of FCGR for SLM Inconel 738 samples based on three different build directions (BD) and two selected laser power is presented and compared with other SLM Inconel alloys. Detailed fractographic analysis on the fractured CT sample and the relationship between BD and ΔK_{th} is demonstrated. EBSD and EDS analysis are conducted to identify the preferred crack growth pathway and its influence on the mechanisms of FCG resistance is addressed. In addition, the measurement of FCGR for SLM Inconel 718 samples is presented, followed by the discussion on its crack pathway based on fractographic analysis and EBSD results. Lastly, the effect of laser power is being discussed based on the effect of key-hole pores on the FCGR behaviour.

5.1 The FCGR graph of SLM Inconel 738 alloy

5.1.1 Effect of build direction (BD) and laser power (P)

The FCGR graph of SLM Inconel 738 for all six conditions (270C⊥BD, 270C//BD, 270C45BD, 320C⊥BD, 320C//BD and 320C45BD) is presented in Figure 108. A clear difference in the crack growth rate between the three different BD samples can be observed, especially near the threshold region (Region 1: da/dN < 1 x 10^{-9} m/cycle). The C⊥BD sample shows the fastest crack growth rate, followed by the C//BD sample, and then the C45BD sample. This translates to a different FCGR threshold values for the three samples, where the C⊥BD and C//BD samples show a ΔK_{th} values of ≈ 6.0 and 6.4 MPa$\sqrt{m}$ respectively, while the C45BD samples shows the highest ΔK_{th} values of ≈ 9.1 MPa$\sqrt{m}$. The three graphs start to slowly merge as the SIF is increased, until all three reached a common value of $\Delta K \approx 65$ MPa$\sqrt{m}$, where all samples start to fracture in Region 3 (da/dN > 1 x 10^{-5} m/cycle).

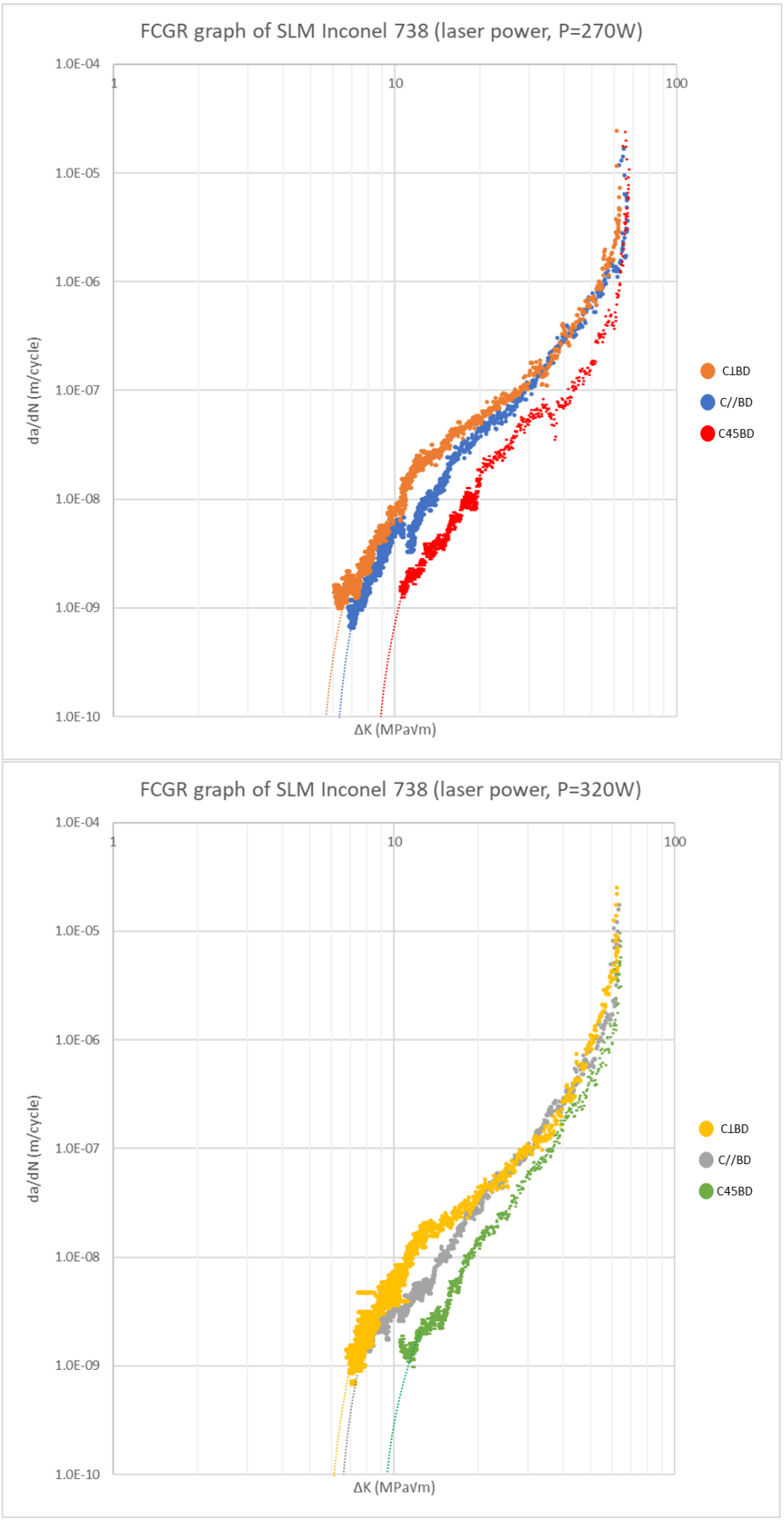

Figure 108 FCGR graph of SLM Inconel 738. Top: SLM laser power setting of P= 270W. Bottom: SLM laser power setting of P = 320 W. The "Top" and "Bottom" graphs contain two FCGR curves of three different build directions, showing that the C⊥BD samples have a highest crack growth rate, followed by C//BD samples and C45BD samples.

The data trends near the threshold region suggest that the ΔK_{th} has almost been reached at da/dN = 1 x 10^{-9} m/cycle. Therefore, the ΔK_{th} values are estimated based on the extrapolation of a best-fit line across the growth rates of 1 – 2 x 10^{-9} until it reaches 10^{-10} m/cycle. All data points collected by the FCGR software (data stored each time the crack size (a) is increased by 20 µm or after every 20, 000 cycles) are plotted in Figure 108 as the scattered data could clearly represent the FCGR curve. In terms of the FCGR behaviour in the Paris region (Region 2: $\Delta K \approx$ 20 – 40 MPa$\sqrt{m}$), the slope of the graph is similar between the C//BD and C45BD samples, while it is less steep for the C⊥BD sample. Yet, the C⊥BD and C//BD samples appear to have slightly higher crack growth rate compared to the C45BD samples. The laser power setting of either 270 W or 320 W showed no significant impact on the FCGR behaviour, as both samples produce similar graph trends as shown in Figure 108.

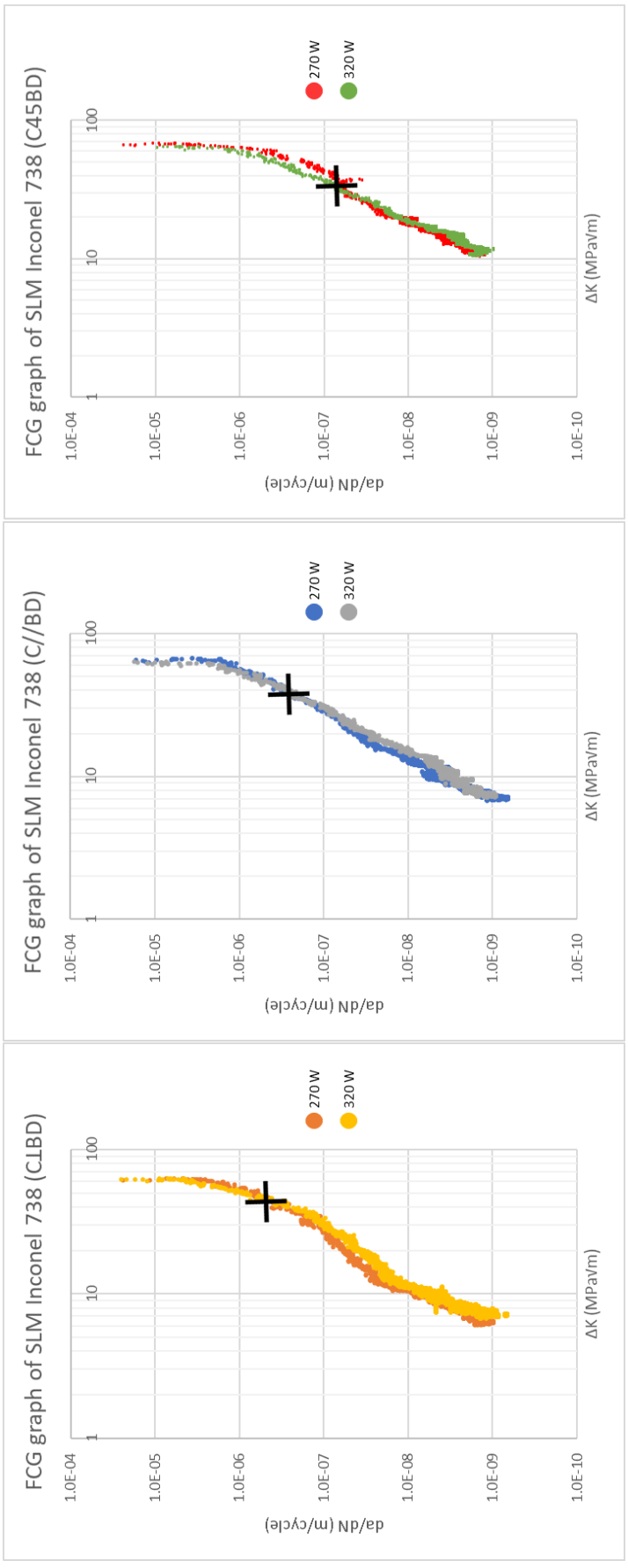

Figure 109 FCGR graph of SLM Inconel 738. Bottom/left: C⊥BD samples. Middle: C//BD samples. Top/right: C45BD samples. Starting from the low da/dN values, the 270 W samples show slightly faster crack growth rate compared to the 320 W samples, however, after the "intersection point" marked as "+", the 370 W samples show faster crack growth rate compared to the 320 W samples.

To illustrate a better FCGR comparison between the 270 W samples and 320 W samples, the FCGR graphs are grouped according to its BD in Figure 109. The graphs in Figure 109 show that the difference in crack growth rate behaviour between the 270 W samples and 320 W samples are small. This means that the difference between their FCGR parameters (which include ΔK_{th} and Paris constants "C" and "m") are also small. In all three BD, the 320 W samples have slightly lower crack growth rates compared to 270 W samples at low ΔK value, which exhibits a slightly higher threshold value for the 320 W samples. However, as the 320 W samples have steeper gradients in the Paris region of the graph as compared to the 270 W samples, the 320 W samples start to show higher da/dN value compared to 270 W samples at the end-tail of the Paris region.

The change which sample having the higher crack growth rate between the 270 W samples and the 320 W samples occurs at ΔK ≈ 40 MPa$\sqrt{m}$, here forth called as the "intersection point". The "intersection point" suggests that the effects of SLM laser power (P) on the FCGR behaviour is dependent on the magnitude of ΔK exerted on the material. As mentioned in Chapter 1, section 1.2.2.1, the laser power (P) subsequently affects the density of keyhole pores (micro pores defect) present in the material. Therefore, the presence of keyhole pore may have only start to influence the crack growth rate at ΔK ≈ 40 MPa$\sqrt{m}$. To address this assumption, Section 5.4 will investigate further on how keyhole pores defects influence the FCGR behaviour of this material. Nonetheless, in terms of FCGR performance, the effect of laser power tested is not as significant as BD, especially in the threshold region.

5.1.2 Comparison with other FCGR graph of SLM Inconel superalloys

Table 9 below summaries the FCGR parameters for all tested SLM Inconel 738 samples, as well as other FCGR results of SLM Inconel superalloys reported in the literature. Note that only FCGR experiment conducted according to ASTM standard are included in Table 9, therefore, the short crack behaviour of SLM Inconel 718 reported by Brynk et al. [115] is not included. It is also important to note that the specimens used to produce the FCGR graphs of SLM Inconel 625 reported by Hu et al. [113] and Poulin et al. [114] went through annealing heat treatment process

of 1100 ºC/1 hr and 870 ºC/1 hr respectively. The post-heat treatment process was performed on the SLM building plate as recommended by the manufacturer, which could affect the presence of residual stress. The effect of residual on the FCGR behaviour of Inconel superalloy has never been studied, but Riemer et al. [98] suggest that residual stress did not significantly affect the FCGR behaviour of SLM 316L stainless steel, while Leuders et al. [150] suggest that residual stress can significantly affect the FCGR behaviour of SLM Ti-6Al-4V. These contrasting results indicate that the effect of residual stress on the FCGR of SLM alloys may differ depending on the materials. Thus, the influence of annealing heat treatment on the FCGR graph of SLM Inconel 625 reported is unknown, as the authors did not conduct a FCGR test on an as-built specimen. Therefore, the comparison is between as-build SLM Inconel 738, as-build SLM Inconel 718 and annealed SLM Inconel 625.

Table 9 A list of FCGR parameters (threshold value, ΔK_{th} and Paris constants, "C" and "m") for SLM Inconel superalloys. Data for the SLM Inconel 738 superalloy is determined in this study, while data for the SLM Inconel 625 and SLM Inconel 718 superalloys are taken from the literature.

Sources and material	Crack growth direction in relation to BD		Region I	Region II	
			ΔK_{th} (MPa$\sqrt{m}$)	C	m
This work					
Inconel 738	P = 320 W	C⊥BD	6.1	5.0×10^{-11}	2.2
		C//BD	6.5	1.0×10^{-12}	3.4
		C45BD	9.2	2.0×10^{-13}	3.5
	P = 270 W	C⊥BD	5.8	9.0×10^{-11}	2.1
		C//BD	6.2	2.0×10^{-12}	3.3
		C45BD	9.0	9.0×10^{-13}	3.2
From literature					
Hu et al., 2019 [113] Inconel 625	C⊥BD		9.1	9.1×10^{-13}	4.2
	C//BD		8.1	8.2×10^{-13}	4.4
Poulin et al., 2018 [114] Inconel 625	C⊥BD		7.5	4.7×10^{-12}	3.0
	C//BD		7.1	3.0×10^{-12}	3.2
	C"45"BD		8.8	2.0×10^{-12}	3.3
	C"FLAT"BD		10.6	2.4×10^{-12}	3.2
Konecna et al., 2016 [116] Inconel 718	C//BD		3.0	4.5×10^{-11}	2.3

Generally, the SLM Inconel 738 superalloy have a better FCGR resistance compared to the SLM Inconel 625 superalloy. In terms of the ΔK_{th} value, the difference between the C⊥BD sample and the C//BD sample (ΔK_{th} for C⊥BD - ΔK_{th} for C//BD) for Inconel 738 is –0.4 MPa$\sqrt{m}$, while for Inconel 625, the value is 1.0 MPa$\sqrt{m}$ and 0.4 MPa$\sqrt{m}$ based on the result reported by Hu et al. and Poulin et al., respectively. A more significantly higher ΔK_{th} value is reported for the C45BD and C"45/FLAT"BD samples for Inconel 738 and Inconel 625 respectively. This signifies that the BD orientation of 45º has significantly increase the FCGR resistance of both Inconel 738 and Inconel 625 alloys. As mentioned in Chapter 2, Poulin et al. [114] suggest that the C"45"BD

sample has a higher ΔK_{th} value because the crack passes though fewer grain boundary (bigger "grain size") compared to the C⊥BD sample. However, they did not explain the reason why C//BD sample having similar ΔK_{th} value as the C⊥BD sample, despite having bigger "grain size" compared to the C"45"BD sample. However, they did mention that the C"45"BD sample has a rougher fractured surface compared to the C⊥BD and C//BD samples. Hence, this chapter intends to study how the BD orientation influence the FCGR resistance (especially for the 45º orientation) by examining the crack growth pathway across its microstructure.

While the ΔK_{th} value is highly influence by the BD orientation, the effect of BD orientation on FCGR behaviour gradually reduces as the ΔK value is increase. In terms of the Paris region, SLM Inconel 738 have similar growth rate compared to the SLM Inconel 625, with the exception of the C45BD sample (of Inconel 738) that has slightly higher FCGR resistance in the Paris region compared to the other samples. To illustrate, the FCGR curve of SLM Inconel 738 is mapped onto the FCGR graph of SLM Inconel 625 in Figure 110, showing that all samples have similar FCGR curve in the Paris region, except for the C45BD sample that has a lower da/dN. Figure 110 also clearly shows that the BD orientation plays a major role on the FCGR behaviour of both Inconel alloys, especially at the low ΔK value. Therefore, based on the FCGR behaviour at the threshold region and the Paris region as discussed above, the best BD orientation for the SLM Inconel 738 and SLM Inconel 625 alloy is C45BD and C"45/FLAT"BD.

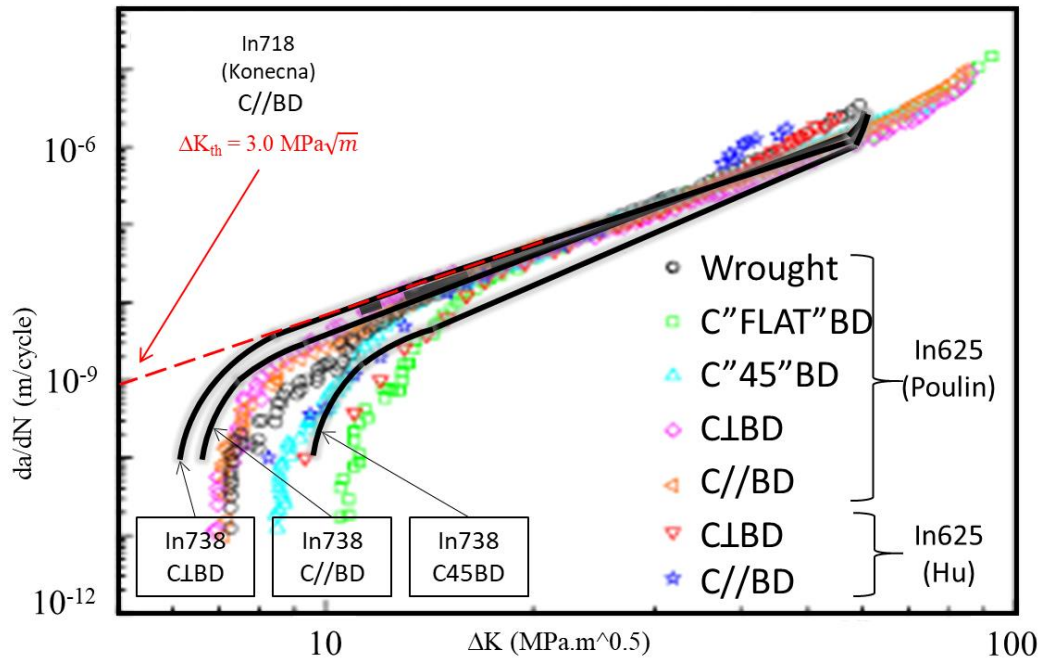

Figure 110 FCGR graph of SLM Inconel superalloys. The graph includes result of SLM Inconel 738 (determined in this study), SLM Inconel 625 (from the literature) and SLM Inconel 718 (from the literature)

On the other hand, a comparison between SLM Inconel 738 and SLM Inconel 718 shows a highly distinct FCGR behaviour, particularly in the threshold region. The threshold value (ΔK_{th}) for SLM Inconel 718 (for C//BD sample) was reported by Konecna et al. [116] to be ΔK_{th} = 3.0 MPa$\sqrt{m}$, which is more comparable to the threshold value of SLM 316L stainless steel [98]. However, its Paris constant value is similar with the C⊥BD sample (of Inconel 738), suggesting that it could have a similar FCGR behaviour with other SLM Inconel alloys at high ΔK values. Nevertheless, as mentioned in Chapter 1, the FCGR graph of SLM Inconel 718 reported by Konecna et al. needs to be further verified as it is very low compared to a typical Inconel superalloy. In addition, the "short crack" behaviour reported by Brynk et al. [115] does not support a possibility of a very low threshold value for SLM Inconel 718 as the threshold value for the short crack experiment lies between $\Delta K_{th} \approx$ 8-10 MPa$\sqrt{m}$. Konecna et al. [116] also claims that they cannot observe any specific microstructure influence on the FCGR behaviour. Therefore, this Chapter will also include a FCGR testing for SLM Inconel 718 (in Section 5.4) with further investigation on its crack growth pathway to identify how its SLM microstructure would influence the movement of a fatigue crack.

5.2 Tortuosity of crack path near the threshold region for SLM Inconel 738 alloy

The fractographic analysis of the fractured CT samples on Inconel 738 was conducted based on the three types of fractured samples mentioned in Chapter 3, Figure 82. One half of the fractured CT samples for each SLM building conditions are shown in Figure 111 below, while the other half of the fractured samples were wire-cut and mounted onto SEM resin to measure its surface roughness based on the fracture profile. Based on the visual observation of samples in Figure 111, the fractured surface appears smooth/straight for the C⊥BD samples, slightly rougher for the C//BD samples and very rough for the C45BD sample. This trend of fractured surface roughness is also accompanied by the increase of ΔK_{th} values across the C⊥BD, C//BD and C45BD samples. In terms of the threshold value, 320 W samples have slightly higher ΔK_{th} values as compared to the 270 W samples, in all three BD orientation. While in terms of the fracture surface roughness, higher magnification image is required to see the difference between them.

Figure 111 Fractured CT sample of SLM Inconel 738. Top: SLM laser power setting P = 320 W, bottom: SLM laser power setting P = 270 W. The threshold values and BD orientations for each sample are indicated below the sample for reference

Figure 112 below shows the SEM images of the fractured profile for all six SLM conditions. Based on visual observation, the roughness of the fractured profile follows the order of: C⊥BD < C//BD << C45BD. The observation of C//BD sample having a rougher fractured profile

compared to the C⊥BD sample is contrary to an FCGR study conducted by Hu et al. [113] on Inconel 625. Hu et al. show that their C⊥BD sample has higher tortuosity compared to the C//BD samples by measuring the distance between the peak and valley of a fracture profile. However, the measurement was based on only one SEM image, covering a distance span of 250 μm. A global crack profile at lower magnification was not provided in their paper. The marked area (white box) in Figure 112 are the locations where crack is growing the at a rate of $da/dN \approx 1 \times 10^{-9}$ m/cycle. These areas represent the fractured surface roughness for the crack growth near the threshold area (located at the tail-end of K-decreasing test). It is crucial to measure the roughness at the area where crack is growing close to the threshold rate, and to have more than one measurement to accurately represent the relationship between the fracture surface roughness and ΔK_{th} value. In addition, Figure 112 also suggests that the 320 W samples have slightly rougher fracture profile as compared to the 270 W samples (comparing between same BD orientation). To verify this observation, the roughness is measured at the marked locations in Figure 112 by using Image J software.

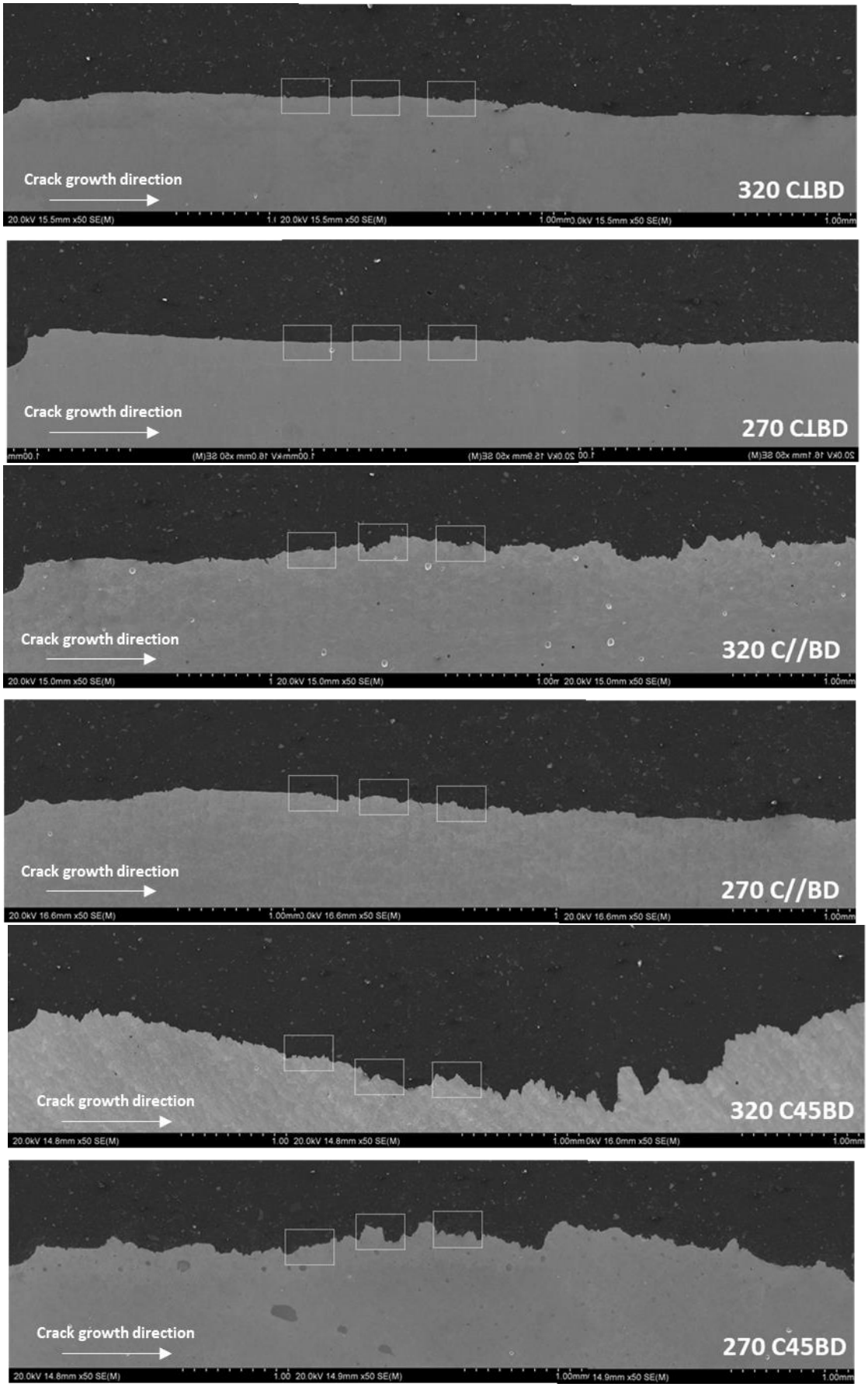

Figure 112 SEM images of fracture profile for SLM Inconel 738. The name of each samples is written on the bottom left corner of each image. The marked areas (white box) are within the threshold region, at which the roughness is measured

Based on the marked area in Figure 112, the fractured surface roughness at the threshold crack growth region is measured by taking the distance between peak-to-trough on the fractured profile (F_{ra}). This measurement method is consistent with the method used by Gray et. al [62] and Hu et al. [113]. Figure 113 shows the measured F_{ra} value for each sample conditions, taken across the threshold crack growth area at three random locations. The average F_{ra} value for each sample condition is calculated and listed as follows:

- Average F_{ra} value for C⊥BD sample:
    - 19.5 µm for 320 W
    - 16.9 µm for 270 W
- Average F_{ra} value for C//BD sample:
    - 38.3 µm for 320 W
    - 35.9 µm for 270 W
- Average F_{ra} value for C45BD sample:
    - 57.3 µm for 320 W
    - 50.4 µm for 270 W

Between the same BD orientations, the average F_{ra} value for the 320 W samples is only slightly higher compared to the 270 W samples. But, between different BD orientations (C⊥BD, C//BD and C45BD), the differences in the average F_{ra} values are more substantial. As shown in Figure 111 and Figure 112, the global roughness of the fractured profile for the C//BD samples appear slightly higher compared to the C⊥BD samples, while the global roughness of the fractured profile for the C45BD samples are distinctly higher. However, the calculated average F_{ra} values shown above (a more localised observation) indicate that the roughness of the fractured profile increases linearly across the C⊥BD samples, followed by the C//BD samples then the C45BD samples. Therefore, the increasing trend of F_{ra} values between the C⊥BD, C//BD and C45BD samples does not match with the non-linear increasing trend of the ΔK_{th} values between the different BD samples.

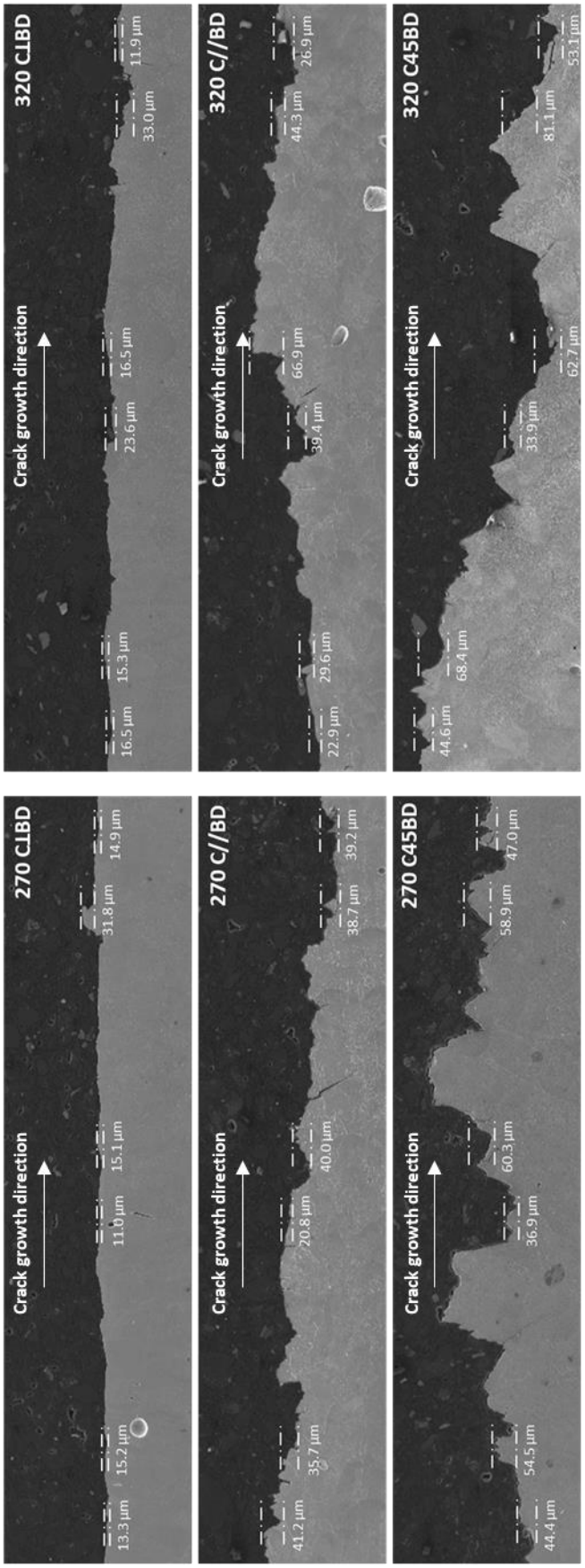

Figure 113 Fractured surface roughness (F_{ra}) measurement at the threshold crack growth area of SLM Inconel 738. Two measurements were taken inside the white box indicated in Figure 112. All sample conditions are indicated on each image.

The graph in Figure 114 below shows the relationship between the fractured surface roughness (F_{ra}) and the ΔK_{th} value at R = 0.1 for SLM Inconel 738, SLM Inconel 625 (by Hu et al. [113]) and AISI 1080 "American Railroads" carbon steel (by Gray et al. [62]). The data on 1080 steel was produced by performing several different post heat treatment conditions, that manipulate its microstructure (grain size, pearlite spacing and pearlite colony size), which subsequently resulted in a different F_{ra} value. Based on Figure 114, all three materials indicate a strong correlation between F_{ra} and ΔK_{th}. However, particularly for the SLM Inconel 738 graph, between the C⊥BD samples and the C//BD samples, even though the F_{ra} value increase by ≈ 20 µm, the ΔK_{th} value remains close. On the other hand, the ΔK_{th} value for the C45BD samples increases significantly compared to the C⊥BD samples and the C//BD samples.

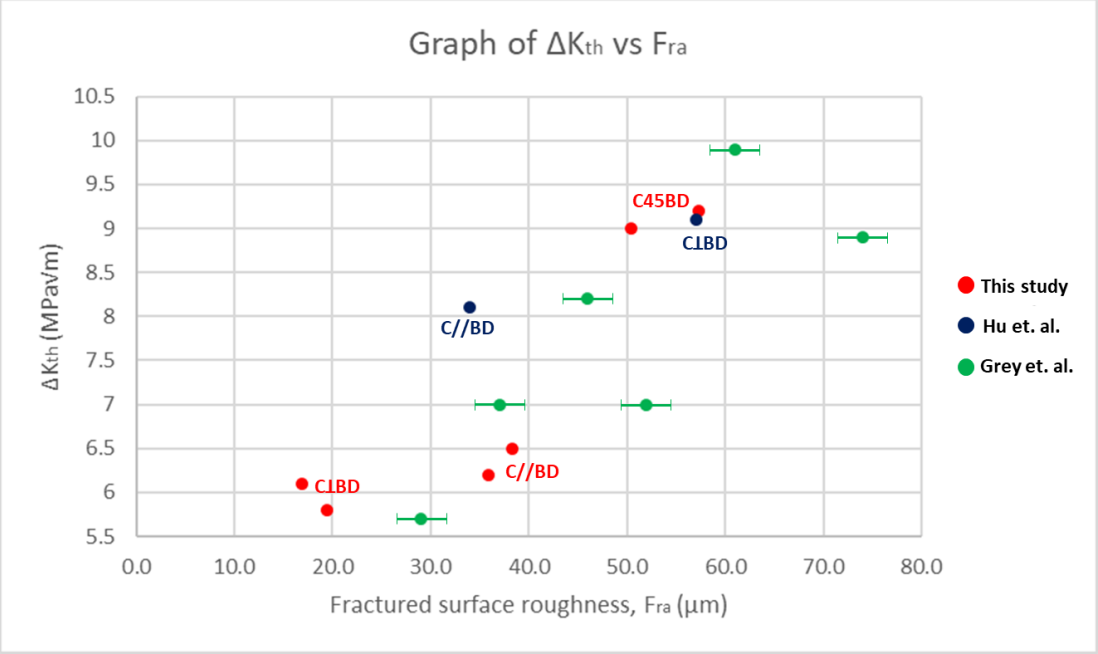

Figure 114 Graph of FCGR threshold value, ΔK_{th} vs fractured surface roughness, F_{ra} for SLM Inconel 738 alloy (this study) SLM Inconel 625 (by Hu et al. [113]) and AISI 1080 "American Railroads" carbon steel (by Gray et al. [62])

The relationship between the fractured surface roughness (F_{ra}) value and the ΔK_{th} value has been proposed by Gray et al. [62] where they introduced the concept of roughness-induced crack closure (RICC). They suggested that having a rougher fractured surface will enhance the effect of crack closure, causing higher resistance for crack growth, which then subsequently causing the ΔK_{th} value to increase. This idea is based on an FCGR experiment that was conducted at two different load ratios, R = 0.1 (high crack closure effect) and R = 0.7 (almost no crack closure

effect). Their result was presented in Chapter 1, Figure 18, showing that the ΔK_{th} value is more affected by different fractured surface roughness at R= 0.1 compared to at R = 0.7. Thus, linking the relationship between F_{ra} value and the ΔK_{th} value with the crack closure effect. However, at R= 0.7, the crack tip remains open with continuously higher stress/strain throughout the loading cycle as compared to at R= 0.1. This continuously high stress/strain factor at R = 0.7 could also explain why the ΔK_{th} value remains low in Figure 18 as the crack growth resistance is reduced [113, 151]. A review paper on crack closure phenomenon by Pippan and Hohenwarter [151] concludes that the concept of RICC is still not certain, and further experimental and theoretical studies are required. Nonetheless, this thesis does not intend to refute or support the concept of RICC.

As shown on Figure 114, the C//BD samples have similar ΔK_{th} value to the C⊥BD samples, despite having higher F_{ra} values, while the C45BD samples have high ΔK_{th} and F_{ra} value compared to the C//BD and C⊥BD samples. The ΔK_{th} values for all the samples are shown to be related to its crack growth pathway. The crack growth pathway for C//BD samples is mostly smooth (similar to the C⊥BD samples) and only branch periodically at a random occurrence, on the other hand, the crack growth path for the C45BD samples is occasionally branched, which resulted in a continuously rougher fractured surface. To illustrate this, SEM images of the fracture path that was obtained from an interrupted FCGR test for all six conditions are shown in Figure 115. Based on the interrupted FCGR test samples, the crack pathway for the C⊥BD samples is continuously straight, similar to the crack pathway for the C//BD samples, but it changes direction periodically, while the crack pathway for the C45BD sample is continuously jagged. This explained the observation seen in Figure 111 where the fractured profile follows the order of: C⊥BD < C//BD << C45BD.

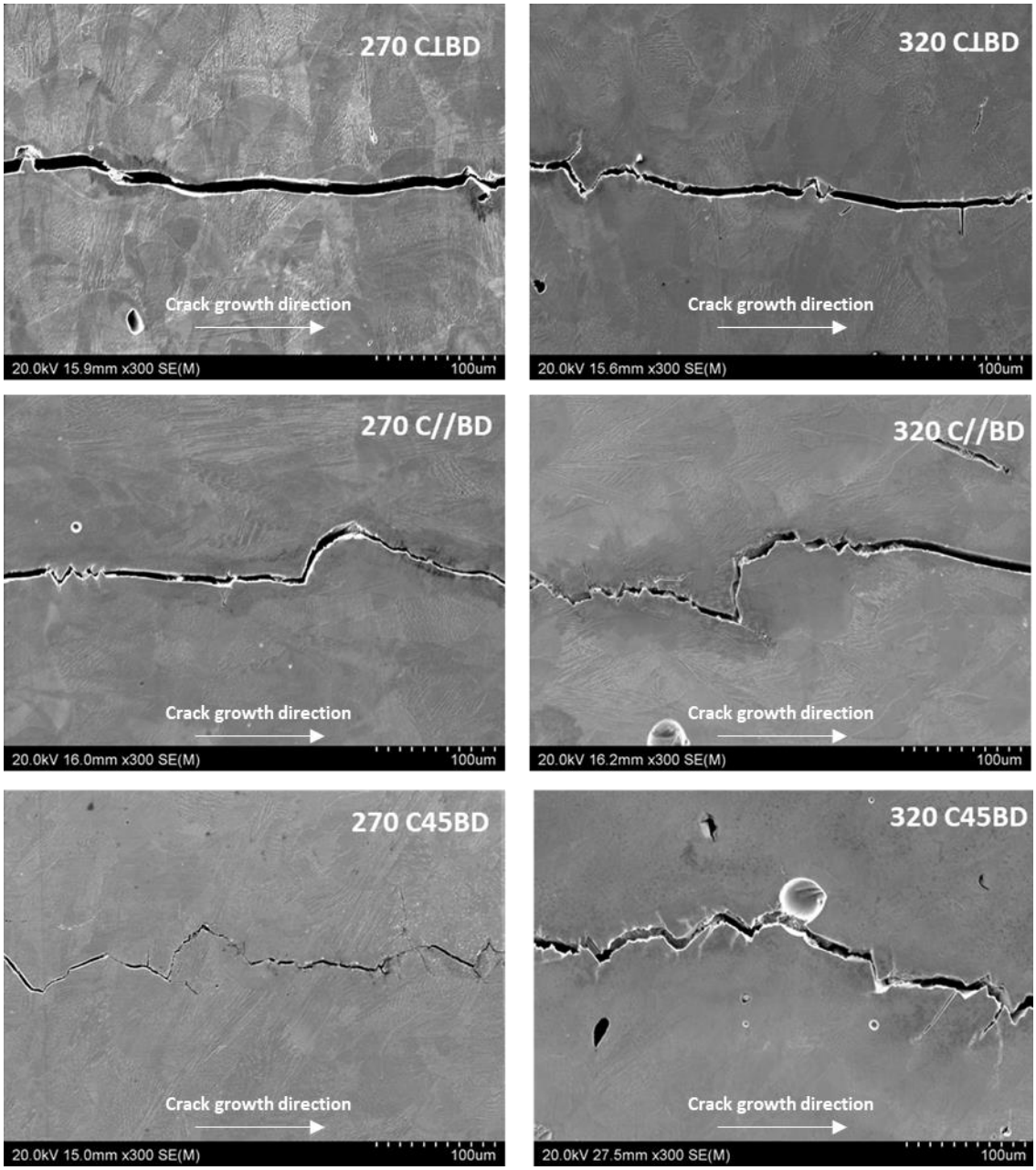

Figure 115 Crack growth path from an interrupted FCGR test of SLM Inconel 738. SLM parameters are indicated on the top right section of each image.

The relationship between the crack growth pathway and the ΔK_{th} can be associated with the effect of crack growth retardation that occurs due to crack deviating and occasionally branching. Figure 116 shows a schematic illustration on how crack branching would affect the crack growth retardation (resistance to FCGR) as presented by Pavlou et al. [152]. Essentially, as the main crack changes direction (branch) the SIF magnitude required to propagate the crack increases which increases the FCGR resistance. The crack growth in the C45BD samples is constantly branching, which cause a continuously high crack retardation effect throughout the crack

formation, thus resulting in a high ΔK_{th} value. In addition, Meggiolaro et al. [153] conducted a FEA evaluation on FCGR retardation due to crack branching where they estimated that the SIF value can be reduced by about 0.63 of its original value, which is approximately the ΔK_{th} ratio between C⊥BD/C45BD. For C//BD, the effect of periodical crack branching does not result in a high crack retardation effect because after the branched crack start propagating back into a straight path, the retarded SIF value immediately recover back to its original value [153]. In summary, the ΔK_{th} value is related to the crack growth pathway, which is continuously deviated/branched for the C45BD sample and only periodically deviated for the C//BD sample. The next Chapter will investigate the cause of crack branching in the crack pathway of SLM Inconel 738 alloy.

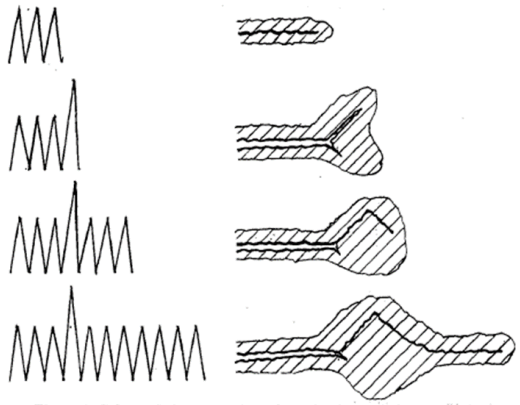

Figure 116 Schematic illustration of overload retardation effect due to crack branching [152]

5.3 Role of grain boundary on the FCGR resistance of SLM Inconel 738 alloy

To further understand how BD affect the FCGR resistance, this section intends to investigate the main microstructure feature that is responsible in promoting crack branching. The SEM image in Figure 117 shows an example of a relatively high magnification image of crack path that was taken from an interrupted FCGR test sample. Based on the observation of SEM images for the interrupted FCGR test samples, there were no evidence of any correlation between crack path and meltpool boundary, or the cell growth direction. However, there are several locations where crack propagate along the grain boundary, marked by white dotted box in Figure 117 (a). The main crack that grows inside/within the grain propagates by linking the slip bands that was generated due to the high stress concentration in front of the crack tip as shown in Figure 117

(b). Since Inconel 738 have a face-centred cubic (F.C.C) atomic arrangement, these slip bands represent the $\{111\}_{fcc}$ planes family which have an angle of 71º or 109º between each other. Therefore, each grain has its own unique slip band orientation which depends on its crystal orientation as discussed in Chapter 4.

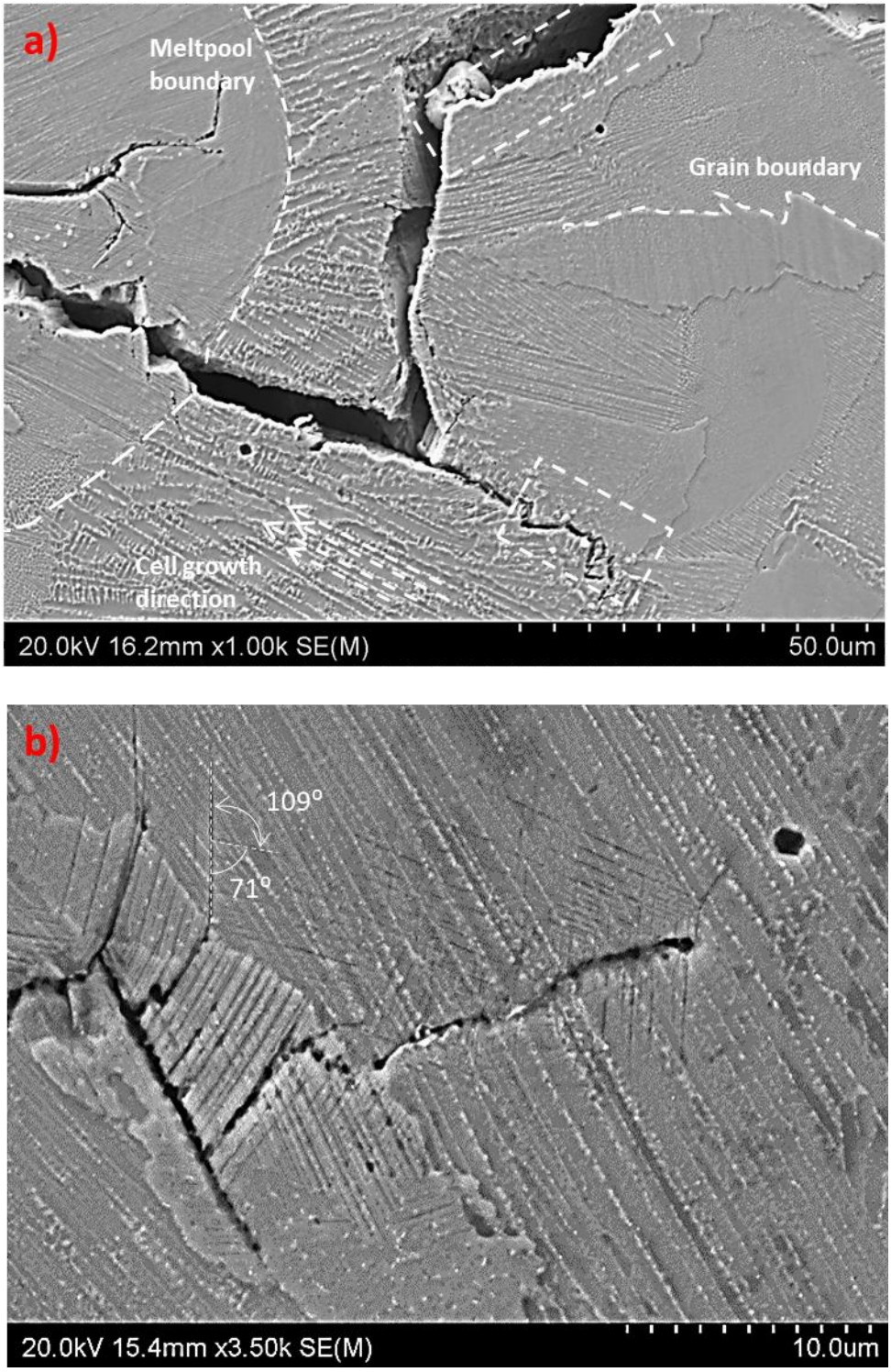

Figure 117 High magnification SEM images of crack growth path for SLM Inconel 738 sample a) near threshold region, with marking on its meltpool boundary, cell growth direction and grain boundary b) crack tip showing the slip bands along the $\{111\}_{fcc}$ planes family

Figure 117 (a) also indicates that the crack growth pathway shared a mix of intergranular (crack propagating along the grain boundary, as marked by the dotted box) and transgranular (crack propagating across the grain boundary) cracking behaviour. Hence, the distribution and orientation of grain boundary would be an instrumental factor in determining the local crack growth pathway direction. As discussed in Chapter 1, Section 1.2, BD orientation plays a major role in the orientation of the SLM columnar shaped grain. Consequently, the BD orientation also influence the orientation of grain boundary and the crack growth pathway. Studies on FCGR behaviour of Inconel 625 alloys [113, 114] (discussed in section 2.1.2.1) imply that the grain boundary acts as a resistance to crack growth rate, where the more grain boundary a crack encounter, the lower the crack growth rate will be. This prediction was introduced based only on their FCGR graph and the number of grain boundary a crack encounter; C⊥BD sample correspond to a small grain size (high number of grain boundary) while C//BD samples correspond to a big grain size (low number of grain boundary). The crack pathway was not being analysed and therefore, to study the mechanism of FCGR resistance, the interrelation between grain boundary and the crack growth path needs to be made clear. Figure 118 below shows the EBSD analysis on all six interrupted FCGR samples (same location as Figure 115) which reveals the crack growth path across the columnar grains.

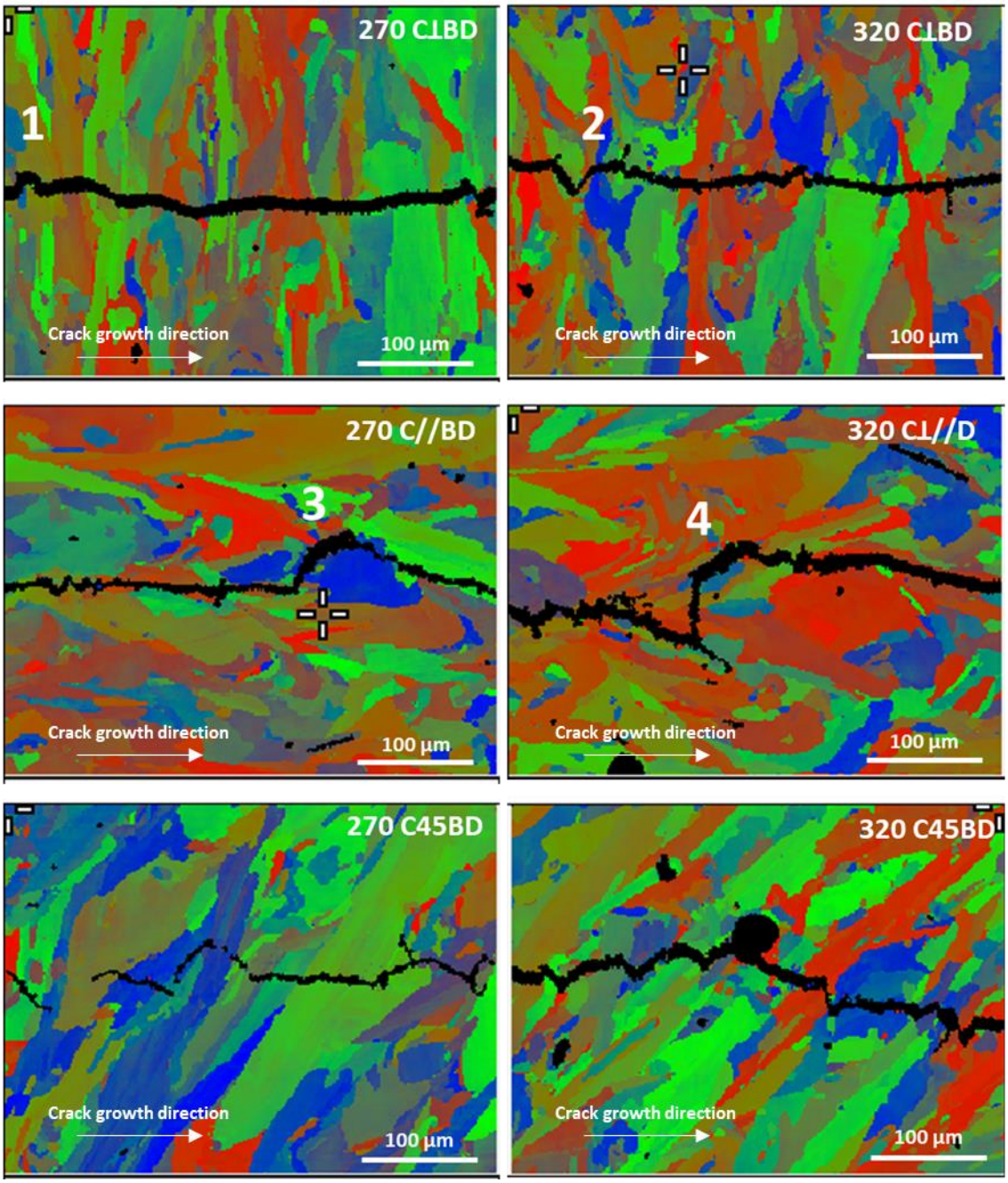

Figure 118 EBSD result on all six conditions of the interrupted FCGR samples. The grain map reveals long columnar shaped grain, with its longer axis mainly orientated along the BD orientation. Each colour represents a single grain that share the same crystal orientation. The black lines reveal the crack growth pathway across the microstructure

Based on the EBSD result in Figure 118, crack does not propagate through grain boundary that is perpendicular or have a high angle (close to 90º) to the crack growth direction. This is because of the loading direction is kept in a vertical orientation, thus the tension stress component in the vertical plane is very small and negligible. This observation can be seen clearly in the C⊥BD sample, where crack growth propagates by crossing the columnar grains, via slip bands which create a smooth and straight path. However, since the grain growth direction is also dependent

on the thermal gradient direction [14], there are a few locations where the grain boundary is askew away from the BD orientation that might cause the straight crack growth path to be deviated.

Figure 119 shows a high magnification image of location "1" (in Figure 118) where the crack growth path is slightly deviated by the grain boundary, causing a small branching effect. On the other hand, location "2" reveals that the deviated crack does not precisely follow grain boundary, due to the high angle of grain boundary (marked in Figure 119). However, the crack still propagates through the $(111)_{fcc}$ plane that is closer to the grain boundary (*slip band 1*), even though *slip ban 2* have a smaller angle relative to the crack growth direction. Therefore, the influence of grain boundary in deviating the crack growth direction in the C⊥BD sample can still be observed, even though it uncommon due to most of the grain boundary is parallel to the BD orientation (90° from the crack growth direction). In addition, the crack also appears to have a mix of brittle (rough) and ductile (smooth) fracture features.

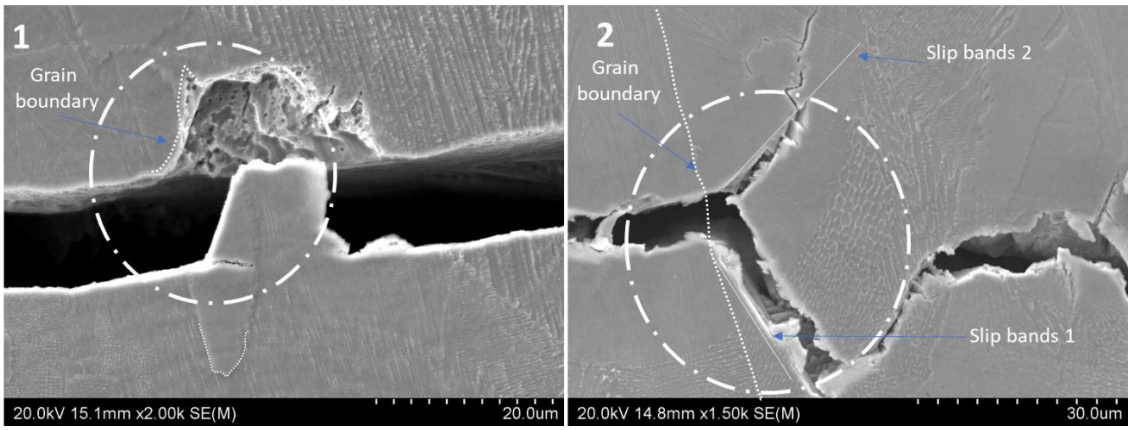

Figure 119 High magnification image of location "1" and "2" in Figure 118, showing the influence of grain boundary in deviating the crack growth pathway

The local crack growth direction was shown to be deviated or branched by the grain boundaries, provided the angle of the grain boundary in relation to the crack path direction is not close to 90º. The potential of grain boundary in deviating crack path is dependent on the presence of brittle carbide phase, that usually forms near the grain boundary [63]. Biezma et al. [154] reported that the increase in percentage of second phase (sigma phase) in 2205 stainless steel changes the

fracture mode of the material from transgranular to intergranular. Based on fractographic observation, the relationship between the amount of sigma phase and the mode of fracture for 2205 stainless steel was summarised by Biezma et al. in Table 10 below. Generally, the presence of second phase precipitate near the grain boundary causes the grain boundary to become more brittle, thus resulted in a more intergranular fracture.

Table 10 The relationship between the percentage of sigma phase precipitate and fracture mode in UNS S32205 stainless steel [154]

% sigma phase	Fractography
1.9	Transgranular by Coalescence Microvoids
14.5	Mixed Transgranular: Coalescence Microvoids* + Quasi-cleavage
18.9	Mixed: Transgranular by Quasi-cleavage* + Intergranular
31.1	Intergranular

Figure 120 shows a TEM analysis on the grain boundary of cast Inconel 738 conducted by Mazur et al. [125], where the presence of MC and $M_{23}C_6$ carbide phase along the grain boundary can be seen. The "M" elements in the MC carbide can be titanium, tantalum, niobium, hafnium, or thorium, while the "M" element in the $M_{23}C_6$ carbide is usually chromium, but nickle-cobalt, molybdenum, iron and tungsten can also substitute [63]. Unlike $M_{23}C_6$ carbide that usually forms a thin film near the grain boundary, MC carbide is a globular, irregular shaped particle that is randomly distributed near the grain boundary. The ununiform distribution of carbides near the grain boundary of Inconel 738 resulted in an ununiform local brittleness of a grain boundary. This ununiform local brittleness of a grain boundary is significant for low crack growth rate (near the threshold region) since the crack is moving at rate of 0.1 nm per cycle (1×10^{-10} m/cycle), comparative to the scale of MC carbide. Therefore, in addition to the orientation of the grain boundary, branching of the local crack growth direction along the grain boundary (intergranular fracture) also depends on the presence of carbides that precipitate along the grain boundary.

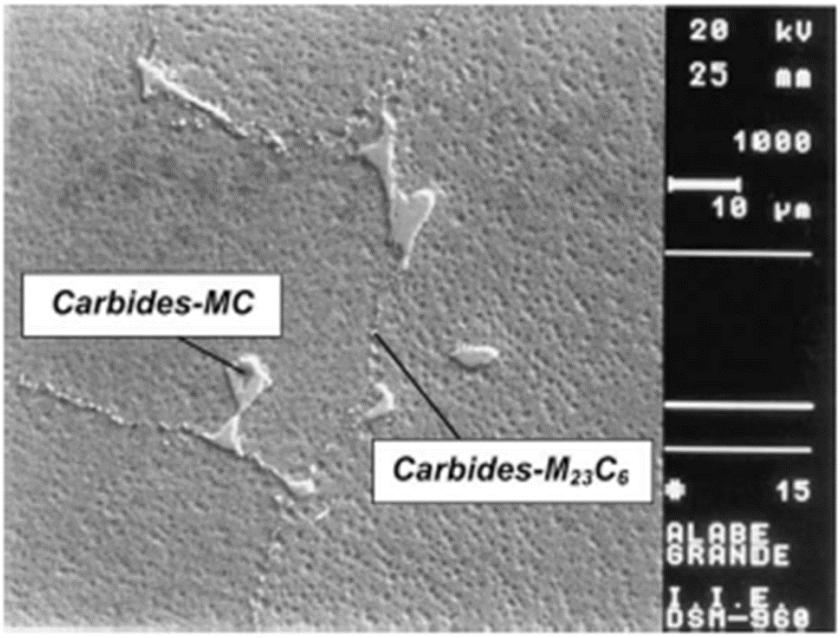

Figure 120 TEM analysis of Inconel 738 showing the present of $M_{23}C_6$ and MC carbides precipitate along the grain boundary [125]

Energy-dispersive X-ray spectroscopy (EDS) analysis is conducted onto the fractured surface of the CT sample to verify the presence of carbide on the grain boundary of SLM Inconel 738 sample. Figure 121 shows a typical fractured surface at the threshold region and the EDS result conducted on the selected area. The rough fractured feature marked as fracture-feature-1 in Figure 121 is likely to represents the grain boundary as the 5 – 50 µm distance between them in the C⊥BD sample matches with the width (shorter axis) of columnar gain shown in Figure 118. In addition, based on the EDS result, the high carbon content at fracture-feature-1 also suggests the presence of carbide in that region. On the other hand, the parallel lines that appear on the fracture-feature-2 are more likely to represent slip bands instead of striation pattern as suggested by Hu et al. [113]. In fact, striation patterns are not visible in the threshold region, and are only observable when the crack growth rate reaches $da/dN > 10^{-7}$ m/cycle [155]. Figure 122 shows a high magnification image of the fracture-fracture-2 area where the parallel lines appear to change orientation as it crosses the rough fracture feature indicating that the crystal orientation changes (different grain), and therefore it is not a striation pattern.

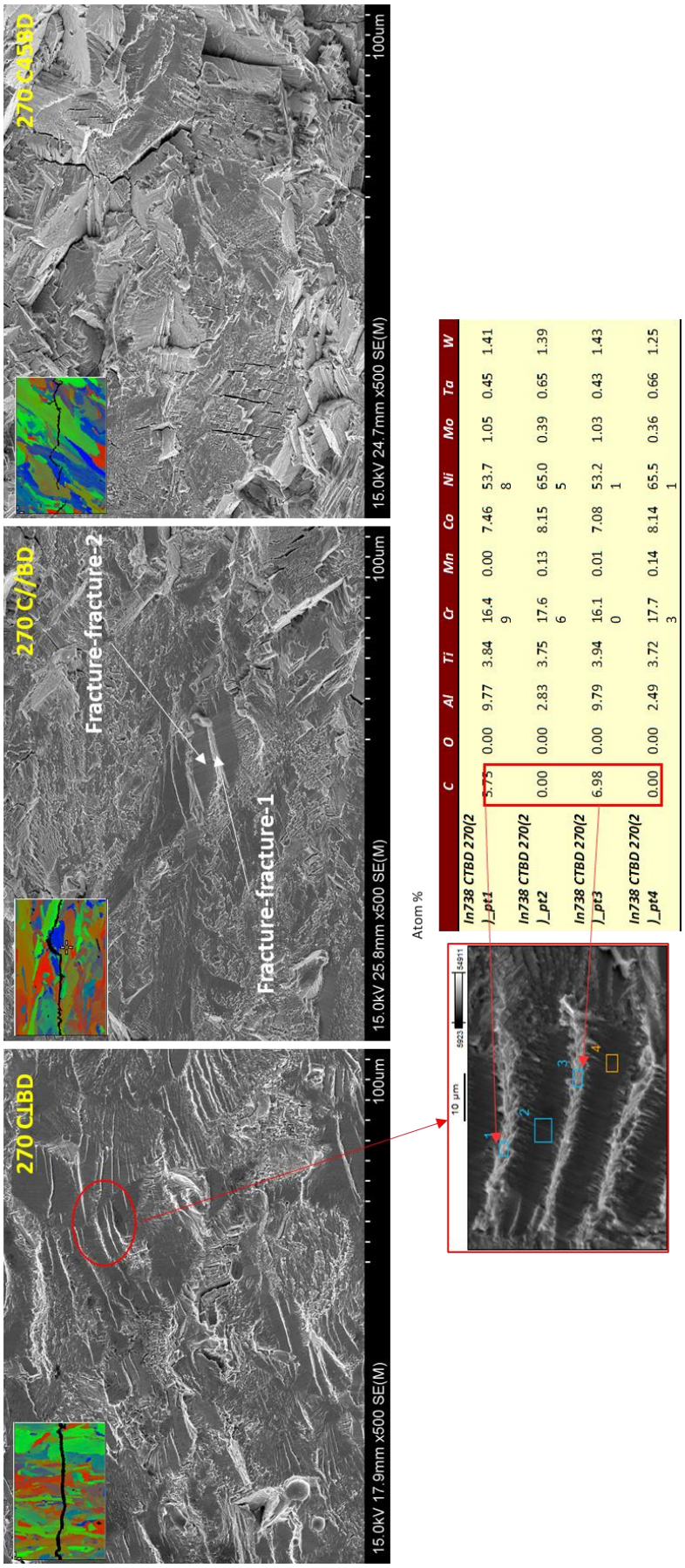

	C	O	Al	Ti	Cr	Mn	Co	Ni	Mo	Ta	W
In738 CTBD 270/2_pt1	5.75	0.00	9.77	3.84	16.49	0.00	7.46	53.78	1.05	0.45	1.41
In738 CTBD 270/2_pt2	0.00	0.00	2.83	3.75	17.66	0.13	8.15	65.05	0.39	0.65	1.39
In738 CTBD 270/2_pt3	6.98	0.00	9.79	3.94	16.10	0.01	7.08	53.21	1.03	0.43	1.43
In738 CTBD 270/2_pt4	0.00	0.00	2.49	3.72	17.73	0.14	8.14	65.51	0.36	0.66	1.25

Figure 121 Fractured surface in the threshold region of SLM Inconel 738 alloy and EDS analysis to determine carbon content at the brittle and ductile fracture feature.

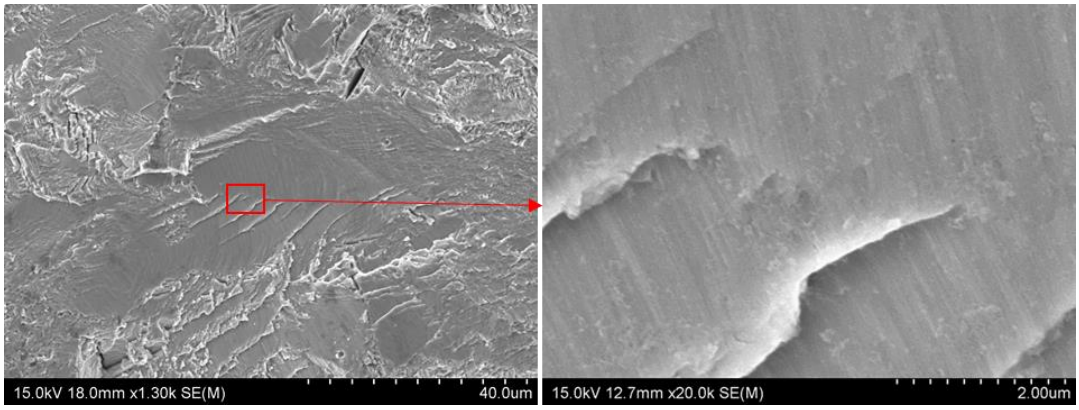

Figure 122 SEM image of the surface fracture of SLM Inconel 738 with high magnification on the slip bands area.

For discussion on the C//BD samples, since majority of the columnar grains are orientated parallel to the crack growth direction, the chances for a crack to encounter a grain boundary that have smaller angle in relative to the crack growth direction is higher compared to the C⊥BD sample. In addition, a crack in the C//BD samples occasionally encounter a grain boundary that is orientated 45º in relation to the crack growth direction, this may cause the crack pathway to deviate in a 45° orientation that resulted in a significant deviation of the growth pathway. Locations "3" and "4" in Figure 118 highlight the area at which crack path encounter a 45° grain boundary and is significantly deviated from the main crack direction.

As illustrated in the EBSD grain map in Figure 118, because of the shape and distribution of the columnar grains in SLM Inconel 738 specimens, a crack in the C//BD sample is expected to occasionally encounter a grain boundary with 45º orientation. On the other hand, a crack in the C45BD sample is expected to always encounter a grain boundary with a 45º orientation. Hence, the crack path in C45BD sample is continuously deviated, resulting in a continuously rough fractured surface. In essence, the encounter of a crack with a 45º oriented grain boundary is shown to promote crack branching and subsequently cause FCGR retardation. The continuous FCGR retardation in the C45BD samples near the threshold region causes continuous resistance for the crack to grow thus increases the ΔK_{th} value.

For further discussion and fractographic demonstration on the role of grain boundary in promoting crack branching for SLM Inconel 738, an EBSD and SEM images of a crack tip from

a C//BD interrupted FCGR test sample is provided in Figure 123. The EBSD grain map image in Figure 123-1 reveals the mix behaviour of transgranular and intergranular cracking in SLM Inconel 738. The high magnification image in Figure 123-2 shows that the crack continues to follow the grain boundary (between the grains colour in green and blue, orientated ~ 45º) instead of following the slip bands, even though the slip bands have a smaller angle in reference to the crack growth direction. This example shows that the grain boundary that is orientated at a 45º angle in reference to the crack growth direction can significantly deviate the crack pathway, which has caused the high fracture surface roughness for the C45BD samples.

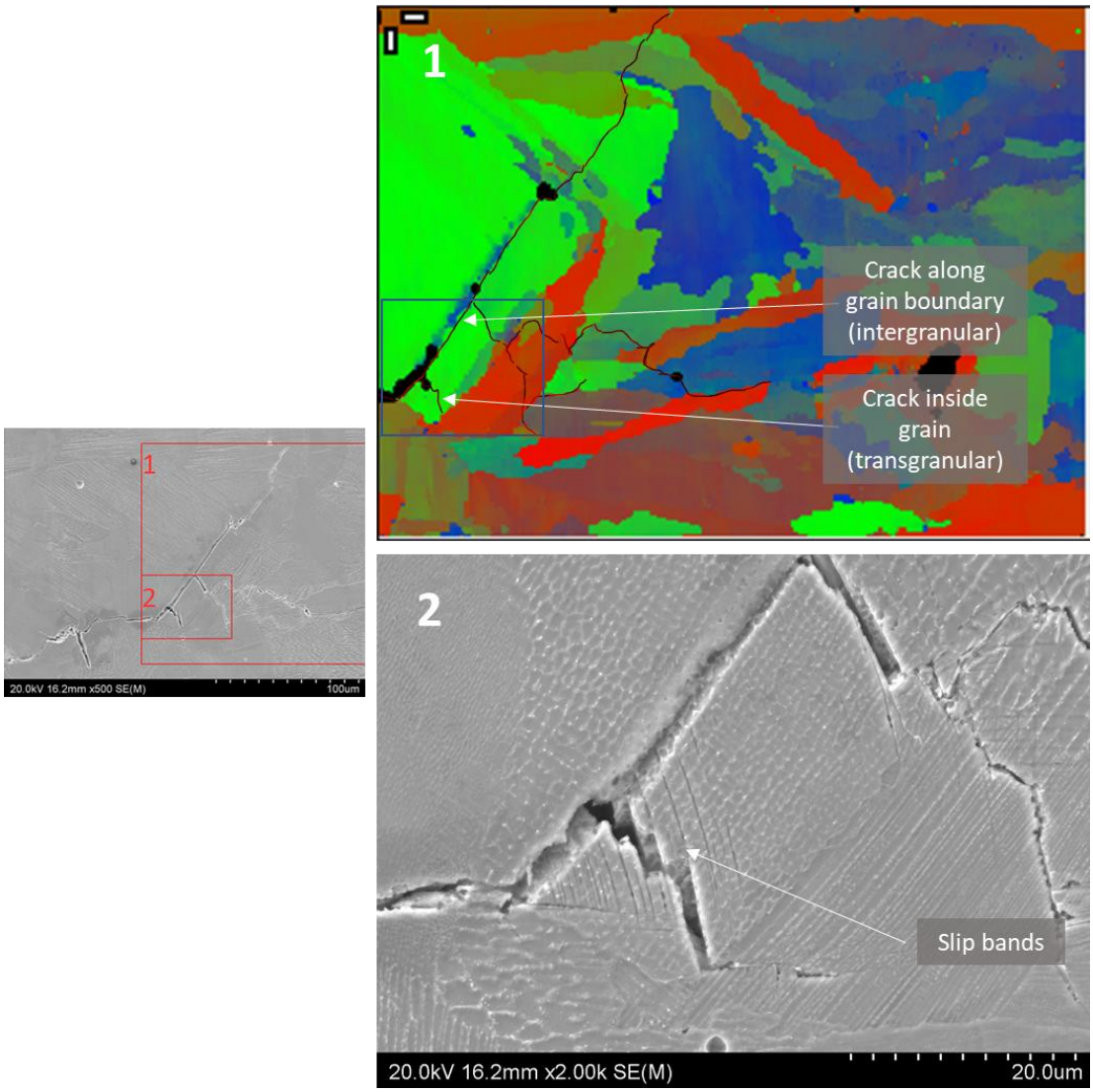

Figure 123 Crack tip of a C//BD FCGR interrupted test sample. 1) EBSD grain map showing the crack growth pathway branching at a 45° angle 2) High magnification SEM image focusing on the crack propagation through the slip bands

The role of grain boundary in deviating the crack growth pathway is also reaffirmed by the difference in the fractured surface roughness between the 270 W and the 320 W samples. The difference in the F_{ra} value between the 270 W and 320 W samples are small, yet the 270 W samples have a slightly lower F_{ra} values compared to the 320 W samples. As mentioned in Chapter 1, section 1.2.2.1, the 320 W samples have slightly more irregular grains (more grains that grow askew away from the BD) as compared to 270 W samples because of the difference in the depth of their meltpool boundary. For a keyhole meltpool, higher laser power would lead to a higher meltpool depth, thus resulted to a steeper meltpool boundaries. Because of this, a higher percentage of horizontal grain growth direction can be seen in the 320 W sample as compared to the 270W sample. Based on the EBSD results in Figure 118, because of the slightly more irregular grain distribution in the 320 W samples, its average columnar grain width (shorter axis) is slightly bigger compared to 270 W sample, which is 15.7 µm compared to 14.2 µm, respectively. This average grain width is calculated by counting the number of grain boundary encountered by a straight line across the C⊥BD grain map in Figure 118, divided by the length of the line. Consequently, because of the slightly more irregular columnar grain in 320 W samples, the crack pathway in the 320 W samples is more easily to be deviated compared to the 270 W sample which reflects the slight difference in the FCGR threshold value between them.

To conclude, the SLM BD parameter plays a major role in the crack growth pathway of SLM Inconel 738 since it regulates the grain boundary orientation. The local brittleness of a grain boundary depends on the segregation of carbides. In addition, the capability of a grain boundary to deviate a crack depends on its orientation in respect to the global crack growth direction. A grain boundary that is orientated 45° to crack growth direction is shown to be able to significantly deviate a crack which resulted in a high fracture surface roughness and high FCGR resistance. Therefore, since a crack that is growing inside the C45BD samples is expected to continuously encounter a 45º angle grain boundary, its local crack growth pathway is continuously deviated which resulted in a higher FCGR resistance compared to the C⊥BD and C//BD samples.

5.4 Effect of key-hole pores on the FCGR behaviour of SLM Inconel 738 alloy

This section intends to study the effect on micro pores on the FCGR behaviour of SLM Inconel 738 alloy. Though, this section is less significant than the previous chapter as the effect of laser power (which influence the micro pores) is not as significant as BD, especially in the threshold region. As mentioned in Chapter 1, section 1.2.2.1, the 320 W samples have higher density of micro pores as compared to the 270 W samples. Figure 124 shows the difference in micro pores density on a random cross section surface between 320 W samples and 270 W samples. These spherical micro pores (also known as "keyhole pores") are caused by the collapsing of entrapped air bubble inside the keyhole-meltpool during the solidification process. Therefore, these pores do not have any sharp edges, unlike the lack of fusion (LOF) defects that have sharp edges and is located between the meltpool boundary. Hu et al. [113] claims that micro void in SLM Inconel 625 did not play a significant role in the FCGR behaviour, which is consistence with the finding on the effect of LOF on the FCGR behaviour of SLM Co-Cr-Mo, discussed in Chapter 4. However, the study on the effect of LOF on the FCGR behaviour of SLM Co-Cr-Mo alloy only focuses at low ΔK value, around 10 – 20 MPa$\sqrt{m}$. As shown in Figure 109, in Section 5.1, at high ΔK value (end tail of Paris region, ΔK ≈ 40 MPa$\sqrt{m}$) the crack growth rate of the 320 W samples (with high number of keyhole pores) begin to become higher than the 270 W sample (with low number of keyhole pores). Therefore, this section aims to identify whether the high number of keyhole pore in the 320 W sample may have accelerated its crack growth at high ΔK magnitude.

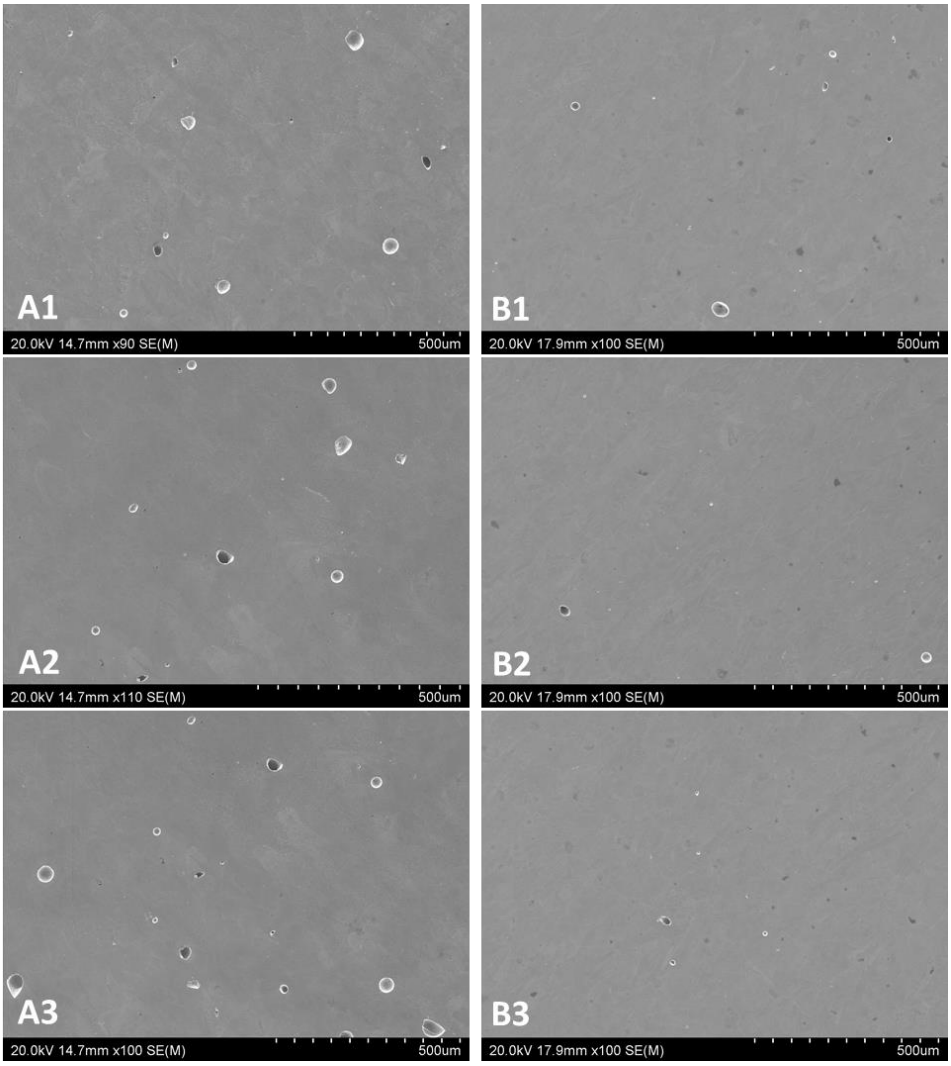

Figure 124 SEM images of micro pores detected on the cross-section surface of polished SLM Inconel 738. A1-A3 represent 320 W samples, B1-B3 represent 270 W samples.

All micro pores in Figure 124 is identified and marked to measure the area percentage of pores ($P_{area\%}$) using ImageJ software. Figure 125 shows the value $P_{area\%}$ for each of SEM images in Figure 124 (with the same image arrangements: A1-A3 represent the 320 W samples and B1-B3 represent 270 W samples). The average $P_{area\%}$ value between the three images of 320 W and 270 W samples are 0.679% and 0.146% respectively. Based on other studies of the density of defects in SLM material of various alloys [156-158], Darvish et al. [13] suggested that $P_{area\%}$ = 0.1% can be interpreted as highly dense, but not fully dense. Therefore, the 270 W sample is close to be regarded as highly dense. The size of the key-hole pores in this material varies up to 65 µm in diameter. The high amounts of pores in the 320 W samples are expected to start imposing decremental effect on the FCGR performance only at high SIF value. This is indicated by the FCGR graph in Figure 109, showing that the crack growth rate for 320 W samples surpass 270

W sample at ΔK ≈ 40 MPa$\sqrt{m}$ ("intersection point"). In order to verify this assumption, the fracture surface at which ΔK reaches ≈ 40 MPa$\sqrt{m}$ will firstly be identified, to determine if there is any coloration between the keyhole pores and the crack growth pathway. Sample with BD orientation of C⊥BD will be used in this study since the crack growth direction is expected to be straight and smooth based on the F_{ra} value calculated in Section 5.2.

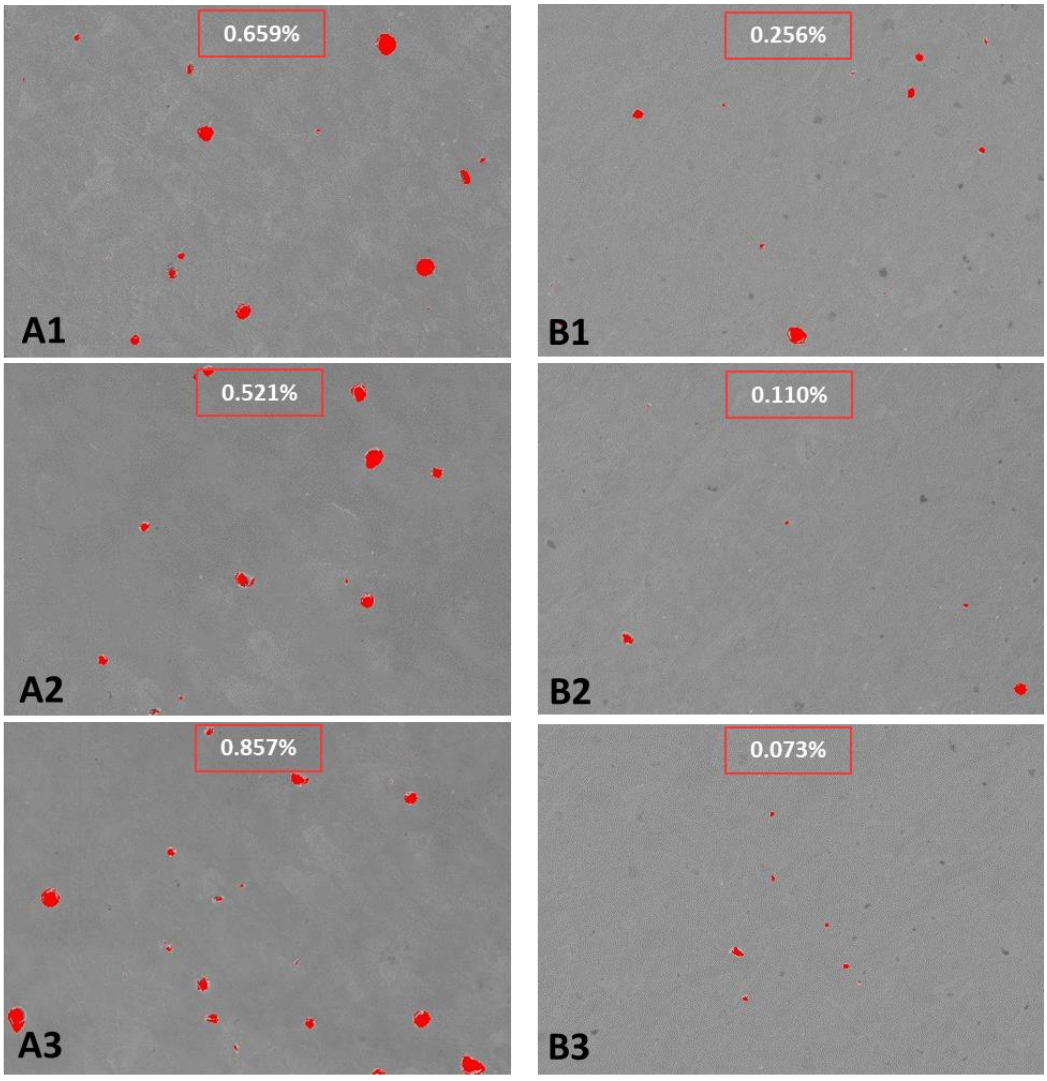

Figure 125 Area percentage of micro pores detected on surface of polished SLM Inconel 738. A1-A3 represent 320 W samples, B1-B3 represent 270 W samples. The percentage number written on top of each images represent the average area percentage of pores, $P_{area\%}$.

In Chapter 4, the effect of LOF ($P_{area\%}$ below 1%) on FCGR behaviour of SLM Co-Cr-Mo alloy is shown to be negligible at low SIF value. This should also apply to the relationship between the keyhole pores and FCGR behaviour of SLM Inconel 738, since keyhole pores does not have any

sharp edges that induce stress concentration. However, Figure 126 shows that the 320 W and 270 W FCGR graphs intersect at high SIF value, suggesting that there is a change in crack growth behaviour between them at high ΔK value. As shown in Figure 109, this pattern of graph intersection is similar for all three BD. The red dotted lines indicate the range of da/dN and ΔK at which 320W sample start to have a higher crack growth rate compared to 270 W sample. The "intersection point" between the two graphs in Figure 126 happens at $\Delta K \approx 40$ MPa$\sqrt{m}$, at which da/dN is in between 10^{-7} – 10^{-6} m/cycle.

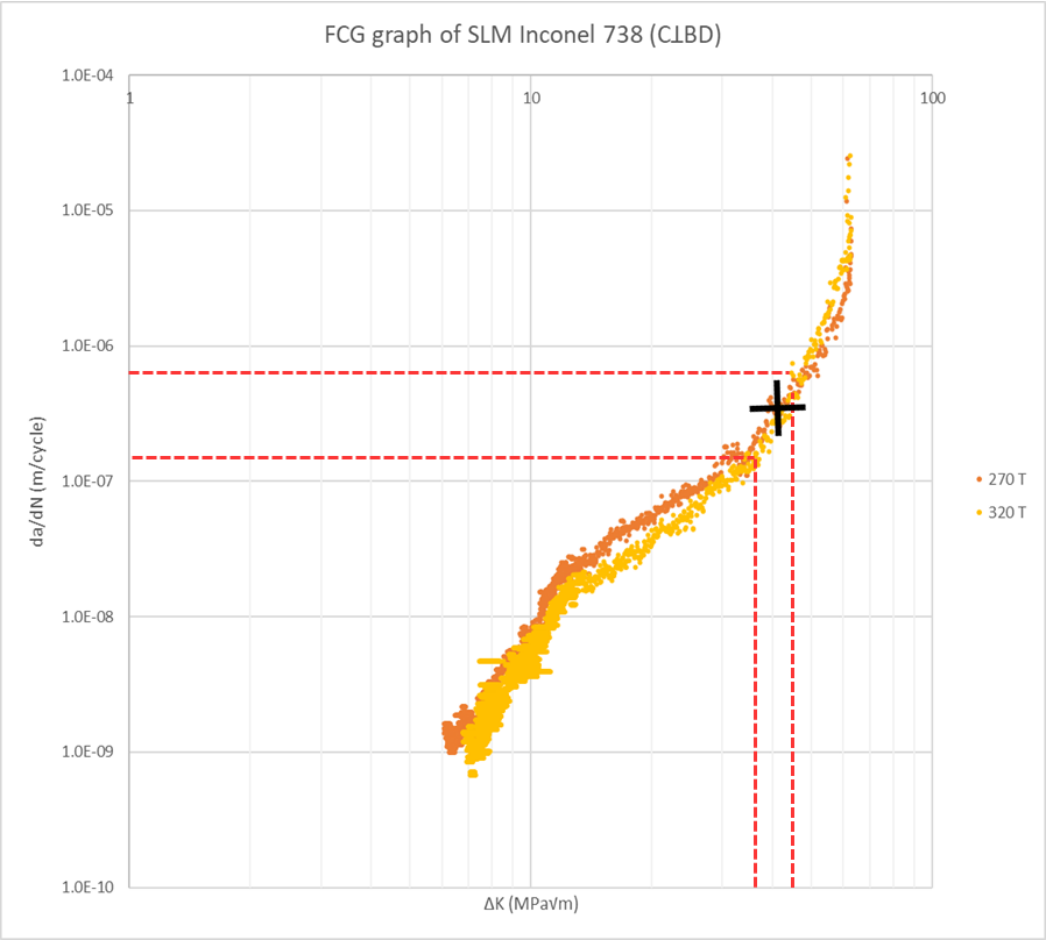

Figure 126 FCGR graph of SLM Inconel 738. A comparison between 320 W and 270 W. Red dotted lines indicate the range or da/dN and ΔK where 320 W sample overtake the crack growth rate of 270 W sample. The intersection point is mark as "+".

The physical location on the fractured CT sample at which the "intersection" occurs was determined by the crack size (a) data that was collected from the FCGR software. Figure 127 shows a graph of da/dN vs (a) for the 320 W and 270 W samples, which correspond to the FCGR graph in Figure 126. Based on the range of da/dN and (a) that is marked with the red dotted lines

in Figure 127, at da/dN =10^{-7} – 10^{-6} m/cycle (where the intersection point occur), the crack size of the CT samples is 'a' ≈ 18 – 20 mm. The process of obtaining the physical location at which the "intersection point" occurs is worth to be mentioned in this Chapter to provide clear evidence on the influence of micro pores on the FCGR behaviour. The fractured surface of the CT samples will be examined at a = 19 mm, to identify if there is any influence of micro posers on the FCGR behaviour.

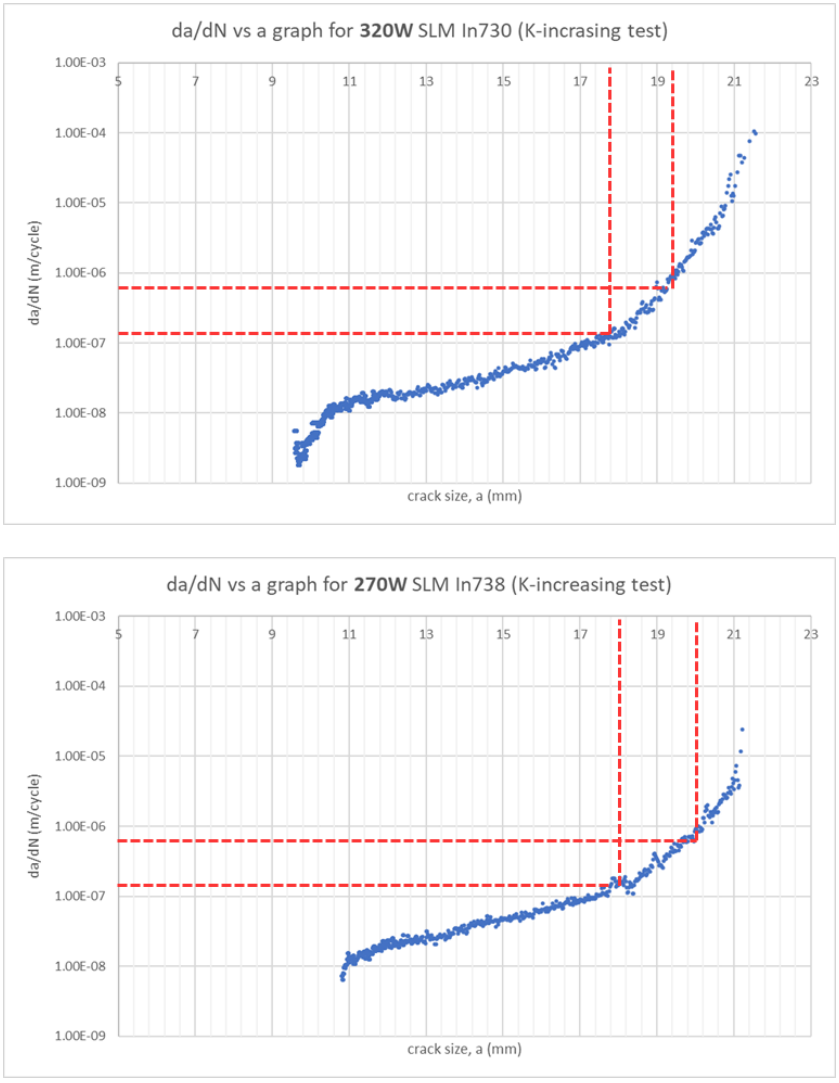

Figure 127 Graph of da/dN vs crack size, a during K-increasing test for: Top: 320 W. Bottom 270 W. The two red lines on both graphs indicates the range at which the "intersection" point occurs, da/dN is in between 10^{-7} – 10^{-6} m/cycle

The fractured surface of the 270 W and 320 W samples is provided in Figure 128 and Figure 129 respectively. The percentage of micro pores on both fractured surfaces at low ΔK value (from a = 5 mm to a = 17 mm) reflects the $P_{area\%}$ value at a cross section, of 0.146% and

0.679% for 270 W sample and 320 W samples, respectively. However, at higher stress intensity factor, as ΔK reaches 40 MPa$\sqrt{m}$ (at crack size, 'a' ≈ 19 mm), the density of micro pores on the fractured surface increases. The red boxes in Figure 128 and Figure 129 are magnified in Figure 130, which clearly show that percentage of micro pores at 'a' = 19 mm is greater than the $P_{area\%}$ at lower SIF value. Qualitatively, this has suggested that, at ΔK ≈ 40 MPa$\sqrt{m}$, the crack pathway has started to propagate through the micro pores. Therefore, since the 320 W sample has higher $P_{area\%}$ then the 270 W sample, the crack growth rate for the 320 W sample at at ΔK ≈ 40 MPa$\sqrt{m}$ will be higher than the 270 W sample.

Micro defects is reported as a significant factor in LCF experiment of SLM material [125, 159, 160], at high stress/strain magnitude, tearing effect causes crack to propagate through the micro defects. Therefore, micro pores only impose significant effect on the FCGR behaviour at high SIF value, in this case, at the end spectrum of Paris region, where ΔK ≈ 40 MPa$\sqrt{m}$. It is also important to note that ΔK = 40 MPa$\sqrt{m}$ is a very high value, where the crack starting to enter Region 3 (catastrophic fracture).

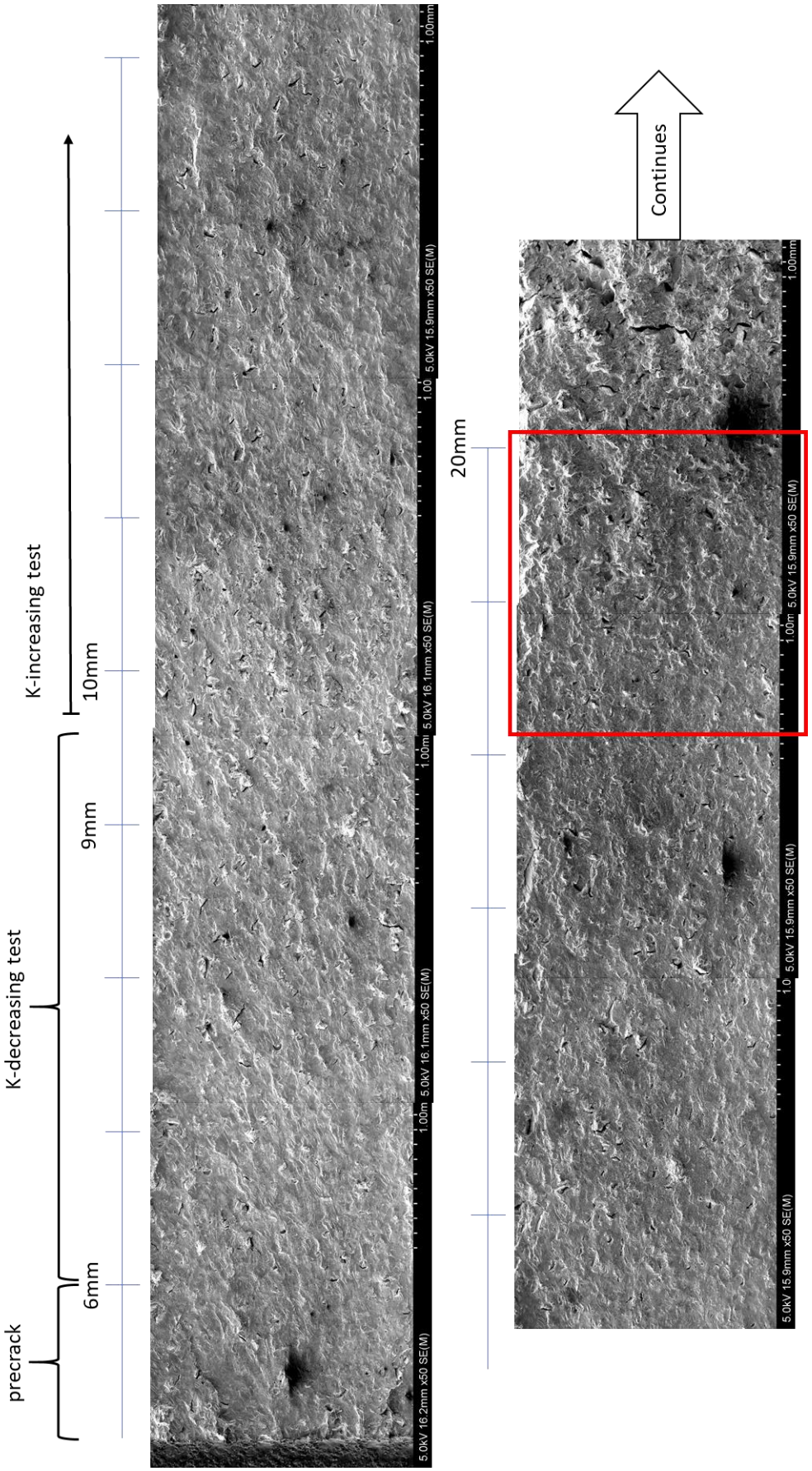

Figure 128 Fractured surface of SLM Inconel 738, representing the 270 W sample on Figure 126. The red box marking represents the area at which "intersection" point occur. The crack size (a) is marked by the blue lines from 5 mm to 20 mm. The CT specimen fractured at 21 mm.

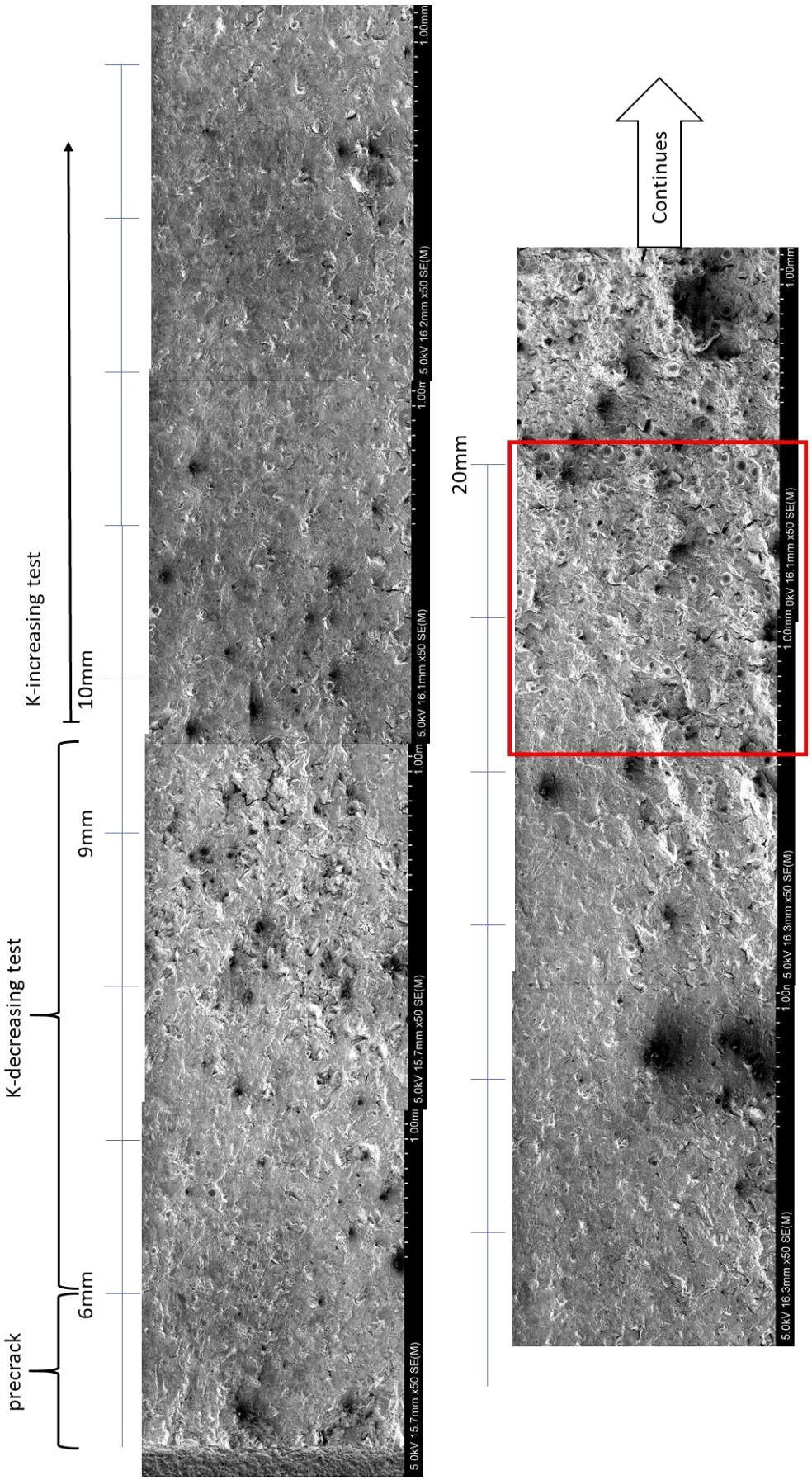

Figure 129 Fractured surface of SLM Inconel 738, representing the 320 W sample on Figure 126. The red box marking represents the area at which "intersection" point occur. The crack size (a) is marked by the blue lines from 5 mm to 20 mm. The CT specimen fractured at 21 mm.

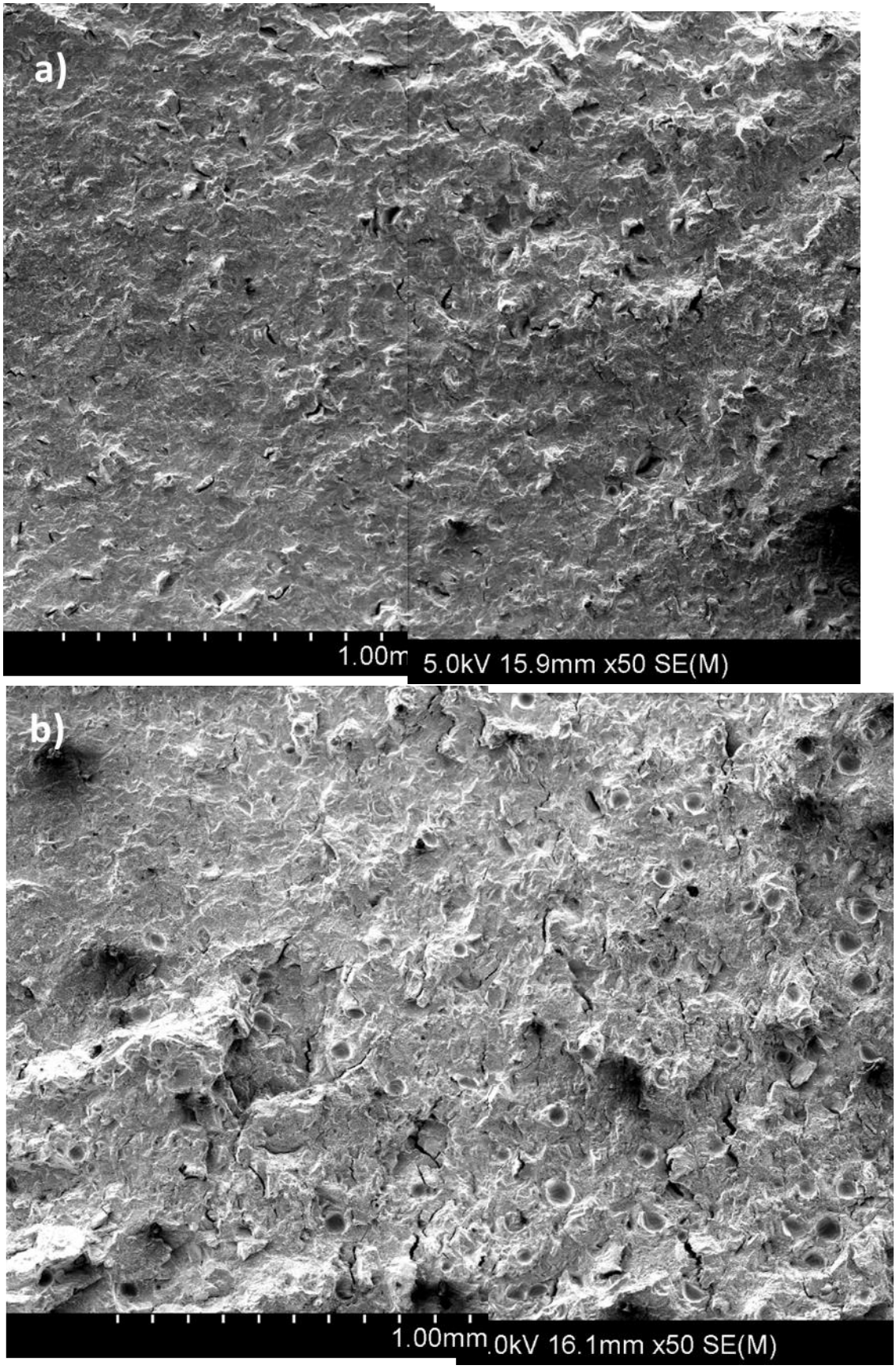

Figure 130 Larger SEM image of the fractured surface at the 'transection point', marked by red box in Figure 128 and Figure 129 a) 270 W sample, b) 320 W sample.

5.5 FCGR of SLM Inconel 718 – further analysis on SLM Inconel alloys

A study on SLM Inconel 718 is also included in this Chapter to further discuss the role of microstructure in the FCGR behaviour of Inconel alloys. Only one building direction (BD) of CT specimen, C45BD, is used to perform the FCGR experiment for SLM Inconel 718. This BD orientation is chosen based on the best BD orientation, that showed the slowest crack growth rate in the previous study of SLM Inconel 738 and the short crack FCGR result reported by Brynk et al. [115], discussed in Chapter 2, section 2.1.2.2. Based on the FCGR graph of SLM Inconel 718 shown in Figure 131, the threshold value is ΔK_{th} = 7.0 MPa$\sqrt{m}$, and the Paris constant C and m are 1.0 x 10^{-12} and 3.3, respectively. Similar to the FCGR study conducted for SLM Inconel 738 and SLM Co-Cr-Mo, FCGR interrupted test (described in Chapter 3, section 3.3.4) is conducted to verify the FCGR graph and to analyse the crack growth pathway. The discontinued data in the Region 1 of the FCGR graph is likely caused by a sudden jump in the FCGR resistance, causing the crack growth rate to reduce abruptly from da/dN = 1 x 10^{-9} to 5 x 10^{-10} m/cycle.

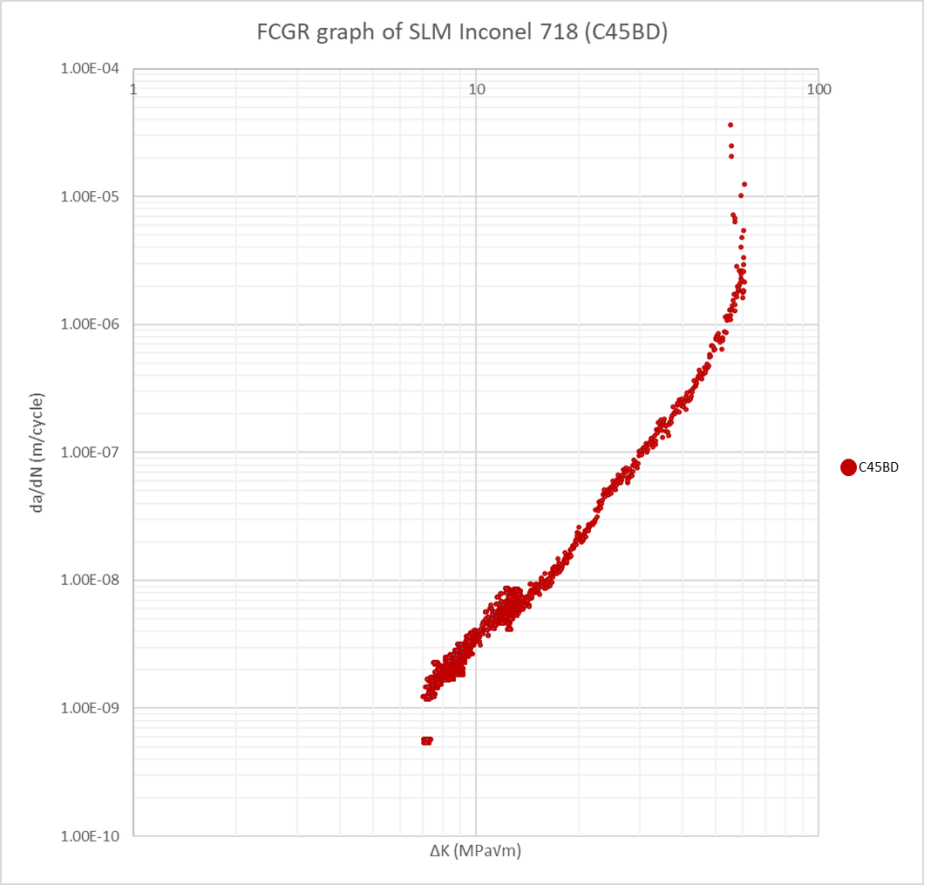

Figure 131 A FCGR graph of SLM Inconel 718. The BD orientation of the CT speciment is C45BD. Threshold value, ΔKth = 7.0 MPa√m. Paris constant, C = 1.0 x 10^-12 and m = 3.3.

The threshold value in this experiment is more than doubled compared to the threshold value reported by Konecna et al. [116] on SLM Inconel 718 with BD orientation C//BD, which is ΔK_{th} = 3.0 MPa$\sqrt{m}$. As discussed earlier in Chapter 2, section 2.1.2.2, the FCGR graph produced by Konecna et al. is likely to be faulty and needs to be verified. Nevertheless, the threshold value in this experiment is slightly lower compared to the traditionally build (cast or wrought) Inconel 718 [161-164], which is $\Delta K_{th} \approx 8 - 14$ MPa$\sqrt{m}$. Figure 132 below shows how the FCGR graph from this work compared with other reported FCGR graph of Inconel 718. Similar to the previous FCRG study for Inconel 738, the FCGR lines at Region 2 (Paris region, $\Delta K = 20 - 40$ MPa$\sqrt{m}$) in Figure 132 appears to coincide with each other, despite the differences in manufacturing processes. Note that only FCGR experiment that was conducted in accordance with ASTM standard is comprised in Figure 132, thus the short crack FCGR result reported by Brynk et al. [115] is not included.

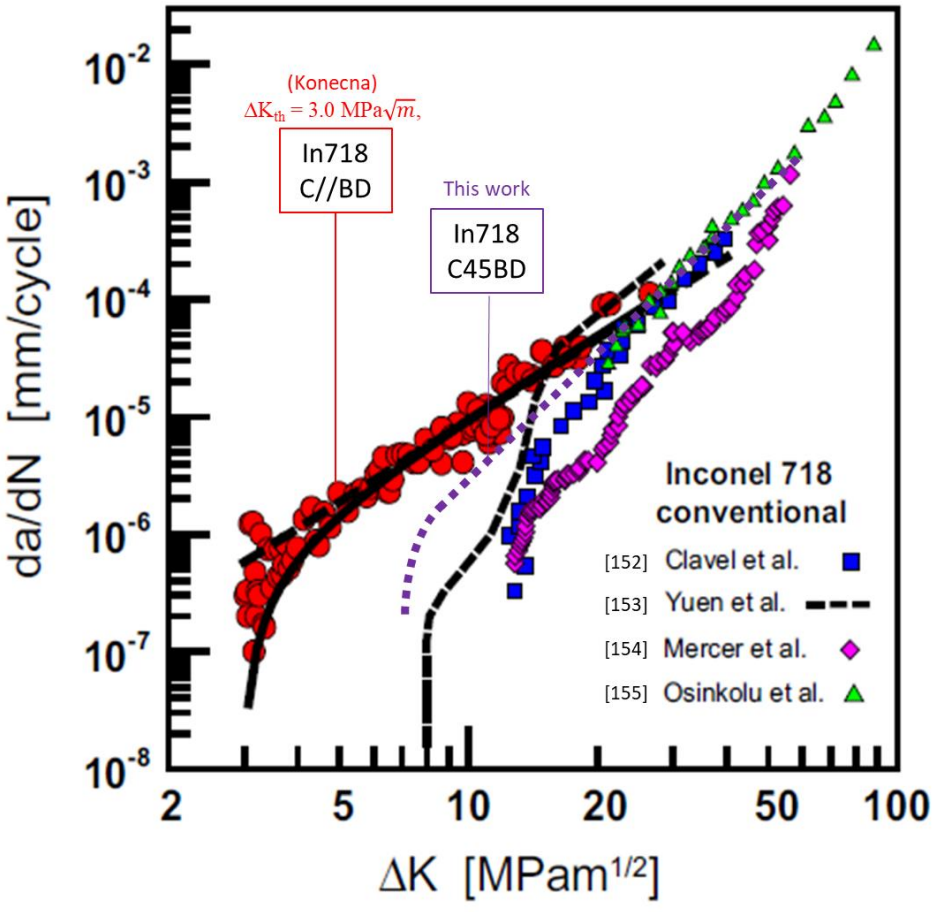

Figure 132 FCGR graphs of Inconel 718. The purple (marked as "This work") and red (marked as "Konecna") lines represent SLM material, while the blue, black, pink and green lines are conventionally (cast or wrought) produced.

The fractured CT sample of SLM Inconel 718 is shown in Figure 133. The angle of crack growth direction in respect to the horizontal axis (θ_C) varies with the magnitude of stress intensity factor (SIF). At the threshold region, θ_C has a value of ≈ 30°, and it gradually reduces as ΔK increases until it reaches 0° at around ΔK ≈ 45 MPa$\sqrt{m}$. The ASTM E647 standard (FCGR experimental standard, described in Chapter 3) requires that the main crack to grow in a horizontal direction and suggested that the FCGR result would be invalid if θ_C > 20°. However, the crack path remains the same even after a rigorous realignment of two FCGR interrupted tests that was conducted afterwards.

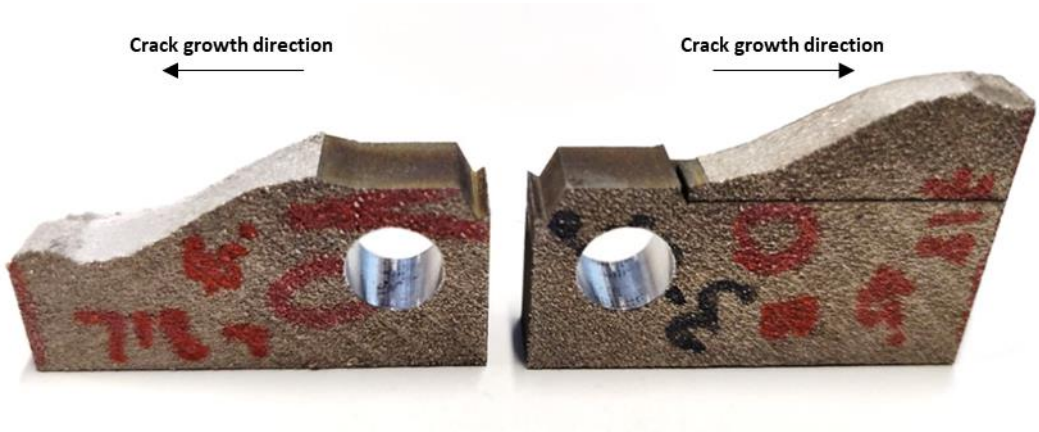

Figure 133 Fractured CT sample of SLM Inconel 718 alloy. The image above consists of a single CT sample that fractured after the FCGR test.

When θ_C > 20° occurs, the compliance polynomial equation shown in equation (5), Chapter 3, would underestimates the actual crack length, and therefore the crack growth rate would also be underestimated [165]. In addition, the SIF value will be overestimated by up to 10% depending on the angle of θ_C. It is important to note that the FCGR graph in Figure 131 violates the "θ_C < 20°" condition. However, based on the FCGR out-of-plane study by Forth et al. [165] on aluminium alloy 2025-T6, the error in measuring the crack size due to the high angle of θ_C (up to 40°) would only slightly reduce the crack growth rate (well below 1 log) and increase the ΔK_{th} value by about 15 – 20 %. Figure 134 shows how θ_C can affect the ΔK and da/dN values. This same study was being used by ASTM E647 to set the θ_C limit to 20°, because as shown in Figure 134, at θ_C = 1 – 26°, the difference in ΔK and da/dN values value is still judged as insignificant. Therefore, based on the experimental result reported by Forth et al. [165] on Al 2025 alloy, the threshold value recorded in this study (ΔK_{th} = 7.0 MPa$\sqrt{m}$, θ_C ≈ 30°), should be lowered by ≈15

%. Thus, the threshold value reported by Konecna et al. of $\Delta K_{th} \approx 3.0$ MPa$\sqrt{m}$ is still considered to be extremely low for a nickel-based superalloy.

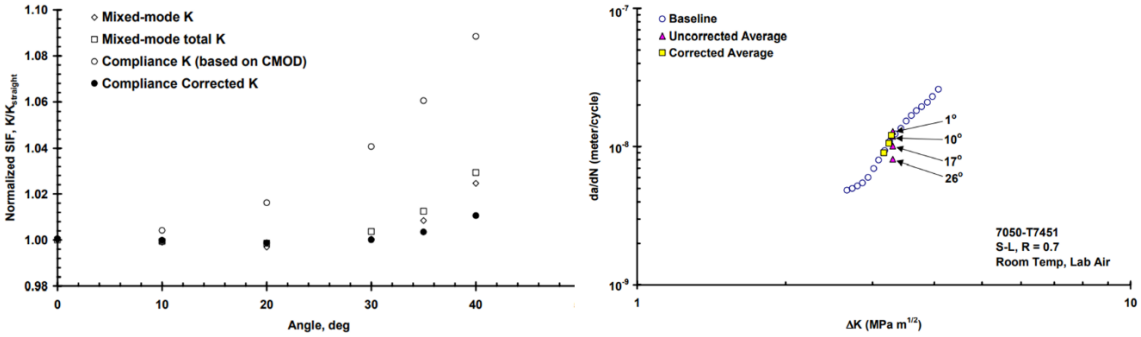

Figure 134 Effect of θ_C onto SIF and da/dN. Result reported by Forth et al. on aluminium alloy 2025-T6 [165]

To study the relationship between the crack growth pathway and the microstructure of SLM Inconel 718, high magnification SEM image of the fractured profile at the threshold and the Paris region is shown in Figure 135. Similar to SLM Inconel 738, there is no correlation between the crack grow pathway and the meltpool boundary, or the cell growth direction. As shown in Figure 135, the global crack growth direction in the threshold region is $\theta_C = 30°$. The local crack growth pathway appears to change direction up to $\theta_C = 55°$, and as low as $\theta_C = 15°$, which creates a slight asperity in the crack profile. Based on Figure 133, the fractured surface at the threshold region still appears to be smooth compared to the high-magnitude zig-zag crack profile seen in SLM Inconel 738 C45BD sample. Because of this the effect of crack growth retardation is lower in SLM Inconel 718, and therefore it has a higher ΔK_{th} value as compared to SLM Inconel 738 C45BD sample.

The threshold region has the highest global θ_C value, which suggest that the crack growth behaviour near the threshold region is greatly intergranular as majority of the grain boundaries are orientated along the BD. This will be further examined by EBSD analysis to reveal the grain map across the crack growth pathway. On the other hand, the local crack growth direction in the Paris region changes at a higher angle that creates a rougher crack profile, which then contributes to a lower global θ_C value. The θ_C value reduces as the magnitude of ΔK increases. This

observation suggests that although the grain boundary in SLM Inconel 718 might be a preferred crack growth pathway, it is also depending on the SIF magnitude experienced by the crack tip. As the magnitude of ΔK is increased (i.e. from the threshold region to the Paris region), the crack growth direction starts to skew away from the BD orientation to propagate in a direction perpendicular to the loading direction.

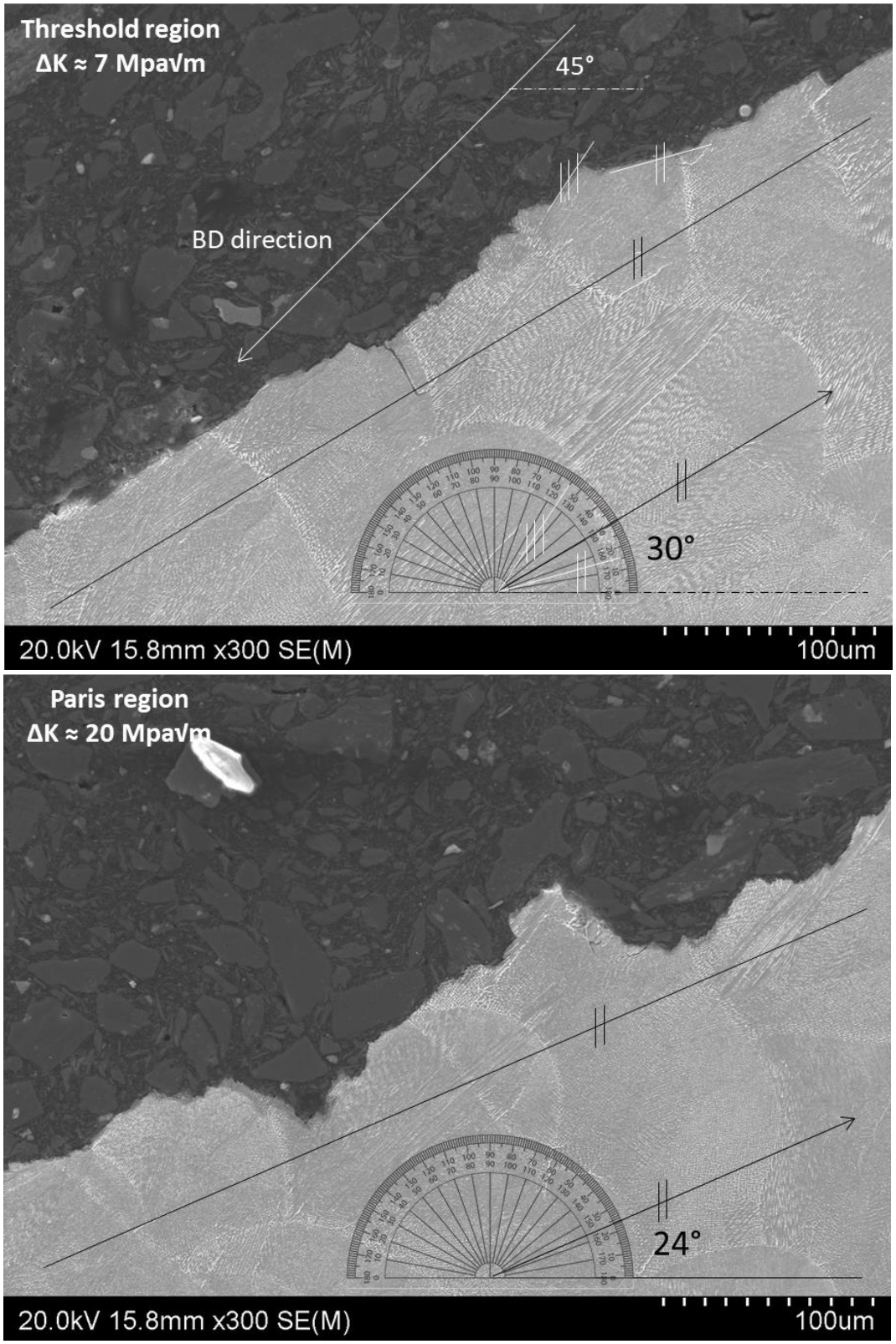

Figure 135 High magnification of the fractured profile for SLM Inconel 718, C45BD. Top: threshold region at ΔK ≈ 7 MPa$\sqrt{m}$. Bottom: Paris region at ΔK ≈ 20 MPa$\sqrt{m}$. The crack growth direction is measured using the parallel lines on the protractor.

As shown in Figure 136, two EBSD analysis (Figure 136a: low magnification and Figure 136b: high magnification) were conducted on the FCGR interrupted test sample of SLM Inconel 718. The interrupted FCGR test started at ΔK = 10.0 MPa$\sqrt{m}$ and ended at ΔK = 7.9 MPa$\sqrt{m}$,

which is near to the threshold region. Based on Figure 136a, the crack pathway appears to travel along the grain boundary ($\theta_c \approx 45°$), and occasionally across the grain boundary in a horizontal direction. A higher magnification image at the crack tip in Figure 136b clearly demonstrates the mix of intergranular (more dominant) and transgranular fracture which causes the global crack growth direction to skew towards the BD orientation, instead of propagating straight/horizontally. This is different from the crack propagation mode in the SLM Inconel 738 C45BD sample, where intergranular fracture is not dominant in the threshold region, producing a globally straight crack growth direction, with a continuously zig-zag (branch) crack profile. Therefore, the effect of crack retardation near the threshold region is lower in SLM Inconel 718 as compared SLM Inconel 738 for C45BD sample. Changing the orientation of BD from 45° to a higher angle could help promote crack branching in SLM Inconel 718 as increasing the angle of grain boundary higher than 45° in relative to the crack growth direction could make it harder for the crack to continue propagate intergranular. Though, the best grain boundary angle, or BD angle relative to its loading direction at which FCGR retardation effect can be maximise is still a research area that needs to be further explored.

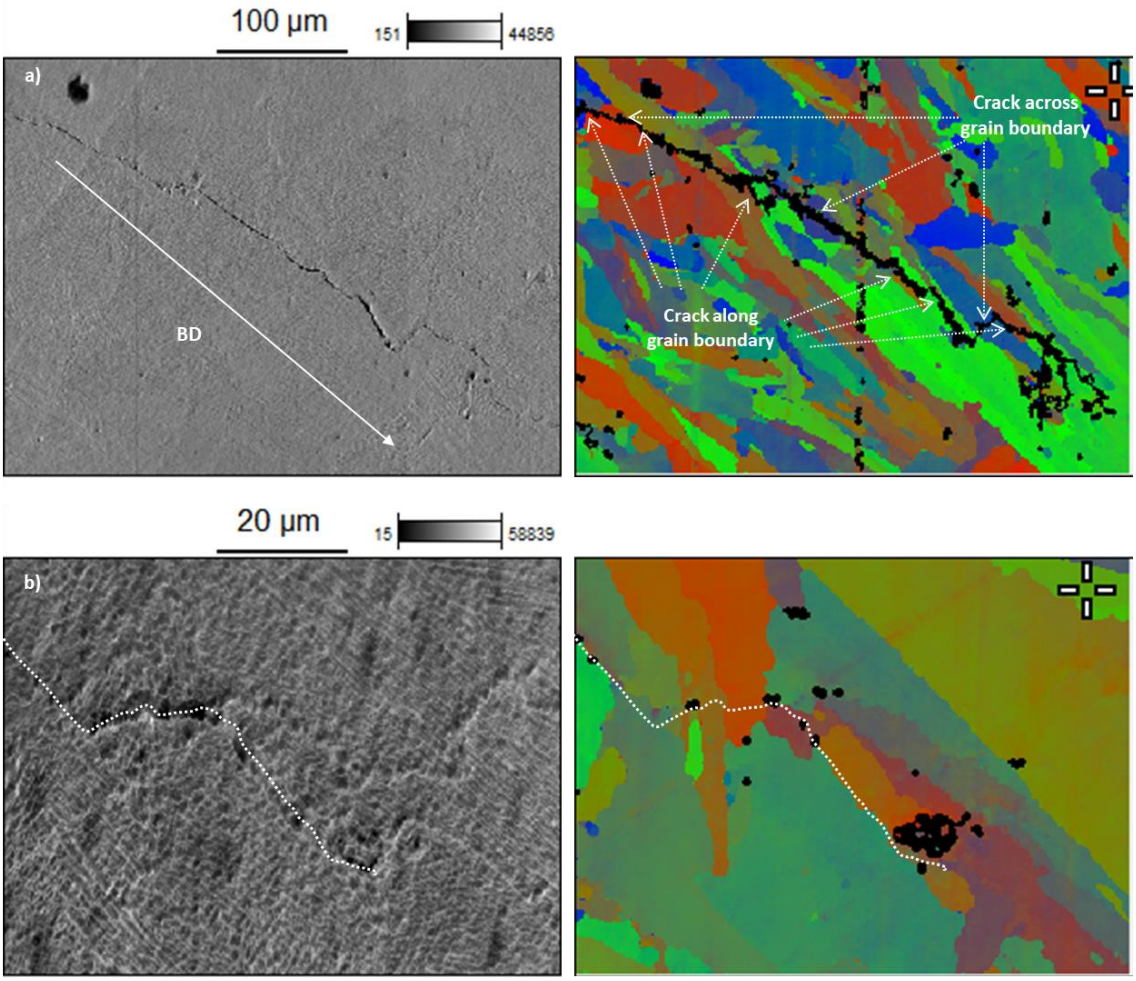

Figure 136 EBSD analysis (right) corresponding to its SEM images (left) on the interrupted FCGR test of SLM Inconel 718 alloy a) middle of crack growth b) crack tip

The difference in the dominant fracture mode of SLM Inconel 738 and SLM Inconel 718 suggests that the grain boundary in SLM Inconel 718 is more brittle compared to the grain boundary in SLM Inconel 738. One possible explanation is because of the induced brittle Laves phase that form along the grain of SLM Inconel 718. Inconel 718 alloys derives its strengthening phase mainly from the body centred tetragonal (B.C.T.) γ" precipitate, Ni_3Nb of 13 – 15 % vol. % and F.C.C γ' precipitate, Ni_3 (Al, Ti) of 4 vol. % [166, 167]. The disk-shaped γ" particle only formed on nickel-based superalloy with niobium, Nb in excess of 4 wt%, which is ideal for Inconel 718. The most significant feature of γ" is its ability to form at moderate temperature, which makes Inconel 718 alloy easy to weld compared to other Inconel alloys [63]. However, in as-built SLM Inconel 718, γ' and γ'' phase precipitates are difficult to form due to the high cooling rate. Instead, brittle H.C.P. Laves phase can easily form [168]. Laves phase in SLM Inconel 718 system is mainly composed of Nb, and based on the Nb-rich clusters, the majority

of the precipitated particles that are lying along the grain boundary for SLM Inconel 718 is highly enriched with Laves phase [168, 169]. Therefore, the brittleness of SLM Inconel 718 grain boundary, which makes it a preferred crack path, could be associated with the induced Laves phase that form along the grain boundary due to the SLM process.

Since the grain boundary plays an important role on the crack growth pathway, the BD orientation in SLM Inconel alloys would also significantly affect the crack growth pathway, and thus affecting the FCGR threshold value. The distribution of grain boundary in C45BD sample for SLM Inconel 738 alloy stimulates crack branching, while its global crack growth direction still follows the maximum tensile stress plane. However, in SLM Inconel 718, because of the dominant intergranular fracture, the global crack growth direction is diverted towards the BD orientation, away from the maximum tensile stress plane which then eliminates the generation of high fractured surface roughness that can cause continuous crack retardation effect. Therefore, the BD orientation in SLM Inconel 718 can still be optimised by increasing the BD orientation higher than 45° to promote crack branching, while maintaining a straight global crack growth direction.

5.6 Summary

The FCGR performance between as-built SLM Inconel 738, Inconel 718 and Inconel 625 (taken from Hu et al. [113] and Poulin et al. [114] reports) are compared, in terms of ΔK_{th} and Paris constant. Based on the FCGR graph of SLM Inconel 738 the effect of laser power (between P = 320 W and 270 W) on the FCGR parameters are minor, while the influence of BD parameters (between C⊥BD, C//BD and C45BD) are shown to be significant, especially in the threshold region.

The C45BD sample in SLM Inconel 738 have the highest threshold value and the roughest surface fracture. The rough surface fracture in the C45BD sample is caused by the continuous crack branching triggered by the constant encounter of crack with grain boundaries that is orientated 45° to the crack growth direction. Consequently, a continuously high crack retardation effect is maintained throughout the life of the crack which then contributed into higher FCGR resistance. On the other hand, because of the BD dependent–grain orientation in SLM material, the crack in the C//BD and C⊥BD have a significantly lower chance of encountering a grain boundary that is orientated 45° to the crack growth direction, which result in a smooth fracture surface for both sample types.

The fracture mode in SLM Inconel 738 alloy is shown to be dominantly transgranular. Nevertheless, there are instances where intergranular fracture occurs and deviate the crack path, especially for the C45BD samples. The intergranular cracking behaviour is dependent on the orientation of the grain boundary, i.e. crack does not propagate through a high angle or 90° grain boundary. Moreover, the local brittleness of the grain boundary is dependent by the brittle carbide precipitates that segregated along the grain boundary. The effect of microstructure defect (micro pores) is shown to be insignificant at lower SIF magnitude. The presence of micro pores in SLM Inconel 738 only start to interfere with the FCGR performance at the end spectrum of Paris region.

The FCGR threshold value for SLM Inconel 718 is slightly lower compared to SLM Inconel 738 and SLM Inconel 625 (based on Hu et al. [113] and Poulin et al. [114] reports). The crack growth behaviour in SLM Inconel 718 is shown to be more dominantly intergranular compared to SLM Inconel 738. This is possibly caused by the induced brittle Laves phase that segregated along the grain boundary due to the high cooling rate in SLM process. As a result, the 45° oriented grain boundaries in the C45BD sample does not promote a zig-zag crack profile, instead, crack continues to propagate through the grain boundary and occasionally travel across the grain.

As a reflection, the interaction between the crack growth and SLM microstructure in this study is only a based on an 2D micrograph which might not represent the actual 3D situation. Even though a proof of concept can be achieved, the actual percentage of crack pathway deviation due to grain boundary orientation in each of the sample cannot be accurately quantified. In addition, since higher angle of crack branching will increase the crack growth retardation effect, the angle of BD in SLM Inconel 738 can still be optimised to increase FCGR resistance. Moreover, the high brittleness of grain boundary in the SLM Inconel 718 sample can be changed by post heat treatment, but this thesis only study SLM as-built conditions. The angle of BD can still be optimised to increase FCGR resistance by conducting experiments on discovering the relationship between BD angles (i.e. C15BD, C30BD, C60BD, C75BD) and ΔK_{th} value, which would provide significant insight in controlling the FCGR threshold value for SLM alloys.

6 Conclusion

The main conclusions of this thesis are summarised as follows:

1. Based on the FCGR parameters of SLM Co-Cr-Mo superalloy (which includes FCGR threshold, ΔK_{th}, and Paris constants, C and m), the FCGR resistance is dependent on the crack growth direction (C) in relation to the building direction (BD) orientation: cracks propagate at a higher rate when C is perpendicular to the BD, C⊥BD, compared to when C is parallel to BD, C//BD. The effect of BD orientation on the FCGR behaviour is related to the crack growth pathway in the two samples orientation tested, where a crack in the C//BD sample would branch out more easily and zigzagged at a higher amplitude compared to the crack in the C⊥BD sample. Based on fractographic analysis of the fractured surface, it is shown that the presence of lack of fusion (LOF) at the amount of less than 1 % does not significantly affect the crack growth pathway, and consequently does not influence the FCGR parameters.

2. For the crack pathway in SLM Co-Cr-Mo alloy, it has been identified that the crack has dominantly propagated in a transgranular manner in both C⊥BD and C//BD samples. The faceted fracture feature that was cause due to crack propagating along the $\{111\}_{fcc}$ planes and the BD-dependent columnar grains orientation in SLM materials have resulted in a relatively longer crack segment for the C//BD sample, thus giving it higher amplitude of zigzagged crack profile as compared to the C⊥BD sample. It has also been found that crack branching occurs in two occasions, 1) when the orientation of the $\{111\}_{fcc}$ planes of a neighbouring grains is forcing the main crack to deviate in an unfavourable (high angle) directions, or 2) in the presence of low angle grain boundary that could potentially deviate the crack growth pathway. The higher chance for a crack to branch out in the C//BD sample causes higher crack retardation effect thus reducing its crack growth rate. Therefore, the C//BD sample has a higher ΔK_{th} value as compared to the C⊥BD sample.

3. Based on the FCGR parameters of C⊥BD, C//BD and as-Cast (provided by the literature) of Co-Cr alloys, the integration of Donahue's Law suggests that the fatigue life of a hip prosthesis is in the order of C//BD >> as-Cast > C⊥BD. This analysis highlights the importance of BD orientation in SLM production as the selection of BD could either make as-SLM material tougher or weaker compared to as-cast materials.

4. The influence of BD orientations (between C⊥BD, C//BD and C45BD) on the FCGR parameters of SLM Inconel 738 superalloy are shown to be significant, especially on the ΔK_{th} value. The C45BD sample is shown to have the highest ΔK_{th} value, as well as the most tortuous fracture profile (highest fracture surface roughness), followed by the C//BD sample, and finally the C⊥BD sample. The rough fracture surface of the C45BD sample is caused by the continuous crack branching, triggered by the constant encounter of a crack with a grain boundary that is orientated at a 45° angle. Consequently, high crack retardation effect is maintained throughout the threshold region which then contributed into a higher FCGR resistance. On the other hand, crack in the C//BD and C⊥BD sample have a significantly lower chance of encountering a grain boundary that is orientated at a 45°angle, which resulted in a smooth fracture surface and low FCGR resistance.

5. It has been identified that majority of the cracks in SLM Inconel 738 superalloy propagated transgranularly, with instances of intergranular fracture that deviate the crack path, especially for the C45BD samples. It is shown that intergranular fracture (crack propagating along the grain boundary) in SLM Inconel 738 superalloy is useful in promoting tortuous crack growth pathway, as demonstrated in the C45BD sample. The occurrence of intergranular fracture in the threshold region is highly dependent on orientation of grain boundaries in respect to the crack growth direction. For example, there is hardly any intergranular cracking in C⊥BD sample as most grain boundaries is orientated at a 90° angle in respect to the crack growth direction, while a grain boundary that is orientated 45° to the crack growth direction is shown to significantly promote

crack branching due to intergranular cracking. In addition, the local brittleness of a grain boundary is also dependent on the segregation of the brittle carbide phase along the grain boundary.

6. For SLM Inconel 718 superalloy, the crack growth behaviour is shown to be more dominantly intergranular compared to SLM Inconel 738 superalloy. The reason for its grain boundary being more brittle compared to SLM Inconel 738 is possibly due to the segregation of the brittle hcp-Laves that is induced in SLM Inconel 718 due to the high cooling rate in SLM process. The crack growth direction in a C45BD sample is shown to be growing at a 30° angle in the threshold region as crack continues to propagate through the grain boundary and occasionally travel across the grains. As a result, the local crack growth direction does not change direction in a zigzag manner, and therefore, the crack retardation effect (FCGR resistance) is reduced. Therefore, the best BD orientation in relative to its loading direction at which FCGR retardation effect can be maximised is still an area that needs to be further explored.

List of References

1. ASTM, *ASTM Standard F2792-12a: Standard terminology for additive manufacturing technologies.* ASTM International, 2012.
2. Ashley, S., *Rapid prototyping is coming of age.* Mechanical Engineering, 1995. **117**(7): p. 62.
3. Tofail, S.A., et al., *Additive manufacturing: scientific and technological challenges, market uptake and opportunities.* Materials today, 2018. **21**(1): p. 22-37.
4. Thompson, S.M., et al., *An overview of Direct Laser Deposition for additive manufacturing; Part I: Transport phenomena, modeling and diagnostics.* Additive Manufacturing, 2015. **8**: p. 36-62.
5. Selcuk, C., *Laser metal deposition for powder metallurgy parts.* Powder Metallurgy, 2011. **54**(2): p. 94-99.
6. Levy, G.N., R. Schindel, and J.-P. Kruth, *Rapid manufacturing and rapid tooling with layer manufacturing (LM) technologies, state of the art and future perspectives.* CIRP annals, 2003. **52**(2): p. 589-609.
7. Frazier, W.E., *Metal additive manufacturing: a review.* Journal of Materials Engineering and performance, 2014. **23**(6): p. 1917-1928.
8. Ladd, C., et al., *3D printing of free standing liquid metal microstructures.* Advanced Materials, 2013. **25**(36): p. 5081-5085.
9. Zenou, M., A. Sa'Ar, and Z. Kotler, *Laser jetting of femto-liter metal droplets for high resolution 3D printed structures.* Scientific reports, 2015. **5**(1): p. 1-10.
10. Visser, C.W., et al., *Toward 3D printing of pure metals by laser-induced forward transfer.* Advanced materials, 2015. **27**(27): p. 4087-4092.
11. Murr, L.E., et al., *Next-generation biomedical implants using additive manufacturing of complex, cellular and functional mesh arrays.* Philosophical Transactions of the Royal Society A: Mathematical, Physical and Engineering Sciences, 2010. **368**(1917): p. 1999-2032.
12. Chen, Z.W., et al., *Grain Growth During Keyhole Mode Pulsed Laser Powder Bed Fusion of IN738LC.* JOM, 2020. **72**(3): p. 1074-1084.
13. Darvish, K., Z.W. Chen, and T. Pasang, *Reducing lack of fusion during selective laser melting of CoCrMo alloy: Effect of laser power on geometrical features of tracks.* Materials & Design, 2016. **112**: p. 357-366.
14. Chen, Z., M. Phan, and K. Darvish, *Grain growth during selective laser melting of a Co–Cr–Mo alloy.* Journal of Materials Science, 2017. **52**(12): p. 7415-7427.
15. Emelogu, A., et al., *Additive manufacturing of biomedical implants: A feasibility assessment via supply-chain cost analysis.* Additive Manufacturing, 2016. **11**: p. 97-113.
16. Lott, P., et al., *Design of an optical system for the in situ process monitoring of selective laser melting (SLM).* Physics Procedia, 2011. **12**: p. 683-690.
17. Campbell, T., et al., *," Could 3D printing change the world", Technologies, Potential, and Implications of Additive Manufacturing, Atlantic Council, Washington, DC.* Washington, DC: Atlantic Council Strategic Foresight Initiative, 2011.
18. Marks, P., *3D printing takes off with the world's first printed plane*. 2011, Elsevier.
19. Bartolotta, P.A. and D.L. Krause, *Titanium aluminide applications in the high speed civil transport.* 1999.
20. Wu, T., et al., *A framework for optimizing the design of injection molds with conformal cooling for additive manufacturing.* Procedia Manufacturing, 2015. **1**: p. 404-415.
21. Bak, D., *Rapid prototyping or rapid production? 3D printing processes move industry towards the latter.* Assembly Automation, 2003. **23**(4): p. 340-345.
22. Shamsaei, N., et al., *An overview of Direct Laser Deposition for additive manufacturing; Part II: Mechanical behavior, process parameter optimization and control.* Additive Manufacturing, 2015. **8**: p. 12-35.

23. Yadollahi, A., et al., *Effects of building orientation and heat treatment on fatigue behavior of selective laser melted 17-4 PH stainless steel.* International Journal of Fatigue, 2017. **94**: p. 218-235.
24. Yadollahi, A., et al., *Effects of process time interval and heat treatment on the mechanical and microstructural properties of direct laser deposited 316L stainless steel.* Materials Science and Engineering: A, 2015. **644**: p. 171-183.
25. Daniewicz, S. and N. Shamsaei, *An introduction to the fatigue and fracture behavior of additive manufactured parts.* International Journal of Fatigue, 2017. **2**(94): p. 167.
26. Bian, L., S.M. Thompson, and N. Shamsaei, *Mechanical properties and microstructural features of direct laser-deposited Ti-6Al-4V.* Jom, 2015. **67**(3): p. 629-638.
27. Stephens, R.I., et al., *Metal fatigue in engineering*. 2000: John Wiley & Sons.
28. Sterling, A.J., et al., *Fatigue behavior and failure mechanisms of direct laser deposited Ti–6Al–4V.* Materials Science and Engineering: A, 2016. **655**: p. 100-112.
29. Leuders, S., et al., *Fatigue strength prediction for titanium alloy TiAl6V4 manufactured by selective laser melting.* Metallurgical and materials transactions A, 2015. **46**(9): p. 3816-3823.
30. Kobryn, P. and S. Semiatin. *Mechanical properties of laser-deposited Ti-6Al-4V*. in *2001 International Solid Freeform Fabrication Symposium*. 2001.
31. Edwards, P. and M. Ramulu, *Fatigue performance evaluation of selective laser melted Ti–6Al–4V.* Materials Science and Engineering: A, 2014. **598**: p. 327-337.
32. Haan, J., et al., *Effect of subsequent Hot Isostatic Pressing on mechanical properties of ASTM F75 alloy produced by Selective Laser Melting.* Powder Metallurgy, 2015. **58**(3): p. 161-165.
33. Kasperovich, G. and J. Hausmann, *Improvement of fatigue resistance and ductility of TiAl6V4 processed by selective laser melting.* Journal of Materials Processing Technology, 2015. **220**: p. 202-214.
34. Jamshidinia, M., F. Kong, and R. Kovacevic. *The numerical modeling of fatigue properties of a bio-compatible dental implant produced by Electron Beam Melting®(EBM)*. in *International Solid Freeform Fabrication Symposium*. 2013.
35. Spierings, A.B., T.L. Starr, and K. Wegener, *Fatigue performance of additive manufactured metallic parts.* Rapid prototyping journal, 2013.
36. Stoffregen, H.A., K. Butterweck, and E. Abele. *Fatigue analysis in selective laser melting: review and investigation of thin-walled actuator housings*. in *25th Solid Freeform Fabrication Symposium*. 2014.
37. Wycisk, E., et al., *Effects of defects in laser additive manufactured Ti-6Al-4V on fatigue properties.* Physics Procedia, 2014. **56**: p. 371-378.
38. Aboulkhair, N.T., et al., *Improving the fatigue behaviour of a selectively laser melted aluminium alloy: Influence of heat treatment and surface quality*. Materials & Design, 2016. **104**: p. 174-182.
39. Kajima, Y., et al., *Fatigue strength of Co–Cr–Mo alloy clasps prepared by selective laser melting.* Journal of the mechanical behavior of biomedical materials, 2016. **59**: p. 446-458.
40. Ahn, D., H. Kim, and S. Lee, *Surface roughness prediction using measured data and interpolation in layered manufacturing.* Journal of materials processing technology, 2009. **209**(2): p. 664-671.
41. Boschetto, A., V. Giordano, and F. Veniali, *Modelling micro geometrical profiles in fused deposition process.* The International Journal of Advanced Manufacturing Technology, 2012. **61**(9-12): p. 945-956.
42. Strano, G., et al., *Surface roughness analysis, modelling and prediction in selective laser melting.* Journal of Materials Processing Technology, 2013. **213**(4): p. 589-597.
43. Takaichi, A., et al., *Microstructures and mechanical properties of Co–29Cr–6Mo alloy fabricated by selective laser melting process for dental applications.* Journal of the mechanical behavior of biomedical materials, 2013. **21**: p. 67-76.
44. Richard, H.A. and M. Sander, *Fatigue crack growth*. 2016: Springer.

45. Griffith, A.A., *VI. The phenomena of rupture and flow in solids.* Philosophical transactions of the royal society of london. Series A, containing papers of a mathematical or physical character, 1921. **221**(582-593): p. 163-198.
46. Irwin, G.R., *Analysis of stresses and strains near the end of a crack transversing a plate.* Trans. ASME, Ser. E, J. Appl. Mech., 1957. **24**: p. 361-364.
47. Rice, J.R., *A path independent integral and the approximate analysis of strain concentration by notches and cracks.* 1968.
48. Irwin, G., *Handbuch der Physik, VI, ed.* Fli~ gge, 1958: p. 558-590.
49. Dugdale, D.S., *Yielding of steel sheets containing slits.* Journal of the Mechanics and Physics of Solids, 1960. **8**(2): p. 100-104.
50. Hahn, G.T. and A.R. Rosenfield, *Local yielding and extension of a crack under plane stress.* Acta Metallurgica, 1965. **13**(3): p. 293-306.
51. E399, A. *Standard test method for plane-strain fracture toughness of metallic materials*. in *American Society of Testing and Materials*. 1997.
52. Paris, P. and F. Erdogan, *A critical analysis of crack propagation laws.* 1963.
53. Paris, P.C., *A rational analytic theory of fatigue.* The trend in engineering, 1961. **13**: p. 9.
54. Bulloch, J. and A. Callagy, *A detailed study of the relationship between fatigue crack growth rate and striation spacing in a range of low alloy ferritic steels.* Engineering Failure Analysis, 2010. **17**(1): p. 168-178.
55. Donahue, R.J., et al., *Crack opening displacement and the rate of fatigue crack growth.* International Journal of Fracture Mechanics, 1972. **8**(2): p. 209-219.
56. Tammas-Williams, S., et al., *The influence of porosity on fatigue crack initiation in additively manufactured titanium components.* Scientific reports, 2017. **7**(1): p. 1-13.
57. Lai, M. and W. Ferguson, *Effect of specimen thickness on fracture toughness.* Engineering fracture mechanics, 1986. **23**(4): p. 649-659.
58. Forman, R.G., V. Kearney, and R. Engle, *Numerical analysis of crack propagation in cyclic-loaded structures.* 1967.
59. Erdogan, F. and M. Ratwani, *Fatigue and fracture of cylindrical shells containing a circumferential crack.* International Journal of Fracture Mechanics, 1970. **6**(4): p. 379-392.
60. Elber, W., *The significance of fatigue crack closure*, in *Damage tolerance in aircraft structures*. 1971, ASTM International.
61. Wolf, E., *Fatigue crack closure under cyclic tension.* Engineering fracture mechanics, 1970. **2**(1): p. 37-45.
62. Gray, G., J. Williams, and A. Thompson, *Roughness-induced crack closure: an explanation for microstructurally sensitive fatigue crack growth.* Metallurgical Transactions A, 1983. **14**(2): p. 421-433.
63. Donachie, M.J. and S.J. Donachie, *Superalloys: a technical guide*. 2002: ASM international.
64. Niinomi, M., *Recent metallic materials for biomedical applications.* Metallurgical and materials transactions A, 2002. **33**(3): p. 477-486.
65. Kellner, T., *The FAA cleared the first 3D printed part to fly in a commercial jet engine from GE.* GE Reports, 2015. **14**.
66. ASTM, A., *F75: Standard Specification for Cobalt-28 Chromium-6 Molybdenum Alloy Castings and Casting Alloy for Surgical Implants (UNS R30075).* West Conshohocken: ASTM International, 2007.
67. Koutsoukis, T., et al., *Selective laser melting technique of Co-Cr dental alloys: a review of structure and properties and comparative analysis with other available techniques.* Journal of Prosthodontics, 2015. **24**(4): p. 303-312.
68. Castillo-Oyagüe, R., et al., *The effect of surface treatments on the microroughness of laser-sintered and vacuum-cast base metal alloys for dental prosthetic frameworks.* Microscopy research and technique, 2012. **75**(9): p. 1206-1212.
69. Zhuang, L. and E. Langer, *Study on Fatigue Threshold Behaviour and Fatigue Crack Propagation in a Cast Co-Cr-Mo Alloy Used for Surgical Implants.* Fatigue & Fracture of Engineering Materials & Structures, 1989. **12**(4): p. 283-293.

70. Chen, Z., et al., *Solidification during selective laser melting of Co-29Cr-6Mo alloy.* JOM, 2019. **71**(2): p. 691-696.
71. Kurosu, S., N. Nomura, and A. Chiba, *Microstructure and mechanical properties of Co-29Cr-6Mo alloy aged at 1023 K.* Materials transactions, 2007. **48**(6): p. 1517-1522.
72. Chiba, A., et al. *Mechanical properties of forged low Ni and C-containing Co-Cr-Mo biomedical implant alloy*. in *Materials Science Forum*. 2005. Trans Tech Publ.
73. Lee, S.-H., et al., *Effect of heat treatment on microstructure and mechanical properties of Ni-and C-free Co–Cr–Mo alloys for medical applications.* Materials transactions, 2005. **46**(8): p. 1790-1793.
74. Lee, S.-H., et al., *Effect of carbon addition on microstructure and mechanical properties of a wrought Co–Cr–Mo implant alloy.* Materials transactions, 2006. **47**(2): p. 287-290.
75. Saldívar-García, A. and H. López, *Microstructural effects on the wear resistance of wrought and as-cast Co-Cr-Mo-C implant alloys.* Journal of Biomedical Materials Research Part A: An Official Journal of The Society for Biomaterials, The Japanese Society for Biomaterials, and The Australian Society for Biomaterials and the Korean Society for Biomaterials, 2005. **74**(2): p. 269-274.
76. Lee, B., H. Matsumoto, and A. Chiba, *Fractures in tensile deformation of biomedical Co–Cr–Mo–N alloys.* Materials Letters, 2011. **65**(5): p. 843-846.
77. Ueki, K., et al., *Synchronous improvement in strength and ductility of biomedical Co–Cr–Mo alloys by unique low-temperature heat treatment.* Materials Science and Engineering: A, 2019. **739**: p. 53-61.
78. INCO, *Tehcnical Data on Alloy IN-738*. 1981: New York, NY, International Nickel Company.
79. Grange, D., et al., *Processing a non-weldable nickel-base superalloy by Selective Laser Melting: role of the shape and size of the melt pools on solidification cracking.* Materialia, 2020. **12**: p. 100686.
80. Perevoshchikova, N., et al., *Optimisation of selective laser melting parameters for the Ni-based superalloy IN-738 LC using Doehlert's design.* Rapid Prototyping Journal, 2017. **23**(5): p. 881-892.
81. Zhang, X., et al., *Cracking mechanism and susceptibility of laser melting deposited Inconel 738 superalloy.* Materials & Design, 2019. **183**: p. 108105.
82. Dinda, G., A. Dasgupta, and J. Mazumder, *Laser aided direct metal deposition of Inconel 625 superalloy: Microstructural evolution and thermal stability.* Materials Science and Engineering: A, 2009. **509**(1-2): p. 98-104.
83. Parimi, L.L., et al., *Microstructural and texture development in direct laser fabricated IN718.* Materials Characterization, 2014. **89**: p. 102-111.
84. Xiao, H., et al., *Laves phase control of Inconel 718 alloy using quasi-continuous-wave laser additive manufacturing.* Materials & Design, 2017. **122**: p. 330-339.
85. Chauvet, E., et al., *Hot cracking mechanism affecting a non-weldable Ni-based superalloy produced by selective electron Beam Melting.* Acta Materialia, 2018. **142**: p. 82-94.
86. Engeli, R., et al., *Processability of different IN738LC powder batches by selective laser melting.* Journal of Materials Processing Technology, 2016. **229**: p. 484-491.
87. Cloots, M., P.J. Uggowitzer, and K. Wegener, *Investigations on the microstructure and crack formation of IN738LC samples processed by selective laser melting using Gaussian and doughnut profiles.* Materials & Design, 2016. **89**: p. 770-784.
88. King, W.E., et al., *Observation of keyhole-mode laser melting in laser powder-bed fusion additive manufacturing.* Journal of Materials Processing Technology, 2014. **214**(12): p. 2915-2925.
89. Rubenchik, A.M., W.E. King, and S.S. Wu, *Scaling laws for the additive manufacturing.* Journal of Materials Processing Technology, 2018. **257**: p. 234-243.
90. Qi, T., et al., *Selective laser melting of Al7050 powder: Melting mode transition and comparison of the characteristics between the keyhole and conduction mode.* Materials & Design, 2017. **135**: p. 257-266.
91. Yadollahi, A. and N. Shamsaei, *Additive manufacturing of fatigue resistant materials: Challenges and opportunities.* International Journal of Fatigue, 2017. **98**: p. 14-31.

92. Lee, H.W., et al., *Microstructure and mechanical anisotropy of CoCrW alloy processed by selective laser melting.* Materials Science and Engineering: A, 2019. **749**: p. 65-73.
93. Lu, Y., et al., *Investigation on the microstructure, mechanical property and corrosion behavior of the selective laser melted CoCrW alloy for dental application.* Materials Science and Engineering: C, 2015. **49**: p. 517-525.
94. Okazaki, Y., *Comparison of fatigue properties and fatigue crack growth rates of various implantable metals.* Materials, 2012. **5**(12): p. 2981-3005.
95. Ritchie, R. and P. Lubock, *Fatigue life estimation procedures for the endurance of a cardiac valve prosthesis: stress/life and damage-tolerant analyses.* 1986.
96. Marrey, R.V., et al., *Fatigue and life prediction for cobalt-chromium stents: a fracture mechanics analysis.* Biomaterials, 2006. **27**(9): p. 1988-2000.
97. ASTM, *ASTM E647-13a: Standard Test Method for Measurement of Fatigue Crack Growth Rates.* 2014.
98. Riemer, A., et al., *On the fatigue crack growth behavior in 316L stainless steel manufactured by selective laser melting.* Engineering Fracture Mechanics, 2014. **120**: p. 15-25.
99. Bucci, R., *Development of a proposed ASTM standard test method for near-threshold fatigue crack growth rate measurement*, in *Fatigue Crack Growth Measurement and Data Analysis*. 1981, ASTM International.
100. E647-83, A., *Standard test method for constant-load-amplitude fatigue crack growth rates above 10^-8 m/cycle.* ASTM International, 1983. **03.01**: p. 71&730.
101. Saxena, A., et al., *Computer-controlled decreasing stress intensity technique for low rate fatigue crack growth testing.* Journal of Testing and Evaluation, 1978. **6**(3): p. 167-174.
102. Zhuang, L. and E. Langer, *Observations on the faceted fatigue fracture of cast Co− Cr− Mo alloy used for surgical implants.* Metallurgical Transactions A, 1989. **20**(1): p. 99-103.
103. Zhuang, L. and E. Langer, *Effects of cooling rate control during the solidification process on the microstructure and mechanical properties of cast Co-Cr-Mo alloy used for surgical implants.* Journal of materials science, 1989. **24**(2): p. 381-388.
104. Masounave, J. and J.-P. Baflon, *Effect of grain size on the threshold stress intensity factor in fatigue of a ferritic steel.* Scripta Metallurgica, 1976. **10**(2): p. 165-170.
105. Taira, S., K. Tanaka, and M. Hoshina, *Grain size effect on crack nucleation and growth in long-life fatigue of low-carbon steel*, in *Fatigue Mechanisms*. 1979, ASTM International.
106. Taylor, D. *An analysis of data on fatigue crack propagation thresholds*. in *Proc. Fatigue*. 1984.
107. Higo, Y., A. Pickard, and J. Knott, *Effects of grain size and stacking fault energy on fatigue-crack-propagation thresholds in Cu-Al aluminium alloys.* Metal Science, 1981. **15**(6): p. 233-240.
108. Bonnheim, N., et al., *Fatigue fracture of a cemented Omnifit CoCr femoral stem: implant and failure analysis.* Arthroplasty today, 2017. **3**(4): p. 234-238.
109. Dall, D.M., et al., *Fracture and loosening of Charnley femoral stems. Comparison between first-generation and subsequent designs.* The Journal of bone and joint surgery. British volume, 1993. **75**(2): p. 259-265.
110. Jazrawi, L.M., et al., *Catastrophic failure of a cemented, collarless, polished, tapered cobalt-chromium femoral stem used with impaction bone-grafting. A report of two cases.* JBJS, 1999. **81**(6): p. 844-7.
111. Lee, E.W. and H.T. Kim, *Early fatigue failures of cemented, forged, cobalt-chromium femoral stems at the neck–shoulder junction.* The Journal of arthroplasty, 2001. **16**(2): p. 236-238.
112. Woolson, S.T., et al., *Fatigue fracture of a forged cobalt-chromium-molybdenum femoral component inserted with cement. A report of ten cases.* JBJS, 1997. **79**(12): p. 1842.

113. Hu, X., et al., *On the fatigue crack growth behaviour of selective laser melting fabricated Inconel 625: Effects of build orientation and stress ratio.* Fatigue & Fracture of Engineering Materials & Structures, 2020. **43**(4): p. 771-787.
114. Poulin, J.-R., V. Brailovski, and P. Terriault, *Long fatigue crack propagation behavior of Inconel 625 processed by laser powder bed fusion: Influence of build orientation and post-processing conditions.* International Journal of Fatigue, 2018. **116**: p. 634-647.
115. Brynk, T., et al., *Fatigue crack growth rate and tensile strength of Re modified Inconel 718 produced by means of selective laser melting.* Materials Science and Engineering: A, 2017. **698**: p. 289-301.
116. Konečná, R., et al., *Long fatigue crack growth in Inconel 718 produced by selective laser melting.* International Journal of Fatigue, 2016. **92**: p. 499-506.
117. Scarlin, R., *Fatigue crack growth in a cast Ni-base alloy.* Materials Science and Engineering, 1975. **21**: p. 139-147.
118. Gauthier, P., H. De Rabaudy, and J. Auvinet, *Secondary cracking process during fatigue crack propagation.* Engineering Fracture Mechanics, 1973. **5**(4): p. 977-981.
119. Zhao, S., Q. Zhang, and L. Liu, *Crack Initiation, Propagation, and Coalescence Experiments in Sandstone Brazilian Disks Containing Pre-Existing Flaws.* Advances in Civil Engineering, 2019. **2019**.
120. Hénaff, G., F. Menan, and G. Odemer, *Influence of corrosion and creep on intergranular fatigue crack path in 2XXX aluminium alloys.* Engineering fracture mechanics, 2010. **77**(11): p. 1975-1988.
121. Kendall, J. and J. King, *Short fatigue crack growth behaviour: data analysis effects.* International Journal of Fatigue, 1988. **10**(3): p. 163-170.
122. Newman Jr, J. and P. Edwards, *Short-crack growth behaviour in an aluminum alloy-an AGARD Cooperative Test Programme*. 1988, ADVISORY GROUP FOR AEROSPACE RESEARCH AND DEVELOPMENT NEUILLY-SUR-SEINE (FRANCE).
123. Suresh, S. and R. Ritchie, *Propagation of short fatigue cracks.* International metals reviews, 1984. **29**(1): p. 445-475.
124. Xiao, L., D. Chen, and M. Chaturvedi, *Effect of boron on fatigue crack growth behavior in superalloy IN 718 at RT and 650 C.* Materials Science and Engineering: A, 2006. **428**(1-2): p. 1-11.
125. Mazur, Z., et al., *Failure analysis of a gas turbine blade made of Inconel 738LC alloy.* Engineering failure analysis, 2005. **12**(3): p. 474-486.
126. Renishaw, *Metal additive manufacturing pamphlet*. 2016. https://resources.renishaw.com/en/details/brochure-metal-additive-manufacturing--85850.
127. Hudak, S., *Fatigue crack growth measurement and data analysis*. Vol. 738. 1981: ASTM International.
128. Paris, P.C., *The fracture mechanics approach to fatigue.* 1964.
129. Yoder, G., L. Cooley, and T. Crooker, *Procedures for precision measurement of fatigue crack growth rate using crack-opening displacement techniques,* in *Fatigue Crack Growth Measurement and Data Analysis*. 1981, ASTM International.
130. Saxena, A. and S. Hudak, *Review and extension of compliance information for common crack growth specimens.* International Journal of Fracture, 1978. **14**(5): p. 453-468.
131. MTS, *MTS TestSuite™ Fracture Templates User Guide*. 2015. p. 100-256-573H.
132. Donald, J. and D. Schmidt, *Computer-controlled stress intensity gradient technique for high rate fatigue crack growth testing.* Journal of Testing and Evaluation, 1980. **8**(1): p. 19-24.
133. Newman, J. *Stress analysis of the compact specimen including the effects of pin loading*. in *Fracture Analysis: Proceedings of the 1973 National Symposium on Fracture Mechanics, Part II*. 1974. ASTM International.
134. Srawley, J.E., *Wide range stress intensity factor expressions for ASTM E 399 standard fracture toughness specimens.* International Journal of Fracture, 1976. **12**(3): p. 475-476.

135. Bucci, R., *Effect of residual stress on fatigue crack growth rate measurement*, in *Fracture Mechanics*. 1981, ASTM International.
136. Bush, R.W., et al. *Fatigue crack growth rate measurements in aluminum alloy forgings: Effects of residual stress and grain flow*. in *Fracture Mechanics: Twenty-Third Symposium*. 1993. ASTM International.
137. Clark, W. and S. Hudak, *Variability in fatigue crack growth rate testing.* Journal of Testing and Evaluation, 1975. **3**(6): p. 454-476.
138. Donald, J., *Preliminary Results of the ASTM E24. 04.03 Round-Robin Test Program on Low Delta-K Fatigue Crack Growth Rates.* ASTM Task Group Report, 1982.
139. Bragg, W.H. and W.L. Bragg, *The reflection of X-rays by crystals.* Proceedings of the Royal Society of London. Series A, Containing Papers of a Mathematical and Physical Character, 1913. **88**(605): p. 428-438.
140. Kikuchi, S., *Diffraction of cathode rays by mica.* Proceedings of the Imperial Academy, 1928. **4**(6): p. 271-274.
141. Kannan, R., *A fracture mechanics study of fatigue in a cobalt-base orthopaedic alloy*. 1982, University of British Columbia.
142. Murr, L., *Open-cellular metal implant design and fabrication for biomechanical compatibility with bone using electron beam melting.* Journal of the mechanical behavior of biomedical materials, 2017. **76**: p. 164-177.
143. Darvish, K., et al., *Selective laser melting of Co-29Cr-6Mo alloy with laser power 180–360 W: Cellular growth, intercellular spacing and the related thermal condition.* Materials Characterization, 2018. **135**: p. 183-191.
144. Pham, M.-S., et al., *The role of side-branching in microstructure development in laser powder-bed fusion.* Nature communications, 2020. **11**(1): p. 1-12.
145. Lindahl, O. and A.G. Lindgren, *Cortical bone in man II. Variation in tensile strength with age and sex.* Acta Orthopaedica Scandinavica, 1967. **38**(1-4): p. 141-147.
146. Kitagawa, H., *Applicability of fracture mechanics to very small cracks or the cracks in the early stage.* Proc. of 2nd ICM, Cleveland, 1976, 1976: p. 627-631.
147. Radaj, D., *Ermüdungsfestigkeit: Grundlagen für Leichtbau.* Maschinen-und Stahlbau, SpringerVerlag, 1995.
148. Jastrzebski, Z.D., *Nature and properties of engineering materials.* 1976.
149. Suresh, S., *Fatigue of materials*. 2004: Cambridge university press.
150. Leuders, S., et al., *On the mechanical behaviour of titanium alloy TiAl6V4 manufactured by selective laser melting: Fatigue resistance and crack growth performance.* International Journal of Fatigue, 2013. **48**: p. 300-307.
151. Pippan, R. and A. Hohenwarter, *Fatigue crack closure: a review of the physical phenomena.* Fatigue & Fracture of Engineering Materials & Structures, 2017. **40**(4): p. 471-495.
152. Pavlou, D., et al., *Estimation of fatigue crack growth retardation due to crack branching.* Computational materials science, 2004. **29**(4): p. 446-452.
153. Meggiolaro, M.A., et al., *Quantitative Evaluation of Fatigue Crack Growth Retardation Due to Crack Branching.* 2004.
154. Biezma, M.V., C. Berlanga, and G. Argandona, *Relationship between microstructure and fracture types in a UNS S32205 duplex stainless steel.* Materials Research, 2013. **16**(5): p. 965-969.
155. Lynch, S., *Progression markings, striations, and crack-arrest markings on fracture surfaces.* Materials Science and Engineering: A, 2007. **468**: p. 74-80.
156. Kamath, C., et al., *Density of additively-manufactured, 316L SS parts using laser powder-bed fusion at powers up to 400 W.* The International Journal of Advanced Manufacturing Technology, 2014. **74**(1): p. 65-78.
157. Sun, Z., et al., *Selective laser melting of stainless steel 316L with low porosity and high build rates.* Materials & Design, 2016. **104**: p. 197-204.
158. Wei, K., et al., *Effect of energy input on formability, microstructure and mechanical properties of selective laser melted AZ91D magnesium alloy.* Materials Science and Engineering: A, 2014. **611**: p. 212-222.
159. Romano, S., et al., *LCF behaviour and a comprehensive life prediction model for AlSi10Mg obtained by SLM.* International Journal of fatigue, 2018. **117**: p. 47-62.

160. Sausto, F., et al., *Anisotropic mechanical and fatigue behaviour of Inconel718 produced by SLM in LCF and high-temperature conditions.* Fatigue & Fracture of Engineering Materials & Structures, 2021. **44**(1): p. 271-292.
161. Clavel, M. and A. Pineau, *Fatigue behaviour of two nickel-base alloys I: Experimental results on low cycle fatigue, fatigue crack propagation and substructures.* Materials Science and Engineering, 1982. **55**(2): p. 157-171.
162. Yuen, J., P. Roy, and W. Nix, *Effect of oxidation kinetics on the near threshold fatigue crack growth behavior of a nickel base superalloy.* Metallurgical Transactions A, 1984. **15**(9): p. 1769-1775.
163. Mercer, C., A. Soboyejo, and W. Soboyejo, *Micromechanisms of fatigue crack growth in a forged Inconel 718 nickel-based superalloy.* Materials Science and Engineering: A, 1999. **270**(2): p. 308-322.
164. Osinkolu, G., G. Onofrio, and M. Marchionni, *Fatigue crack growth in polycrystalline IN 718 superalloy.* Materials Science and Engineering: A, 2003. **356**(1-2): p. 425-433.
165. Forth, S.C., et al., *Fatigue crack growth rate and stress-intensity factor corrections for out-of-plane crack growth.* Journal of ASTM International, 2005. **2**(1): p. 1-14.
166. Oblak, J., D. Paulonis, and D. Duvall, *Coherency strengthening in Ni base alloys hardened by DO 22 γ′ precipitates.* Metallurgical Transactions, 1974. **5**(1): p. 143-153.
167. Devaux, A., et al., *Gamma double prime precipitation kinetic in Alloy 718.* Materials Science and Engineering: A, 2008. **486**(1-2): p. 117-122.
168. Zhang, B., et al., *Mechanical properties and microstructure evolution of selective laser melting Inconel 718 along building direction and sectional dimension.* Materials Science and Engineering: A, 2020. **794**: p. 139941.
169. Tucho, W.M., et al., *Microstructure and hardness studies of Inconel 718 manufactured by selective laser melting before and after solution heat treatment.* Materials Science and Engineering: A, 2017. **689**: p. 220-232.